EEG dipole source analysis in a realistic head model

EEG-dipoollokalisatie met behulp van een realistisch hoofdmodel

Bart Vanrumste

Promotoren: Prof. dr. I. Lemahieu
Prof. dr. P. Boon

Proefschrift ingediend tot het behalen van de graad van
Doctor in de Toegepaste Wetenschappen

Vakgroep Elektronica en Informatiesystemen
Voorzitter: Prof. dr. ir. J. Van Campenhout
Faculteit Toegepaste Wetenschappen
Academiejaar 2001 – 2002

UNIVERSITEIT
GENT

Acknowledgments

This work has been carried out as a joint cooperation between the Epilepsy Monitoring Unit of the Neurology Department and the MEDISIP research group of the Department of Electronics and Information Systems, both at Ghent University. With this work I have contributed to the development of techniques which analyze medical signals. The knowledge that patients with epilepsy may benefit from this, has been one of the major motivations to perform this research.

I want to thank all the people who contributed to this work. I especially wish to thank my promotor prof. dr. Ignace Lemahieu for the opportunity he offered me to perform this research in the MEDISIP group and for his support and motivation. Furthermore, prof. dr. Paul Boon, my co-promotor is gratefully acknowledged for having offered me the choice to perform this research in the Epilepsy Research group, for the insight he has given me in the area of epilepsy and for the support and motivation during the realization of this work. I also want to thank both promoters for the opportunity they have given me to present my work at international conferences.

Furthermore, I like to thank prof. dr. ir. Jan Van Campenhout, chairman of the Department of Electronics and Information Systems, for his feedback and interest in my research. Prof. dr. De Reuck, head of the Department of Neurology is kindly acknowledged for his hospitality to host me in his department. I want to thank prof. dr. Rik Achten, head of the MR department, for providing me MR images for the construction of the realistic head models.

I further want to thank the members of the MEDISIP group for the pleasant working atmosphere. More specifically I want to acknowledge dr. ir. Gert Van Hoey, for a fruitful cooperation in the area of EEG dipole source analysis. His profound way of working has been stimulating for me. I'm very grateful to the members of the weekly research meeting, chaired by dr. ir. Rik Van de Walle. Their feedback was of great value. I also want to thank Rita Breems for her secretarial assistance.

I want to thank the staff of the Department of Neurology for their sympathy and interest in my work. Especially ir. Michel D'Havé for his technical support and his constructive feedback. Also dr. Kristl Vonck is acknowledged for the pleasant cooperation and her continuous willingness to assist me in my research.

I'm very grateful to prof. dr. Ignace Lemahieu, prof. dr. Paul Boon, dr. ir. Rik Van de Walle, ir. Didier Bouden, ir. Peter Van Hese and lic. Philippe Gekiere for critically reading this thesis and making several constructive remarks. I believe that their suggestions have increased the clearness and the quality of my work.

Dr. Päivi Laarne of the Tampere University of Technology, Finland, is kindly acknowledged for her stimulating ideas on the finite difference method and for her hospitality during my stay there.

I also want to thank dipl.-math. Marcus Mohr of the University of Erlangen for the fruitful cooperation in the area of numerical methods and for his hospitality during my stay there.

'Het Bijzonder Onderzoeksfonds' of Ghent University and the 'Clinical Epilepsy Grant' of Ghent University Hospital are acknowledged for financially supporting this work.

Everyone who contributed to my education is also kindly acknowledged for their part in my personal discovery of the world we live in.

I acknowledge my family, friends and parents-in-law for their sympathy and support. I especially want to thank my parents who have respected and supported my personal choices and have been understanding throughout my education.

Finally, I want to dedicate this work to my wife Marleen, and my son Brecht whose presence, understanding and caring were indispensable during the preparation of this contribution.

ir. Bart Vanrumste
Ghent, June 20, 2001.

Abbreviations

BEM	boundary element method
CSF	cerebrospinal fluid
EEG	electro-encephalogram
FDM	finite difference method
FDRM	finite difference reciprocity method
FEM	finite element method
MR	magnetic resonance
PET	positron emission tomography
RRE	relative residual energy
SNR	signal-to-noise-ratio
SOR	successive overrelaxation
SPECT	single photon emission computed tomography
VCM	volume conductor model
VS	ventricular system

Contents

Hoofdstuk 0

Nederlandstalige samenvatting

0.1 Algemene inleiding

0.1.1 Situering van het onderzoek

Het elektro-encefalogram (EEG) meet potentiaalverschillen op het scalpoppervlak in functie van de tijd. Normaal worden er 20 tot 40 elektroden op de scalp geplaatst. Het EEG kan gebruikt worden voor de diagnose van epilepsie. Het EEG van epilepsiepatiënten heeft een abnormale amplitude en golfvorm, die kan gedetecteerd worden door een neuroloog. Dit EEG kan veroorzaakt worden door een actief focaal hersengebied dat de aanval uitlokt. Een methode om dit hersengebied te detecteren op basis van het EEG, is EEG-dipoollokalisatie. Door gebruik te maken van enerzijds een volumegeleidermodel van het hoofd en anderzijds een elektrisch bronmodel —hier een dipool— kan men pogen die bronparameters te zoeken die een potentiaaldistributie geven die best overeenstemt met de gemeten potentialen.

Het doctoraatsonderzoek dat hierna voorgesteld wordt, situeert zich in het gebied van EEG-dipoollokalisatie.

Overzicht

In paragraaf 0.2 wordt het begrip EEG-dipoollokalisatie ingeleid. Er wordt dieper ingegaan op de generators van het EEG. Epilepsie en de manifestaties van epilepsie in het EEG worden ook besproken. Verder wordt ook het zogenaamd voorwaarts probleem behandeld, dat voor een gegeven elektrische bron de potentialen berekent aan de elektroden. Het daarbij aansluitende invers pro-

bleem —van de potentialen naar de bron— wordt ook belicht.

Om het voorwaarts probleem op te lossen in een realistisch hoofdmodel kan men gebruik maken van de eindige-differentiemethode (Eng. FDM: finite difference method). In paragraaf 0.3 wordt een validatie gegeven van de FDM in combinatie met reciprociteit. Bij deze validatie wordt gebruik gemaakt van het analytisch-oplosbaar sferisch hoofdmodel.

In paragraaf 0.4 wordt de dipoolpositiefout berekend, veroorzaakt door fouten in het volumegeleidermodel. Eerst wordt de dipoolpositiefout onderzocht die ontstaat door het niet incorporeren van het ventriculair systeem (d.i. een holte gevuld met cerebrospinaal vocht). Daarna wordt de dipoolpositiefout onderzocht die ontstaat door het niet incorporeren van een gat in de schedel. Tenslotte wordt de dipoolpositiefout berekend, veroorzaakt door het verkeerd inschatten van de schedelgeleidbaarheid.

In paragraaf 0.5 vergelijken we de dipoolpositiefout die te wijten is aan ruis voor een sferisch hoofdmodel en voor een realistisch hoofdmodel. We proberen daarbij te weten te komen voor welk ruisniveau het sferisch model nagenoeg even goed scoort als het realistisch model.

Het EEG van twee patiënten wordt behandeld in paragraaf 0.6. De dipool wordt geschat gebruikmakend van een sferisch en een realistisch hoofdmodel.

Tenslotte worden de belangrijkste besluiten en de originele bijdragen nog eens opgesomd in paragraaf 0.7.

Publicatie van de onderzoeksresultaten

Dit doctoraatsonderzoek heeft geleid tot één artikel in een internationaal tijdschrift [135], één artikel voorwaardelijk aanvaard [138] in een internationaal tijdschrift, en één artikel ingediend bij een internationaal tijdschrift [137]. Daarnaast zijn er 15 bijdragen op internationale conferenties [122–134, 136, 139] geleverd. Bij al deze bijdragen was ik eerste auteur. Op twee conferenties werd dit werk bekroond [125, 134].

Vervolgens heb ik geassisteerd in het onderzoek van anderen, wat geleid heeft tot 6 publicaties als coauteur [11, 14, 18, 98, 107, 115]. Ik word ook vermeld als coauteur in 21 abstracts en artikels die verschenen zijn in de verslagen van internationale conferenties [10, 13, 16, 17, 19, 70, 97, 106, 108–114, 116–121].

Verder werden 2 thesissen [21, 94] begeleid die betrekking hebben op dipoollokalisatie.

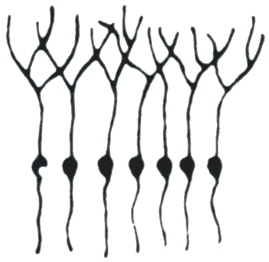

Figuur 1: Piramidale cellen in een open bronconfiguratie. Van [101].

0.2 EEG-dipoollokalisatie van epileptische golven

0.2.1 Elektro-encefalografie (EEG)

Wat genereert het EEG?

De neurofysiologische basis van het EEG vindt men terug in [102]. De hersenen bestaan uit 10^{10} zenuwcellen of neuronen. Slechts een bepaald type neuronen is verantwoordelijk voor het EEG, nl. de piramidale cellen, weergegeven in figuur 1. Op een bepaald moment van hun werking wordt er op een bepaalde plaats langs de lengteas lading geïnjecteerd in het extracellulair milieu, terwijl er op een andere plaats langs dezelfde lengte-as lading verwijderd wordt uit het extracellulair milieu. Om meetbare scalppotentialen te genereren moet er een cluster piramidale cellen nagenoeg synchroon deze activiteit vertonen. Verder moet de configuratie van deze cellen zo zijn dat ze elkaars extracellulair veld versterken, zoals geïllustreerd in figuur 1. We spreken dan van een open bronconfiguratie.

0.2.2 Epilepsie

Epilepsie is een hersenaandoening waarbij af en toe een overmatige, synchrone, elektrische hersenactiviteit optreedt, in een beperkte of uitgestrekte hersenzone [77]. Een epileptische aanval, die gepaard gaat met deze elektrische activiteit, kan zich manifesteren in de vorm van korte perioden van afwezigheid, spanning van de spieren, stuiptrekkingen en bewustzijnsindaling. De oorzaken kunnen velerlei zijn: hersenschade bij een ongeval, de aanwezigheid van tumoren, intoxicaties, of aangeboren afwijkingen van het hersenweefsel. Ongeveer 0.5 % tot 1 % van de bevolking lijdt aan epilepsie [8].

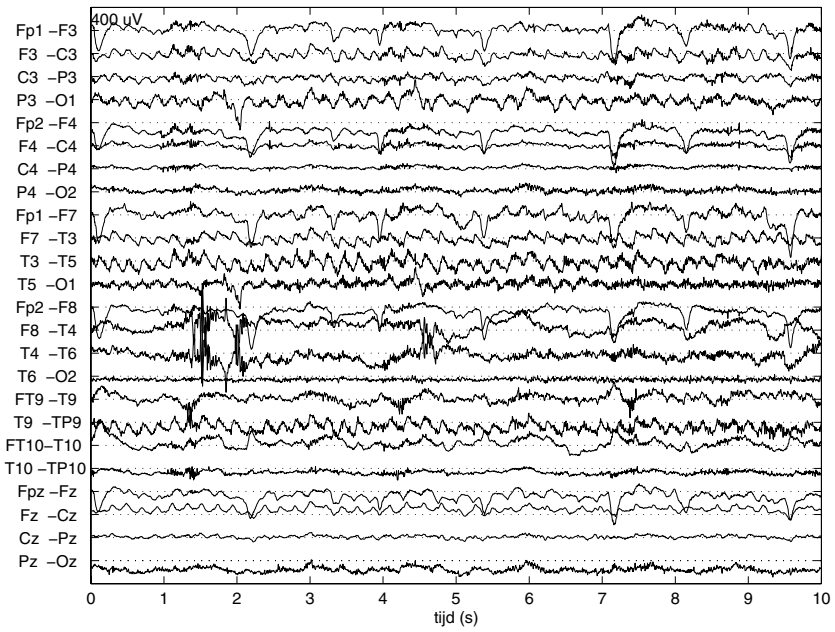

Figuur 2: Een fragment van 10 s tijdens een aanval.

De epilepsieaanvallen kunnen ingedeeld worden in twee groepen. Enerzijds hebben we de partiële aanvallen, waarbij slechts een beperkte hersenzone betrokken is. Anderzijds zijn er de gegeneraliseerde aanvallen, waarbij de epileptische elektrische activiteit in het hele brein aanwezig is.

Het EEG bij aanvang van een aanval wordt gekenmerkt door een ritmische activiteit met een frequentie van 5 tot 6 Hz. Dit EEG wordt ook wel het ictaal EEG genoemd en is geïllustreerd in figuur 2.

Naast het ictaal EEG hebben we ook fragmenten tussen aanvallen door, die wijzen op epilepsie. De fragmenten noemt men interictaal EEG, en kunnen door een neuroloog gedetecteerd worden. Figuur 3 illustreert interictaal EEG. Voor t = 4.5 s wordt een zogenaamde ‘spike’ getoond.

Epilepsieheelkunde

Verschillende criteria dienen voldaan te zijn alvorens men overgaat tot epilepsieheelkunde. Vooreerst dient nagegaan te worden of anti-epileptische medicatie geen invloed heeft op het onderdrukken van aanvallen. Dit schijnt zo te zijn voor ongeveer 25 % van de patiënten met epilepsie [8]. Men spreekt dan van refractaire epilepsie. Daarnaast dient er een focaal gebied verantwoordelijk te

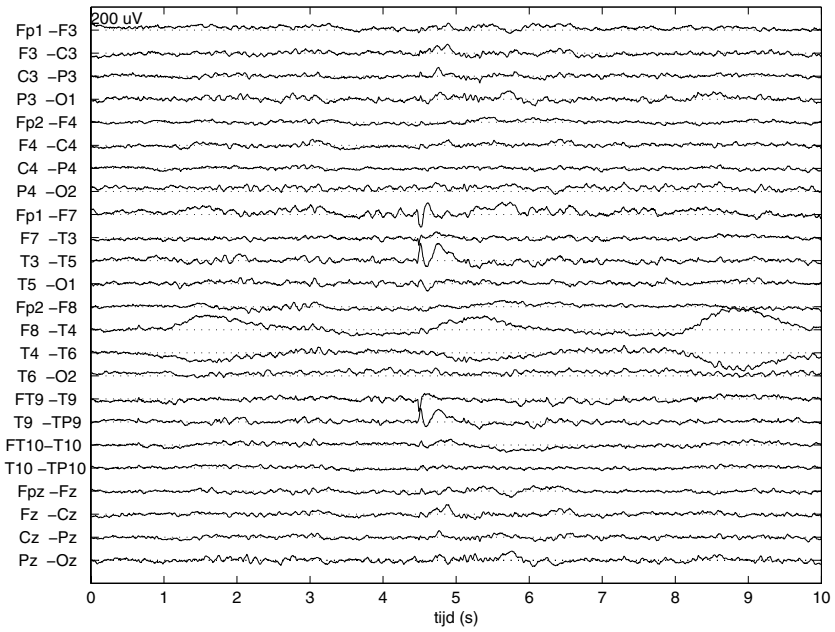

Figuur 3: Een fragment van 10 s interictaal EEG. Op t = 4.5 s merkt men een spike op.

zijn voor de start van de aanval. Tenslotte mag de verwijdering van het stukje hersenweefsel niet leiden tot belangrijke neurologische stoornissen.

Om het focale gebied —ook wel epileptogene zone genoemd— te detecteren worden er verschillende preheelkundige onderzoeken uitgevoerd. Eén van die onderzoeken is langetermijn video/EEG-monitoring (3 tot 5 dagen). De medicatie kan dan verminderd worden, zodat een registratie van een habituele aanval mogelijk is. Door interpretatie van het EEG en het gedrag bij aanvang van een aanval, kan men de epileptogene zone lokaliseren. Verder wordt ook gebruik gemaakt van medische beeldvorming en neuropsychologische testen, ter aanduiding van de epileptogene zone. De hierboven vermelde onderzoeken zijn niet-invasief en brengen dus geen risico op complicaties met zich mee.

Wanneer alle onderzoeken hetzelfde gebied suggereren, dan kan er een heelkundige ingreep gepland worden, zodra men kan aanduiden dat er zich geen neurologische stoornissen zullen voordoen door de verwijdering van het stukje hersenweefsel. Als de onderzoeken niet eenduidig hetzelfde gebied suggereren, wordt normaal overgegaan tot het plaatsen van diepte-elektroden in het hersenweefsel. De elektroden worden dan geplaatst rond mogelijke kandidaat epileptogene zones. Dit is een invasief onderzoek met een reëel risico op complicaties [8].

EEG-dipoollokalisatie, gebruikmakend van epileptische golven

Wanneer we het ictaal of interictaal EEG inspecteren, is het mogelijk om een kwalitatieve lokalisatie uit te voeren. Naburige elektrodekoppels die een sterk signaal meten in vergelijking met andere koppels, bevinden zich dicht bij de elektrische bron. Wanneer we nu gebruik maken van een volumegeleidermodel en een bronmodel, kunnen we ook op een kwantitatieve manier de generator van het EEG bepalen. Als we een stroomdipool veronderstellen als bron en een sferisch hoofdmodel, (dit wordt in volgende paragraaf uitgewerkt) dan kunnen we de dipoolparameters schatten voor een gegeven EEG. Deze handeling wordt ook wel EEG-dipoollokalisatie genoemd. Figuur 4 illustreert een geschatte dipool voor interictaal EEG.

Dipoollokalisatie kan beschouwd worden als een bijkomend niet-invasief onderzoek in de preheelkundige evaluatie van epilepsiepatiënten. Dit bijkomend onderzoek wordt uitgevoerd in de hoop het aantal invasieve registraties terug te schroeven. Een recente publicatie van onze onderzoeksgroep bevestigt deze hoop [14].

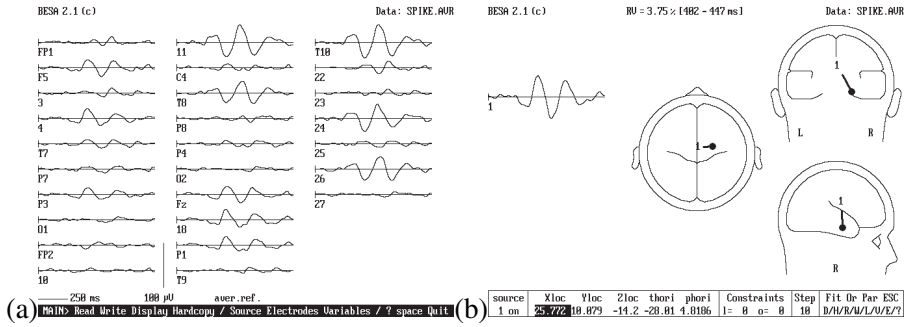

Figuur 4: Het interictaal EEG (a) te samen met de geschatte dipool (b) in een sferisch hoofdmodel.

0.2.3 Het voorwaarts probleem

Het voorwaarts probleem start van een gegeven elektrische bron en berekent de potentialen aan de scalpelektroden.

Poissons vergelijking en de randvoorwaarden

Voor het frequentiegebied dat van toepassing is voor EEG-signalen, zijn de capacitieve en inductieve effecten in het volumegeleidermodel van het hoofd verwaarloosbaar [82]. Zo kan het volumegeleidermodel als puur resistief gezien worden.

Uit de vergelijkingen van Maxwell kan men dan Poissons differentiaalvergelijking afleiden [62]:

$$\nabla \cdot (\sigma \nabla V) = -I\delta(\mathbf{r} - \mathbf{r}_2) + I\delta(\mathbf{r} - \mathbf{r}_1). \tag{1}$$

Hier stelt V de potentiaal voor in een punt $\mathbf{r}$ van het volumegeleidermodel, σ is de geleidbaarheid ter hoogte van $\mathbf{r}$. Het macroscopisch punt, waar een cluster neuronen lading injecteert in het extracellulair milieu, wordt voorgesteld door $\mathbf{r}_1$. In het macroscopisch punt $\mathbf{r}_2$ verwijdert de cluster neuronen, lading van het extracellulair milieu. De $\delta(\mathbf{r} - \mathbf{r}_*)$ stelt de deltafunctie voor.

Tussen een compartiment met geleidbaarheid σ_1 en dat met geleidbaarheid σ_2 gelden de volgende randvoorwaarden:

$$\mathbf{J_1} \cdot \mathbf{e}_n = \mathbf{J_2} \cdot \mathbf{e}_n, \tag{2}$$

$$(\sigma_1 \nabla V_1) \cdot \mathbf{e}_n = (\sigma_2 \nabla V_2) \cdot \mathbf{e}_n, \tag{3}$$

met $\mathbf{e}_n$ de normaalvector met eenheidslengte op de rand en $\mathbf{J}$ de stroomdichtheidsvector, met eenheden I/m^2. De stroom die het ene compartiment verlaat

dient het andere binnen te dringen. Er is aldus geen opstapeling van lading mogelijk.

Geen stroom kan vloeien in de lucht buiten het hoofd, omdat de geleidbaarheid van lucht quasi nul is. We verkrijgen aldus voor de buitenrand van het hoofd de homogene Neumann randvoorwaarden:

$$\mathbf{J_1} \cdot \mathbf{e}_n = 0, \tag{4}$$

$$(\sigma_1 \nabla V_1) \cdot \mathbf{e}_n = 0. \tag{5}$$

Verder gelden voor de binnenranden, die niet met lucht verbonden zijn, de Dirichlet randvoorwaarden:

$$V_1 = V_2. \tag{6}$$

De stroomdipool

Daar $\mathbf{r}_1$ en $\mathbf{r}_2$ zeer dicht bij elkaar gelegen zijn, kan men ook spreken van een stroomdipool. De stroomdipool wordt beschreven door een positieparameter $(\mathbf{r}_1 + \mathbf{r}_2)/2$. Verder wordt de stroomdipool ook nog beschreven door een oriëntatieparameter gegeven door de eenheidsvector $\mathbf{e}_d$, gaande van de monopool die stroom verwijdert, naar de monopool die stroom injecteert. De dipoolsterkte is gegeven door $I.q$ met $q = |\mathbf{r}_1 - \mathbf{r}_2|$. De dipooloriëntatie en de dipoolsterkte worden soms verenigd in de dipoolmomentvector $\mathbf{d}$:

$$\mathbf{d} = I\ q\ \mathbf{e_d}. \tag{7}$$

Oplossingen van het voorwaarts probleem met een dipool

De vergelijking van Poisson kan analytisch opgelost worden voor een dipool in een drielagig sferisch hoofdmodel [2, 91]. Het binnenste compartiment krijgt dan de geleidbaarheid van de hersenen, de schil erboven de geleidbaarheid van de schedel en de buitenste schil de geleidbaarheid van de scalp.

Door de vooruitgang in de medische beeldvorming is het mogelijk om een 3D-beeld van het hoofd van een patiënt te maken. Daarbij wordt het beeld gesegmenteerd [43] in verschillende compartimenten. Aan elk compartiment wordt een geleidbaarheid toegekend, afhankelijk van het soort weefsel in dat compartiment. Zo kan men een meer realistisch volumegeleidermodel construeren. In deze complexe geometrie kan de vergelijking van Poisson slechts numeriek opgelost worden.

De randelementenmethode (Eng. boundary element method BEM) is één van de methodes om Poissons vergelijking numeriek op te lossen. Hier worden de randen van de verschillende compartimenten bedekt met driehoekjes. De

potentialen kunnen dan berekend worden voor de hoekpunten van de driehoeken of in de centra van de driehoeken. Deze punten worden ook wel knopen genoemd. De potentialen aan de knopen worden bekomen door een matrix te inverteren waarvan de rang gelijk is aan het aantal knopen, gevolgd door een matrixvermenigvuldiging. Voor een andere dipool hoeven we dan slechts de matrixvermenigvuldiging opnieuw uit te voeren, wat een snelle operatie is. Dit is een interessante eigenschap daar in het invers probleem (zie later) verschillende voorwaartse evaluaties nodig zijn. Voor elk compartiment dat men bijvoegt, wordt het steeds lastiger om de matrix te inverteren, wat het aantal compartimenten limiteert in de randelementenmethode. Verdere referenties naar de randelementenmethode vindt men in [32, 35, 40, 68, 96].

De eindige-elementenmethode (Eng. finite element method FEM) is ook een numerieke methode die de vergelijking van Poisson oplost in het hele volumegeleidermodel. We delen het volume op in kleine aaneensluitende elementen, bijvoorbeeld tetraëders. Hier is het in principe mogelijk elk volume-elementje een andere geleidbaarheid toe te kennen. In elk hoekpunt van zo'n element kunnen we dan de potentiaal berekenen voor een gegeven dipool. Per knoop is er een vergelijking beschikbaar, waarin de potentiaal voor die knoop en naburige potentialen een lineaire combinatie vormen. We verkrijgen zo een systeemmatrix waarvan de rang gelijk is aan het aantal knopen. Het direct inverteren, zoals voor de randelementenmethode, is niet meer mogelijk door de veelheid aan knopen. We maken dan gebruik van iteratieve oplossingsmethoden voor ijle systeemmatrices [29]. De gesegmenteerde MR beelden worden weergegeven in een 1 mm^3 kubisch rooster, zodat deze geometrie nog dient getransformeerd te worden naar een tetraëdrisch rooster [104]. Meer informatie over de eindige-elementenmethode in het domein van EEG-dipoollokalisatie kan gevonden worden in [5, 25, 50, 141, 144].

De eindige-differentiemethode

In het verder verloop van dit werk gebruiken we de eindige-differentiemethode (Eng. finite difference method FDM). Deze methode stelt ons in staat een groot aantal compartimenten in te voeren. Verder kan het kubisch rooster op een eenvoudige manier opgesteld worden vertrekkende van de gesegmenteerde MR-beelden. Bovendien zijn er efficiënte iteratieve methoden voorhanden voor het oplossen van ijle matrices voortkomend van gestructureerde roosters. Een voorbeeld is de meerroostermethode (Eng: multigrid method) [22]. Anisotropie kan ook geïncorporeerd worden in het volumegeleidermodel [90]. De laatste twee voordelen worden echter niet uitgebuit in dit doctoraat.

Veronderstellen we een punt P in het centrum van een kubus G_0 met ribbe

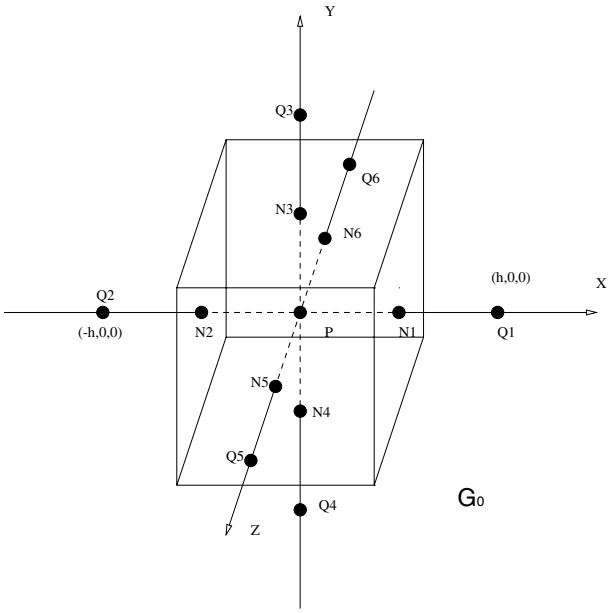

Figuur 5: Een punt P met zijn buren Q_i $(i = 1 \cdots 6)$. De kubus G_0 wordt ook voorgesteld.

h. De geleidbaarheid in de kubus is σ_0. De buren langs de Cartesiaanse assen worden voorgesteld met Q_i $(i = 1, \ldots, 6)$, zoals geïllustreerd in figuur 5. Poissons vergelijking is omgevormd tot een lineaire vergelijking, door gebruik te maken van het 'box integration scheme' [69]. We bekomen dan:

$$\sum_{i=1}^{6} \alpha_i V_{Q_i} - \alpha_0 V_P = I_P, \tag{8}$$

met α_i en α_0:

$$\begin{aligned} \alpha_i &= 2h \frac{\sigma_0 \sigma_i}{\sigma_0 + \sigma_i}, \\ \alpha_0 &= \sum_{i=1}^{6} \alpha_i. \end{aligned}$$

Het rechterlid van de vergelijking (8) is:

$$I_P = \int\int\int_{G_0} \begin{array}{l} -I\delta(x - x_2)\delta(y - y_2)\delta(z - z_2) \\ +I\delta(x - x_1)\delta(y - y_1)\delta(z - z_1) \end{array} dx\, dy\, dz. \tag{9}$$

Wanneer volume G_0 één van beide monopolen bevat, wordt I_P gelijk aan I of $-I$. De eenheid van α_i is Ω^{-1}. Wanneer verder $I_P = 0$, dan stelt vergelijking

(8) de knooppuntswet van Kirchoff voor. Voor elk kubuscentrum verkrijgen we aldus een lineaire vergelijking. Veronderstellen we dat het hoofd opgedeeld is in n kubussen, dan stelt $\mathbf{V} \in \mathbb{R}^{n\times 1}$ de potentialen voor in de kubuscentra en $\mathbf{I} \in \mathbb{R}^{n\times 1}$ de rechterleden van vergelijking (8). De systeemmatrix $\mathbf{A} \in \mathbb{R}^{n\times n}$ heeft per rij maximaal 6 niet-diagonaalelementen verschillend van nul, zoals geïllustreerd in vergelijking (8). Daarbij is $\mathbf{A}$ ijl. In matrixnotatie verkrijgen we dan :

$$\mathbf{A}\,\mathbf{V} = \mathbf{I}. \tag{10}$$

Dit stelsel wordt opgelost door gebruik te maken van iteratieve oplossingsmethoden voor ijle matrices. Wij pasten 'successive overrelaxation' toe [84].

0.2.4 Het invers probleem

Het invers probleem schat de elektrische bronparameters voor een gegeven EEG. Vooreerst dient men op te merken dat een gegeven potentiaaldistributie niet correspondeert met één unieke bronconfiguratie t.t.z. verschillende bronconfiguraties kunnen dezelfde potentiaaldistributie genereren. Om het aantal mogelijke oplossingen te reduceren, maken we gebruik van het dipoolmodel. We onderstellen dan een dipool met een vaste positie en een vaste oriëntatie in functie van de tijd. De dipoolsterkte kan wel nog variëren in functie van de tijd. Dit blijkt een goed model te zijn voor focale activiteit.

Dipoollokalisatie voor één tijdsmonster

Het oplossen van het invers probleem gaat gepaard met het iteratief veranderen van de dipoolparameters. De dipoolparameters zijn de dipoolpositie $\mathbf{r} = (x, y, z)^T \in \mathbb{R}^{3\times 1}$, en de dipoolmomentvector die men kan ontbinden in zijn Cartesiaanse dipoolcomponenten, $\mathbf{d} = (d_x, d_y, d_z)^T \in \mathbb{R}^{3\times 1}$. Figuur 6 illustreert de drie componenten. De potentialen aan de l elektroden voor een dipool met positieparameters $\mathbf{r}$ en dipoolcomponenten $\mathbf{d}$, zijn voorgesteld door $\mathbf{U}_{model} \in \mathbb{R}^{l\times 1}$. De relatie tussen de dipoolcomponenten $\mathbf{d}$ en de potentialen $\mathbf{U}_{model}$ wordt weergegeven door een matrixoperator $\mathbf{L} = (\mathbf{U}(\mathbf{r}, \mathbf{e}_x), \mathbf{U}(\mathbf{r}, \mathbf{e}_y), \mathbf{U}(\mathbf{r}, \mathbf{e}_z)) \in \mathbb{R}^{l\times 3}$, de 'leadfield' operator:

$$\mathbf{U}_{model} = \mathbf{L}(\mathbf{r}) \cdot \mathbf{d}, \tag{11}$$

met $\mathbf{U}(\mathbf{r}, \mathbf{e}_x) \in \mathbb{R}^{l\times 1}$ de potentialen aan de elektroden voor een dipool met positie $\mathbf{r}$, en met dipoolmomentvector $\mathbf{e}_x$ de eenheidsvector langs de x-as. Op een analoge manier zijn $\mathbf{U}(\mathbf{r}, \mathbf{e}_y)$ en $\mathbf{U}(\mathbf{r}, \mathbf{e}_z)$ bepaald.

Het EEG gemeten aan de l elektroden wordt weergegeven door $\mathbf{U}_{in} \in \mathbb{R}^{l\times 1}$. Voor het gegeven EEG, worden die dipoolparameters gezocht die de

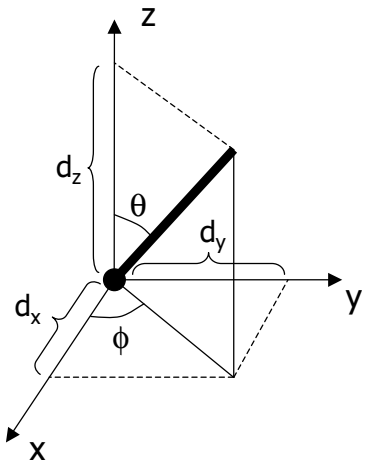

Figuur 6: De drie componenten van de dipool.

relatief residuele energie (RRE) minimaliseren:

$$RRE = \frac{\|\mathbf{U}_{in} - \mathbf{U}_{model}\|^2}{\|\mathbf{U}_{in}\|^2}.$$

met $\|.\|^2$ de Euclidische norm. De RRE geeft de fractie van de energie aan die niet met een dipool kan verklaard worden.

De zoekruimte is 6-dimensionaal voor één tijdsmonster. We moeten de 3 positieparameters en de 3 componenten schatten. We kunnen evenwel de zoekruimte terugbrengen van 6 naar 3 dimensies, door voor elke dipoolpositie $\mathbf{r}$ de optimale componenten $\mathbf{d}_{opt}$ te berekenen als oplossing van het overgedetermineerd stelsel vergelijkingen $\mathbf{U}_{in} = \mathbf{L}(\mathbf{r}) \cdot \mathbf{d}$. Er wordt hier gebruik gemaakt van de kleinste-kwadratenoplossing [29]:

$$\mathbf{d}_{opt} = \mathbf{L}^{+} \cdot \mathbf{U}_{in},$$

met $\mathbf{L}^{+} = (\mathbf{L}^T\mathbf{L})^{-1}\mathbf{L}^T$ de Moore-Penrose pseudo-inverse van $\mathbf{L}$. De RRE wordt dan:

$$RRE = \frac{\|\mathbf{U}_{in} - \mathbf{L} \cdot \mathbf{d}_{opt}\|^2}{\|\mathbf{U}_{in}\|^2} = \frac{\|(\mathbf{1_l} - \mathbf{L}\mathbf{L}^{+}) \cdot \mathbf{U}_{in}\|^2}{\|\mathbf{U}_{in}\|^2}, \qquad (12)$$

met $\mathbf{1_l} \in \mathbb{R}^{l \times l}$ de eenheidsmatrix. Hier is de RRE enkel afhankelijk van $\mathbf{r}$. De oplossing van EEG-dipoollokalisatie wordt dus gevonden door iteratieve aanpassing van de 3 positieparameters.

Dipoollokalisatie voor meerdere tijdsmonsters

Dipoollokalisatie kan ook uitgevoerd worden voor een tijdsinterval van s monsterwaarden. Het gemeten EEG kan dan als volgt voorgesteld worden: $\mathbf{U}_{in} \in \mathbb{R}^{l \times s}$.

We veronderstellen een dipool met een vaste positie en een vaste oriëntatie, maar met een variërende dipoolsterkte als functie van de tijd als onderliggende bron. De oriëntatieparameters van de dipool, voorgesteld met $\mathbf{e}_d$ in vergelijking (7), kunnen ook weergegeven worden door de hoeken ϕ, θ (zie figuur 6). De potentialen berekend met het volumegeleidermodel $\mathbf{U}_{model} \in \mathbb{R}^{l \times s}$ zijn dan:

$$\mathbf{U}_{model} = \mathbf{L}(\mathbf{r}) \cdot \mathbf{e}_d(\phi, \theta) \cdot \mathbf{a}, \tag{13}$$

met $\mathbf{e}_d \in \mathbb{R}^{3 \times 1}$ de eenheidscomponenten, en $\mathbf{a} \in \mathbb{R}^{1 \times s}$ de dipoolsterkte in functie van de tijd. We kunnen hier de optimale $\mathbf{a}_{opt}$ berekenen voor een gegeven dipoolpositie en gegeven eenheidscomponenten door het oplossen van $\mathbf{U}_{in} = \mathbf{L} \cdot \mathbf{e}_d \cdot \mathbf{a}$ volgens de kleinste-kwadratenmethode. Als RRE vinden we dan:

$$RRE = \frac{\|\mathbf{U}_{in} - \mathbf{L}\mathbf{e}_d\mathbf{a}_{opt}\|_F^2}{\|\mathbf{U}_{in}\|_F^2} = \frac{\|(\mathbf{1}_l - (\mathbf{L}\mathbf{e}_d)(\mathbf{L}\mathbf{e}_d)^+)\mathbf{U}_{in}\|_F^2}{\|\mathbf{U}_{in}\|_F^2}, \tag{14}$$

met $\| \cdot \|_F$ de Frobeniusnorm [29].

De minimalisatie van de RRE wordt uitgevoerd gebruikmakend van het Nelder-Mead simplex-algoritme [75, 84].

0.3 Validatie van de FDRM

0.3.1 Inleiding en methoden

De FDM en de FEM kunnen gemakkelijk een groot aantal compartimenten met elk hun specifieke geleidbaarheid introduceren. Dit in tegenstelling tot de BEM, die slechts enkele compartimenten vlot kan behandelen. Doordat het volume gediscretiseerd wordt, i.p.v. het oppervlak zoals bij BEM, hebben we bij de FDM en FEM een groot aantal onbekenden (de potentialen in de knopen) en vergelijkingen. Dit heeft tot gevolg dat het oplossen van het stelsel vergelijkingen volgens de klassieke directe methode niet haalbaar is en dat we onze toevlucht moeten nemen tot iteratieve methoden. Iteratieve methoden geven de oplossing van het stelsel voor een gegeven bronconfiguratie. Voor een gegeven dipool zou men dan het voorwaarts probleem kunnen oplossen door de potentialen te berekenen met de iteratieve methoden. Eén zo'n berekening voor een 2 mm en 3 mm rooster duurt respectievelijk 2 min 7 s en 25 s. Het oplossen van

het invers probleem wordt dan wel zeer rekenintensief, daar in het invers probleem typisch honderden voorwaartse evaluaties nodig zijn. Gebruikmakend van reciprociteit, kan men het aantal keren dat een iteratieve methode dient toegepast te worden, enkel afhankelijk maken van het aantal elektroden. In dit onderzoek maken we gebruik van de eindige-differentiemethode in combinatie met reciprociteit (Eng. finite difference reciprocity method FDRM). De bedoeling van dit onderzoek bestaat erin de nauwkeurigheid van de dipoollokalisatie te valideren gebruikmakend van de FDRM in het drielagig sferisch model.

Het sferisch hoofdmodel bestaat uit drie compartimenten. Van binnen naar buiten hebben we het hersen-, schedel- en scalpcompartiment. De drie randen tussen de compartimenten hebben een straal van 80 mm, 85 mm en 92 mm. De schedelgeleidbaarheid is nog controversiëel. Sommige groepen gebruiken een schedelgeleidbaarheid die 16 keer lager ligt dan de geleidbaarheid van het zachte weefsel (scalp en hersenen) [53, 80]. Andere groepen rapporteren een schedelgeleidbaarheid die 80 keer lager ligt dan de geleidbaarheid van het zachte weefsel [27, 37, 87]. We hebben gekozen voor de laatste waarde daar er ook gevonden is dat de fouten in de dipoolpositie en -oriëntatie groter zijn wanneer die waarde gebruikt wordt [56]. We beschouwen hier dus de resultaten onder de slechtste condities.

De validatie van de dipoollokalisatie gebruikmakend van FDRM gebeurt als volgt: voor 1743 testdipolen, gelegen in het coronale vlak, gaande door het centrum van het sferisch hoofdmodel, wordt de potentiaal aan de scalpelektroden berekend, gebruikmakend van de analytisch uitdrukking. Dit levert ons de exacte potentialen aan de scalpelektroden. Dan wordt het invers probleem opgelost voor een set van deze potentialen, gebruikmakend van FDRM als voorwaartse evaluatie. Daarbij wordt de afstand tussen de originele dipoolpositie en de geschatte positie berekend. Verder wordt ook de hoek tussen de originele en geschatte dipoolmomentvector berekend.

Deze simulaties zijn uitgevoerd voor een kubisch rooster met een ribbe van 2 mm en 3 mm.

Verder hebben we een set van 27 en 44 elektroden gebruikt, dit om de invloed van het aantal elektroden op de dipoolpositie- en -oriëntatiefout te bestuderen. Figuur 7 toont de elektrode posities en de Cartesiaanse assen. De Cartesiaanse assen zijn hier en in het verdere verloop van het werk als volgt georiënteerd: de x-as gaat van het linkeroor naar het rechteroor, de y-as gaat van achter naar voor en de z-as gaat van onder naar boven.

We hebben aldus 4 configuraties nl. VGM-2mm-44el, VGM-2mm-27el, VGM-3mm-44el en VGM-3mm-44el (VGM staat voor volumegeleidermodel).

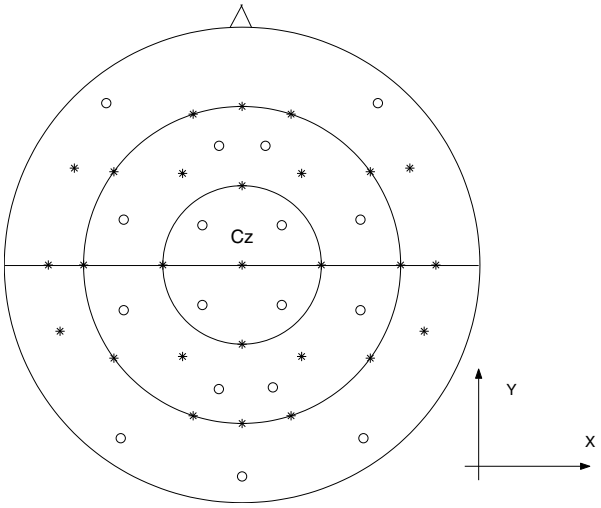

Figuur 7: Het bovenaanzicht van de elektrodeposities. De 27 elektroden '*' en de 17 bijkomende elektroden ∘ zijn aangeduid. Tevens zijn de x- en de y-as aangeduid. De grote cirkels stellen posities voor met een constante azimutale hoek θ. Van de binnennaar de buitencircel is θ respectievelijk 45°, 90° en 120°.

0.3.2 Reciprociteit

Om de potentiaal U_{AB} tussen twee scalpelektroden A en B te weten te komen voor een dipool met positie $\mathbf{r} \in \mathbb{R}^{3\times1}$ en componenten $\mathbf{d} \in \mathbb{R}^{3\times1}$, gaat men als volgt te werk: we injecteren een virtuele stroom I_{AB} in elektrode A en verwijderen dezelfde hoeveelheid stroom in B. We berekenen voor deze bronconfiguratie, gebruikmakend van de FDM, de potentialen V in de knopen van het volumegeleidermodel. (merk op dat we de notatie U gebruiken voor elektrodepotentialen, terwijl we de notatie V gebruiken voor potentialen bekomen met het numeriek model) Voor de werking van de FDM verwijzen we naar paragraaf 0.2. In figuur 8 zijn stroomdichtheidsvectoren $\mathbf{J} = -\sigma\nabla V$ en de equipotentiaallijnen aangeduid in het hersencompartiment. Gebruikmakend van reciprociteit [62, 88] kunnen we schrijven:

$$U_{AB}(\mathbf{r}, \mathbf{d}) = \frac{\mathbf{d}^T \cdot \nabla V(\mathbf{r})}{I_{AB}}, \tag{15}$$

met $\nabla V(\mathbf{r}) = (\partial V/\partial x, \partial V/\partial y, \partial V/\partial z)^T \in \mathbb{R}^{3\times1}$. We hebben zo via een omweg de potentiaal U_{AB} berekend, niet door een stroomdipool als bron te gebruiken, maar door twee monopolen ter hoogte van scalpelektroden te ge-

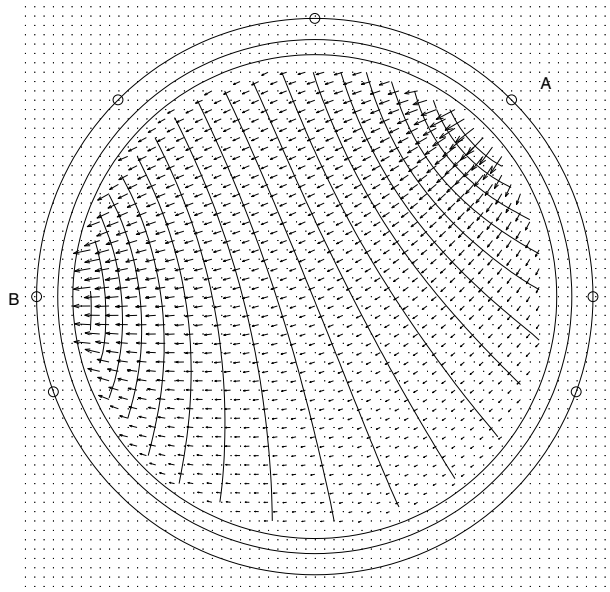

Figuur 8: De stroomdichtheidsvectoren **J** en de equipotentiaallijnen voor een stroom die geïnjecteerd wordt aan elektrode A en verwijderd wordt aan elektrode B.

bruiken. Wanneer we voor andere dipoolparameters het potentiaalverschil dienen te weten, dan hoeven we niet opnieuw een numerieke berekening uit te voeren. Dan is het voldoende vergelijking (15) te herevalueren, wat de rekenbelasting aanzienlijk vermindert. Verder hoeft de dipoolpositie niet samen te vallen met een knoop. Er kan gebruik gemaakt worden van trilineaire interpolatie bij het berekenen van $\nabla V(\mathbf{r})$. We willen hier nog eens benadrukken dat met één numerieke berekening, het potentiaalverschil U_{AB} kan bekomen worden voor alle mogelijke dipoolposities en -oriëntaties.

Wanneer er nu l elektroden zijn, kunnen we daaruit $l-1$ lineair onafhankelijke potentialen distilleren. We dienen aldus $l-1$ keer op iteratieve wijze een stelsel op te lossen met een monopool ter hoogte van één elektrode en een andere monopool ter hoogte van een andere elektrode.

0.3.3 Dipoollokalisatiefouten door de FDRM

Het drielagig sferisch model wordt gediscretiseerd in twee roosters. Het ene heeft 110483 kubussen met ribbe 3 mm en het andere heeft 372189 kubussen met ribbe 2 mm. Voor de 27 en 44 elektroden moeten we dan 26 en 43 keer het voorwaarts probleem numeriek oplossen. In elke kubus berekenen we de

	CPU-tijd		grootte datastructuur	
	26 voorw	43 voorw	26 voorw	43 voorw
3 mm	10 min 50 sec	17 min 55 sec	22 Mbyte	36 Mbyte
2 mm	55 min 02 sec	91 min 01 sec	74 Mbyte	122 MByte

Tabel 1: De CPU-tijd en de grootte van de datastructuur voor een 3 mm en een 2 mm rooster.

potentiaal door gebruik te maken van de 'successive overrelaxation method (SOR)'. Tabel 0.3.3 geeft de CPU-tijd weer voor een SUN Ultra 60, 360 MHz. De grootte van de datastructuren is ook gegeven.

De gemiddelde positiefout voor de 1743 testdipolen bij gebruik van VGM-2mm-44el is 2.0 mm, voor VGM-2mm-27el is dit 2.2 mm, voor VGM-3mm-44el 3.1 mm, en voor VGM-3mm-27el 3.4 mm.

Figuur 9 stelt de cumulatieve distributie voor, voor de vier onderzochte configuraties en voor de gegeven 1743 testdipolen. We stellen vast dat de positiefout in het algemeen kleiner is dan het dubbel van de roostergrootte, i.e. 4 mm voor een 2 mm rooster en 6 mm voor een 3 mm rooster. Dit is zelfs onafhankelijk van de keuze van het aantal elektroden.

In figuur 10 is de positiefout weergegeven in functie van de testdipoolpositie en -oriëntatie. De eerste en tweede rij stellen de resultaten voor, voor de configuraties VGM-2mm-44el en VGM-3mm-44el, respectievelijk. De eerste, tweede en derde kolom stellen positiefouten voor, voor dipolen die respectievelijk parallel met de x-as, y-as en z-as georiënteerd worden.

Het is duidelijk dat voor een rooster van 3 mm grotere fouten op te merken zijn dan voor een rooster van 2 mm.

De fouten zijn duidelijk te wijten aan het gebruik van een rooster met een knooppuntafstand verschillend van nul. De links-rechtssymetrie is te wijten aan het feit dat zowel de elektrodeposities als het rooster links-rechtssymetrisch zijn.

We hebben verder vastgesteld dat de oriëntatiefouten kleiner zijn dan 4° en dit voor alle configuraties.

We hebben ook de ruisgevoeligheid bij het oplossen van het invers probleem bij gebruik van de FDRM onderzocht. We vonden dat de ruisgevoeligheid bij gebruik van de FDRM in de inverse berekeningen niet groter is dan de ruisgevoeligheid bij gebruik van de analytische uitdrukking in de inverse berekeningen.

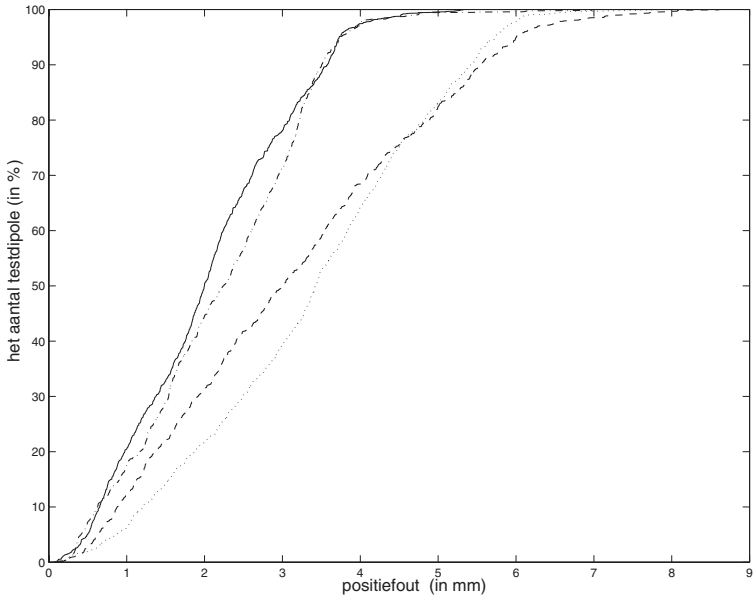

Figuur 9: De cumulatieve distributie van de dipoolpositiefout voor de configuraties VGM-2mm-44el(-), VGM-2mm-27el($\cdot - \cdot$), VGM-3mm-44el(- -), en VGM-3mm-27el($\cdot\cdot$).

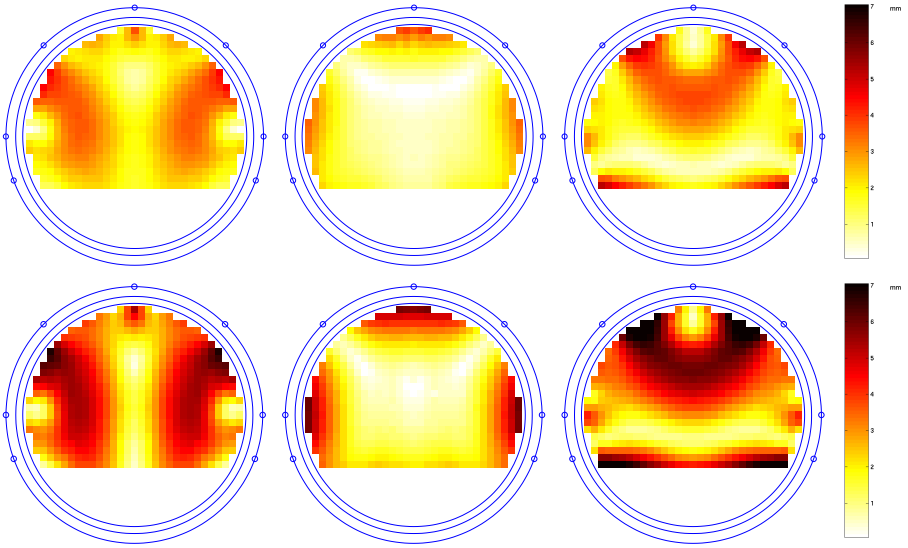

Figuur 10: De positiefout in functie van de testdipoolpositie en -oriëntatie. De eerste en tweede rij stellen de resultaten voor, voor de configuraties VGM-2mm-44el en VGM-3mm-44el, respectievelijk. De eerste, tweede en derde kolom stellen positiefouten voor, voor dipolen die respectievelijk parallel met de x-as, y-as en z-as georiënteerd worden.

0.4 Dipoolpositiefouten door volumegeleiderfouten

0.4.1 Inleiding

We onderzoeken de dipoolpositiefout voor drie fouten in het volumegeleidermodel (VGM).

Eerst vragen we ons af wat de dipoolpositiefout is die te wijten is aan het niet incorporeren van het ventriculair systeem (VS) in het VGM. Het VS bestaat uit een holte in de hersenen gevuld met cerebrospinaal vocht. Dit vocht heeft ongeveer een acht keer hogere geleidbaarheid dan het hersenweefsel eromheen.

Een tweede vraag die we ons stellen is: wat is de dipoolpositiefout te wijten aan het niet incorporeren van een gat van 20 mm diameter in de schedel. Bij het installeren van diepte-elektroden worden cirkelvormige stukjes schedel weggenomen. Door het verkregen gat worden de diepte-elektroden aangebracht.

De laatste simulatie onderzoekt de positiefout te wijten aan een schedelgeleidbaarheid ter waarde van 1/80 van die van het zachte weefsel, in de veronderstelling dat de werkelijke verhouding 1/16 is. In de literatuur is er geen eensgezindheid over de geleidbaarheid van de schedel. Sommige publicaties [27, 37, 87] rapporteren een geleidbaarheid van de schedel die 80 keer kleiner is dan de geleidbaarheid van het omringende zachte weefsel, i.e. scalp- en hersenenweefsel. Anderzijds zijn er publicaties verschenen [53, 80] die een geleidbaarheid voorstellen die 16 keer kleiner is dan de geleidbaarheid van het omringend zachte weefsel.

Verder hebben we ook onderzocht wat de invloed is van het aantal elektroden op de dipoolpositiefout.

0.4.2 Methode

We maken gebruik van het segmentatie onderdeel van het softwarepakket SPM [3], om van 3D MR-beelden, het scalp-, schedel-, hersen- en ventriculairsysteemcompartiment te bekomen.

Van dit gesegmenteerde hoofd maken we 4 volumegeleidermodellen. Ze bestaan uit een kubisch rooster met kubusribbe 2 mm. De relatieve geleidbaarheden per compartiment en per VGM worden weergegeven in tabel 2. Merk op dat er ook een compartiment met naam 'gat' aanwezig is. Wanneer de waarde van de geleidbaarheid van het gat dezelfde is als die van de schedel, dan is er geen gat aanwezig. Anderzijds, als de geleidbaarheid van het gat dezelfde is als die van het hersen- en scalpcompartiment, zoals in VGM-3, dan is er wel een gat aanwezig in de schedel.

compartimenten	VGM-1	VGM-2	VGM-3	VGM-4
scalp	1	1	1	1
schedel	$\frac{1}{16}$	$\frac{1}{16}$	$\frac{1}{16}$	$\frac{1}{80}$
hersenen	1	1	1	1
VS	8	1	8	8
gat	$\frac{1}{16}$	$\frac{1}{16}$	1	$\frac{1}{80}$

Tabel 2: De relatieve geleidbaarheid van de verschillende volumegeleidermodellen.

Het voorwaarts- en invers probleem worden opgelost door gebruik te maken van de FDRM. Het voorwaarts probleem wordt voor een gegeven VGM opgelost voor 2458 testdipolen, gelegen in een centrale coronale en axiale doorsnede. Het invers probeem wordt dan opgelost met een ander VGM.

0.4.3 Dipoolpositiefouten te wijten aan het niet incorporeren van het ventriculair systeem

VGM-1 wordt gebruikt om het voorwaarts probleem op te lossen. Met de bekomen potentialen wordt het invers probleem verder opgelost met VGM-2, die het VS niet bevat. De dipoolpositiefout is dan de afstand tussen de originele testdipoolpositie en de positie bekomen door het oplossen van het invers probleem. In figuur 11(a) wordt voor 53 elektroden (—+—) en voor 27 elektroden ($- \cdot \circ - \cdot$) het histogram weergegeven. De intervalbreedte is hier 0.5 mm. Het midden van het interval wordt aangeduid met '+' voor 53 elektroden en '$\circ$' voor 27 elektroden. We merken op dat het histogram voor 53 elektroden wat verschoven is naar links. Dus bij het toenemen van het aantal elektroden, is er een verkleining van de dipoolpositiefout. Verder merken we op dat het gros van de dipolen een positiefout heeft tussen 0-3 mm. De maximale fout die we kunnen vinden, bedraagt 7.6 mm voor 27 elektroden en 6.1 mm voor 53 elektroden.

In de eerste rij van figuur 12 wordt de dipoolpositiefout weergegeven die te wijten is aan het niet incorporeren van het VS, in functie van de dipoolpositie en -oriëntatie. De configuratie met 53 elektroden wordt afgebeeld. De eerste kolom geeft de resultaten weer voor de testdipool in de coronale doorsnede. Hier zijn de dipolen langs de x-as georiënteerd (horizontaal in het weergegeven vlak). De tweede kolom geeft de resultaten weer voor de testdipool in de axiale doorsnede, met de dipool langs de y-as georiënteerd (verticaal in het weergegeven vlak). De kleurschaal stelt de dipoolpositiefout voor. De staart van de pijltjes toont de oorspronkelijke testdipoolpositie, terwijl de kop van de

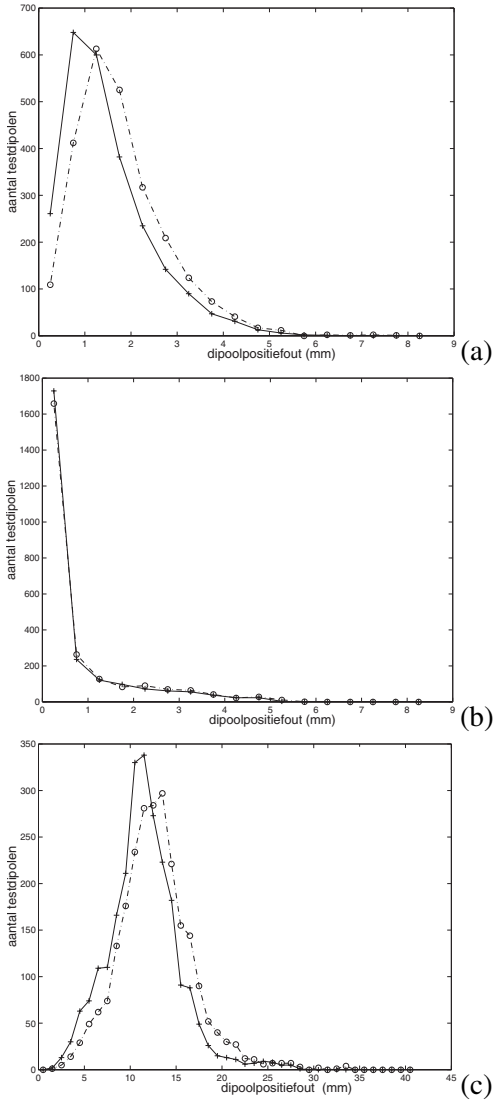

Figuur 11: Het histogram van de dipoolpositiefout voor 53 elektroden (—+—) en voor 27 elektroden ($- \cdot \circ - \cdot$). Figuur (a), (b) en (c) stellen het histogram voor van de dipoolpositiefout, voor het niet incorporeren van het VS, het niet incorporeren van een gat, en het onderschatten van de schedelgeleidbaarheid, respectievelijk. In het geval van figuren (a) en (b) is de intervalbreedte 0.5 mm en voor figuur (c) is de intervalbreedte 1 mm.

pijltjes de positie voorstelt bij het oplossen van het invers probleem. Merk wel op dat die positie geprojecteerd is in het vlak van de testdipolen. De grootste fouten zijn te vinden rond het VS.

0.4.4 Dipoolpositiefouten te wijten aan het niet incorporeren van een gat in de schedel

Hier berekenen we het voorwaarts probleem met VGM-3. Het invers probleem wordt opgelost door gebruik te maken van VGM-1. In figuur 11(b) wordt het histogram weergegeven. We merken op dat de histogrammen voor 27 en voor 53 elektroden zo goed als samenvallen. Dit betekent dat de toename van het aantal elektroden de positiefout bijna niet beïnvloedt. We merken tevens op dat de meeste positiefouten te vinden zijn in het interval 0-1 mm. Verder is de maximale positiefout 5.6 mm en 5.2 mm voor respectievelijk 27 en 53 elektroden.

In de tweede rij van figuur 12 zijn de positiefouten weergegeven die te wijten zijn aan het niet incorporeren van een gat in de schedel. Merk op dat gebieden verder verwijderd van het gat weinig invloed ondervinden van het niet incorporeren van het gat in de schedel. Voor dipolen met een oriëntatie loodrecht op het gat vinden we vooral positiefouten vóór het gat in het schedelcompartiment, zoals geïllustreerd in de tweede rij, eerste kolom van figuur 12. Wanneer anderzijds de oriëntatie tangentieel is t.o.v. het gat, zoals in de tweede rij, tweede kolom van figuur 12, dan vinden we vooral fouten aan weerszijden van het gat, maar minder vóór het gat.

0.4.5 Dipoolpositiefouten te wijten aan het onderschatten van de schedelgeleidbaarheid

We passen VGM-1 toe om de potentialen voorwaarts uit te rekenen. Verder gebruiken we VGM-4 bij het oplossen van het invers probleem. Voor het voorwaarts probleem is de schedelgeleidbaarheid 1/16 van de scalpgeleidbaarheid. Terwijl in het invers probleem de geleidbaarheid 1/80 is van de scalpgeleidbaarheid. Dus in het invers probleem is de schedelgeleidbaarheid 5 maal kleiner dan in het voorwaarts probleem. We hebben hier dus te maken met een onderschatting van de schedelgeleidbaarheid. De maximale dipoolpositiefout is hier 34.4 mm en 28.0 mm voor respectievelijk 27 en 53 elektroden. Het is duidelijk dat de fouten hier van een grotere orde zijn dan in de vorige twee gevallen. In figuur 11(c) vinden we dat voor 53 elektroden het histogram wat naar links is opgeschoven. Opmerkelijk is dat de meeste testdipolen een positiefout hebben in het interval 5-20 mm.

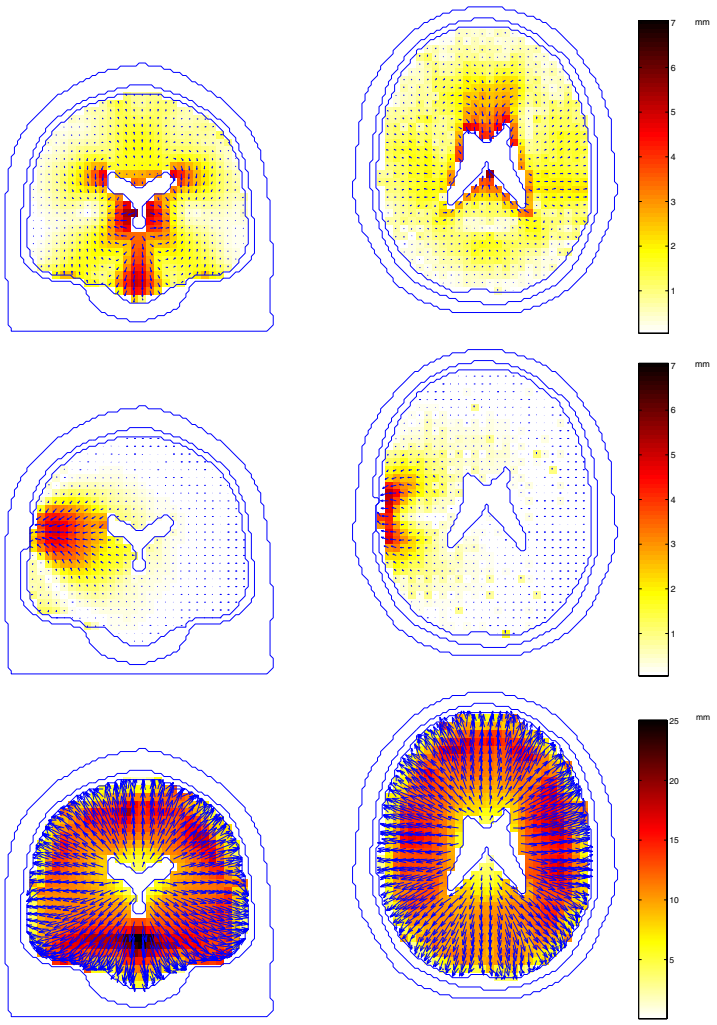

Figuur 12: De eerste en tweede kolom stellen de dipoolpositiefouten voor, respectievelijk voor de coronale doorsnede met testdipooloriëntatie langs de x-as en de axiale doorsnede met testdipooloriëntatie langs de y-as. We gebruiken 53 scalpelektroden. De eerste, tweede en derde rij stellen de dipoolpositiefouten voor, te wijten aan het niet incorporeren van het VS, het niet incorporeren van een gat in de schedel en het te laag inschatten van de schedelgeleidbaarheid. De kleur duidt de dipoolpositiefout aan. De staart van de pijltjes stelt de testdipoolpositie voor, terwijl de kop van de pijltjes de positie voorstelt na het oplossen van het invers probleem. De pijltjes zijn wel geprojecteerd in het vlak van de testdipolen.

De derde rij van figuur 12 stelt de positiefout voor die te wijten is aan het onderschatten van de schedelgeleidbaarheid. We merken vooreerst op dat we dipoolpositiefouten krijgen voor bijna alle testdipolen. De dipool wordt radiaal naar buiten toe geplaatst in vergelijking met de oorspronkelijke positie. Verder dient opgemerkt te worden dat de kleurschaal anders geschaald is (0-25 mm) dan in de twee gevallen erboven (0-7 mm). We kunnen dus besluiten dat de impact op de dipoolpositiefout door het onderschatten van de schedelgeleidbaarheid veel groter is dan die door het niet incorporeren van VS of door het niet incorporeren van een gat in het VGM.

0.5 Vergelijken van de dipoolpositiefouten te wijten aan ruis

0.5.1 Inleiding en methoden

Tot nu toe hebben we dipoolpositiefouten onderzocht die te wijten zijn aan het gebruik van de numerieke methode en aan VGM fouten. Een volgende stap is om dipoolpositiefouten te onderzoeken die te wijten zijn aan ruis. De vraag die hierbij aansluit is: loont het nog de moeite, gegeven het ruisniveau van het EEG-signaal, om geavanceerde volumegeleidermodellen te gebruiken of niet. In de volgende studie proberen we daarop een antwoord te geven.

De performantie bij het oplossen van het invers probleem is vergeleken voor het 3-lagig sferisch model en het realistisch model. Wanneer we het realistisch hoofdmodel beschouwen, veronderstellen we dat de dipoolpositiefout Δr_i^{real} (de afstand tussen de testdipoolpositie en geschatte positie) slechts te wijten is aan de aanwezigheid van ruis. Deze dipoolpositiefout wordt in figuur 13 voorgesteld door (b). Wanneer echter het sferisch model gebruikt wordt, is de dipoolpositiefout Δr_i^{sfeer} enerzijds te wijten aan het gebruik van het eenvoudig sferisch model en anderzijds aan ruis. Deze fout wordt voorgesteld in figuur 13 door (a). Voor een set van 1000 ruishebbende distributies die afkomstig zijn van dezelfde ruisloze distributie worden de gemiddelde dipoolpositiefouten $E(\Delta r_i^{real})$ en $E(\Delta r_i^{sfeer})$ berekend. De ruisloze distributie wordt bekomen door het voorwaarts probleem op te lossen in het realistisch hoofdmodel voor een gegeven testdipool. De performantie van het realistisch en het sferisch model worden dan vergeleken door $E(\Delta r_i^{real})$ en $E(\Delta r_i^{sfeer})$ te vergelijken.

Voordat we verder gaan moeten we het ruisniveau definiëren. Het ruisniveau is de verhouding tussen de RMS-waarde (Eng. root-mean-square) van additieve ruis en de RMS-waarde van de ruisloze potentialen. In wat hier voorgesteld wordt, maken we gebruik van Gaussiaanse ruis, die niet gecorreleerd

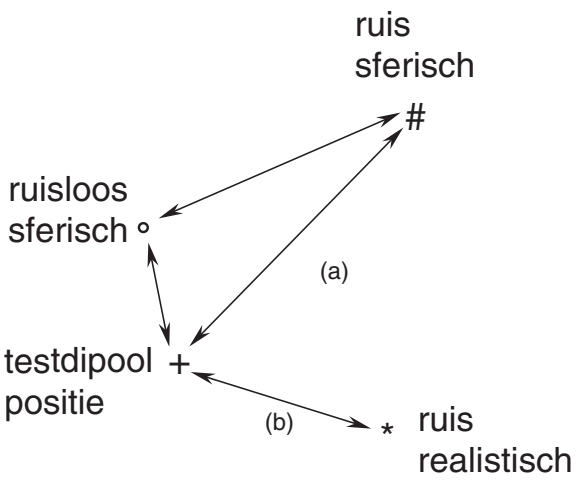

Figuur 13: De plaatsvectoren.

is tussen naburige elektroden en ook niet tussen opeenvolgende tijdsmonsters. Verder is de gemiddelde waarde gelijk aan nul. Aldus stemt de RMS-waarde voor ruis overeen met de standaardafwijking van de Gaussiaanse ruis. We kunnen stellen dat een ruisniveau van 0.2 ongeveer overeenkomt met dat van een spike. Als we verschillende spikes in het EEG aantreffen, kunnen we de piekactiviteit aligneren en ze vervolgens optellen, in de hoop het signaal te versterken en de ruis te onderdrukken. Voor zo'n uitgemiddelde spike bekomen we een ruisniveau van ongeveer 0.1.

We hebben de geschatte dipoolpositie berekend, door gebruik te maken van locale linearisatie [39,92], i.p.v. het iteratief oplossen van het invers probleem. Met deze techniek kunnen we door een matrixvermenigvuldiging te weten komen wat de afwijkingen zijn in de dipoolparameters voor kleine afwijkingen van het EEG te wijten aan ruis. Dit gaat veel sneller dan de methode waarbij op een iteratieve wijze de dipoolparameters aangepast worden. Voor de ruisniveaus gebruikt in deze studie, hebben we ter validatie de dipoolpositiefouten die berekend werden met deze techniek, vergeleken met de dipoolpositiefouten die bekomen werden met de klassieke iteratieve methode. We hebben een goede overeenkomst gevonden tussen beide procedures voor dipoolpositiefouten.

Keren we nu terug naar de gemiddelde dipoolpositiefouten. We merken op dat zowel $E(\Delta r_i^{sfeer})$ als $E(\Delta r_i^{real})$ afhankelijk zijn van het ruisniveau. Wanneer het ruisniveau stijgt, zullen deze waarden ook stijgen. $E(\Delta r_i^{sfeer})$

is echter groter dan $E(\Delta r_i^{real})$, omdat er bij de eerste zowel een fout optreedt die te wijten is aan ruis als één die te wijten is aan het vereenvoudigd volumegeleidermodel. Voor $E(\Delta r_i^{real})$ treedt er een fout op die enkel te wijten is aan ruis. Waneer $E(\Delta r_i^{sfeer})$ veel groter is dan $E(\Delta r_i^{real})$ voor een gegeven testdipool, blijft het de moeite waard om een realistisch hoofdmodel te gebruiken. Wanneer anderzijds $E(\Delta r_i^{sfeer})$ van dezelfde grootte is als $E(\Delta r_i^{real})$, dan doet het er niet zoveel toe welke van beide volumegeleidermodellen gebruikt wordt. Bijgevolg introduceren we $\Delta R = E(\Delta r_i^{sfeer}) - E(\Delta r_i^{real})$.

We maken hier gebruik van 1416 testdipolen, waarvoor we voor elk $E(\Delta r_i^{sfeer})$, $E(\Delta r_i^{real})$ en ΔR berekend hebben, voor verschillende ruisniveaus.

Verder hebben we bekeken of het toenemen van het aantal elektroden van 27 naar 44 in het één van beide modellen bevoordeelt. We hebben ook het aantal tijdsmonsters laten toenemen om de impact daarvan op de gemiddelde dipoolpositiefout van beide modellen te onderzoeken. $E(\Delta r_i^{sfeer})$, $E(\Delta r_i^{real})$ en ΔR worden daarvoor berekend in volgende configuraties:

- Configuratie 27el-1s-Gauss bestaat uit 27 elektroden, één tijdsmonster en Gaussiaanse ruis.
- In configuratie 44el-1s-Gauss worden 44 elektroden gebruikt i.p.v. 27.
- In configuratie 27el-6s-Gauss worden 6 tijdsmonsters gebruikt i.p.v. één.

Ter volledigheid dienen we nog iets te zeggen over de volumegeleidermodellen. Uit de gesegmenteerde MR-beelden met voxelgrootte 1 mm^3, wordt een kubisch VGM ontwikkeld met een kubusribbe van 2 mm. We onderscheiden het VS-, het hersen-, het schedel- en scalpcompartiment, met de relatieve geleidbaarheden van respectievelijk 8, 1, 1/16, en 1. Als numerieke methode gebruiken we opnieuw de FDRM. Het sferisch model is als volgt geconstrueerd: door de 27 of 44 coördinaten van de elektrodeknopen in het kubisch rooster wordt een bestpassende sfeer geconstrueerd met straal R. Deze sfeer stelt dan de buitenste schil voor van het sferisch model. De grens tussen het scalp- en schedelcompartiment heeft dan een straal van $85/92R$ en de grens tussen het schedel- en hersencompartiment heeft dan een straal van $80/92R$. De elektroden worden radiaal geprojecteerd op de buitenste sfeer.

0.5.2 Simulaties voor 27el-1s-Gauss

In figuur 14 worden $E(\Delta r_i^{sfeer})$, $E(\Delta r_i^{real})$ en ΔR weergegeven in respectievelijk de eerste, tweede en derde rij, en dit in functie van de dipoolpositie

en -oriëntatie. De eerste, tweede en derde kolom stellen de waarden voor, voor dipolen die georiënteerd zijn volgens de x-, y- en z-as. Verder zijn de waarden weergegeven voor een ruisniveau van 0.1. In de onderste rij is de contour voor $\Delta R = 5$ mm voorgesteld. Slechts 13% van de testdipolen heeft een ΔR die groter is dan 5 mm. Voor dipolen die langs de y-as georiënteerd zijn, zijn er geen groter dan 5 mm.

Vervolgens geven de kleuren, in figuur 15, ΔR weer in functie van de dipoolpositie en -oriëntatie enerzijds, en in functie van het ruisniveau anderzijds. De eerste, tweede, derde en vierde rij hebben een ruisniveau van respectievelijk 0, 0.05, 0.1 en, 0.2. Naarmate het ruisniveau stijgt, daalt de ΔR.

Het gemiddelde over alle 1416 testdipolen van $E(\Delta r_i^{sfeer})$, $E(\Delta r_i^{real})$ en ΔR is weergegeven in de kolommen die respectievelijk aangeduid zijn met A_s, A_r en $A_{\Delta R}$ in tabel 3. Merk op dat we tevens kunnen schrijven dat $A_{\Delta R} = A_s - A_r$. In de sub-tabel die de waarden weergeeft voor de configuratie 27el-1s-Gauss, vinden we een toename zowel van A_s als van A_r, bij een toename van het ruisniveau. We merken op dat voor A_r de toename proportioneel is met het ruisniveau. Voor een toename van het ruisniveau van 0 naar 0.2, neemt $A_{\Delta R}$ af van 5.5 mm naar 1.8 mm. Verder worden in de kolom $\# > 5$ van tabel 3 het relatief aantal testdipolen weergegeven met een ΔR die groter is dan een vooropgestelde drempel van 5 mm. In het ruisloos geval hebben 60% van de testdipolen een ΔR die groter is dan 5 mm. Voor een ruisniveau van 0.1, wat correspondeert met het ruisniveau van uitgemiddelde spikes, hebben slechts 13.4% een waarde groter dan 5 mm. Voor een ruisniveau van 0.2, wat correspondeert met het ruisniveau van een spike, zijn slechts 7.6% van de ΔR-waarden groter dan 5 mm.

Voor de configuratie van 27 elektroden, één tijdsmonster en Gaussiaanse ruis, stellen we dus vast dat de belangrijkheid van het realistisch model afneemt t.o.v. het sferisch model, naarmate het ruisniveau toeneemt.

0.5.3 Simulaties voor de configuratie 44el-1s-Gauss

In figuur 16 wordt ΔR voorgesteld in functie van de dipoolpositie en -oriëntatie. De eerste en tweede kolom geven de waarden weer voor een ruisniveau 0.0 en 0.1. Wanneer we de eerste rij van figuur 16 vergelijken met de eerste rij van figuur 15, merken we op dat $\Delta R = E(\Delta r_i^{sfeer})$ kleiner is voor verschillende testdipolen. Aldus levert het sferisch model kleinere dipoolpositiefouten op voor sommige testdipolen (maar niet voor alle) bij een toename van het aantal elektroden van 27 naar 44. Deze resultaten zijn ook gevonden door [145]. In deze figuren merken we verder op voor ruisniveau 0.1 dat ΔR

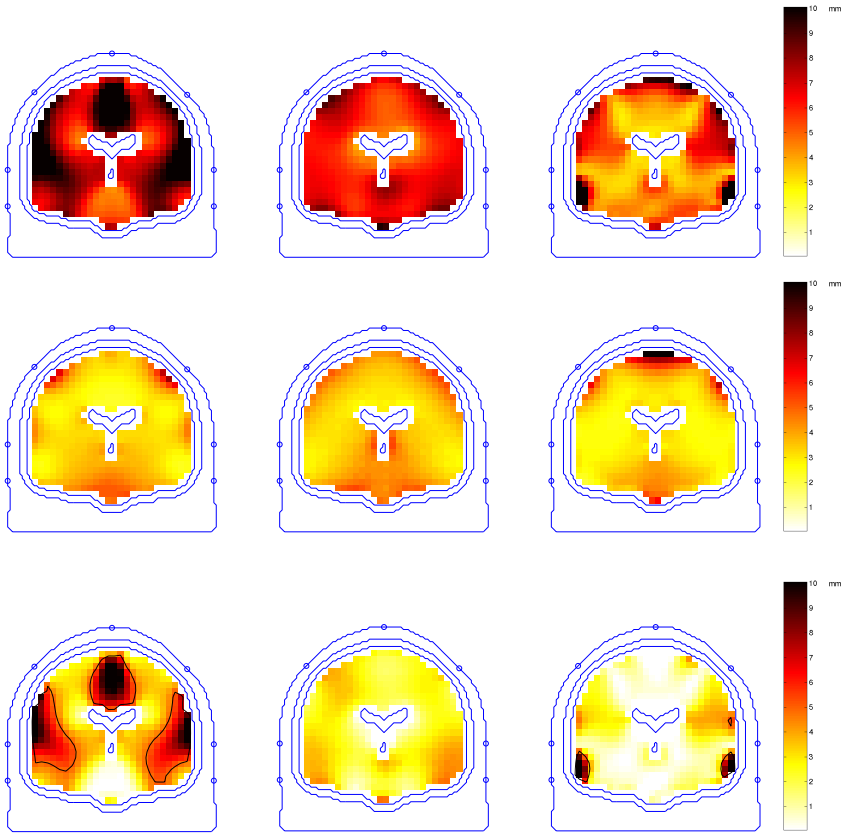

Figuur 14: De kleuren geven $E(\Delta r_i^{sfeer})$, $E(\Delta r_i^{real})$ en ΔR weer in respectievelijk de eerste, tweede en derde rij, en dit in functie van de dipoolpositie en -oriëntatie. De eerste, tweede en derde kolom stellen de waarden voor, voor dipolen die georiënteerd zijn volgens de x-, y- en z-as, respectievelijk. Verder zijn de waarden weergegeven voor een ruisniveau van 0.1. In de onderste rij is de contour voor $\Delta R = 5$ mm voorgesteld.

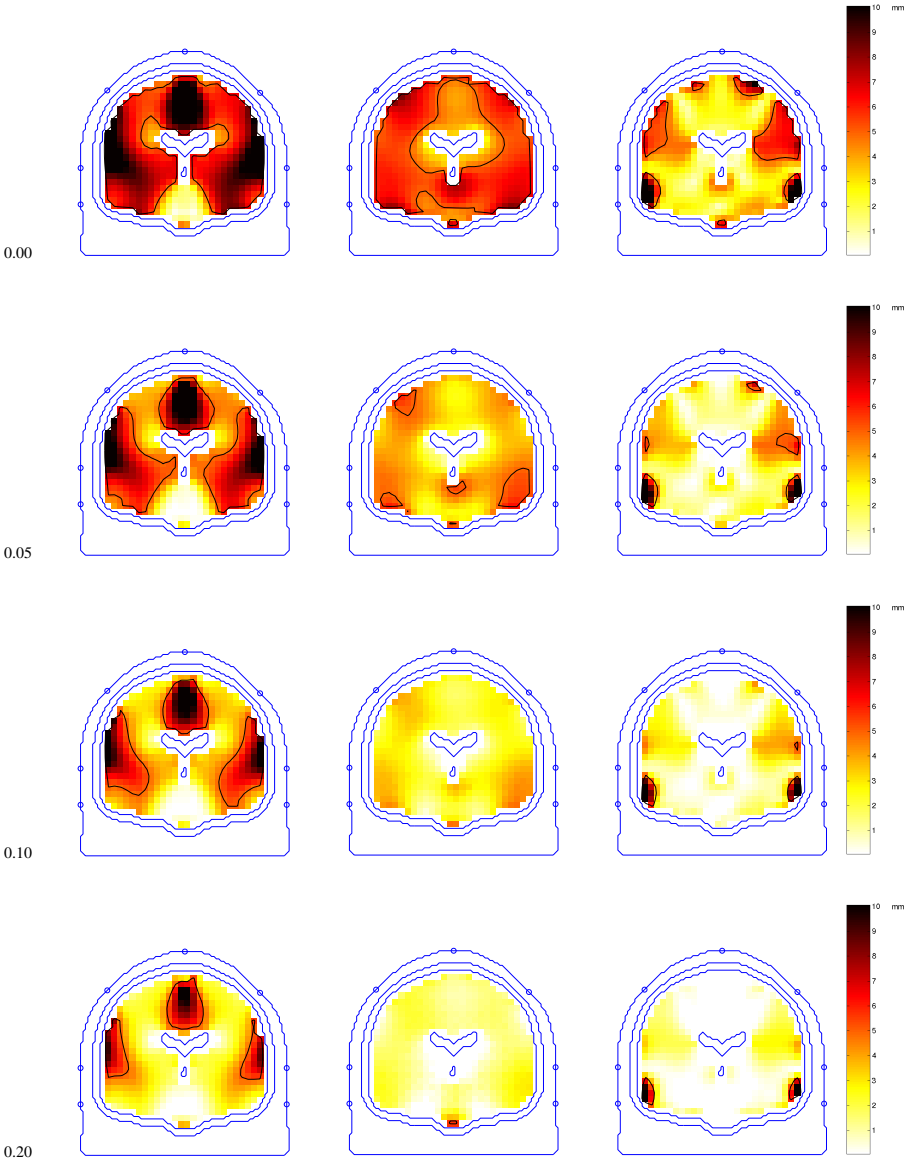

Figuur 15: De kleuren geven ΔR weer in functie van het ruisniveau. In de eerste, tweede, derde en vierde rij, worden de ruisniveaus 0, 0.05, 0.1 en 0.2 gebruikt. De eerste, tweede en derde kolom stellen de waarden voor, voor dipolen die georiënteerd zijn volgens de x-, y- en z-as. Verder is de contour voor $\Delta R = 5$ mm voorgesteld.

ruisniveau	27el-1s-Gauss			
	A_s(mm)	A_r(mm)	$A_{\Delta R}$(mm)	# $> 5(\%)$
0.0	5.5	0.0	5.5	60.0
0.05	5.8	1.8	4.0	25.5
0.1	6.6	3.6	3.1	13.4
0.2	9.0	7.2	1.8	7.6
ruisniveau	44el-1s-Gauss			
	A_s(mm)	A_r(mm)	$A_{\Delta R}$(mm)	# $> 5(\%)$
0.0	4.7	0.0	4.7	43.7
0.05	4.8	1.0	3.8	26.6
0.1	5.1	2.1	3.0	14.8
0.2	6.3	4.3	2.0	6.5
ruisniveau	27el-6s-Gauss			
	A_s(mm)	A_r(mm)	$A_{\Delta R}$(mm)	# $> 5(\%)$
0.0	5.5	0.0	5.5	60.0
0.05	5.6	0.7	4.9	44.5
0.1	5.7	1.4	4.3	31.0
0.2	6.2	2.9	3.3	16.1

Tabel 3: Het gemiddelde over alle 1416 testdipolen van $E(\Delta r_i^{sfeer})$, $E(\Delta r_i^{real})$ en ΔR is weergegeven in de kolommen die aangeduid zijn met A_s, A_r en $A_{\Delta R}$. Verder worden ook het relatief aantal testdipolen met een ΔR groter dan 5 mm weergegeven in kolom $\# > 5$. Deze waarden zijn gegeven in functie van het ruisniveau en voor de configuraties 27el-1s-Gauss, 44el-1s-Gauss en 27el-6s-Gauss.

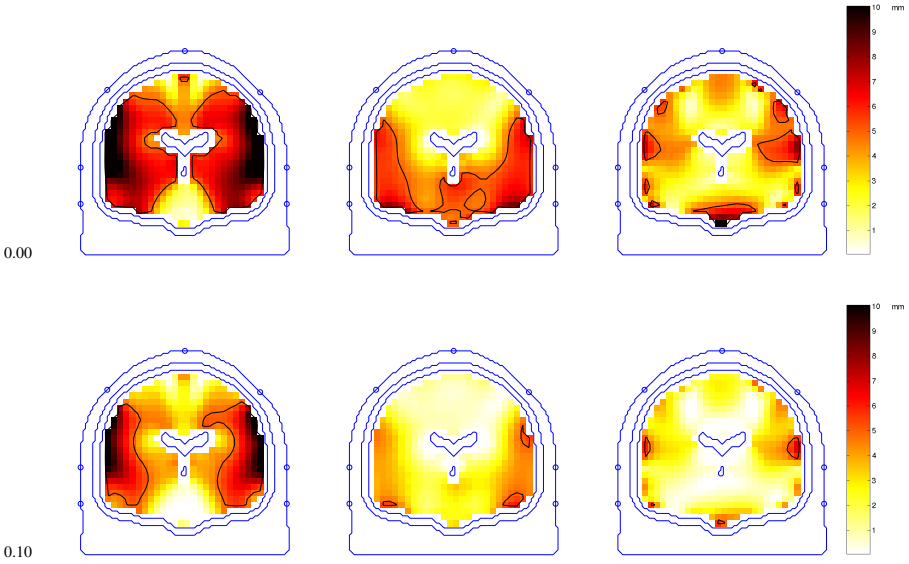

Figuur 16: De eerste en tweede rij stellen ΔR voor, voor een ruisniveau van 0.0 en 0.1 bij de configuratie 44el-1s-Gauss. De eerste, tweede en derde kolom stellen de waarden voor, voor een dipool georiënteerd langs de x-, y- en z-as. De contour voor ΔR gelijk aan 5 mm is ook weergegeven.

voor sommige testdipolen groter wordt en kleiner voor andere, bij een toename van het aantal elektroden van 27 naar 44.

In figuur 17(a) worden de resultaten voorgesteld voor een testdipool die aanleiding geeft tot een daling van ΔR bij het toenemen van het aantal elektroden. De volle lijn en streeplijn door de oorsprong stellen $E(\Delta r_i^{real})$ voor, voor respectievelijk 27 en 44 elektroden. De curven die niet door de oorsprong gaan, stellen $E(\Delta r_i^{sphere})$ voor, voor respectievelijk 27 en 44 elektroden. We merken op dat $E(\Delta r_i^{real})$ afneemt bij een toename van het aantal elektroden, maar dat de afname van $E(\Delta r_i^{sphere})$ nog veel groter is, zodat $\Delta R = E(\Delta r_i^{sphere}) - E(\Delta r_i^{real})$ afneemt, wat men ook uit figuur 17 kan afleiden.

In figuur 17(b) worden de resultaten voorgesteld voor een dipool die aanleiding geeft tot een stijging van ΔR, bij het toenemen van het aantal elektroden. Hier merken we op dat de daling van $E(\Delta r_i^{sphere})$ kleiner is dan de daling van $E(\Delta r_i^{real})$, zodat ΔR toeneemt.

In tabel 3 stellen we bij het ruisloze geval een reductie van A_s vast van 5.5 mm voor 27 elektroden, naar 4.7 mm voor 44 elektroden. Verder zijn de

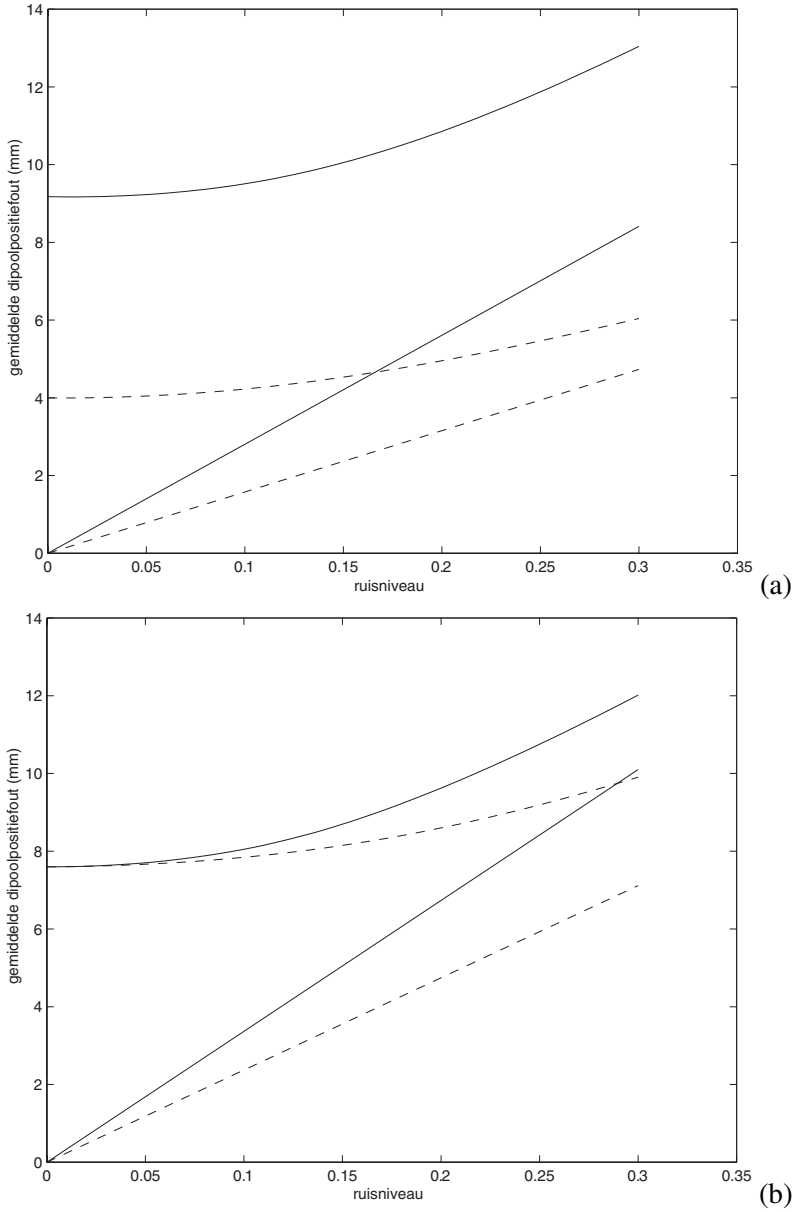

Figuur 17: De volle lijnen (—) in (a) en (b) stellen $E(\Delta r_i^{sphere})$ en $E(\Delta r_i^{real})$ voor, in functie van het ruisniveau voor de configuratie 27el-1s-Gauss. De streeplijnen (- -) in (a) en (b) stellen $E(\Delta r_i^{sphere})$ en $E(\Delta r_i^{real})$ voor, voor de configuratie 44el-1s-Gauss.

A_s-waarden bij aanwezigheid van ruis kleiner dan die voor 27 elektroden. Uit tabel 3, leiden we of dat A_r trager toeneemt voor configuratie 44el-1s-Gauss met een toenemend ruisniveau, dan voor de configuratie 27el-1s-Gauss. Dit wordt bevestigd in de literatuur [67]. In deze publicatie wordt er verder ook meegedeeld dat de gemiddelde dipoolpositiefout proportioneel is met één over de wortel van het aantal sensoren. Bij een toename van het aantal sensoren zal aldus de positiefout afneemt. Verder merken we op dat bij aanwezigheid van ruis, de gemiddelde waarde over alle dipolen van ΔR niet veel verschilt van de waarden gevonden voor de configuratie 27el-1s-Gauss. Voor het ruisloze geval vinden we dat het aantal testdipolen met ΔR groter dan 5 mm teruggelopen is van 60% voor 27 elektroden tot 43% voor 44 elektroden. Voor ruisniveaus verschillend van nul is het aantal dipolen met een ΔR groter dan 5 mm niet zo verschillend van het aantal gevonden in de configuratie 27el-1s-Gauss. We besluiten hieruit dat het toenemen van het aantal elektroden van 27 naar 44 weinig invloed heeft op de performantie van het realistisch model versus het sferisch model.

0.5.4 Simulaties voor de configuratie 27el-6s-Gauss

In tabel 3 is A_s in het ruisloze geval A_s dezelfde als die voor één tijdsmonster. Dit is te begrijpen, daar een systematische fout te wijten aan het gebruik van het sferisch model niet kan gecompenseerd worden door meer tijdsmonsters in acht te nemen. In het geval er ruis aanwezig is, merken we toch een reductie op van A_s vergeleken met de waarden gevonden in de configuratie 27el-1s-Gauss.

A_r is ook kleiner bij het gebruik van 6 tijdsmonsters i.p.v. één tijdsmonster. Dit kan terug onderbouwd worden met in de literatuur [36, 115] gevonden resultaten. De positiefout te wijten aan Gaussiaanse ruis blijkt omgekeerd evenredig te zijn met de wortel van het aantal tijdsmonsters. De A_r-waarden zijn inderdaad gedaald met $1/\sqrt{6} \approx 0.4$, vergeleken met de waarden gevonden voor de configuratie 27el-1s-Gauss bij eenzelfde ruisniveau. Verder observeren we een toename van de $A_{\Delta R}$, vergeleken met het geval waar slechts 1 tijdsmonster wordt genomen. Er zijn ook een groter aantal testdipolen die een ΔR groter dan 5 mm hebben, vergeleken met de configuratie die gebruik maakt van 1 tijdsmonster.

In figuur 18 stellen de curven met volle lijnen $E(\Delta r_i^{sfeer})$ en $E(\Delta r_i^{real})$ voor, in functie van het ruisniveau, voor 1 tijdsmonster en voor een gegeven testdipool. De curven met streeplijnen stellen $E(\Delta r_i^{sfeer})$ en $E(\Delta r_i^{real})$ voor, in functie van het ruisniveau, voor 6 tijdsmonsters. We merken hier op dat $E(\Delta r_i^{sfeer})$ is afgenomen voor een gegeven ruisniveau en voor een toename van het aantal tijdsmonsters. Maar $E(\Delta r_i^{real})$ is bij hetzelfde ruisniveau nog

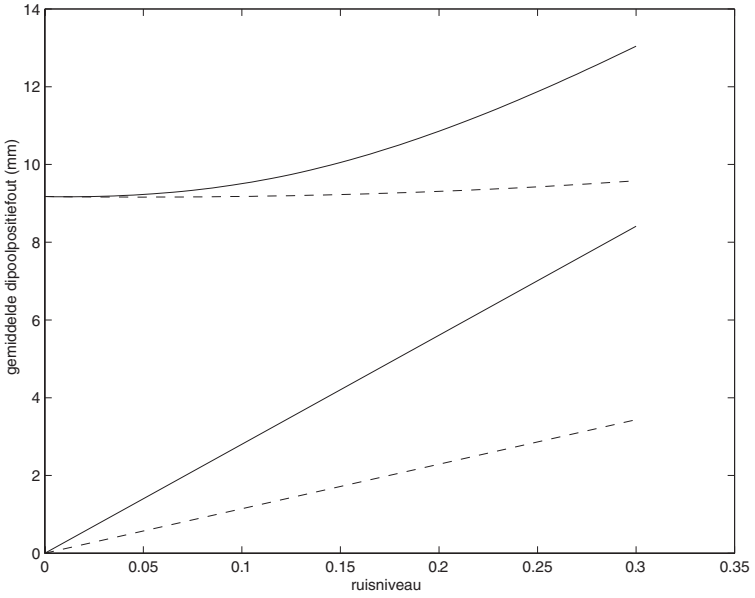

Figuur 18: De curven met volle lijnen stellen $E(\Delta r_i^{sfeer})$ en $E(\Delta r_i^{real})$ voor in functie van het ruisniveau, voor de configuratie 27el-1s-Gauss en voor een gegeven testdipool. De curven met streeplijnen stellen $E(\Delta r_i^{sfeer})$ en $E(\Delta r_i^{real})$ voor in functie van het ruisniveau, voor de configuratie 27el-6s-Gauss en voor dezelfde testdipool.

veel meer afgenomen, zodat ΔR toeneemt.

Het laten toenemen van het aantal monsterwaarden kan ook gezien worden als een reductie van het ruisniveau, wanneer men de curven van één tijdsmonster beschouwt, zoals in figuur 18. Wanneer het ruisniveau daalt in het geval van één tijdsmonster, zal de ΔR toenemen. We kunnen daaruit afleiden dat ΔR toeneemt met een toename van het aantal tijdsmonsters.

We kunnen dus concluderen dat voor het toenemen van het aantal tijdsmonsters, het realistisch model belangrijker gaat worden dan het sferisch model.

0.5.5 Simulaties met achtergrond-EEG

We hebben ook simulaties uitgevoerd met achtergrond-EEG. Achtergrond-EEG is de elektrische activiteit van de vele andere actieve hersenzones die geen verband houdt met de te zoeken activiteit afkomstig van het focaal gebied. De potentialen van naburige elektroden bij achtergrond-EEG zijn gecorreleerd. Ook de potentialen van opeenvolgende tijdsmonsters zijn gecorreleerd. Vergeleken met Gaussiaanse ruis vonden we zowel een toename van $E(\Delta r_i^{sfeer})$,

$E(\Delta r_i^{real})$ en ΔR voor een gegeven ruisniveau en een gelijke configuratie. Maar wanneer we de resultaten van de verschillende configuraties vergelijken binnen de groep van achtergrond-EEG, dan gelden dezelfde conclusies als voor Gaussiaanse ruis.

0.6 Gevalsanalyse

0.6.1 Inleiding

EEG-dipoollokalisatie wordt al sinds het begin van de jaren '90 uitgevoerd binnen de Epilepsie Monitoring Eenheid te Gent. Er werd vooral gewerkt met het softwarepakket BESA© [95] dat gebruik maakt van het sferisch hoofdmodel. De klinische relevantie van dit onderzoek is uitgebreid gerapporteerd [9, 12, 15]. In wat volgt zullen we EEG-dipoollokalisatie uitvoeren in een realistisch hoofdmodel. Hierbij maken we gebruik van het interictale EEG van twee patiënten met epilepsie.

0.6.2 Eerste patiënt

Patiëntinformatie en het EEG

De eerste patiënt is een 24-jarige man die vanaf zijn zestiende aan epilepsie lijdt. Hij is opgenomen in het preheelkundig evaluatieprotocol. Dit protocol omvat langtermijn video/EEG-monitoring, MR-beeldvorming, neuropsychologische testen, nucleaire beeldvorming. De resultaten van dit protocol suggereren een rechts-mediaal temporale focus. De patiënt werd heelkundig behandeld op 15/11/97 en is sindsdien aanvalsvrij. De rechter hypocampus en het anterieure stuk van de temporaalkwab zijn verwijderd.

Het EEG wordt bemonsterd aan 200 Hz door het Beehive© (TELEFACTOR, USA) monitoring systeem. In figuur 19 wordt het EEG voorgesteld op één tijdsas. De gemiddelde waarde van alle elektrodepotentialen wordt als referentiepotentiaal genomen. We merken op dat de interictale activiteit zich voordoet vanaf t = 300 ms. Het 40 ms tijdsinterval (of 8 tijdsmonsters) waarbinnen we een dipoolschatting hebben uitgevoerd is ook aangeduid met verticale lijnen.

De RMS-waarde van de eerste 250 ms wordt gebruikt om een idee te krijgen van de ruisbijdrage (het achtergrond-EEG). Vervolgens wordt de RMS-waarde voor het signaal berekend. Hiervoor gebruiken we de 40 ms, aangeduid op figuur 19. Het ruisniveau wordt dan 0.16, de signaal-ruis-verhouding (SRV), die één over het ruisniveau is, wordt dan 6.1.

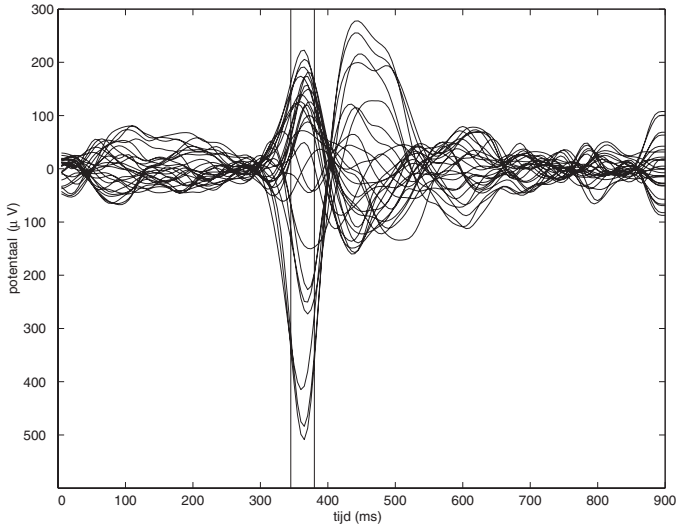

Figuur 19: Een voorstelling van het EEG op één tijdsas. De referentie is de gemiddelde potentiaal aan alle elektroden. De interictale activiteit start vanaf 300 ms. Het interval dat gebruikt wordt voor het schatten van de dipool is aangeduid met verticale lijnen.

Detectie van elektroden en constructie van het volumegeleidermodel

De patiënten die aan een langetermijn video/EEG-monitoring onderworpen zijn, krijgen bij het verblijf in het ziekenhuis ook een T1-gewogen MR. De bedoeling is ondermeer de elektroden te detecteren. Metalen objecten, zoals de elektroden, genereren geen signaal bij MR-beeldvorming. Om toch tot detectie van de elektroden over te gaan, plaatst men kleine sfeertjes met een diameter van 5 mm op de elektroden. In figuur 20 kan men die sfeertjes duidelijk zien oplichten.

We detecteren dan verder de sfeertjes op basis van patroonherkenning [117, 121] en kennen aan elk gedetecteerd sfeertje een elektrodelabel toe.

Bij de 27 gedetecteerde posities zoeken we een bestpassende sfeer met straal R. De sfeertjes bevinden zich ongeveer 8 mm boven het scalpoppervlak. De straal van de buitenste schil van het drielagig sferisch model wordt dan $R - 8$ mm. Een typische keuze van de buitenste schillen van het schedel- en hersencompartiment is dan respectievelijk $(R-8)85/92$ en $(R-8)80/92$. De elektrodeposities in het sferisch model worden bekomen door een radiale projectie van de posities van de sfeertjes op de buitenste schil. Het realistisch hoofdmodel wordt bekomen door de MR-beelden te segmenteren, door

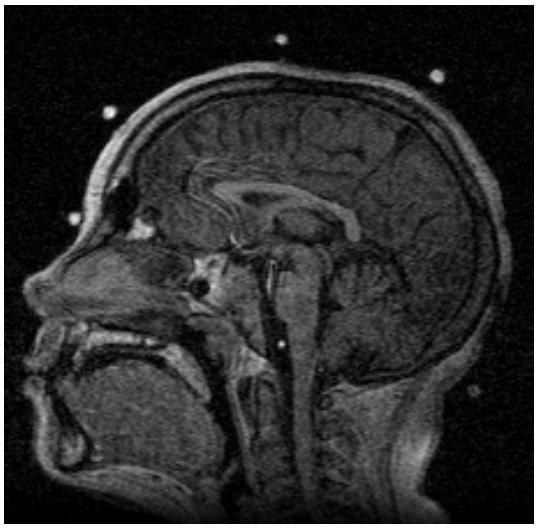

Figuur 20: Een sagitale doorsnede, waarop duidelijk verschillende sfeertjes zichtbaar zijn.

gebruik te maken van SPM [3]. Het hersen-, schedel- en scalpcompartiment kennen we een homogene isotrope geleidbaarheid toe, met relatieve geleidbaarheid van respectievelijk 1, 1/16 en 1. Dezelfde verhoudingen zijn gebruikt voor het sferisch model. Het volumegeleidermodel bestaat ongeveer uit een half miljoen kubussen met een ribbe van 2 mm. We passen FDRM toe. Daarbij dienen we 26 numerieke voorwaartse berekeningen uit te voeren waarbij we gebruik maken van iteratieve methoden voor het oplossen van ijle stelsels. De iteratieve methode die we gebruiken is de 'successive overrelaxation method'.

Dipoollokalisatie

De dipoolparameters worden aangepast tot er een minimum bereikt is in de relatieve residuele energie weergegeven in vergelijking (2.41).

Het inverse probleem wordt eerst opgelost in het sferisch model en wordt dan geprojecteerd op het MR-beeld [126–128, 132]. De eerste rij van figuur 21 stelt de projectie voor van de dipool op een axiale, coronale en sagitale doorsnede.

Het invers probleem is ook opgelost met het realistisch hoofdmodel. De tweede rij in figuur 21 stelt de dipool voor bij gebruik van het realistisch hoofdmodel. In het gele oppervlak is de relatieve residuele energie kleiner dan het dubbel van het minimum, dat 3.5 % bedraagt.

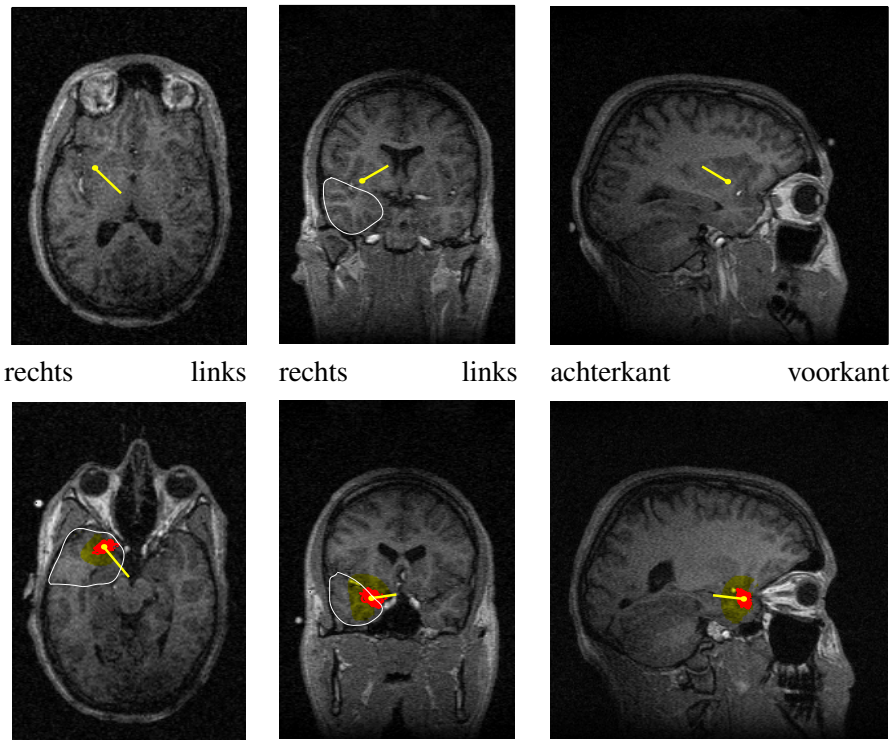

Figuur 21: De dipool is geprojecteerd op een axiale, coronale en sagitale doorsnede. In de eerste rij wordt de dipool berekend bij gebruik van het drielagig sferisch model. In de tweede rij wordt gebruik gemaakt van het realistisch hoofdmodel. Het gele oppervlak stelt de relatieve residuele energie voor die kleiner is dan het dubbel van het minimum. De rode punten rond het minimum stellen geschatte posities voor, voor gesimuleerde signalen met eenzelfde SRV als het reële EEG. Het heelkundig verwijderd gebied is omcirkeld.

We hebben het voorwaarts probleem opgelost in het realistisch hoofdmodel voor de geschatte dipoolparameters. Vervolgens wordt achtergrond-EEG opgeteld bij de bekomen potentialen zodat er een signaal verkregen wordt met dezelfde SRV als gevonden voor het reële signaal. Voor een groot aantal ruishebbende potentiaalsets wordt dan het inverse probleem opgelost. De rode verzameling puntjes rond het minimum in figuur 21 stelt de vele geschatte posities voor. De gemiddelde dipoolpositiefout bedraagt hier 4.2 mm. Hierdoor krijgen we een idee van de dipoolpositiefout te wijten aan achtergrond-EEG.

De afstand tussen de dipoolpositie bij gebruik van het sferisch en realistisch model bedraagt 21.4 mm. De hoek tussen beide dipolen bedraagt 18.1°. We merken op dat het sferisch model de dipool hoger en meer naar achter schat dan het realistisch model.

Het operatief verwijderd gebied is eveneens aangeduid op figuur 21. We merken op dat het realistisch model een geschatte positie oplevert die dichter bij dat gebied gelokaliseerd is dan het sferisch model.

0.6.3 Tweede patiënt

Patiëntinformatie en het EEG

De tweede patiënt is een 37-jarige vrouw die epilepsie heeft sinds de leeftijd van 34 jaar. Het preheelkundig onderzoek was suggestief voor een linker-mediaal temporale focus. Alhoewel de patiënt een geschikte kandidaat was voor heelkunde, heeft ze uit eigen wil beslist toch niet verder te gaan met de resectie.

Het EEG is opnieuw voorgesteld op één tijdsas in figuur 22. De verticale lijnen geven het 40 ms interval (8 monsters) weer dat gebruikt wordt voor de analyse. Het ruisniveau bedraagt 0.20 en de SRV bedraagt 4.6.

De detectie van de elektroden en de constructie van het volumegeleidermodel gebeurt op analoge manier als bij de eerste patiënt.

Dipoollokalisatie

Figuur 23 stelt de projectie voor van de dipool op de respectievelijke MR-beelden. De gele zone toont het gebied waar de relatieve residuele energie kleiner is dan het dubbel van het minimum, wat 5.17 % bedraagt. De gemiddelde positiefout voor gesimuleerde dipolen met eenzelfde SRV bedraagt 4.8 mm.

De afstand tussen de geschatte dipool in het sferisch model en in het realistisch model bedraagt 20.1 mm. De hoek tussen beide oriëntaties bedraagt 5.3°.

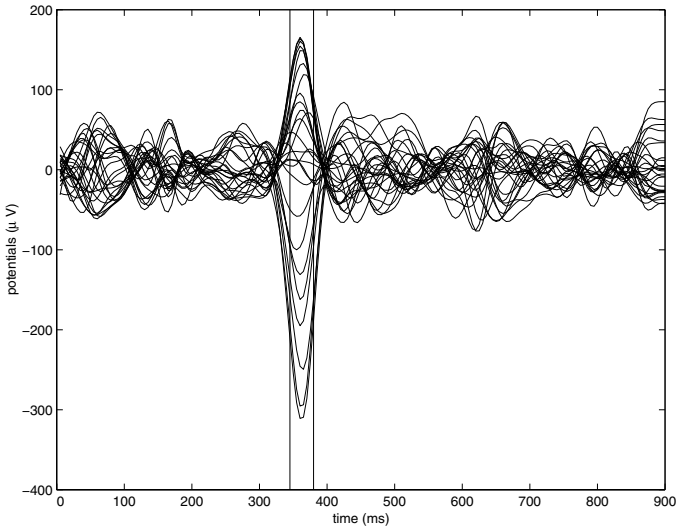

Figuur 22: Een voorstelling van het EEG op één tijdsas. De referentie is de gemiddelde potentiaal van alle elektroden. De interictale activiteit start vanaf 300 ms. Het interval dat gebruikt wordt voor het schatten van de dipool is aangeduid met verticale lijnen.

We merken hier opnieuw op dat het sferisch model de dipool hoger en meer naar achter schat.

Verder is in figuur 23 het gebied aangeduid dat hypothetisch zou verwijderd worden. We merken op dat de dipool geschat met het realistisch hoofdmodel, nauwer bij dit gebied aansluit dan de positie van het sferisch hoofdmodel.

0.6.4 Besprekingen

We hebben gevonden dat in beide gevallen de geschatte dipool bij gebruik van het realistisch hoofdmodel nauwer aansluit bij het (hypothetisch) weggesneden gebied. Toch willen we de resultaten met een zekere omzichtigheid behandelen. We zullen hierna enkele mogelijke oorzaken bespreken voor een verkeerd schatten van de elektrische bron.

Terwijl het focaal hersengebied, dat verantwoordelijk is voor de start van de epilepsieaanval, actief is, zijn er in de hersenen nog vele andere gebieden actief die niet synchroon zijn met het focale gebied. Die gebieden genereren dan achtergrond-EEG. Als we veronderstellen dat we een ideaal volumegeleidermodel hebben en een ideaal bronmodel hebben, dan nog zullen we dipoolpositiefouten maken door deze achtergrondactiviteit. Bij het veelvuldig

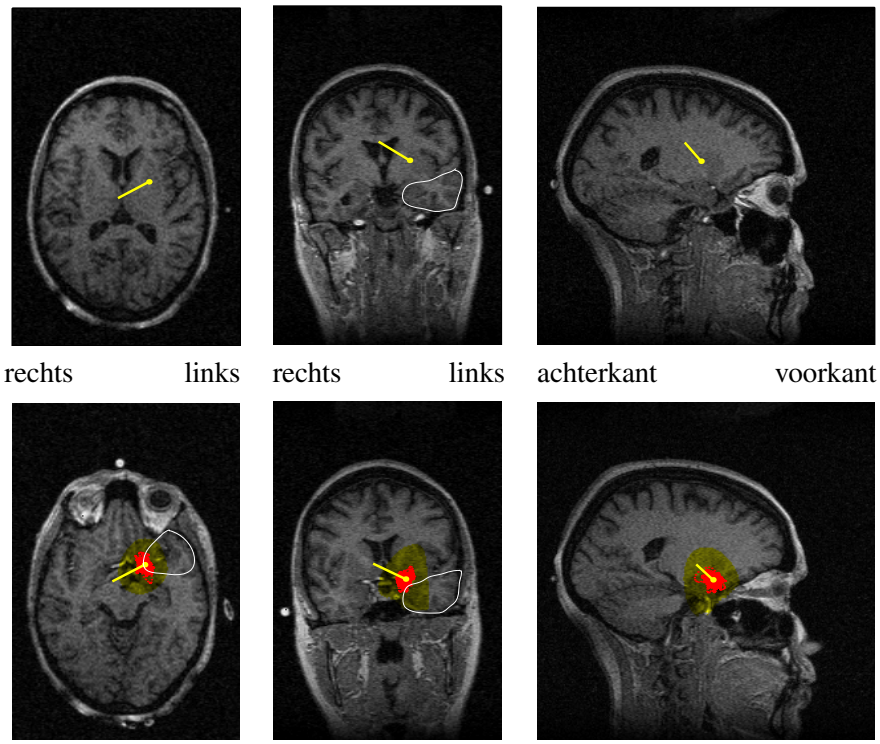

Figuur 23: De dipool is geprojecteerd op een axiale, coronale en sagitale doorsnede. In de eerste rij wordt de dipool berekend bij gebruik van het drielagig sferisch model. In de tweede rij wordt gebruik gemaakt van het realistisch hoofdmodel. In het gele oppervlak is de relatieve residuele energie kleiner dan het dubbel van het minimum. Het rode gebied rond het minimum stelt geschatte posities voor, voor een gesimuleerd signaal, met eenzelfde SRV als het reële EEG. Het hypothetisch heelkundig verwijderde gebied is omcirkeld.

voorkomen van gelijkaardige spikes, kan men overgaan tot uitmiddelen van het EEG. Dit wordt gedaan in de hoop dat de achtergrondactiviteit weggemiddeld wordt en de focale activiteit versterkt. Een andere mogelijkheid is meer tijdsmonsters in beschouwing te nemen. We hebben in paragraaf 0.5.4 opgemerkt dat de toename van het aantal tijdsmonsters met eenzelfde ruisniveau de dipoolpositiefout doet afnemen. Daar de focale activiteit slechts van beperkte duur is, is er een bovengrens aan het aantal monsters dat kan gebruikt worden.

Een tweede oorzaak van positiefouten is het gebruik van een gediscretiseerd model met een eindige roostergrootte. We merken wel op dat die fout kleiner is dan de fout te wijten aan het gebruik van het sferisch model. We hebben in paragraaf 0.3 gevonden dat de gemiddelde positiefout ongeveer overeenkomt met de knooppuntafstand. In dit geval bedraagt die dan ongeveer 2 mm.

Een andere bron van positiefouten is de schedelgeleidbaarheid. Zoals in paragraaf 0.4 reeds vermeld, is er geen eensgezindheid over de schedelgeleidbaarheid. Wij hebben de waarde genomen die vermeld werd in de meest recente publicatie [80]. De dipoolpositiefout die te wijten is aan het onderschatten van de geleidbaarheid, kan aanleiding gegeven (zie figuur 11(c)) tot fouten tussen 5 en 15 mm.

Het laten toenemen van het aantal elektroden heeft een gunstig effect op het onderdrukken van ruis, zoals verduidelijkt in paragraaf 0.5.3, en dus ook op de dipoolpositiefout. De toename van het aantal elektroden heeft weinig invloed op het wegwerken van positiefouten bij gebruik van de FDRM, zoals verduidelijkt in paragraaf 0.3. Ook dipoolpositiefouten te wijten aan het verkeerd inschatten van de schedelgeleidbaarheid, zijn weinig gevoelig aan een toename van het aantal elektroden (zie paragraaf 0.4).

Verder dienen we ook te vermelden dat de geleidbaarheid van verschillende weefsels anisotroop is. Wanneer we die weefsels benaderen door een isotrope geleidbaarheid, maken we fouten in het volumegeleidermodel. Die fouten geven op hun beurt aanleiding tot fouten in de lokalisatie van de dipool [24, 64].

Een ander probleem is de constructie van het schedelcompartiment uit de MR-beelden. Daar bot geen signaal geeft op T1-gewogen MR-beelden, is het ook moeilijk om bot uit het MR-beeld te segmenteren. Normaal vertrekken we van het hersencompartiment en passen we de dilatie-operator erop toe [63]. Een betere manier is gebruik te maken van CT-beelden, waar bot wel een sterk signaal genereert. Het gebruik van gedilateerde hersenen kan ook tot dipoolpositiefouten leiden [48].

Een laatste mogelijke oorzaak voor het verkeerd lokaliseren van de dipool is de onderliggende elektrische bron. Wanneer het stukje elektrisch actief hersenweefsel sterk gekromd is, zou de dipool, die dan als een soort resultante

bron kan beschouwd worden, toch wat verwijderd zijn van het stukje cortex. Bovendien kan het dipoolmodel een verkeerde of zinloze schatting opleveren als verschillende van elkaar verwijderde hersenzones simultaan actief zijn.

Studies met hoofdfantomen [59] en geplaatste bronnen hebben aangeduid dat de dipoolpositiefouten met een realistisch model van de orde van 8 mm zijn. Daarbij rekening houdend met de hierboven vermelde oorzaken van dipoolpositiefouten, kunnen we stellen dat de nauwkeurigheid van het schatten van een dipool ongeveer 10 mm is.

0.7 Algemene besluiten

We sommen hier nog eens de belangrijkste besluiten en originele bijdragen op.

In paragraaf 0.3 wordt het gebruik van FDRM bij het oplossen van het inverse probleem gevalideerd in een analytisch oplosbaar drielagig sferisch model. In de FDRM wordt de FDM gecombineerd met reciprociteit. De FDM biedt ons de mogelijkheid om een groot aantal weefsels met verschillende geleidbaarheden in te voeren in het volumegeleidermodel. Reciprociteit stelt ons in staat om het aantal numerieke voorwaartse berekeningen enkel afhankelijk te maken van het aantal scalpelektroden. Dit levert een aanzienlijke reductie op van numerieke voorwaartse berekeningen, als je dit vergelijkt met het geval waarbij de potentialen bij elke voorwaartse evaluatie in het invers probleem numeriek berekend moeten worden. We vinden dat de dipoolpositiefout in het algemeen niet groter is dan het dubbel van de rooster grootte. Verder is de gemiddelde dipoolpositiefout voor 1745 testdipolen en voor een 2 mm rooster met 44 elektroden gelijk aan 2.0 mm, voor een 2 mm rooster en 27 elektroden gelijk aan 2.2 mm, voor een 3 mm rooster en 44 elektroden gelijk aan 3.1 mm en voor een 3 mm rooster en 27 elektroden gelijk aan 3.4 mm. De oriëntatiefout is steeds kleiner dan 4° en dit zowel voor het 2 mm als het 3 mm rooster en voor de 44 en 27 elektroden. We hebben ook de ruisgevoeligheid van het invers probleem bij gebruik van de FDRM vergeleken met de ruisgevoeligheid bij toepassing van de analytische methode. We vinden geen grotere ruisgevoeligheid voor de FDRM vergeleken met de analytische. Het onderzoek naar de performantie van het oplossen van het invers probleem door gebruik te maken van de FDRM in een analytisch oplosbaar sferisch model, is een origineel aspect van dit onderzoek. Delen van dit onderzoek zijn voorgesteld op internationale conferenties en verschenen als uittreksel of artikel in verslagen van die conferenties [123, 125, 133]. Dit werk is tevens ingediend als artikel bij een internationaal tijdschrift [138].

In de simulatiestudie van paragraaf 0.4 hebben we onderzocht wat de dipoolpositiefout is die te wijten is aan het niet incorporeren van het VS, het

niet incorporeren van een gat in de schedel en het onderschatten van de schedelgeleidbaarheid. Voor 27 en 53 elektroden is de maximale dipoolpositiefout respectievelijk 7.6 mm en 6.1 mm bij het niet incorporeren van het VS. Bij het niet incorporeren van een gat in de schedel is dit 5.6 mm en 5.2 mm en bij het onderschatten van de schedelgeleidbaarheid is dit 33.4 mm en 28.0 mm. We vinden de grootste dipoolpositiefouten als het VS niet geïncorporereerd is, vooral rond het VS. Bij het niet incorporeren van een gat in de schedel, zijn de grootste positiefouten vooral te vinden rond het gat in het hersencompartiment. De positiefout te wijten aan het onderschatten van de schedelgeleidbaarheid is merkbaar in het hele hersencompartiment. De dipool is hier typisch radiaal naar buiten toe geschat. Tevens is de positiefout van een grotere orde dan die in de twee voorgaande gevallen. Het laten toenemen van het aantal elektroden brengt slechts een marginale verbetering van de dipoolpositiefout teweeg. De originele aspecten omvatten het gebruik van een groot aantal testdipolen, zodat het mogelijk is beelden te maken met dipoollocatiefouten in functie van de dipoolpositie. Verder is de impact van het aantal elektroden op de dipoolpositiefout ook een originele bijdrage bij het niet incorporeren van het VS en het gat. Het onderzoek dat hier is voorgesteld, heeft aanleiding gegeven tot een publicatie in een internationaal tijdschrift [135]. Verder is er een deel van dit werk opgenomen als een abstract in de verslagen [134] van een internaltionale conferentie, waar het tevens is voorgesteld.

Het doel van het onderzoek in paragraaf 0.5 is om de performantie te vergelijken van het drielagig sferisch model met die van het realistisch model, in EEG-dipoollokalisatie met de aanwezigheid van ruis. De performantie kan uitgedrukt worden met een gemiddelde dipoolpositiefout bij gebruik van een groot aantal ruishebbende potentialen met eenzelfde ruisniveau. Hoe kleiner die fout, hoe beter een model scoort. Wanneer nu voor een gegeven ruisniveau en voor een groot aantal testdipolen de gemiddelde dipoolpositiefout voor een sferisch model, $E(\Delta r_i^{sfeer})$, veel groter is dan die voor een realistisch model, $E(\Delta r_i^{real})$, dan is het zinvol om het realistisch hoofdmodel te gebruiken i.p.v. het sferisch hoofdmodel. Anderzijds, wanneer voor een gegeven ruisniveau en voor een groot aantal testdipolen $E(\Delta r_i^{sfeer})$ en $E(\Delta r_i^{real})$ nagenoeg even groot zijn, dan doet het er niet toe welk van beide modellen gebruikt wordt. De performantie van het realistisch model vergeleken met het sferisch model neemt af bij een toename van het ruisniveau. De toename van het aantal elektroden heeft een beperkte invloed op de performantie van het realistisch model, vergeleken met de performantie van het sferisch model in EEG-dipoollokalisatie. De performantie van het realistisch model stijgt t.o.v. het sferisch model bij een toename van het aantal tijdsmonsters. Een origineel aspect van dit onderzoek is dat de gemiddelde dipoolpositiefouten bekomen

met het sferisch en realistisch model, vergeleken worden.

Deze studie is ingediend als artikel in een internationaal tijdschrift [137]. Verschillende onderdelen van deze studie zijn voorgesteld op internationale conferenties en tevens opgenomen als artikels in de verslagen van die conferenties [136, 139].

In paragraaf 0.6 hebben we de dipool geschat voor een stukje interictaal EEG van twee patiënten met epilepsie. Daarvoor wordt gebruik gemaakt van een sferisch hoofdmodel en een realistisch hoofdmodel. Door de elektronenmerkers, gedetecteerd in de MR-beelden, is er een best passende sfeer geconstrueerd. Die geeft op haar beurt aanleiding tot de constructie van het drielagig sferisch model. gebruikmakend van dit model, wordt de dipool geschat en vervolgens terug op het corresponderende MR-beeld geplaatst. Verder worden de MR-beelden van elk van de patiënten gesegmenteerd. De FDRM wordt dan toegepast om de dipool te schatten in een realistisch hoofdmodel. Het gebruik van de FDRM voor het schatten van de dipoolbron met is een origineel aspect van deze studie. Vervolgens plaatst men de dipool terug op het MR-beeld. De afstand tussen de geschatte dipolen in het sferisch en realistisch hoofdmodel bedraagt voor beide gevallen ongeveer 20 mm. De dipoolpositie bij het realistisch hoofdmodel bevindt zich dichter bij het (hypothetisch) weggesneden gebied dan de positie gevonden met het sferisch model. Als we rekening houden met de verschillende oorzaken van dipoolpositiefouten en met fantoomstudies, dan kunnen we besluiten dat de nauwkeurigheid van EEG-dipoollokalisatie in de gunstigste omstandigheden ongeveer 10 mm bedraagt. De resultaten die bekomen zijn door het projecteren van de dipool op MR-beelden, geschat met het sferisch model, zijn gerapporteerd op verschillende internationale conferenties, en zijn als abstract of artikel in verslagen van die conferenties verschenen [126–128, 132]. Een groep van ongeveer 30 patiënten werden geanalyseerd op een analoge manier als hierboven. De resultaten hiervan werden ook voorgesteld op internationale conferenties en zijn als artikel of als abstract in de verslagen van die conferenties verschenen [10, 13, 17, 19, 113]. De klinische relevantie van EEG-dipoollokalisatie bij gebruik van realistische hoofdmodellen, werd bekend gemaakt in internationale tijdschriften [11, 14, 18].

Chapter 1

General introduction

1.1 Research environment

The electroencephalogram (EEG) measures potential differences between scalp electrodes as a function of time. These potential differences are generated by electrically active brain tissue. Typically 20 to 40 electrodes are placed on the scalp surface.

In a clinical setting, the EEG is applied for the diagnosis of epilepsy. The EEG of patients with epilepsy may have an abnormal amplitude and waveform. For patients with so-called 'partial' epilepsy, a focal group of brain cells is responsible for an epileptic seizure. This group of cells is called the epileptogenic zone. Epilepsy is commonly treated with anti-epileptic drugs. For a subgroup of patients, anti-epileptic drugs are not sufficient to suppress their seizures. A possible solution is resective surgery, which aims at removing the epileptogenic zone. During the presurgical evaluations of these patients, several examinations are performed to locate this zone. One of these examinations is long-term (3-5 days) video/EEG monitoring. By inspecting the EEG and the behavior of the patient at the onset of a seizure, neurologists can localize the epileptogenic zone in the brain. EEG source analysis is another technique that can be used, providing that focal EEG changes are detected. When assuming a volume conductor model of the human head and assuming a source model, which electrically simulates active brain tissue, it is possible to localize the electrical source. This is typically done by calculating the source parameters that generate electrode potentials which best fit the measured EEG activity. This technique, which is called EEG source analysis, is the main topic of this thesis. It is our hope that this additional localizing tool may contribute to the successful presurgical evaluation of patients with epilepsy.

1.2 Overview

Chapter 2 is an introduction to neurophysiology and EEG source analysis in epilepsy. The chapter starts with a brief introduction to brain anatomy and neurophysiology. We focus the discussion on how brain tissue generates the EEG. The application areas of EEG and the requirements to measure EEG are presented. Next we focus on epilepsy. The EEG correlates of epileptic seizures are discussed. The concept of epilepsy surgery and the presurgical evaluation are also presented. The so-called 'forward problem' calculates the potentials at the scalp electrodes for a given electrical source. When applying a spherical head model, analytical solutions to the forward problem exist. We illustrate such a solution. When realistic head models are considered in the forward problem, numerical methods must be applied. The different numerical methods for this application are discussed. A comparison between these different methods is also presented. Finally chapter 2 deals with the so-called 'inverse problem'. The inverse problem tries to find the source parameters that best describe the measured potentials. A measured set of scalp potentials can be generated by more than one source configuration. Subsequently there is no unique relationship between scalp potentials and electrical source configurations. We restrict our source model to a single current dipole. An algorithm is presented which solves the inverse problem for a single time instance and for multiple time samples.

In chapter 3 the finite difference reciprocity method (FDRM) is validated in a spherical head model. This is a method to numerically calculate the forward problem in a realistic head model. This method combines the finite difference method and reciprocity. One of the advantages of the finite difference method is the possibility to introduce a large number of regions with various conductivities within the volume conductor model. This requires a large number of computational points which leads to iterative solvers for large sparse linear systems. Reciprocity eases the computational burden involved by these iterative methods. The FDRM for solving the inverse problem is validated as follows: applying the analytical equation the exact electrode potentials are calculated. Then the inverse problem is solved utilizing the FDRM. The dipole location and orientation error are evaluated. The sensitivity to noise of the inverse problem when applying the FDRM is also investigated.

In chapter 4 we apply the FDRM to study dipole location errors due to volume conductor model (VCM) errors. For the introduction of depth electrodes a trepanation (a removal of a circular piece of skull) needs to be performed. First we try to answer the following question: what is the dipole location error caused by omitting a hole in the skull? This is investigated by calculating

the scalp potentials with a hole included in the VCM. The inverse problem is solved without a hole in the VCM. The ventricular system (VS) is a cavity filled with cerebrospinal fluid located in the brain. The VS has a different conductivity than the surrounding brain tissue. The next question to be answered is: what is the dipole location error due to omitting the ventricular system? The procedure is as follows: the forward problem is calculated with the VS included, the inverse problem is solved without the VS included in the VCM. The third problem that is addressed is the controversy on the value of the skull conductivity. In the recent literature, the skull conductivity is estimated 16 times smaller than the soft-tissue conductivity (brain and scalp). Older values in the literature report a conductivity which is 80 times smaller than the soft-tissue conductivity. We have investigated the dipole location error due to underestimating the skull conductivity, i.e., applying a conductivity which is 80 times smaller instead of 16 times smaller than the soft-tissue. When addressing the three aforementioned questions we also studied the impact of the number of electrodes on the dipole location error.

In chapter 5 the results of EEG dipole source analysis, utilizing a spherical and realistic head model, are compared in the presence of noise. A major issue is whether it is still worthwhile constructing more demanding realistic head models. We apply Gaussian noise and background EEG as noise contributors. From a noiseless potential distribution obtained with the realistic head model, a large number of noisy potential distributions are generated. The average dipole location error is computed for these noisy distributions applying a spherical and realistic head model in the inverse procedure. When applying a realistic head model in the inverse procedure, the dipole location error is assumed to be caused by noise only. With a spherical head model, the location error is due to noise and due to the simplified VCM. We also investigate the impact of increasing the number of electrodes on the average location errors, when applying both models. Finally the impact of increasing the number of time samples on the average dipole location error is studied in both models.

In chapter 6 two case studies are presented. Epochs of EEG selected from long-term video/EEG-monitoring recordings are analyzed. Both a realistic and spherical head model are constructed and applied to calculate the dipole. The resulting dipoles are then mapped on the corresponding MR-images. The position of the dipole is then compared with the surgically removed area. Finally, the limitations of EEG dipole source analysis are discussed.

In chapter 7 the general conclusions are summarized. The original contributions of this work are highlighted also.

1.3 Publications of research results

This research has led to two publications in international peer-reviewed journals [135, 138]. Furthermore, one publication has been submitted to an international journal [137]. Parts of this work have been presented at 6 international congresses and resulted in an article published in the congress proceedings [122–124, 126, 136, 139]. Nine contributions to international congresses have been published as an abstract in the congress proceedings [125, 127–134]. All these publications were first-authored. At two of these conferences the author was awarded for his contribution [125, 134].

He also assisted in related research areas, which has led to 6 publications in international peer-reviewed journals [11, 14, 18, 98, 107, 115], as a co-author. Six contributions as a co-author are reported in international congresses with an article in the congress proceedings [70, 97, 109, 110, 117, 118]. And 15 contributions as a co-author are published as an abstract in the congress proceedings [10, 13, 16, 17, 19, 106, 108, 111–114, 116, 119–121].

Finally the author has supervised two M.Sc. dissertations in the field of EEG dipole source analysis [21, 94].

Chapter 2

Neurophysiology and EEG source analysis

2.1 Introduction

Neurophysiology is the branch of neuro-science that studies the functioning of the nervous system. In this chapter the basic aspects of neurophysiology are summarized to allow understanding of how the electroencephalogram (EEG) is generated. The EEG measures and records scalp potentials as a function of time. The process of retrieving the electrical sources which generate the EEG is called EEG source analysis. Different aspects of EEG source analysis are also presented.

First, the basics of brain anatomy and neurophysiology are discussed in section 2.2.

Aspects related to the generation of the EEG are illustrated in section 2.3. In this section, answers to the following questions are put forward: (1) which neurophysiological phenomena are responsible for generating an EEG signal and (2) what are the requirements needed to measure these phenomena.

In section 2.4 the acquisition and applications of EEG are presented. The 10-20 international system electrode placement is also discussed.

We then focus on epilepsy in section 2.5. The definition of epilepsy and the epileptogenic manifestations in the EEG are discussed. We further describe the presurgical evaluation and the epilepsy surgery protocol.

In section 2.6 Poisson's differential equation is presented. A focal electrical source in the brain is often modeled by a current dipole. The concept of a current dipole is also described in this section.

In EEG source analysis, the EEG potentials generated by an electrical source in the brain are calculated by solving the forward problem. This corre-

sponds to solving Poisson's equation. In section 2.7, the forward problem is solved in different volume conductor models. First, the potentials for a dipole in an infinite homogenous conductor are presented. Next, the potentials at the outer surface of a three-shell spherical head model are calculated by a semi-analytical equation. To solve the forward problem in a realistic head model obtained from medical imaging, numerical methods are needed. The boundary element method, the finite element method and the finite difference method are therefore described and compared.

The electrical source which best fits the measured EEG potentials is obtained by solving the inverse problem in EEG source analysis. In section 2.8, the inverse problem is presented. There is no unique solution for this problem because several sources can generate the same scalp potentials. However, to find a solution, we restrict the source model to a single current dipole. The dipole's parameters are searched for so that the potentials it generates, optimally fits the measured potentials.

2.2 Brain anatomy and neurophysiology

2.2.1 Brain anatomy

Based on [51] a review chapter in a handbook of EEG, an introduction to the anatomy of the brain is given. First, the anatomy on the cellular level is presented. Then, the gross anatomy is described.

The brain consists of about 10^{10} nerve cells or neurons. The shape and size of the neurons vary but they all possess the same anatomical subdivision, as illustrated in figure 2.1. The soma or cell body contains the nucleus of the cell. The dendrites, arising from the soma and repeatedly branching, are specialized in receiving inputs from other nerve cells.Via a single axon, impulses are sent to other neurons. The axon's end is divided into branches which form synapses with other neurons. The synapse is a specialized interface between two nerve cells. The synapse consists of a cleft between a presynaptic and a postsynaptic neuron, as illustrated in figure 2.1. At the end of the branches originating from the axon, the presynaptic neuron contains small rounded swellings which contain the neurotransmitter substance.

Next, the gross anatomy of the brain is presented. In figure 2.2, which presents a coronal slice of the brain, a part of the ventricular system is depicted. The ventricular system consists of cavities in the brain which are filled with cerebrospinal fluid. The larger inner part of the brain contains only the axons of the nerve cells and looks white, as illustrated in figure 2.2. It is therefore called the white matter. The cell body and dendrites of the neurons are restricted to

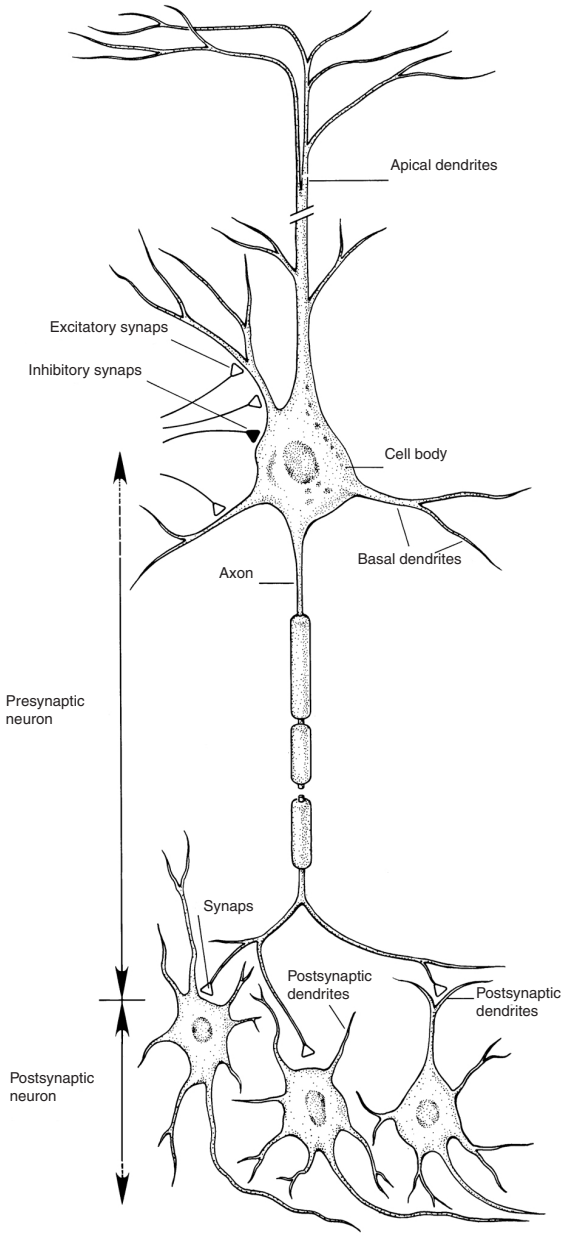

Figure 2.1: The neuron.

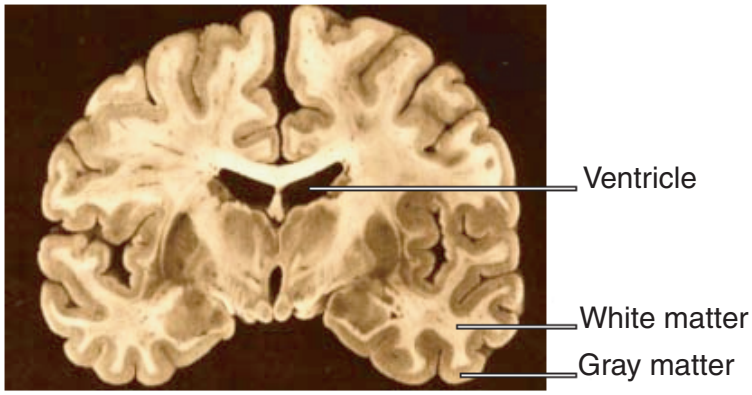

Figure 2.2: A coronal slice of the brain.

the darker areas in figure 2.2, where they form the gray matter as illustrated in figure 2.2. The gray matter can be found at the outermost surface of the brain, the cortex, and in some deeper structures. In a patch of gray matter with a surface area of 1 mm^2, about 50000 neurons are present.

In the cortical gray matter the cells are arranged in six layers, as illustrated in figure 2.3. The thickness of the cortical gray matter varies between 1 mm and 4 mm. In figure 2.3, two large pyramidal cells (white) are visualized in layers 3 and 5. It will be shown in the next section that these cells are responsible for generating the EEG. They consist of apical and basal dendrites as illustrated in figure 2.1. The apical dendrites are located in the outermost layers 1 and 2 of the cortical gray matter. The basal dendrites are located in layers 3-5 of the cortical gray matter.

The sulci are fissures in the brain cortex. The rounded areas between the fissures are called gyri. The fissures have been used to subdivide the brain in four lobes, i.e. the frontal, parietal, occipital and temporal lobe, as illustrated in figure 2.4.

2.2.2 Neurophysiology

At rest the intracellular environment of a neuron is negatively polarized at - 60 mV compared to the extracellular environment. The potential difference is due to an unequal distribution of Na^+, $K^+$and Cl^-ions across the cell membrane. This unequal distribution is maintained by the $Na^+$and K^+ion pumps located in the cell membrane.

The main task of a neuron is to transport signals. This is achieved by an

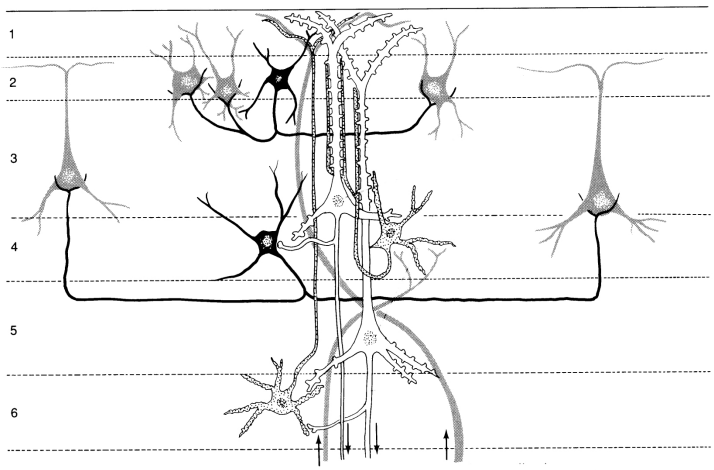

Figure 2.3: The layered cortex. The white cells correspond with pyramidal cells. From [66].

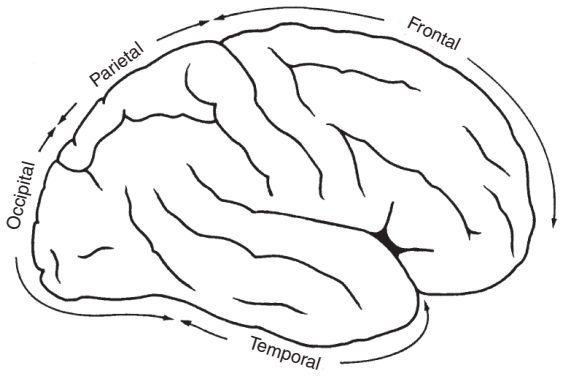

Figure 2.4: The four lobes in the brain. From [51].

alternating chain of electrical and chemical events. Active neurons secrete a neurotransmitter, which is a chemical substance, at the synaptic side. The synapses are mainly localized at the dendrites and the cell body of the postsynaptic cell. A postsynaptic neuron has a large number of receptors on its membrane that are sensitive for this neurotransmitter. The neurotransmitter in contact with the receptors changes the permeability of the membrane for charged ions. Neurotransmitters can exert different functions. Excitatory neurotransmitters allow signals to proliferate. These molecules cause an influx of positive ions which results in a depolarization. This means that the potential difference between the intra- and extracellular environment decreases. Instead of -60 mV, the potential difference becomes -40 mV. This depolarization is also called an excitatory postsynaptic potential (EPSP). Inhibitory neurotransmitters stop the proliferation of signals by causing an outflow of positive ions resulting in a hyperpolarization. A hyperpolarization means that the potential difference between the intra- and extracellular environment increases. This potential change is also called an inhibitory postsynaptic potential (IPSP). There are a large number of synapses from different presynaptic neurons in contact with one postsynaptic neuron. At the cell body all EPSP and IPSP are integrated. When a net depolarization of the intracellular compartment at the cell body reaches a certain threshold, an action potential is generated that proliferates along the axon to other neurons.

Figure 2.5 illustrates the excitatory and inhibitory postsynaptic potentials. It also shows the generation of an action potential.

2.3 The generators of the EEG

The physiological principles of EEG are found in [93] and [102]. The electrodes used in scalp EEG are large and remote. They only detect summed activities of a large number of neurons which are synchronously electrically active. The action potentials can be large in amplitude (70-110 mV) but they have a small interval of time (0.3 ms). A synchronous firing of action potentials of neighboring neurons is unlikely. It is believed that the postsynaptic potentials are the generators of the extracellular potential field which can be recorded with an EEG. Their interval of time is larger (10-20 ms). This enables summed activity of neighboring neurons. However their amplitude is smaller (0.1-10 mV).

Besides having more or less synchronous activity, the neurons need to be regularly arranged to have a measurable scalp EEG signal. The spatial properties of the neurons must be so that they amplify each other's extracellular potential fields. The neighboring pyramidal cells are organized so that the

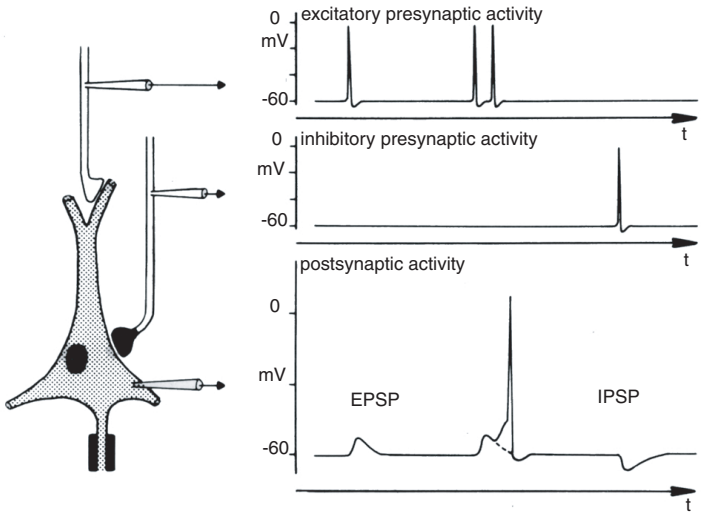

Figure 2.5: The excitatory (EPSP) and inhibitory (IPSP) post synaptic potentials are illustrated. An action potential is also depicted. From [102].

axes of their dendrite tree are parallel with each other and orthogonal to the cortical surface, as illustrated in figure 2.6. Hence, these cells are suggested to be the generators of the EEG.

In what follows, we focus on EPSP, located at the apical dendrites of a pyramidal cell. The excitatory neurotransmitter causes an influx of positive ions at the postsynaptic membrane as illustrated in figure 2.7(a) and depolarizes the local cell membrane. This causes a lack of extracellular positive ions at the apical dendrites of the postsynaptic neuron. A redistribution of positively charged ions also takes place at the intracellular side. Ions flow from the apical dendrite to the cell body and depolarize the membrane potentials at the cell body. Subsequently positive charged ions become available at the extracellular side at the cell body and basal dendrites.

A migration of positively charged ions takes place from the cell body and the basal dendrites to the apical dendrite occurs, which is illustrated in figure 2.7(a) with current lines. This configuration generates extracellular potentials. Other membrane activities start to compensate for the massive intrusion of the positively charged ions at the apical dendrite, however these mechanisms are beyond the scope of this work and can be found elsewhere [62].

A simplified equivalent electric circuit is presented in figure 2.7(b) to il-

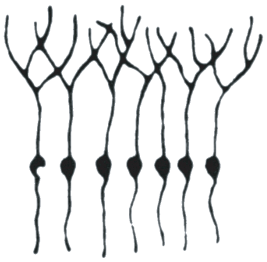

Figure 2.6: Neurons which amplify each other's extracellular fields. From [101].

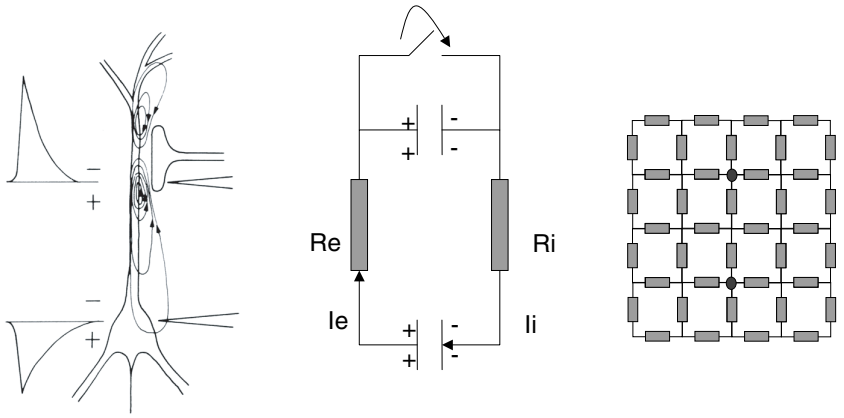

Figure 2.7: A neuron with an excitatory synapse at the apical dendrite is presented in (a) [101]. A simplified equivalent circuit is depicted in (b). The extracellular environment can be represented by a resistive network as illustrated in (c).

lustrate the initial activity of an EPSP. At rest, the potential difference between the intra- and extracellular compartment can be represented by charged capacitors. One capacitor models the potential difference at the apical dendrites side, while a second capacitor models the potential difference at the cell body and basal dendrite side. The potential difference over the capacitors is 60 mV. The excitatory neurotransmitter causes a massive intrusion of positively charged ions at the postsynaptic membrane at the apical dendrite side. In the equivalent circuit, this is modeled by a switch that is closed. The capacitor at the cell body side discharges which causes a current flow I_e over the extracellular resistor R_e and I_i over the intracellular resistor R_i. The repolarization of the cell membrane at the apical side or the initiation of the action potential is not modeled with this simple equivalent electrical circuit. More advanced equivalent electrical circuits can be found elsewhere [62]. The fact that a current flows through an extracellular resistor indicates that potential differences in the extracellular space can be measured.

A simplified electrical model for this active cell consists of two current monopoles: a current sink at the apical dendrite side which removes positively charged ions from the extracellular environment, and a current source at the cell body side which injects positively charged ions in the extracellular environment. The current source and sink are represented by the two dots in figure 2.7(c). The extracellular resistance R_e can be decomposed in the volume conductor model in which the active neuron is embedded, as illustrated in figure 2.7(c). In section 2.7, we come back to the various volume conductor models used.

2.4 Electroencephalography

2.4.1 Recording EEG

When cortical areas are simultaneously active, potential differences are generated between electrodes positioned on the scalp surface. The EEG records these potential differences as a function of time. The electrodes are placed in standard positions. Figure 2.8 presents the 10-20 international system electrode placement [49]. The electrode positions are found by dividing the line between the nasion and inion, and the line between the preauricular points, into intervals which are 10% or 20% of the original length, as illustrated in figure 2.8. In this work we apply the 10-20 international system of electrode placement with three additional electrodes above each of the temporal brain areas (FT9, FT10, T9, T10, TP9, TP10), as illustrated in figure 2.9. A total of 27 electrodes are used. Furthermore, each electrode is given a label as illustrated

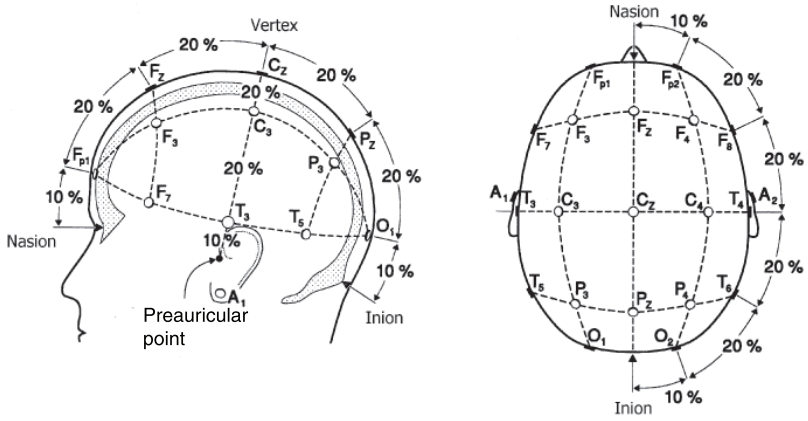

Figure 2.8: A representation of the 10-20 international system electrode placement. From [62]

in figure 2.9.

Modern acquisition equipment, samples the EEG and stores it digitally. The sample rate typically varies between 100 Hz and 1 kHz. Digital signal processing [99] or signal detection software [58, 105] can then be applied. In figure 2.10 an epoch of a 10 s EEG is presented. The potential difference as a function of time is presented for the electrode pairs given in front of each channel.

The magnetic fields as a function of time can also be measured. This technique is called magnetoencephalography (MEG) [39]. However we will not go into this matter.

2.4.2 The application areas of EEG

One application area is sleep disorders [78]. Staging of sleep phases is mainly based on EEG characteristics. EEG of a patient complaining from sleeplessness or from fatigue, can be recorded and abnormalities in the EEG may be found when compared with a normal sleep EEG.

Another application area are the evoked potentials [100]. By stimulating peripheral nerves, evoked potentials can be generated in the EEG. We distinguish visual, auditory and somatosensory stimuli. These evoked potentials are much smaller in amplitude than the available background EEG. However they are time-locked. A large number of similar stimuli may be delivered and the corresponding EEG is recorded. The EEG traces are aligned and their

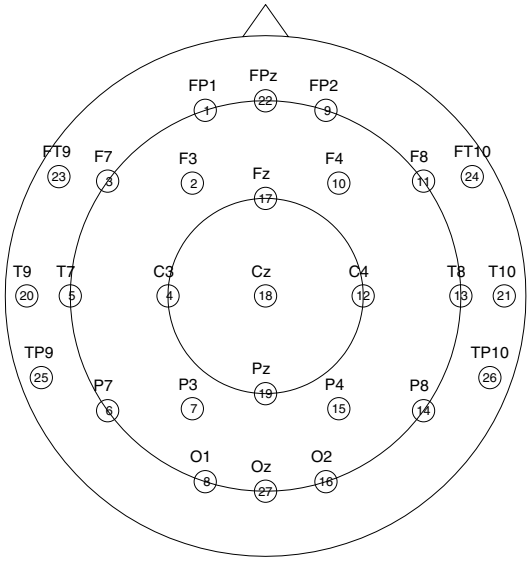

Figure 2.9: A top view of the electrode positions. The large circles represent positions with a constant azimuthal angle θ. From the inner to the outer circle we have an angle θ of $45°, 90°$ and $120°$, respectively. The 27 electrodes are also labeled.

activity is summed. This to amplify the evoked potentials and to reduce the background EEG. This technique can be applied to test the functioning of the peripheral nerves and the integrity of various central nervous pathways.

A third application area is epilepsy. The techniques presented in this work are mainly developed for this application. Therefore we deal with this application in a separate section. Some aspects of the present work can be applied in the area of evoked potentials also.

2.5 Epilepsy

2.5.1 Epileptic seizures

Epilepsy is a disease where the synchronous electrical activity of a focal or large brain area is abnormal [77]. This activity is often called an epileptic discharge. An epileptic seizure is the clinical manifestation of epilepsy. Depending on the size and the location of this area in the brain, different manifestations can occur, such as a short period of absence, tension of muscles, convulsions and unconsciousness. Several causes of this abnormal discharge can be found, e.g., brain damage due to head trauma, a lack of oxygen at birth,

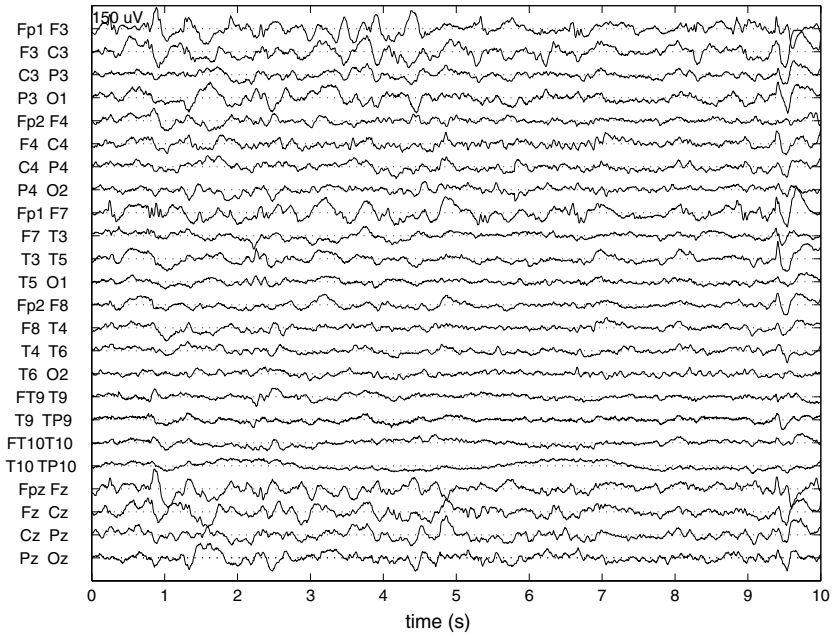

Figure 2.10: EEG Epoch of 10 s. The electrode pairs between which the potential difference is plotted, are shown in front of each channel.

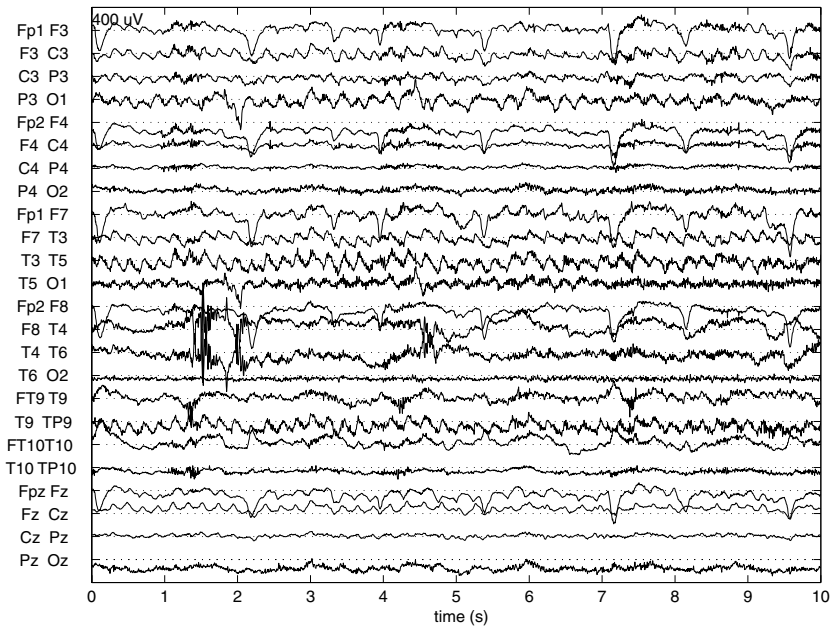

Figure 2.11: Epoch of 10 s EEG during a seizure.

presence of tumors, intoxication or brain malformation. Approximately 0.5 % to 1 % of the population is affected by epilepsy [8].

Epileptic seizures can be subdivided in two groups, i.e., partial and generalized seizures. In partial seizures only a limited brain area is involved in the epileptic discharge. On the other hand, the generalized seizures have an epileptic discharge in the entire brain.

2.5.2 Epilepsy and the EEG

Patients with epilepsy can have special features in their EEG [77]. At the onset of an epileptic seizure, rhythmic activity can be observed with a frequency of 5 to 6 Hz. The EEG measured during a seizure is called ictal EEG. The amplitude is usually higher than when no seizure occurs. For patients with partial epilepsy, the EEG in the early stage of the seizure is generated by the electrically active focal brain area (ictal onset zone). Later on in the seizure, artifacts occur in the EEG due to muscle activity. Figure 2.11 shows an epoch of 10 s EEG of an epileptic seizure.

A second feature in the EEG of patients with epilepsy occurs in between seizures, and is called interictal EEG. This EEG can consist of a spike (a brief

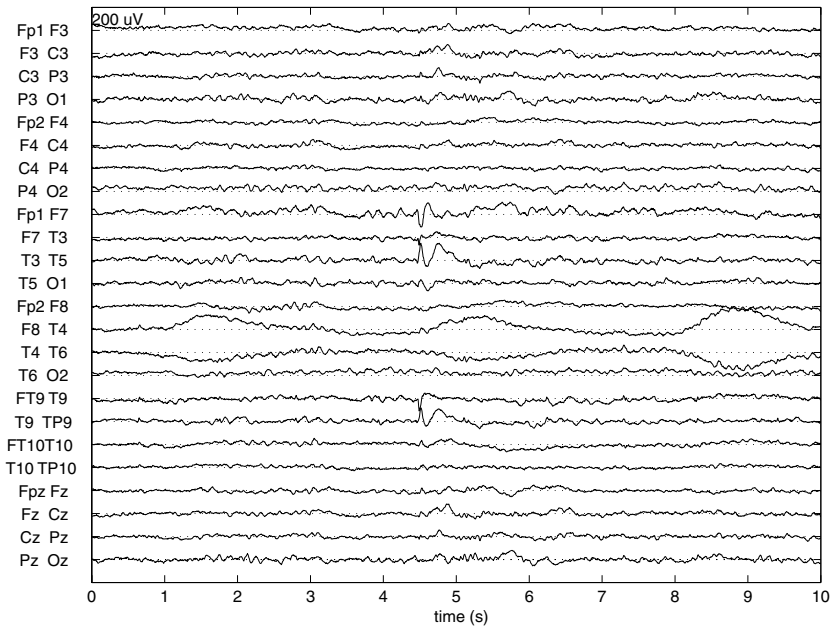

Figure 2.12: Epoch of 10 s interictal EEG. At t = 4.5 s a spike occurs.

electrical event) with a time duration of 20 to 70 ms, a sharp wave with a time duration of 70 to 200 ms and a spike-wave-complex, consisting of a spike followed by a wave. It is believed that the brain areas generating the interictal EEG are the same as the ones generating the ictal EEG [47]. Figure 2.12 shows a spike at t = 4.5 s. This activity has a high amplitude for the EEG signals Fp1-F7, T3-T5 and T9-TP9.

The potential differences between electrodes located close to the onset zone typically have a higher amplitude than potential differences further away from this zone. By inspecting the amplitude of the EEG we are then able to roughly localize the active brain area. Based on this principle, dipole source analysis, applied in this thesis, is performed.

2.5.3 Epilepsy surgery

The criteria for epilepsy surgery are failure of adequate anti-epileptic drugs and the demonstration of a focal origin in a part of the brain that can be removed without causing unacceptable neurological deficit.

It is known that in about 25 % of patients with epilepsy seizures can not be controlled with anti-epileptic drugs [8]. This is called refractory epilepsy.

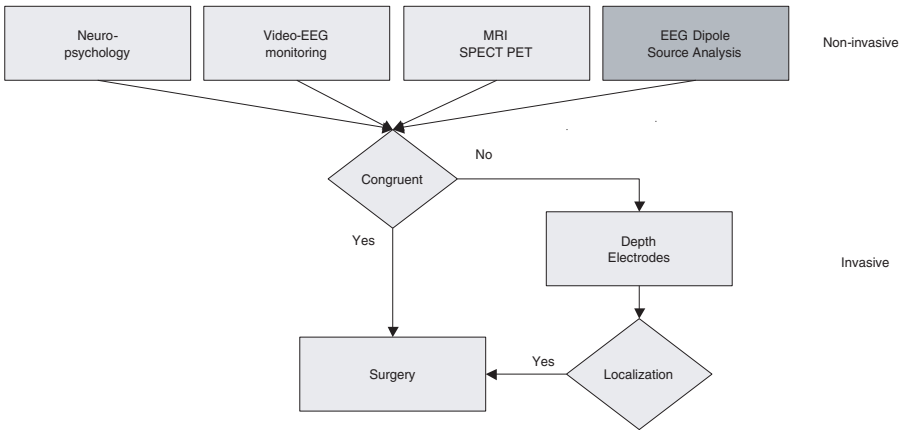

Figure 2.13: Flowchart of the presurgical evaluation.

Those patients in whom an epileptogenic zone (area causing epilepsy) can be identified can be treated with resective surgery. Subsequently only patients with partial refractory epilepsy are candidates for surgery. It is furthermore obvious that the removal of brain tissue should not lead to a neurological deficit. A minor reduction of memory due to surgery may be acceptable for a patient having multiple seizures each week. However when the onset zone is localized for example in the speech areas of the brain, surgery can not be performed.

The aim of the presurgical evaluation is to detect the epileptogenic zone. Several technical examinations need to be performed to localize this zone. When the findings of the different examinations lead to the same area, surgery can be considered. Figure 2.13 shows a flowchart of the presurgical evaluation.

After a thorough neurological examination a series of noninvasive examinations are carried out. Video/EEG monitoring is a long-term (3 to 5 days) recording of the EEG and the video of the patient. Anti-epileptic drugs may be tapered or completely withdrawn to precipitate a habitual seizure. The analysis of the behavioral changes and the EEG abnormalities during the seizure, both presented on a split-screen, is of major importance to localize the epileptogenic zone [8]. Neuroimaging techniques such as computed tomography (CT) and magnetic resonance (MR) imaging, may detect structural abnormalities in the brain [103]. Positron emission tomography (PET) provides information on cerebral blood flow and oxygen and glucose metabolism. Areas of glucose hypometabolism are often associated with the epileptogenic zone [31]. Single photon emission computed tomography (SPECT) can be used to evaluate

regional changes in blood flow which may be suggestive for an epileptogenic zone [8]. Neuropsychological tests investigate the higher cognitive functioning such as speech and memory. The results of these tests can also be applied to localize a dysfunction of certain brain areas.

When these different investigations indicate the same epileptogenic zone, and when no major neurological deficit is expected by removal of this area, a multidisciplinary team decides to perform resective surgery.

However when the results of presurgical investigations are not congruent, a long-term invasive EEG monitoring may be considered. Rigid or flexible depth electrodes with a variable number of contact points are inserted into the brain through a trepanation, i.e. a removal of a circular piece of skull. Furthermore, grids consisting of a thin layer of Silastic and numerous embedded electrodes can also be introduced [8]. Invasive electrodes are placed in the vicinity of brain areas that have a high probability of being the epileptogenic zone. When by inspecting the invasive recordings, an epileptogenic zone can be distinguished, resective surgery may be performed. Invasive examinations carry a risk of complications such as infections in 2 % of the patients [8].

2.5.4 EEG dipole source analysis

By inspecting the ictal or interictal EEG it is possible to perform a localization of the generating electrical source qualitatively. However, when a volume conductor model and an electrical source model are introduced, it is also possible to perform a quantitative localization.

A focal electrical source may be represented by a current dipole. A dipole has three position parameters, two orientation parameters and one magnitude parameter (see subsection 2.6.6). EEG dipole source analysis aims at retrieving the dipole which best fits the measured EEG.

EEG dipole source analysis of ictal and interictal EEG of the same patient is demonstrated in figure 2.14. The dipole is computed with a three-shell spherical head model (see subsection 2.7.2). In the left column the interictal (first row) and ictal (second row) EEG is presented. The dipole position and orientation are given in a schematic representation of the head in the second column. The dipole magnitude as a function of time is shown in the second column as well.

EEG dipole source analysis is an additional noninvasive examination in the presurgical evaluation of epilepsy, as illustrated on the diagram in figure 2.13. The aim is to extract quantitative information about the ictal onset zone from the EEG [12]. This additional noninvasive technique is introduced in the hope that the number of invasive recordings can be reduced in the future. A recent

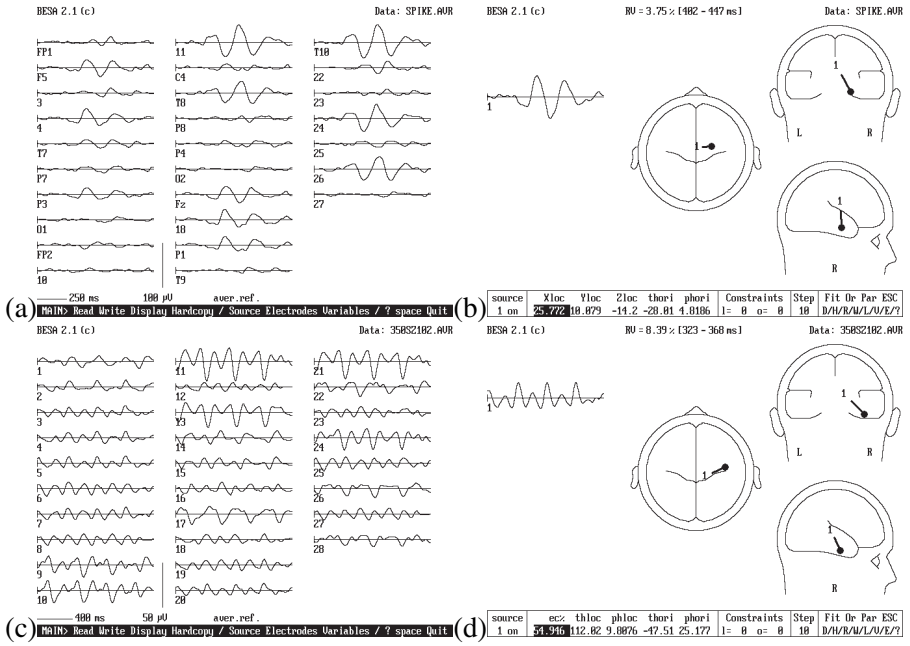

Figure 2.14: The first column shows the interictal (a) and ictal (c) activity. The second column shows the dipole position and orientation for the interictal (b) and ictal (d) activity. Furthermore the dipole magnitude as a function of time is given in the second column.

publication [14] of our group confirms this hope.

The dipole model and EEG source analysis are explained in the following sections.

2.6 Poisson's equation, boundary conditions and dipoles

2.6.1 Quasi-static conditions

It is shown in [82] that no charge can be piled up in the conducting extracellular volume and that at one moment in time all the fields are triggered by the active electric source. Hence, no time delay effects are introduced. All fields and currents behave as if they were stationary at each instance. These conditions are also called quasi-static conditions. They are not static because the neuronal activity changes with time. But the changes are slow compared to the propagation effects.

2.6.2 Applying the divergence operator to the current density

Poisson's equation gives a relationship between the potentials at any position in a volume conductor and the applied current sources. The mathematical derivation of Poisson's equation via Maxwell's equations, can be found in text books on electromagnetism [85]. However we have derived Poisson's equation with the divergence operator. In this way we emphasize the physical aspect of the problem. Furthermore, the concepts introduced above, such as current source and current sink, are used when applying the divergence operator.

Definition

The current density is a vector field and can be represented by $\mathbf{J}(x, y, z)$. The unit of the current density is A/m^2. The divergence of a vector field $\mathbf{J}$ is defined as follows :

$$\nabla \cdot \mathbf{J} = \lim_{G \to 0} \frac{1}{G} \oint_{\partial G} \mathbf{J}.d\mathbf{S}. \tag{2.1}$$

The integral over a closed surface ∂G represents a flux or a current. This integral is positive when a net current leaves the volume G and is negative when a net current enters the volume G. The vector $d\mathbf{S}$ for a surface element of ∂G with area dS and outward normal $\mathbf{e}_n$, can also be written as $\mathbf{e}_n dS$. The unit of $\nabla \cdot \mathbf{J}$ is A/m^3 and is called the current source density [34] symbolized

with I_m. Generally we can write:

$$\nabla \cdot \mathbf{J} = I_m. \tag{2.2}$$

Applying the divergence operator to the extracellular current density

First we investigate a small volume in the extracellular space, not enclosing a current source or current sink. The current flowing into the infinitely small volume must be equal to the current leaving that volume. This is due to the fact that no charge can be piled up in the extracellular space. The surface integral of equation (2.1) is then zero, hence $\nabla \cdot \mathbf{J} = 0$.

In the second case we assume a volume enclosing the current sink with position parameters $\mathbf{r_1}(x_1, y_1, z_1)$. The current sink represents the removal of positively charged ions at the apical dendrite of the pyramidal cell. The integral of equation (2.1) remains equal to $-I$ while the volume in the denominator becomes infinitesimally small. This gives a singularity for the current source density. This singularity can be written as a delta function: $-I\delta(\mathbf{r} - \mathbf{r}_1)$. The negative sign indicates that current is removed from the extracellular volume. The delta function indicates that current is removed at one point in space.

For the third case we construct a small volume around the current source at position $\mathbf{r_2}(x_2, y_2, z_2)$. The current source represents the injection of positively charged ions at the cell body of the pyramidal cell. The current source density equals $I\delta(\mathbf{r} - \mathbf{r}_2)$. Figure 2.15 represents the current density vectors for a current source and current sink configuration. Furthermore, three boxes are presented corresponding with the three cases discussed above.

Uniting the three cases given above, we obtain:

$$\nabla \cdot \mathbf{J} = I\delta(\mathbf{r} - \mathbf{r}_2) - I\delta(\mathbf{r} - \mathbf{r}_1). \tag{2.3}$$

2.6.3 Ohm's law and the potential field

The relationship between the current density $\mathbf{J}$ in A/m^2 and the electric field $\mathbf{E}$ in V/m is given by Ohm's law:

$$\mathbf{J} = \sigma\mathbf{E}, \tag{2.4}$$

with $\sigma(\mathbf{r}) \in \mathbb{R}^{3\times3}$ being the place dependent conductivity tensor. Macroscopic tissues such as the brain and skull are electrically anisotropic. This means that the conductivity is direction dependent. For example, white matter has a smaller conductivity in its longitudinal direction than along its axial direction. Nicholson [76] measured that the conductivity longitudinal to fibers

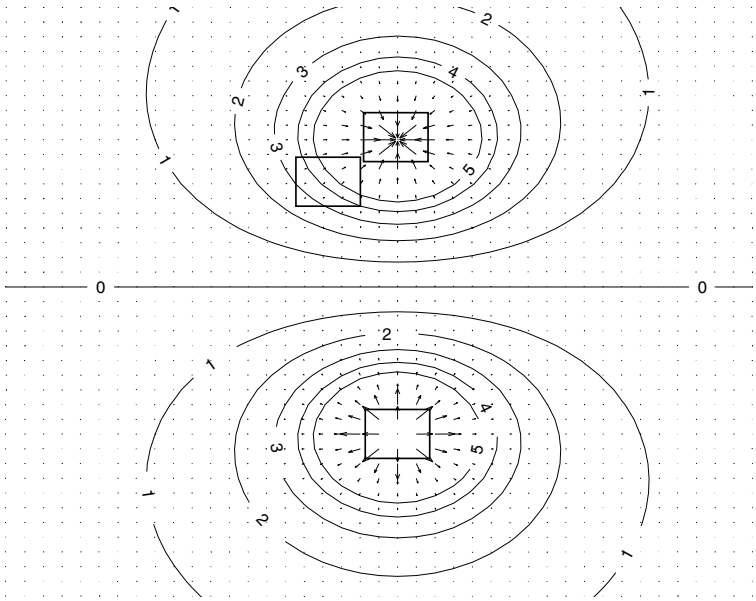

Figure 2.15: The current density in the vicinity of a current source and current sink is depicted. The equipotential lines are also given. Boxes are illustrated which represent the volumes G.

of white matter in a cat brain was 10 times as high as that in a direction axial to the fibers. Furthermore, the skull can also be considered anisotropic. The conductivity in a tangential direction is higher than in a direction perpendicular to the skull [24].

However, like in most studies on source localization, we have used an isotropic conductivity in the rest of the work. Thus the place dependent conductivity tensor becomes a place dependent scalar σ with units $A/(Vm) = S/m$.

We now introduce the scalar potential field V, using Volt as unit. This is possible due to the fact that under quasi-static conditions $\nabla \times \mathbf{E} = \mathbf{0}$ holds [85]. The link between the potential field and the electric field is given utilizing the gradient operator,

$$\mathbf{E} = -\nabla V. \tag{2.5}$$

The vector ∇V at a point gives the direction in which the scalar field V most rapidly increases. The minus sign in equation (2.5) indicates that the electric field is oriented from an area with a high potential to an area with a low potential. Figure 2.15 also illustrates some equipotential lines generated by a current source and a current sink.

2.6.4 Poisson's equation

When equation (2.2), equation (2.4) and equation (2.5) are combined, Poisson's differential equation is obtained in general form:

$$\nabla \cdot (\sigma \nabla V) = -I_m. \tag{2.6}$$

For the problem at hand, equation (2.3), equation (2.4) and equation (2.5) are combined yielding:

$$\nabla \cdot (\sigma \nabla V) = -I\delta(\mathbf{r} - \mathbf{r}_2) + I\delta(\mathbf{r} - \mathbf{r}_1). \tag{2.7}$$

In the Cartesian coordinate system equation (2.7) becomes:

$$\begin{aligned} \frac{\partial}{\partial x}(\sigma\frac{\partial V}{\partial x}) + \frac{\partial}{\partial y}(\sigma\frac{\partial V}{\partial y}) + \frac{\partial}{\partial z}(\sigma\frac{\partial V}{\partial z}) &= -I\delta(x - x_2)\delta(y - y_2)\delta(z - z_2) \\ &\quad +I\delta(x - x_1)\delta(y - y_1)\delta(z - z_1). \end{aligned} \tag{2.8}$$

The potentials V are calculated with equations (2.7) or (2.8) for a given current source density I_m in a volume conductor model. In this work volume conductor models are constructed which resemble the human head. These models consist of different regions, each having a specific conductivity which we assume isotropic. A few examples are the scalp, skull, brain and ventricular system region.

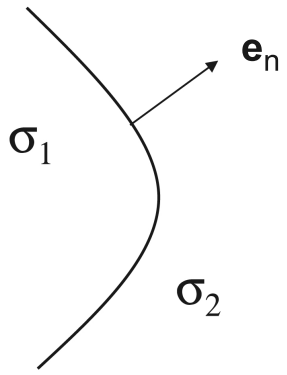

Figure 2.16: The boundary between two regions, with conductivity σ_1 and σ_2. The normal vector $\mathbf{e}_n$ to the interface is also shown.

2.6.5 Boundary conditions

At the interface between two regions boundary conditions are to be taken into account. Figure 2.16 illustrates such a an interface. A first boundary condition is based on the inability to pile up charge at the interface. All charge leaving one region through the interface must enter the other region. Or, all current (charge per second) leaving a region with conductivity σ_1 through the interface enters the neighboring region with conductivity σ_2:

$$\mathbf{J_1} \cdot \mathbf{e}_n = \mathbf{J_2} \cdot \mathbf{e}_n, \tag{2.9}$$

$$(\sigma_1 \nabla V_1) \cdot \mathbf{e}_n = (\sigma_2 \nabla V_2) \cdot \mathbf{e}_n, \tag{2.10}$$

where $\mathbf{e}_n$ is the normal component on the interface.

No current can be injected into the air outside the human head due to the very low conductivity of the air. Therefore the current density at the surface of the head reads:

$$\mathbf{J_1} \cdot \mathbf{e}_n = 0, \tag{2.11}$$

$$(\sigma_1 \nabla V_1) \cdot \mathbf{e}_n = 0. \tag{2.12}$$

Equations (2.10) and (2.12) are called the Neumann boundary condition and the homogenous Neumann boundary condition, respectively.

The second boundary condition only holds for internal interfaces. These interfaces are not connected with air. By crossing the internal interface the

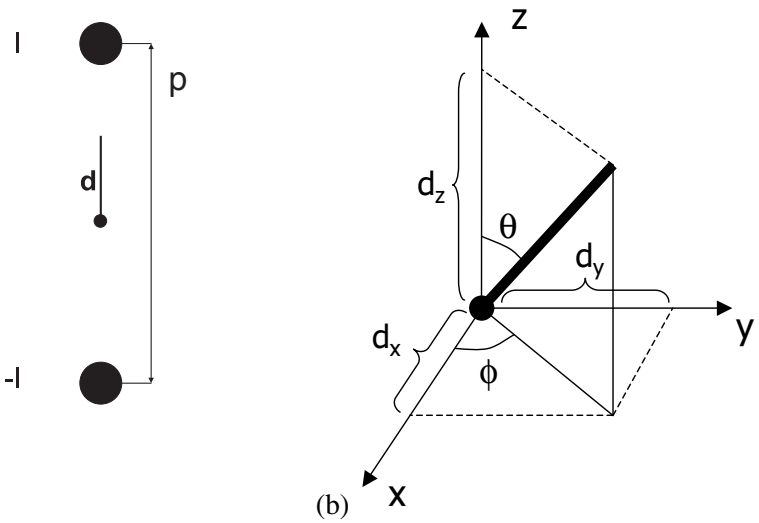

(a) (b)

Figure 2.17: (a) The dipole parameters for a given current source and current sink configuration. (b) The dipole with its components.

potential cannot have discontinuities,

$$V_1 \;=\; V_2. \tag{2.13}$$

This equation represents the Dirichlet boundary condition.

2.6.6 The current dipole

Current source and current sink inject and remove the same amount of current I and they represent an active pyramidal cell at a microscopic level. They can be modeled as a current dipole as illustrated in figure 2.17. The position parameter $\mathbf{r}$ of the dipole is typically chosen half way between the two monopoles. The dipole moment vector $\mathbf{d}$ is directed from the current sink to the current source. The unity vector of the dipole moment vector is given by $\mathbf{e_d}$. Its magnitude is defined as $|\mathbf{d}| = I\ p$, with p the distance between the two monopoles. Hence we can write:

$$\mathbf{d} = I\ p\ \mathbf{e_d}. \tag{2.14}$$

It is often so that the dipole moment is decomposed in three dipoles located at the same position of the original dipole and each oriented along one of the

Cartesian axes. The magnitude of each of these dipoles is equal to the orthogonal projection on the respective axes as illustrated in figure 2.17(b). We can write:

$$\mathbf{d} = d_x\mathbf{e}_x + d_y\mathbf{e}_y + d_z\mathbf{e}_z, \tag{2.15}$$

with $\mathbf{e}_x$, $\mathbf{e}_y$ and $\mathbf{e}_z$ being the unity vectors along the three axes. Furthermore, d_x, d_y and d_z are often called the dipole components. Notice that Poisson's equation (2.7) is linear. A potential V at an arbitrary point, generated by a dipole at a position $\mathbf{r}$ and orientation $\mathbf{d}$, can be decomposed in:

$$V(\mathbf{r}, \mathbf{d}) = d_x V(\mathbf{r}, \mathbf{e}_x) + d_y V(\mathbf{r}, \mathbf{e}_y) + d_z V(\mathbf{r}, \mathbf{e}_z). \tag{2.16}$$

This decomposition will be used to solve the inverse problem in section 2.8.

The equivalent current dipole

A large group of pyramidal cells need to be more or less synchronously active in a cortical patch to have a measurable EEG signal. Furthermore, all these cells are oriented with their longitudinal axis orthogonal to the cortical surface. Due to this arrangement the superposition of the individual electrical activity of the neurons results in an amplification of the potential distribution. A large group of electrically active pyramidal cells in a small patch of cortex can be represented as one equivalent dipole on the macroscopic level [41, 74].

2.7 The forward problem

The forward problem starts from a given current source, and calculates the resulting potentials in the volume conductor (represented by V). These potentials are obtained by solving Poisson's equation (2.6). The electrode potentials are represented by the symbol U and may be a subset of the potentials V in the volume conductor. In what follows a solution to Poisson's equation is given for different configurations.

2.7.1 Dipole field in an infinite conductor

We introduce the potential field generated by a current dipole with moment vector $\mathbf{d} = d\,\mathbf{e}_\mathbf{d}$ at a position $\mathbf{r}_{dip}$ in an infinite conductor with conductivity σ. The potential field is given by:

$$V(\mathbf{r}, \mathbf{r}_{dip}, \mathbf{d}) \quad = \quad \frac{\mathbf{d}.(\mathbf{r} - \mathbf{r}_{dip})}{4\pi\sigma\|\mathbf{r} - \mathbf{r}_{dip}\|^3}, \tag{2.17}$$

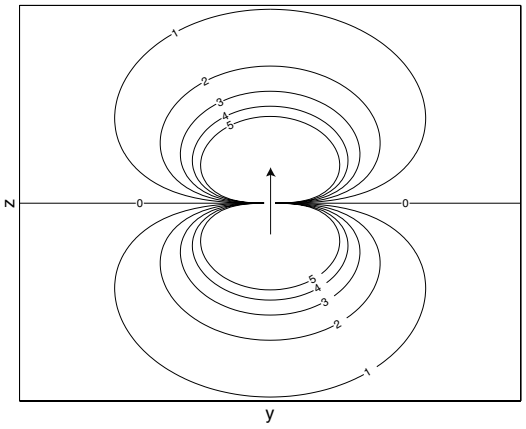

Figure 2.18: The equipotential lines of a dipole oriented along the z-axis.

with $\mathbf{r}$ being the position where the potential is calculated. Assume that the dipole is located in the origin of the Cartesian coordinate system and oriented along the z-axis. Then we can write:

$$V(\mathbf{r}, \mathbf{0}, d\mathbf{e}_z) \quad = \quad \frac{d\cos\theta}{4\pi\sigma r^2}, \tag{2.18}$$

where θ represents the angle between the z-axis and $\mathbf{r}$ and $r = \|\mathbf{r}\|$. Some equipotential lines in the yz-plane are shown in figure 2.18.

Equation (2.18) shows that a dipole field attenuates with $1/r^2$. Notice that V, from equation (2.17), to which an arbitrary constant is added, is also a solution of Poisson's equation. Therefore a reference potential must be chosen. Here, the equipotential plane orthogonal to the orientation and running through the dipole position is set equal to zero.

2.7.2 The spherical head model

The first volume conductor models of the human head consisted of a homogeneous sphere [33]. However it was soon noticed that the skull had a conductivity which was significantly lower than the conductivity of the scalp and the brain tissue. Therefore the volume conductor model of the head needed further refinement and a three-shell concentric spherical head model was introduced. In this model, the inner sphere represents the brain, the intermediate layer represents the skull and the outer layer represents the scalp. For this geometry a semi-analytical solution of Poisson's equation exists which is presented in [2, 91]. A semi-analytical expression given by a infinite series of

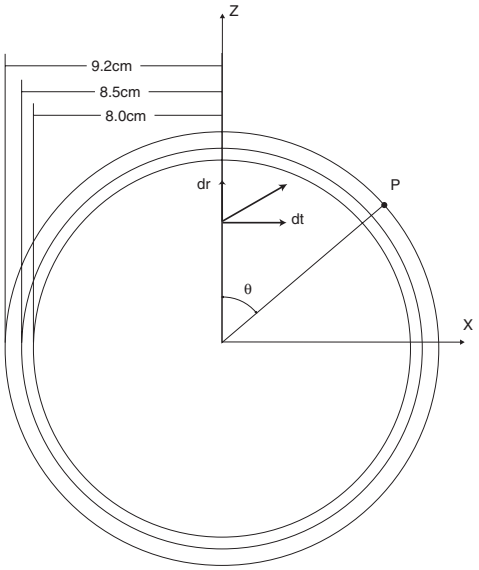

Figure 2.19: A three-shell concentric spherical head model is depicted. The dipole is located on the z-axis and the potential is measured at the scalp point P located in the xz-plane.

terms. Consider a dipole located on the z-axis and a scalp point P, located in the xz-plane, as illustrated in figure 2.19. The dipole components located in the xz-plane i.e., the radial component d_r and the tangential component d_t, are also shown in figure 2.19. The component orthogonal to the xz-plane, does not contribute to the potential at the scalp point P due to the fact that the zero potential plane of this component traverses P. The potential V at the scalp point P for the proposed dipole is given by:

$$\begin{aligned} V &= \frac{1}{4\pi SR^2}\sum_{i=1}^{\infty}\frac{X(2i+1)^3}{g_i(i+1)i}b^{i-1}[id_rP_i(\cos\theta) \\ &\quad +d_tP_i^1(\cos\theta)], \end{aligned} \tag{2.19}$$

with g_i given by:

$$\begin{aligned} g_i &= [(i+1)X+i][\frac{iX}{i+1}+1] \\ &\quad +(1-X)[(i+1)X+i](f_1^{i_1}-f_2^{i_1}) \\ &\quad -i(1-X)^2(f_1/f_2)^{i_1}. \end{aligned} \tag{2.20}$$

The symbols introduced are shown in table 2.1.

d_r	the radial dipole component
d_t	the tangential dipole component
R	the radius of the outer shell
S	the conductivity of the scalp and brain tissue(soft tissue)
X	the ratio between the skull and soft tissue conductivity
b	the relative distance of the dipole from the center
θ	polar angle of the surface point see figure 2.19
$P_i(.)$	the Legendre polynomial
$P_i^1(.)$	the associated Legendre polynomial
i	index
i_1	equals $2i + 1$
r_1	the radius of the inner shell
r_2	the radius of the middle shell
f_1	equals r_1/R
f_2	equals r_2/R

Table 2.1: The symbols introduced in subsection 2.7.2.

Equation (2.19) gives the scalp potentials generated by a dipole located on the z-axis, with zero dipole moment along the y-axis. To find the scalp potentials generated by an arbitrary dipole, the coordinate system has to be rotated accordingly. In the remainder of this work we will use the three-shell spherical head model with the typical radii of the outer boundary of the brain, skull and scalp region equal to 8 cm, 8.5 cm and 9.2 cm, respectively. We have truncated the infinite series of equation (2.19) to the first 40 terms. The maximum scalp potential obtained with the truncated series, deviates less than 0.1% from the case where 100 terms are applied, for dipoles with a radial position smaller than 95% of the maximum brain radius.

For completeness it is mentioned that there are also semi-analytical solutions available for layered spheroidal anisotropic volume conductors [46, 73].

2.7.3 Solving the forward problem in a realistic head model

Modern medical imaging (such as CT and MR imaging) is able to generate 3D images of the human head. These images present anatomical information. Different tissues can have different voxel intensities. It is possible to divide the image in several regions having the same voxel intensity. This process is often called segmentation of medical images [43]. We have applied the SPM99 segmentation tool for T1-weighted MR images [3]. This tool generates (e.g.) the brain and scalp region. These regions can be used to construct a volume

conductor model of the human head. Each region is allocated a conductivity. The obtained volume conductor model is also called a realistic head model. More on the construction of the realistic head model can be found in subsection 4.4.1.

To solve Poisson's equation in a realistic head model numerical methods are needed. In what follows we will discuss three such methods.

2.7.4 The boundary element method

A numerical method to solve Poisson's equation in a realistic head model is the boundary element method (BEM). This method is used in commercially available software [1,35]. The BEM calculates the potentials at digitized boundaries between homogeneous isotropic conducting regions. To illustrate the method, three commonly used regions are assumed, i.e., the brain, skull and scalp region. The air-scalp interface, scalp-skull interface and the skull-brain interface are represented as S_1, S_2 and S_3. Furthermore, σ_i^+ and σ_i^- are the conductivity of the medium located to the exterior and interior of interface S_i, respectively. From Poisson's equation, an integral equation [6,38] is derived to calculate the potential V at $\mathbf{r} \in S_k$:

$$V(\mathbf{r}) = \frac{2\sigma_0}{\sigma_k^- + \sigma_k^+} V_0(\mathbf{r}) + \frac{1}{2\pi} \sum_{j=1}^{3} \frac{\sigma_j^- - \sigma_j^+}{\sigma_k^- + \sigma_k^+} \int_{\mathbf{r}' \in S_j} V(\mathbf{r}') \frac{\mathbf{r}' - \mathbf{r}}{\|\mathbf{r}' - \mathbf{r}\|^3} d\mathbf{S}, \tag{2.21}$$

where σ_0 corresponds with the medium in which the dipole source is located, and $V_0(\mathbf{r})$ is the potential in $\mathbf{r}$ for an infinite medium with conductivity σ_0 as in equation (2.17). $d\mathbf{S}$ is a vector oriented orthogonal to a surface element and $\|d\mathbf{S}\|$ is the area of that surface element. The first term of the right hand side of equation (2.21) gives the potentials for an infinite medium. The second term corrects for applying a bounded medium by introducing sources on the interfaces.

The interface S_i is digitized in n_i triangles, (see figure 2.20) and in each triangle center the potentials are calculated with equation (2.21). The following set of linear equations is then obtained:

$$\begin{pmatrix} \mathbf{V^1} \\ \mathbf{V^2} \\ \mathbf{V^3} \end{pmatrix} = \begin{pmatrix} \mathbf{V_0^1} \\ \mathbf{V_0^2} \\ \mathbf{V_0^3} \end{pmatrix} + \begin{pmatrix} \mathbf{B^{11}} & \mathbf{B^{12}} & \mathbf{B^{13}} \\ \mathbf{B^{21}} & \mathbf{B^{22}} & \mathbf{B^{23}} \\ \mathbf{B^{31}} & \mathbf{B^{32}} & \mathbf{B^{33}} \end{pmatrix} \begin{pmatrix} \mathbf{V^1} \\ \mathbf{V^2} \\ \mathbf{V^3} \end{pmatrix}. \tag{2.22}$$

The total number of triangles is given by $n = n_1 + n_2 + n_3$. $\mathbf{V} = (\mathbf{V^1 V^2 V^3})^T \in \mathbb{R}^{n \times 1}$ are unknown potentials at the triangle centers and $\mathbf{V_0} = (\mathbf{V_0^1 V_0^2 V_0^3})^T \in \mathbb{R}^{n \times 1}$ are the potentials at the triangle centers due

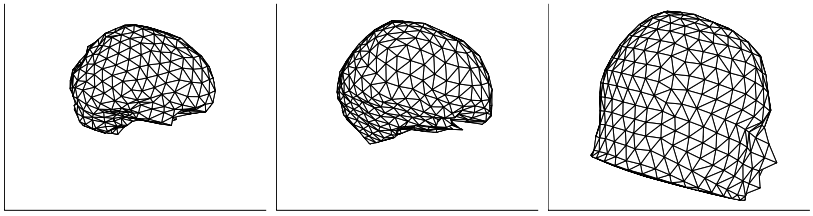

Figure 2.20: Triangulated surfaces of the brain, skull and scalp region used in BEM.

to a dipole in an infinite medium. The coefficients of $\mathbf{B}^{ij} \in \mathbb{R}^{n_i \times n_j}$ give the contributions of the potentials at interface j to the potentials at interface i. These coefficients are calculated by solving the integral in equation (2.21). The solution of equation (2.22) is:

$$\mathbf{V} = (\mathbf{1}_n - \mathbf{B})^{-1}\mathbf{V_0}, \tag{2.23}$$

with $\mathbf{1}_n \in \mathbb{R}^{n \times n}$ being the unity matrix . Once $(\mathbf{1}_n - \mathbf{B})^{-1}$ is computed, then the potentials at the boundaries can be obtained by matrix multiplication with $\mathbf{V_0}$. For another dipole, $\mathbf{V_0}$ is calculated and multiplied with the already available $(\mathbf{1}_n - \mathbf{B})^{-1}$, since $(\mathbf{1}_n - \mathbf{B})^{-1}$ is not dependent of the dipole parameters. The BEM has a rich history in bioelectric field problems and further references can be found in [32, 35, 40, 68, 96].

2.7.5 The finite element method

One other method to solve Poisson's equation in a realistic head model is the finite element method (FEM). To equation (2.6) with boundary conditions (2.10), (2.12), (2.13) we apply the Galerkin approach [50]. First, equation (2.6) is multiplied with a test function ϕ and then integrated over the volume G representing the entire head. We obtain:

$$\int_G \phi \nabla \cdot (\sigma \nabla V) dG = -\int_G \phi I_m dG. \tag{2.24}$$

Applying Green's first identity for integration:

$$\int_G (\nabla \phi) \cdot (\sigma \nabla V) dG = \int_{\partial G} \phi \, \sigma \nabla V \cdot \mathbf{dS} - \int_G \phi \nabla \cdot (\sigma \nabla V) dG, \tag{2.25}$$

to equation (2.24) in combination with the boundary conditions (2.12), yields the 'weak formulation' of the forward problem:

$$\int_G \nabla \phi \cdot (\sigma \nabla V) dG = \int_G \phi I_m dG. \tag{2.26}$$

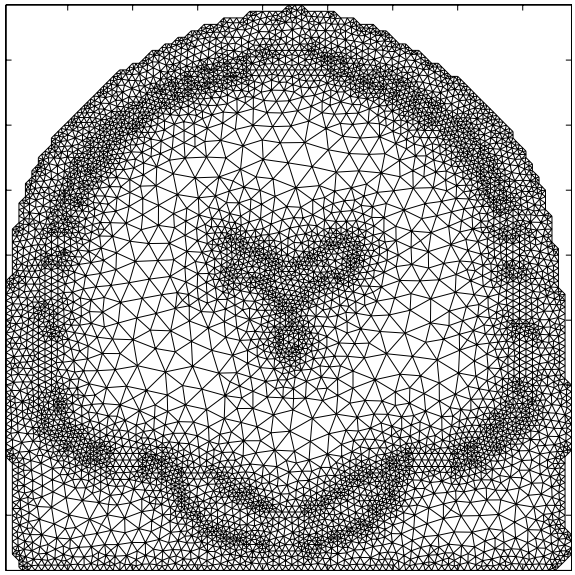

Figure 2.21: A digitization of the 2D coronal slice of the head. The 2D elements are the triangles.

The entire 3D-volume conductor is digitized in small elements such as tetrahedrons. Figure 2.21 illustrates a 2D conductor model digitized with triangles. A tessellation procedure is required to obtain the digitized elements. The computational points $\{V_i\}_{i=1}^n$ can be identified with the vertices of the elements (n is the number of vertices). The unknown potential $V(x, y, z)$ is approximated by

$$V(x, y, z) \simeq \sum_{i=1}^{n} V_i \phi_i(x, y, z), \tag{2.27}$$

where $\{\phi_i\}_{i=1}^n$ denotes a set of test functions also called basis functions.

They have a local support, i.e. the area in which they are non-zero is limited to adjacent elements. Moreover, the basis functions span a space of piecewise polynomial functions. A 2D illustration of a basis function is given in figure 2.22. Furthermore, they have the property that they are each equal to unity at the corresponding computational point and equal to zero at all other computational points.

Substituting (2.27) and ϕ_i for $i = 1, \ldots, n$ as test function in (2.26) produces n equations in n unknown $\mathbf{V} = [V_1 \ldots V_n]^T \in \mathbb{R}^{n \times 1}$. Due to the local support of the basis function, each equation consists only of a linear combi-

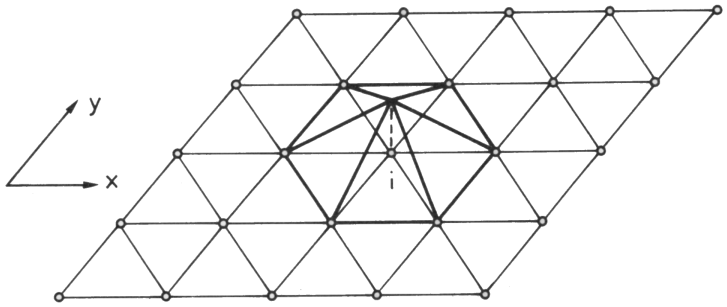

Figure 2.22: A 2D basis function is shown.

nation of V_i and its adjacent computational points. Hence the system matrix $\mathbf{A} \in \mathbb{R}^{n \times n}$ is sparse. In matrix notation we obtain:

$$\mathbf{A} \cdot \mathbf{V} = \mathbf{I}, \tag{2.28}$$

with $\mathbf{I} \in \mathbb{R}^{n \times 1}$ the source terms obtained by integration of the right hand side of equation (2.26). To solve equation (2.28), iterative solvers for large sparse systems are used as given in [29]. For more on FEM in EEG source analysis we refer to [5, 25, 50, 144].

2.7.6 The finite difference method

The numerical method used in this thesis is the finite difference method (FDM). In the next section a comparison is made between the different numerical methods. A motivation to apply FDM is also given. Therefore, the derivation of a linear equation from Poisson's equation will be handled in more depth. The differential equation (2.8) with boundary condition (2.10), (2.12), (2.13) is transformed into a linear equation utilizing the 'box integration' scheme [69]. Consider an inner node P in a cubic grid with internode spacing h. The six neighboring nodes are Q_i $(i = 1, \ldots, 6)$. For our convenience we assume that the coordinates for P are $(0, 0, 0)$ and for Q_i $(i = 1, \ldots, 6)$ $(h, 0, 0)$, $(-h, 0, 0)$, $(0, h, 0)$, $(0, -h, 0)$, $(0, 0, h)$ and $(0, 0, -h)$, respectively. Let us denote N_i the midpoint of PQ_i. Consider an integration of (2.8) over the cubic volume G_0 with side h, as illustrated in figure 2.23. The conductivity σ_0 in G_0 is assumed to be constant. The integration of the first term of the right

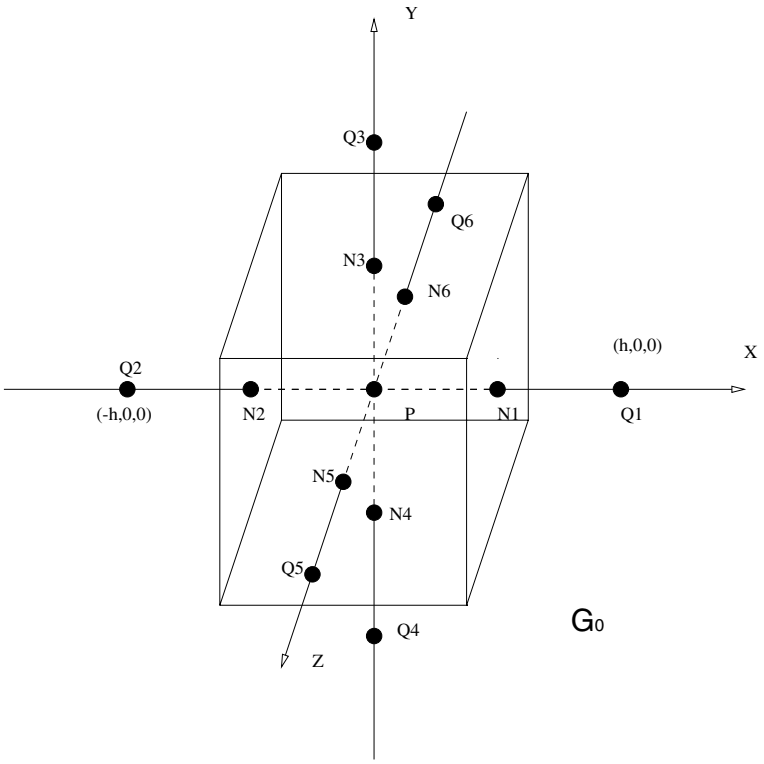

Figure 2.23: A typical node P with its neighbors Q_i $(i = 1 \cdots 6)$. The volume G_0 is given by the box.

hand side of equation (2.8) gives,

$$\begin{aligned} \int\int\int_{G_0} \frac{\partial}{\partial x}(\sigma_0 \frac{\partial V}{\partial x}) dx\, dy\, dz &= \int\int \sigma_0 \frac{\partial V}{\partial x}\, dy\, dz|_{x=\frac{h}{2}} \\ &\quad - \int\int \sigma_0 \frac{\partial V}{\partial x}\, dy\, dz|_{x=-\frac{h}{2}}, \end{aligned} \tag{2.29}$$

By using the mid-point rule:

$$\int_a^b \int_c^d f(y,z) dy dz \approx f(\frac{a+b}{2}, \frac{c+d}{2})(b-a)(d-c), \tag{2.30}$$

the integrals are removed in (2.29) and we obtain:

$$\begin{aligned} \int\int\int_{G_0} \frac{\partial}{\partial x}(\sigma_0 \frac{\partial V}{\partial x}) dx\, dy\, dz &\approx h^2 \sigma_0 \frac{\partial V}{\partial x}|_{x=\frac{h}{2}, y=0, z=0} \\ &\quad - h^2 \sigma_0 \frac{\partial V}{\partial x}|_{x=-\frac{h}{2}, y=0, z=0}. \end{aligned} \tag{2.31}$$

Note that each volume element G_0 can have a different conductivity. At the interfaces of each element the boundary conditions have to be obeyed. We introduce a virtual potential V_{N_1} and write the boundary condition at N_1 (see figure 2.23):

$$\begin{aligned} \sigma_0 \frac{\partial V}{\partial x}|_{x=\frac{h}{2}} &= \sigma_1 \frac{\partial V}{\partial x}|_{x=\frac{h}{2}}, \\ \sigma_0 \frac{V_{N_1} - V_P}{\frac{h}{2}} &= \sigma_1 \frac{V_{Q_1} - V_{N_1}}{\frac{h}{2}}. \end{aligned} \tag{2.32}$$

G_1 with center Q_1 has a conductivity σ_1. Solving (2.32) for V_{N_1} yields,

$$V_{N_1} = \frac{\sigma_0 V_P + \sigma_1 V_{Q_1}}{\sigma_0 + \sigma_1}. \tag{2.33}$$

When substituting (2.33) into the left-side expression of (2.32), the first term of (2.29) becomes :

$$h^2 \sigma_0 \frac{\partial V}{\partial x}|_{x=\frac{h}{2}, y=0, z=0} = 2h \frac{\sigma_0 \sigma_1}{\sigma_0 + \sigma_1}(V_{Q_1} - V_P).$$

The similar sequence of steps is applied to the second term in (2.29) and for the integration of the partial derivatives in y and z of (2.8). Introducing α_i and α_0 as

$$\begin{aligned} \alpha_i &= 2h \frac{\sigma_0 \sigma_i}{\sigma_0 + \sigma_i}, \\ \alpha_0 &= \sum_{i=1}^{6} \alpha_i, \end{aligned}$$

we obtain as a finite difference approximation of (2.8):

$$\sum_{i=1}^{6} \alpha_i V_{Q_i} - \alpha_0 V_P = I_P, \tag{2.34}$$

with

$$I_P = \int\int\int_{G_0} \begin{array}{l} -I\delta(x-x_2)\delta(y-y_2)\delta(z-z_2) \\ +I\delta(x-x_1)\delta(y-y_1)\delta(z-z_1) \end{array} dx\,dy\,dz. \tag{2.35}$$

For volumes G which contain a current monopole, I_P becomes I or $-I$. α_i has the dimension of Ω^{-1} and corresponds with the conductance between P and Q_i. Furthermore for $I_P = 0$ we obtain Kirchoff's law at the node P. For each node of a cubic grid we obtain a linear equation given by (2.34). The unknown potentials at the n computational points are represented by $\mathbf{V} \in \mathbb{R}^{n\times 1}$. The source terms represented by $\mathbf{I} \in \mathbb{R}^{n\times 1}$ are calculated in each of the n cubes utilizing equation (2.35). $\mathbf{I}$ has two nonzero elements representing the current sink and current source. Notice that in the linear equation (2.34) only the neighboring computational points are included. The system matrix $\mathbf{A} \in \mathbb{R}^{n\times n}$ has at most six off-diagonal elements and is a sparse matrix. In matrix notation we can write:

$$\mathbf{A}.\mathbf{V} = \mathbf{I}. \tag{2.36}$$

To solve this large sparse set of equations iterative methods are used. We have utilized successive overrelaxation [84] as discussed in appendix A.

2.7.7 Comparing the various numerical methods

The three methods BEM, FEM and FDM can all be used to solve the forward problem of EEG source analysis in a realistic head model.

A first difference between BEM versus FEM and FDM is the domain in which the solutions are calculated. In BEM the solutions are calculated on the boundaries between the homogenous isotropic conducting regions. In FEM and FDM the solution of the forward problem is calculated in the entire volume. Subsequently, FEM and FDM lead to a larger number of computational points than BEM.

The potential at an arbitrary point can be determined with FEM and FDM by interpolation of computational points in its vicinity, while for BEM it is necessary to reapply the Barnard formula [6] and numerical integration.

Another important aspect is the computational efficiency. In BEM, a full matrix $(\mathbf{1}_n - \mathbf{B})$, represented in equation (2.23), needs to be inverted. Direct

solvers must be used such as Gaussian elimination [29]. Once the matrix is inverted, only a matrix multiplication is needed to obtain the scalp potentials. When the scalp potentials have to be known for another dipole, $\mathbf{V_0}$ in equation (2.23) must be recalculated and multiplied with the available $(\mathbf{1}_n - \mathbf{B})^{-1}$. This limited computational load is an attractive feature when solving the inverse problem, where a large number of forward evaluations need to be performed. The inverse problem will be explained in the next section.

In FEM and FDM, a direct inversion of the large sparse matrices found in (2.28) and (2.36) is not possible due to the dimension of the matrices. Typically 500000 computational points are considered which leads to system matrices of 500000 equations with 500000 unknowns, which can not be solved in a direct manner with the computers now available. However, matrices found in FEM and FDM can be inverted for a given source configuration or right-hand side term, applying iterative solvers such as the successive overrelaxation method or the conjugate gradient method [29]. A disadvantage of the iterative solvers is that for each source configuration the solver has to be reapplied. In the inverse problem a large number of forward calculations must be evaluated for different dipole positions and orientations. The FEM and FDM would be computationally inefficient when for each dipole an iterative solver was used. We have overcome this inefficiency by applying the reciprocity theorem, as will be explained in chapter 3. Furthermore, there are also fast iterative solvers available, for structured grids. One of such solvers is the multigrid method [22, 45, 70].

When a large number of conducting regions is introduced, a large number of boundaries needs to be sampled for BEM. This leads to a large full system matrix, hence a lower numerical efficiency. The FEM and FDM are not sensitive to the number of regions introduced. In principle, it is possible to give each tetrahedron or cube a different conductivity.

In FDM the computational points are fixed in the cube centers, while in FEM and BEM, the computational points (i.e. the vertices of the tetrahedrons and triangle centers, respectively) can be chosen more freely. Therefore, for the same amount of nodes FEM can better represent the irregular interfaces between the different regions than FDM.

However, the segmented medical images which are used to obtain the realistic volume conductor model, are constructed out of cubic voxels with a volume of 1 mm^3. From these voxels one can easily generate a grid with a side that is a multiple of the voxel edge. For FEM and BEM additional tessellation algorithms [104] must be used to obtain the tetrahedron elements and the surface triangles, respectively.

A summary of the comparison between BEM, FEM and FDM is given in

	BEM	FEM	FDM
position computational points	surface	volume	volume
free choice computational points	yes	yes	no
system matrix	full	sparse	sparse
solvers	direct	iterative	iterative
number of regions	small	large	large

Table 2.2: Comparison of the different methods for solving Poisson's equation in a realistic head model.

table 2.2. We have chosen for FDM to solve the forward problem in EEG source analysis. This method gives us the ability to introduce a large number of regions without additional computational costs. Furthermore, the cubic volume conductor model is easily constructed from the image-derived geometric information. Other potential advantages are the use of efficient iterative solvers and the possibility to incorporate anisotropy [90]. However these last two advantages are not exploited in this work.

2.8 The inverse problem in EEG source analysis

The process of locating the electrical source starting from the measured potentials at the scalp surface is called the inverse problem.

It turns out that for a given potential distribution on the scalp surface an infinite number of source configurations can be generated that all correspond with the given potential distribution. [44]. Hence there is no unique solution for a given potential distribution on the scalp surface.

To reduce the number of solutions of the inverse problem, source models can be introduced. For example, the current dipole can be used as a source model. This reduces the electrical sources to one dipole. Using a single dipole source implies that only one focal region with parallel oriented pyramidal cells is synchronously electrically active. For large parts of the EEG, different regions of the brain contribute to the EEG. A single dipole source model would then be an insufficient representation. For certain events however, a focal group of active neurons generates a large electrical activity. These events are: epileptic spikes, early stages of an epileptic seizure [9, 15, 30], and evoked potentials [100]. In these cases a dipole may be a good choice as an electrical source.

2.8.1 Dipole source localization

Solving the inverse problem with a dipole source requires the iterative modification of the independent dipole parameters, three location parameters $\mathbf{r} = (x, y, z)^T \in \mathbb{R}^{3\times1}$, and three component parameters $\mathbf{d} = (d_x, d_y, d_z)^T \in \mathbb{R}^{3\times1}$, where ^{T} denotes the transpose operator. The location parameters x, y and z are the Cartesian coordinates. The three component parameters can also be represented by two orientation parameters, the azimuthal ϕ and elevation θ angle, and the dipole magnitude. A dipole with its three components is illustrated in figure 2.17(b). The potential values at the l scalp electrodes for a dipole at position $\mathbf{r}$ and orientation $\mathbf{d}$ are represented by $\mathbf{U}_{model} \in \mathbb{R}^{l\times1}$. The relationship between the dipole components $\mathbf{d}$ and the potential values $\mathbf{U}_{model}$ can be described by a matrix operator $\mathbf{L}(\mathbf{r}) = (\mathbf{U}(\mathbf{r}, \mathbf{e}_x), \mathbf{U}(\mathbf{r}, \mathbf{e}_y), \mathbf{U}(\mathbf{r}, \mathbf{e}_z)) \in \mathbb{R}^{l\times3}$, the so-called lead-field matrix, where $\mathbf{U}(\mathbf{r}, \mathbf{e}_x) \in \mathbb{R}^{l\times1}$ represents the electrode potentials for a unity dipole, oriented along the x-axis and simular for $\mathbf{U}(\mathbf{r}, \mathbf{e}_y)$ and $\mathbf{U}(\mathbf{r}, \mathbf{e}_z)$. We refer also to equation (2.16) in subsection 2.6.6. In matrix notation we write:

$$\mathbf{U}_{model} = \mathbf{L}(\mathbf{r}) \cdot \mathbf{d}. \tag{2.37}$$

Dipole source localization for one point in time

The EEG measured by l electrodes at a single time instant can be represented by $\mathbf{U}_{in} \in \mathbb{R}^{l\times1}$. The three location parameters $\mathbf{r}$ and the three component parameters $\mathbf{d}$ of the dipole are obtained by finding the global minimum of the relative residual energy (RRE):

$$RRE(\mathbf{r}, \mathbf{d}) = \frac{\|\mathbf{U}_{in} - \mathbf{U}_{model}\|^2}{\|\mathbf{U}_{in}\|^2}. \tag{2.38}$$

with $\|.\|^2$ the Euclidean norm. The RRE indicates the fraction of energy which cannot by modeled by the dipole. The solution of the inverse problem can be found by iteratively adjusting the six dipole parameters until a global minimum of RRE is found. However the total number of parameters that have to be optimized can be reduced from six to three. For a given dipole position $\mathbf{r}$, the optimal components in the least-squares sense [29] $\mathbf{d}_{opt}$ are found from the best approximated solution of the overdetermined system of linear equations $\mathbf{U}_{in} = \mathbf{L}(\mathbf{r}) \cdot \mathbf{d}$:

$$\mathbf{d}_{opt} = \mathbf{L}^+ \cdot \mathbf{U}_{in} \text{ with } \mathbf{L}^+ = (\mathbf{L}^T\mathbf{L})^{-1}\mathbf{L}^T,$$

where $\mathbf{L}^+$ denotes the Moore-Penrose pseudo-inverse of the lead-field matrix $\mathbf{L}$. The relative residual energy becomes

$$RRE(\mathbf{r}) = \frac{\|\mathbf{U}_{in} - \mathbf{L} \cdot \mathbf{d}_{opt}\|^2}{\|\mathbf{U}_{in}\|^2} = \frac{\|(\mathbf{1}_l - \mathbf{L}\mathbf{L}^+) \cdot \mathbf{U}_{in}\|^2}{\|\mathbf{U}_{in}\|^2}, \tag{2.39}$$

where $\mathbf{1_l} \in \mathbb{R}^{l \times l}$ represents the unity matrix. The relative residual energy is only dependent on the dipole position $\mathbf{r}$. The solution of the dipole source localization can be found by iteratively adjusting the three position parameters. For each iteration, the lead-field matrix $\mathbf{L}$ is calculated. This corresponds with three forward evaluations of the unity dipoles oriented along the three axes. Next the RRE is calculated utilizing (2.39).

Dipole localization for multiple time samples

Dipole source localization can also be performed for a time interval or epoch of s consecutive time samples. The measured scalp potentials can then be written as $\mathbf{U}_{in} \in \mathbb{R}^{l \times s}$.

A fixed-dipole solution is obtained by keeping the location and orientation (azimuth and elevation angles ϕ and θ) fixed during the epoch, while its intensity can vary with time [71]. The basic assumption is that the EEG can be modeled as a dipole whose location during the time interval of observation is fixed inside the brain and that the variation in scalp potentials is due only to variations in the dipole magnitude. In this case, finding the optimal fixed dipole requires the simultaneous optimization of the three location parameters in $\mathbf{r}$ as well as the two orientation parameters ϕ and θ. For each possible location $\mathbf{r}$ and orientation (ϕ, θ), the potentials are written

$$\mathbf{U}_{model} = \mathbf{L}(\mathbf{r}) \cdot \mathbf{e}_d(\phi, \theta) \cdot \mathbf{a}, \tag{2.40}$$

with $\mathbf{e}_d \in \mathbb{R}^{3 \times 1}$ a unit dipole along the chosen direction and $\mathbf{a} \in \mathbb{R}^{1 \times s}$ the time-varying dipole magnitudes. The optimal dipole magnitudes $\mathbf{a}_{opt}$ in a least-squares sense are found from the solution of the system of linear equations $\mathbf{U}_{in} = \mathbf{L}(\mathbf{r}) \cdot \mathbf{e}_d(\phi, \theta) \cdot \mathbf{a}_{opt}$. Similar to equations (2.39), the RRE can be written

$$RRE(\mathbf{r}, \phi, \theta) = \frac{\|\mathbf{U}_{in} - \mathbf{L}\mathbf{e}_d\mathbf{a}_{opt}\|_F^2}{\|\mathbf{U}_{in}\|_F^2} = \frac{\|(\mathbf{1}_l - (\mathbf{L}\mathbf{e}_d)(\mathbf{L}\mathbf{e}_d)^+)\mathbf{U}_{in}\|_F^2}{\|\mathbf{U}_{in}\|_F^2}, \tag{2.41}$$

with $\|\cdot\|_F$ being the Frobenius norm of a matrix [29].

Optimization method

The iterative adjustment of the dipole parameters, until the global minimum of the RRE is found, can be performed with different methods. Non gradient-based optimization methods only use evaluations of the cost function RRE in each iteration. Gradient-based minimization techniques use evaluations of both the RRE and its partial derivatives with respect to the optimized parameters, and are therefore typically faster as they require less iteration steps to reach the solution. We used the non gradient-based Nelder-Mead simplex method [75] because of its relative simplicity and robustness to local minima in the cost function [84]. The algorithm is stopped when the maximal distance between points of the simplex becomes lower than 0.001 mm.

2.8.2 Distributed sources

In this thesis only a single dipole source is used which represents focal electric activity. However there has been a considerable amount of research done in the area of distributed sources. In this case the electrical activity is not confined to one focal area: several brain regions can be active simultaneously. For more information on these methods we refer to [52, 61, 81].

2.9 Summary

In this chapter the basic concepts of neurophysiology and an introduction on EEG source analysis were presented.

The nerve cells or neurons contain a cell body, dendrites, and an axon. Pyramidal cells are a type of neurons consisting of apical dendrites located close to the cortical surface. The longitudinal axes of this type of neurons are orthogonal to the cortical surface. Communication between neurons is facilitated by neurotransmitters that are released in the synaptic cleft. Synapses in pyramidal cells occur at the membrane of the cell body as well as at dendrites. We further focused on a synaptic cleft at the apical dendrite. When for example an excitatory neurotransmitter is injected in the cleft, a massive influx of positive charge occurs. A redistribution of charge is started and an extracellular current starts flowing from the cell body. A simplified electrical model for this process consists of the current source and current sink. For this source configuration Poisson's equations and its boundary conditions were derived. Poisson's differential equation connects the electrical source with the potential field it generates. When the distance between the current source and current sink becomes infinitesimally small, a current dipole is obtained. The

forward problem solves Poisson's equation, i.e. it calculates the potentials for a given source configuration. The forward problem is solved in an infinite homogeneous isotropic conductor. The potentials attenuate with $1/r^2$, where r represents the distance from the measuring point to the current dipole. For a given dipole the semi-analytical equation calculates the potentials at the outer surface in a three-shell spherical head model. To solve Poisson's equation in realistic head models, obtained from medical imaging, numerical methods are used. We have discussed and compared BEM, FEM and FDM. The inverse problem tries to find the sources which generate a given EEG. There is no unique solution for the inverse problem. However, we have restricted our source model to a single current dipole. The parameters of the dipole which best fit the given EEG signal are obtained with the simplex method.

The BEM and FEM are studied in two M.Sc. theses [21, 94], which were supervised by the author.

Chapter 3

Validating the Finite Difference Method and Reciprocity

3.1 Introduction

The finite difference method (FDM) has as one of its chief advantages the ability to introduce a large number of regions. In principle every cubic element could have a different conductivity. The FDM generates a large linear system. The system matrix is sparse. Iterative solvers for sparse matrices are needed to solve this linear system. In this chapter the reciprocity theorem is introduced to reduce the computational burden associated with the iterative solvers. The finite difference method is combined with the reciprocity theorem and will be henceforth called the finite difference reciprocity method (FDRM). The performance of the FDRM in solving the inverse problem is validated in a three-shell spherical head model. This is done as follows: for a given test dipole the potentials at the electrodes are calculated using the analytical expression. Next, the inverse problem is solved applying the FDRM. The volume conductor model applied with the FDRM is the digitized three-shell spherical head model. The fitted dipole parameters are compared with the ones of the test dipole. The dipole position and orientation errors are then deduced. The smaller these errors are the better the method performs.

The sensitivity to noise using FDRM in EEG dipole source analysis is also investigated.

The rest of the chapter is organized as follows: in section 3.2 the motivation and the aim of the study are presented. Section 3.3 deals with reciprocity.

Additional information on reciprocity can also be found in appendix B. In section 3.4, the finite difference method and the inverse solver are presented. The position and orientation errors found when applying the FDRM are presented in section 3.5. The results on noise sensitivity are given in section 3.6. Some further considerations are presented in section 3.7. Finally in section 3.8, a summary and the original contributions are presented.

3.2 Motivation and aim of the study

We first remind some concepts given in chapter 2. The forward problem starts from a given dipole and calculates the potentials measured at the scalp electrodes. The inverse problem seeks the optimum dipole parameters for a given potential distribution at the scalp electrodes. We wish to stress that a large number (several hundreds) of forward evaluations must be performed in order to find the optimum dipole parameters corresponding with the measured scalp potentials. As such, relatively fast forward evaluations need to be used in the inverse problem, in order to obtain the optimal dipole fit in a reasonable amount of time.

Numerical methods solve the forward problem in realistic head models. The boundary element method (BEM) [35, 68] calculates the potentials in nodes at the interfaces of homogeneous isotropically conducting regions as also presented in subsection 2.7.4. In general, three regions are distinguished: the brain which is enclosed by the skull, which is enclosed by the scalp region. The geometrical shape of the head is obtained from segmented magnetic resonance images. After preprocessing, the BEM solves the forward problem with one matrix multiplication making it an attractive method to solve the inverse problem.

In reality, several tissues with different conductivities are generally located in the same BEM region. To incorporate larger sets of tissues with different conductivities, methods such as the finite element [5, 25, 144] and finite difference method [55–57, 60, 65, 90, 123, 135, 142] (FEM, FDM) must be used. In FDM, which is the method used in this study, the conducting volume is digitized on a cubic grid. The potential value at the center of each element or node is written as a linear combination of the potentials of six adjacent nodes, as is explained in subsection 2.7.6. Due to the large number of cubic elements, general solvers of linear systems cannot be used to obtain the potentials in the nodes. Iterative solutions for large sparse systems of linear equations are needed to obtain these potentials for a given source.

With a dipole as an electrical source, we need to solve the forward problem numerically for each position and orientation we wish to evaluate while solv-

ing the inverse problem. Typical several hundreds of forward problems need to be calculated to solve one inverse problem. This procedure is rather time consuming taking into account that the calculation time for solving the forward problem numerically. In a 3 mm and a 2 mm grid one forward calculation takes about 30 s and 2 minutes, respectively.

We utilize the finite difference reciprocity method (FDRM) which is able to incorporate multiple inhomogeneities utilizing the FDM, and which is able to perform inverse calculations with a limited number of numerically solved potential distributions, by using the reciprocity theorem. The number of numerical calculations is limited by the number of scalp electrodes considered and not by the number of forward evaluations needed in the inverse procedure. In the past, authors have used the reciprocity theorem in combination with FEM and FDM [56, 57, 141]. In section 3.7, we will compare the results found in these publications with our results.

The aim of this study is to evaluate the performance of the method in solving the inverse problem in the three-shell spherical head model, for a large number of test dipoles. The exact electrode potentials are calculated by utilizing the analytical expression. These potentials are then used to investigate the dipole position and orientation error resulting from utilizing the FDRM, with a 2 mm and a 3 mm grid, in the inverse procedure. We also study the impact of increasing the number of scalp electrodes on the performance of the FDRM in solving the inverse problem. Furthermore, we investigate the dipole position error when Gaussian noise is added to each of the scalp electrodes.

3.3 Reciprocity

In EEG dipole source analysis a large number of forward evaluations needs to be performed before the optimal dipole parameters are found. It would be too demanding to perform a forward calculation for each dipole with an iterative solver. Therefore, the reciprocity theorem is utilized to reduce the number of forward calculations performed with an iterative solver. Reciprocity was introduced in EEG source analysis by Rush and Driscoll [88].

To obtain the potential difference U_{AB} between electrode A and B, for a dipole at position $\mathbf{r} \in \mathbb{R}^{3\times1}$ and with components $\mathbf{d} = (d_x, d_y, d_z)^T \in \mathbb{R}^{3\times1}$, the following steps have to be carried out. The flowchart in figure 3.1 shows the consecutive steps.

- A fictive current I_{AB} of arbitrary value is introduced which enters the head at electrode A and leaves the head at electrode B.
- Utilizing the FDM we then calculate the potentials $V(hi, hj, hk)$

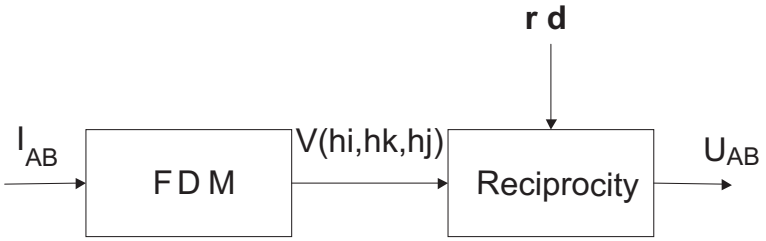

Figure 3.1: The consecutive steps when applying the FDRM.

with h the internode spacing and i, j, k the node numbers along the Cartesian axes. Figure 3.2 illustrates the equipotential lines and current density vectors $\mathbf{J} = -\sigma\nabla V$ in the brain region, with $\nabla V = (\partial V/\partial x, \partial V/\partial y, \partial V/\partial z)^T$. The partial derivative $\partial V/\partial x$ is approximated by $[V(h(i+1), hj, hk) - V(h(i-1), hj, hk)]/2h$. The partial derivatives $\partial V/\partial y, \partial V/\partial z$ are obtained in a similar way.

- The reciprocity theorem is then used. This theorem gives [62, 88],

$$U_{AB}(\mathbf{r}, \mathbf{d}) = \frac{\mathbf{d}^T \cdot \nabla V(\mathbf{r})}{I_{AB}}, \tag{3.1}$$

with U_{AB} the potential difference between the scalp electrodes A and B generated by the dipole at position $\mathbf{r}$ and orientation $\mathbf{d}$. This expression is derived in appendix B. When $\mathbf{r}$ does not coincide with a node, then $\nabla V(\mathbf{r})$ is obtained with tri-linear interpolation [84].

By solving only one forward calculation numerically, by introducing current monopoles at electrodes A and B, and storing the obtained node potentials in a data structure, we can obtain U_{AB} for every dipole position and orientation.

If l scalp electrodes are used to measure the EEG, $l-1$ electrode pairs can be found with linear independent potential differences. Therefore $l-1$ numerical forward calculations are performed and stored in data structures. For further, the $l-1$ potential differences at the $l-1$ electrode pairs are transformed in l average referenced potentials at the l electrodes.

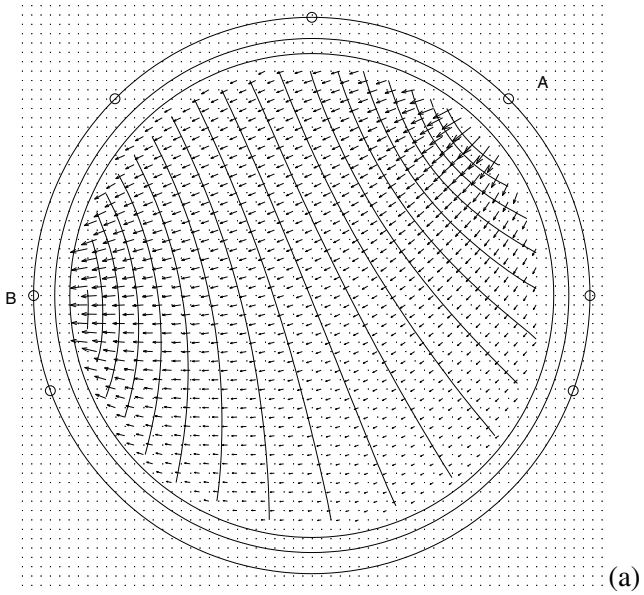

(a)

Figure 3.2: The current density $\mathbf{J} = \sigma \nabla V$ and the equipotential lines are illustrated when introducing a current I_{AB} at electrode A and removing the same amount at electrode B.

	CPU times		data structure size	
	26 forw	43 forw	26 forw	43 forw
3 mm	10 min 50 sec	17 min 55 sec	22 Mbyte	36 Mbyte
2 mm	55 min 02 sec	91 min 01 sec	74 Mbyte	122 MByte

Table 3.1: The CPU times and the data structure sizes for a 3 mm and a 2 mm grid and for 26 and 43 forward calculations.

3.4 The FDM and the inverse problem

3.4.1 The finite difference method

The FDM is extensively discussed in subsection 2.7.6. The three-shell spherical head model is digitized on a cubic grid. We have applied a 2 mm and 3 mm grid size. Realistic volume conductor models are obtained from segmented 3D MR images which have cubic voxels with a side of 1 mm. It is then convenient to generate cubic grids having a side which is a multiple of this voxel side.

Calculation time and memory requirements

In appendix A, the successive overrelaxation (SOR) method is presented which solves the forward calculations numerically. It was found in this appendix that the optimal overrelaxation parameters used in SOR are $\omega = 1.93$ and $\omega = 1.95$ for a 3 mm and a 2 mm grid, respectively. The CPU times needed to solve the forward calculations on a 3 mm and 2 mm grid are 25 sec and 2 min 7 sec, respectively, on a Sun Ultra 60 workstation with a 360 MHz processor. For 27 electrodes, 26 forward calculations need to be solved and for 44 electrodes, 43 forward calculations need to be solved. A further reduction of the calculation time can be obtained when more advanced solvers are used such as multigrid solvers [45, 70].

The number of nodes used for the 3 mm and 2 mm grid is equal to 110483 and 372189, respectively. The potentials at the nodes are stored in a data structure with double precision (8 byte). The size of this data structure for a 3 mm and 2 mm grid is, 883864 bytes and 2977512 bytes, respectively. Table 3.1 gives the CPU times and the data structure size when applying a 3 mm and 2 mm grid and for 26 and 43 forward calculations.

3.4.2 The inverse calculation

The inverse problem in dipole source analysis finds the optimal dipole parameters for the given scalp potentials. The EEG measured by l electrodes at a

single time instant can be represented by $\mathbf{U}_{in} \in \mathbb{R}^{l\times 1}$. The three position parameters and the three components of the dipole are obtained by finding the global minimum of the relative residual energy (RRE):

$$RRE = \frac{\|\mathbf{U}_{in} - \mathbf{U}_{model}\|^2}{\|\mathbf{U}_{in}\|^2},$$

with $\mathbf{U}_{model} \in \mathbb{R}^{l\times 1}$ the electrode potentials obtained by the forward evaluation in the inverse problem. For more details on solving the inverse problem we refer to section 2.8.

3.5 The dipole position and orientation error with FDRM

3.5.1 Setup of the simulation

The performance in solving the inverse problem with the FDRM is evaluated for a three-shell spherical head model. The radii for the outer boundaries of brain, skull and scalp in the three-shell spherical head model are 80, 85, and 92 mm, respectively.

The skull conductivity is still a controversial issue. A recent study of the human-skull conductivity in vitro and in vivo [80] yielded a conductivity ratio between the soft tissue (scalp and brain) and skull of about 16. In other [27, 87] publications, the conductivity ratio between the soft tissue and skull was found to be 80. In our validation study we have used the conductivity of the skull which is 80 times smaller than the conductivity of the soft tissue. We have chosen this ratio based on the fact that the dipole position and orientation errors are found to be larger [56] when applying a ratio of 80 instead of 16. Subsequently, applying a ratio of 80 gives us the worst-case results.

An analytical expression exists which generates the exact potentials at the electrodes for a given dipole in the brain region [91].

The 10-20 international electrode placement [49] is used with on each side 3 additional inferior temporal electrodes which adds up to 27 electrodes illustrated as '*' in figure 3.3. This electrode placement is used in our long-term epilepsy-monitoring unit and is chosen for that reason. To have a higher spatial sampling of the potentials at the scalp surface, 17 extra electrodes are placed, illustrated as '$\circ$' in figure 3.3, adding up to 44 electrodes. In the light of patient comfort in the long-term monitoring, 17 extra electrodes are still acceptable. We have chosen the node located closest to the electrode position as the electrode node in the discretized volume conductor models.

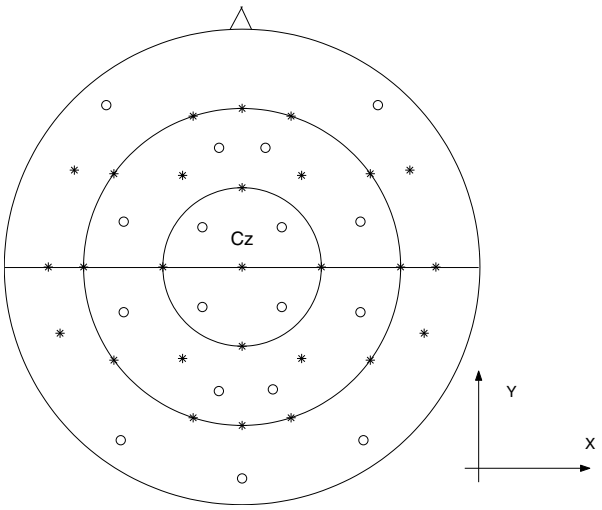

Figure 3.3: Top view of the electrode positions. The large circles represent positions with a constant azimuthal angle θ. From the inner to the outer circle we have an angle θ of 45°, 90° and 120°, respectively. The 27 electrodes '*' and the additional 17 electrodes '$\circ$' are illustrated. The coordinate axes are also shown.

In this work the Cartesian axes are placed as follows: the x-axis is oriented from the center to the right ear, the y-axis is oriented from the center to the nose, and the z-axis (not illustrated) is oriented from the center to the vertex electrode 'Cz'.

The test dipoles are placed in the brain region on the coronal slice containing the vertex electrode 'Cz', as illustrated in figure 3.4. The line going through 'Cz' in figure 3.3 represents the coronal slice. For each test dipole position three dipoles are generated with a dipole orientation along the x-, y- and z-axis. For a total of 1743 dipoles the position and orientation error is investigated for solving the inverse calculations with the FDRM.

The dipole position error is the distance between the original and the fitted dipole. The dipole orientation error is the angle between the orientation of the original and the fitted dipole.

Four volume conductor model (VCM) configurations are considered:

- The first configuration consists of a discretized volume conductor model with 2 mm node spacing and 44 scalp electrodes (VCM-2mm-44el).

- The second configuration consists of a 2 mm grid with 27 electrodes (VCM-2mm-27el).

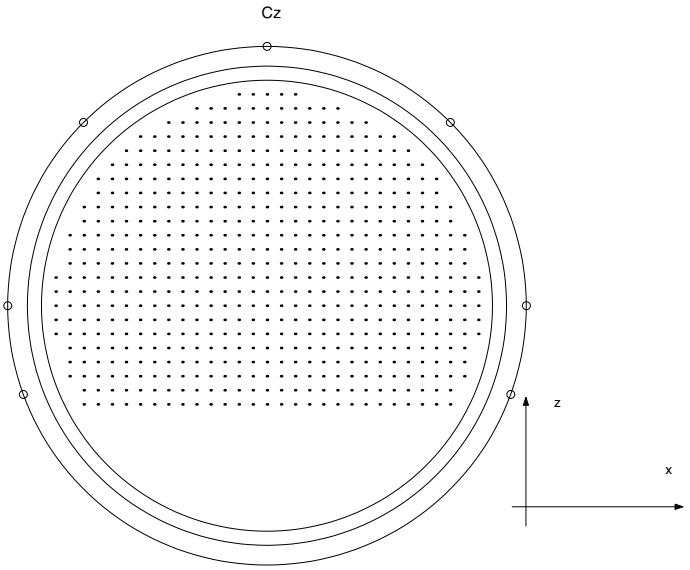

Figure 3.4: The dipole test positions, illustrated with dots, are located on the coronal slices containing the vertex electrode 'Cz'.

- The third configuration consists of a 3 mm grid with 44 electrodes (VCM-3mm-44el).

- The fourth configuration consists of a 3 mm grid with 27 electrodes (VCM-2mm-27el).

3.5.2 Results

The average position error for the 1743 test dipoles and for the configurations VCM-2mm-44el, VCM-2mm-27el, VCM-3mm-44el and VCM-3mm-27el is 2.0 mm, 2.2 mm, 3.1 mm and 3.4 mm, respectively.

Figure 3.5 illustrates the cumulative distribution of the position error for the 4 configurations. For example, 60 % of all the test dipoles have a position error smaller than 2.2 mm, 2.5 mm, 3.5 mm and 3.8 mm for VCM-2mm-44el, VCM-2mm-27el, VCM-3mm-44el and VCM-3mm-27el, respectively. It can also be observed that the position error due to utilizing the FDRM is in general smaller than twice the internode spacing of the grid, hence 4 mm for a 2 mm grid and 6 mm for a 3 mm grid, independent of the number of electrodes, i.e, 27 or 44.

The dipole position error as a function of the test dipole position and orientation, is given in figure 3.6. The color scale indicates the distance in mm between the original and the fitted dipole. The first, second, and third column presents the dipole position error for dipoles oriented along the x-, y- and z-axis, respectively. Row one, two, three and four in figure 3.6 present the dipole position errors due to utilizing configurations VCM-2mm-44el, VCM-2mm-27el, VCM-3mm-44el and VCM-3mm-27el, respectively. We can observe by comparing VCM-2mm-44el and VCM-3mm-44el, that for the same test dipole positions, the dipole position error is obviously smaller utilizing a 2 mm grid than a 3 mm grid. The same observation is made when comparing VCM-2mm-27el and VCM-3mm-27el in figure 3.6.

We can further notice by comparing VCM-2mm-44el and VCM-2mm-27el that the distribution of the position error is not the same when utilizing an extended set of scalp electrodes. The same result is found when comparing VCM-3mm-44el and VCM-3mm-27el.

In figure 3.7 the cumulative distribution of the dipole orientation error is illustrated for the four configurations considered. From this figure we can conclude that the dipole orientation error is always smaller than 4°.

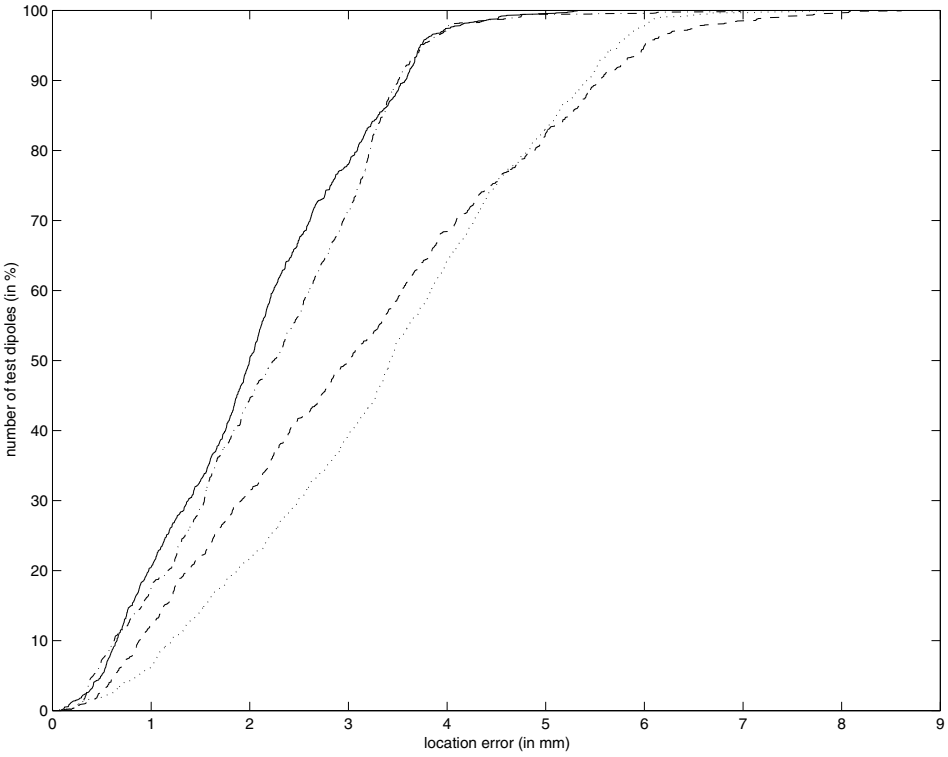

Figure 3.5: The cumulative distribution of the position error is given when utilizing VCM-2mm-44el(-), VCM-2mm-27el(· — ·), VCM-3mm-44el(- -), and VCM-3mm-27el(··).

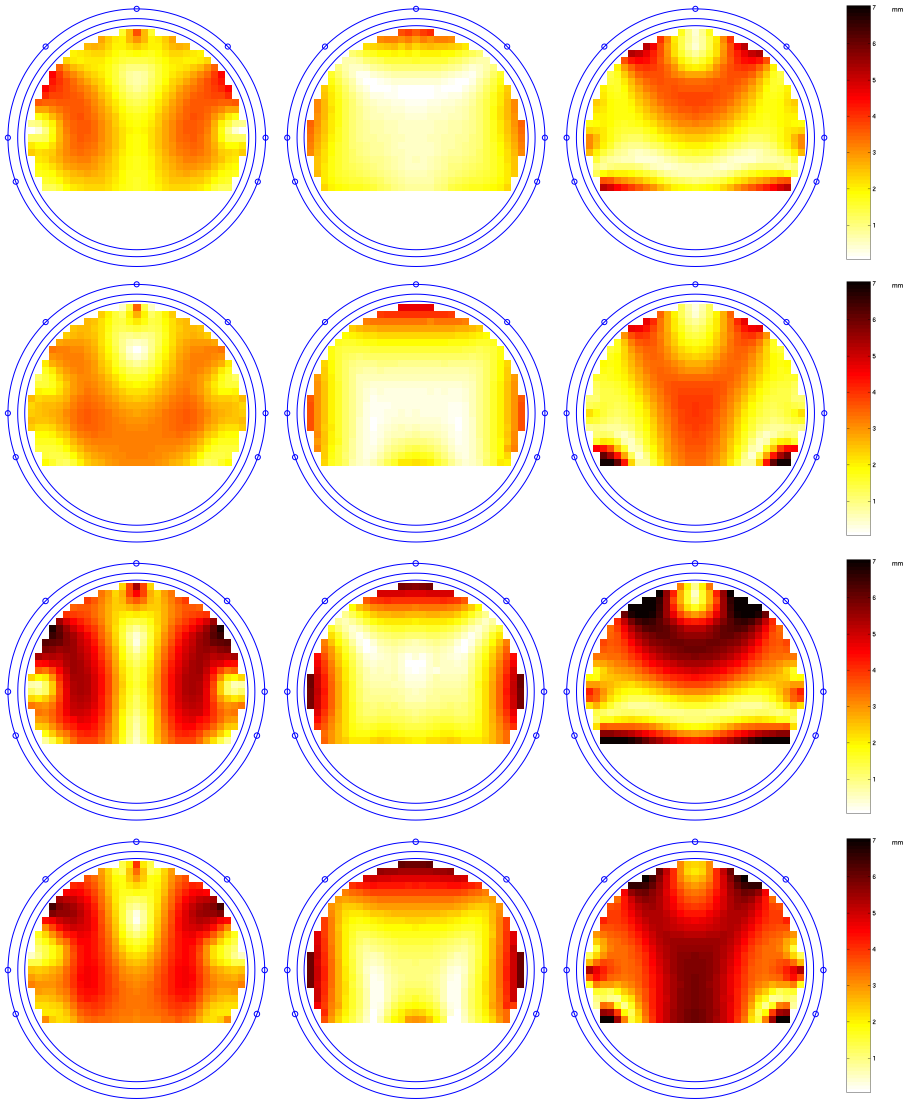

Figure 3.6: The spatial distribution of the dipole position error is given. The color scale indicates the distance in mm between the original and the fitted dipole. The first, second, and third column presents the dipole position error for dipoles oriented along the x-, y- and z-axis, respectively. Rows one, two, three, and four present the dipole position errors due to utilizing configurations VCM-2mm-44el, VCM-2mm-27el, VCM-3mm-44el and VCM-3mm-27el, respectively.

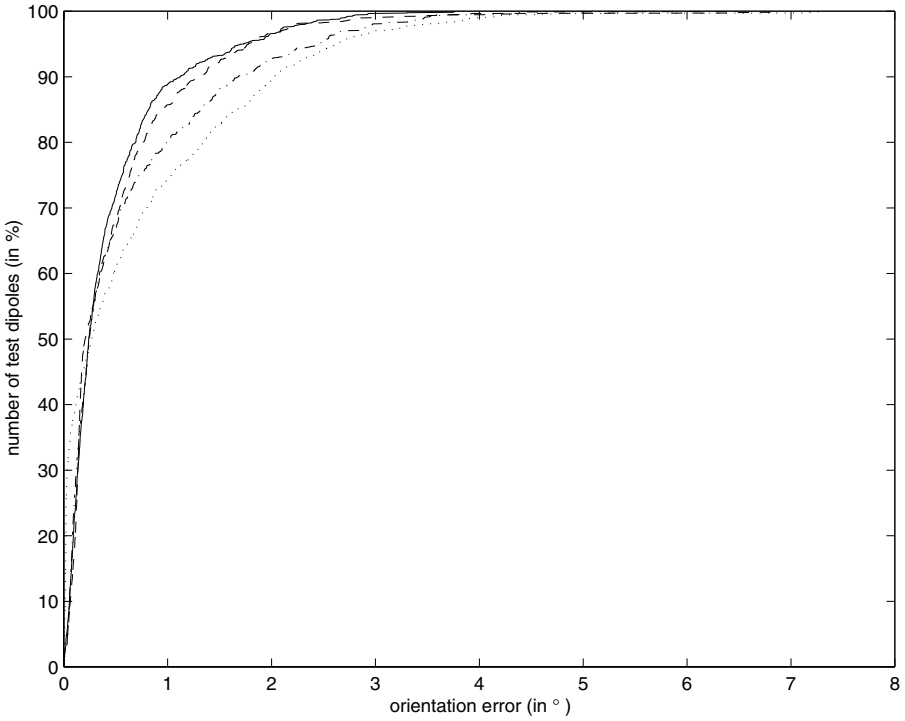

Figure 3.7: The cumulative distribution of the orientation error is given when utilizing VCM-2mm-44el(-), VCM-2mm-27el(· — ·), VCM-3mm-44el(- -), and VCM-3mm-27el(··).

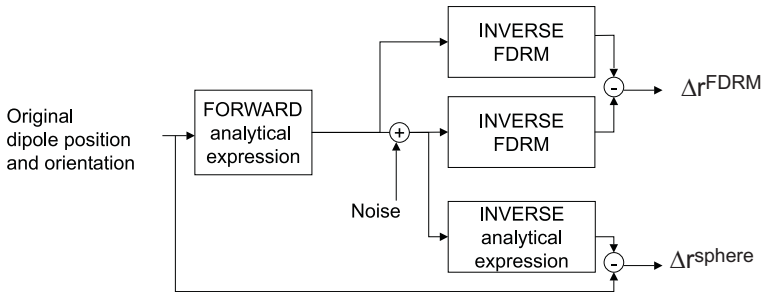

Figure 3.8: The consecutive steps when investigating the sensitivity to noise.

3.6 The sensitivity to noise

3.6.1 Setup of the simulation

In this section, noise values are added to the electrode potentials obtained from the analytical expression. The noise values have a Gaussian distribution with standard deviation $\mathcal{N}$ and zero mean. These values are uncorrelated between the scalp electrodes and are therefore called spatially white. The signal-to-noise ratio (SNR) is defined as the root-mean-square of the average referenced potential generated by a dipole, divided by $\mathcal{N}$. Noise is an important issue in chapter 5. A calculation of the SNR for real data is given in chapter 6.

Figure 3.8 gives a flowchart of the steps taken to investigate the sensitivity to noise. Each noisy set of potentials is subjected to an inverse calculation yielding a fitted dipole position. The inverse problem is solved applying FDRM. If we define the position error as the distance between the original and the fitted dipole (illustrated as (a) in figure 3.9), we mix 2 types of errors: on the one hand the position error induced by the use of FDRM in the inverse procedure, studied in the previous section, and on the other hand the error due to the noise itself. To eliminate the first, we define the position error due to noise Δr^{FDRM} as the distance between the dipole position obtained from a dipole fit without noise and the position obtained from a fit with noise (illustrated with (b) in figure 3.9).

The inverse problem is also solved with the classical method utilizing the analytical expression. The dipole position error Δr^{sphere} is illustrated with (c) in figure 3.9. This gives us a reference to which FDRM can be compared.

The average dipole position error for the 400 sets of noisy potentials are calculated, applying FDRM and the configurations VCM-2mm-27el and VCM-3mm-27el.

These values are compared with the average dipole position error found for

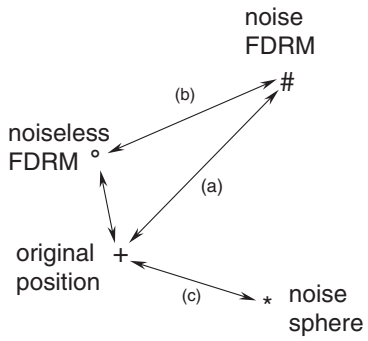

Figure 3.9: Dipole position errors due to noise and due to applying the FDRM.

the case where the inverse problem is solved utilizing the analytical expression and 27 electrodes.

This experiment is carried out for 2 test dipoles: one located in the center of the spheres and one located at 50 mm along the vertical axis, both with an orientation along the vertical axis. Furthermore, 2 SNRs are applied i.e. 10 and 20.

3.6.2 Results

Table 3.2 gives the average position error due to noise represented by $E(\cdot)$. Furthermore, $\Delta r^{FDRM}_{3mm-27el}$ and $\Delta r^{FDRM}_{2mm-27el}$ are the distance between the fitted dipole position in the noiseless case and the fitted dipole position in the noisy case for the configurations VCM-3mm-27el and VCM-2mm-27el, respectively. Δr^{sphere}_{27el} is the distance between the original dipole position and the fitted dipole position in the noisy case when applying the analytical expression as forward evaluation. By inspecting the rows of table 3.2 we can observe that the average position errors by using the VCM-2mm-27 and VCM-3mm-27 are similar to the position errors utilizing the analytical expression. Hence this indicates that the sensitivity to noise when utilizing the FDRM is of the same order as the one found utilizing the analytical expression.

In figure 3.10 the dots present the dipole fits applying noisy potentials. The inverse problem is solved using the FDRM on the 3 mm grid. The test dipoles are located at position (0,0,0) and (0,0,50) mm and orientation along the z-axis. The position error can be inspected for the x- and z-coordinate. The y-coordinate is projected on the coronal slice. In figure 3.10 a SNR of 10 is used. The '+' indicates the original dipole position and the '$\times$' indicates the fitted dipole position without noise. We can notice from figure 3.10 that

position	SNR	$E(\Delta r^{FDRM}_{3mm-27el})$	$E(\Delta r^{FDRM}_{2mm-27el})$	$E(\Delta r^{sphere}_{27el})$
z-axis		(mm)	(mm)	(mm)
0	10	2.9	3.0	3.1
	20	1.5	1.5	1.6
50	10	2.3	2.3	2.3
	20	1.2	1.1	1.2

Table 3.2: Average position error due to noise utilizing VCM-3mm-27, VCM-2mm-27, and the analytical expression in the inverse problem, for dipoles positioned on the z-axis with eccentricity of 0 mm and 50 mm, respectively. Both test dipoles have an orientation along the z-axis. The SNR values are 10 and 20.

the cloud of dots is densely concentrated in the vicinity of '$\times$' rather than of '+'. This indicates that the dipole location error applying noisy EEG is also subjected to the systematic errors in the inverse problem solver.

3.7 Further considerations

The position errors observed in the noise-free case are only due to nonzero grid spacing. For example, we have chosen the node of the structured grid which is closest to the electrode position as the electrode node. Usually the electrode position and the electrode node do not coincide. Subsequently this contributes to the dipole position errors. The left-right symmetry of the position errors in figure 3.6 is due to the left-right symmetric electrode distribution and the left-right symmetry of the computational grid.

A potential disadvantage is that the method, for now, is rather slow compared with the BEM. However by applying faster solvers, such as the multigrid solvers, the calculations can be sped up with a factor 4 [70].

Finally, we compare the results found in our study with the ones found in the literature. The forward evaluation of reciprocity in combination with the FDM was first investigated in [55]. This paper evaluated the forward problem applying the FDRM. The potentials were calculated in the volume conductor model for a current source and sink, diametrically placed on the surface of a three-shell spherical head model. These potentials were compared with the ones found utilizing the analytical expression. It was found that a 2 mm cubic grid yields potentials which are in good agreement with the ones found applying the analytical expression.

Furthermore the same group published an article [57] in which the inverse problem was calculated for 45 test dipoles. They solved the forward problem

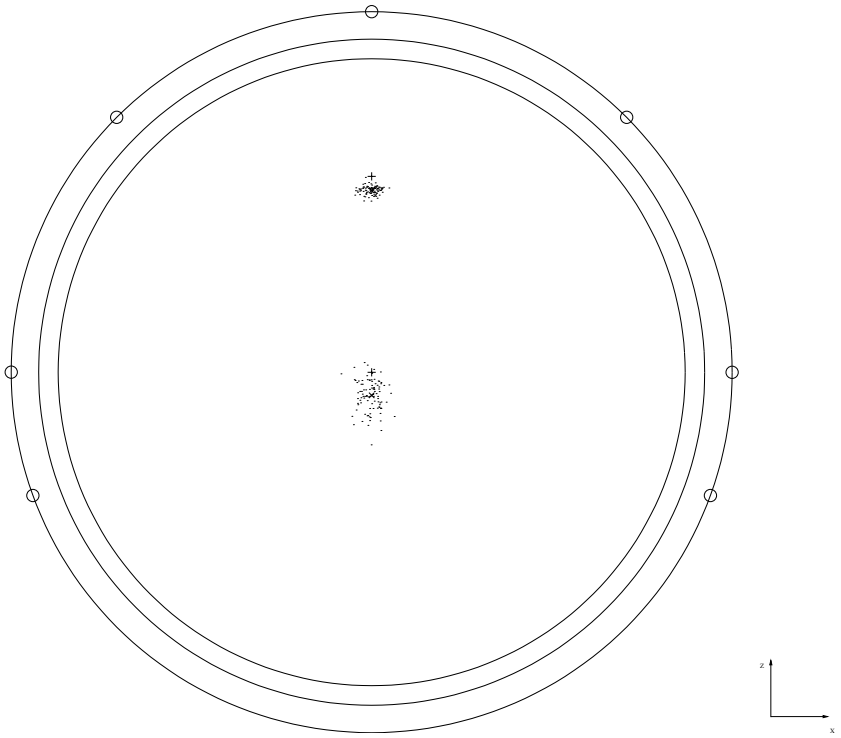

Figure 3.10: The dots represent solutions of the inverse problem for noisy potentials. The inverse problem is solved using FDRM on the 3 mm grid. The '+' indicates the original dipole position while the '$\times$' represents the fitted position without noise. A SNR of 10 is used.

with the FDM in a realistic head model, using a dipole source. Then they used the FDRM in the forward evaluations of the inverse procedure to retrieve the original test dipole. The average position error was 2.8 mm, when applying 19 electrodes and 2 mm for 58 electrodes. The orientation errors were on average 8° and 6.5° for 19 and 58 electrodes, respectively. These results are in agreement with our results. However, one can argue that the potentials calculated in the forward problem were already exposed to errors due to the utilization of the FDM. Subsequently it is difficult to evaluate whether the dipole position errors are due to the errors in the inverse procedure or due to errors in the forward problem.

Reciprocity in combination with the FEM, is introduced in [141]. They calculated the potentials at the scalp with the FEM and with a dipole source. Then they applied the FEM in combination with the reciprocity theorem to calculate the optimal dipole at each element of the FEM grid. The dipole with the lowest residual energy was found close to the original source. We are not aware of a more systematic validation of reciprocity in combination with the FEM.

Finally, the results found for a state of the art BEM as applied in [59] are compared with the results found in our study. A part of their study dealt with the validation of the BEM in a three-shell spherical head model. Each shell was tessellated by 2292 triangles, with a side of about 6-8 mm. Thirty-two test dipoles were placed in different areas of the brain. Furthermore, three electrode sets were applied: 65 electrodes, mainly placed at the left back portion of the scalp, 61 electrodes more homogeneously spread over the scalp surface and a dense grid of 148 electrodes. The average position error for these three electrode sets were, 1.78 mm, 2.04 mm and 1.77 mm, respectively. These values are of the same order as the values found in our simulation for a 2 mm grid, more specifically, we found average position errors of 2.2 mm and 2.0 mm for 27 and 44 electrodes, respectively.

3.8 Summary and original contributions

The FDM gives us the opportunity to easily incorporate tissue with a specific conductivity (such as the ventricular system, white and gray matter, bore holes in the skull, air cavities, etc.) in the head model. The reciprocity theorem gives us the ability to limit the number of numerical calculations to the number of electrode pairs considered. This leads to a substantial reduction of the calculation time compared to the procedure in which for each forward evaluation in the inverse problem, an iteratively solved potential distribution needs to be calculated. The performance of FDRM in EEG dipole source lo-

calization was investigated in the three-shell spherical head model for 1745 test dipoles and for 2 mm and 3 mm grid sizes. We have found that the position error is in general not larger than twice the internode distance. Furthermore, the dipole position error marginally dependents of the number (27 or 44) of electrodes used. The average position error for VCM-2mm-44el, VCM-2mm-27el, VCM-3mm-44el and VCM-2mm-27el is 2.0 mm, 2.2 mm, 3.1 mm, and 3.4 mm, respectively. The orientation error is always smaller than 4° for all the test dipoles and all the FDRM configurations considered. We have also compared the sensitivity to noise using FDRM in the inverse problem of EEG dipole source analysis with the sensitivity to noise using the analytical expression. We have found that FDRM is not more sensitive to noise than the method using the analytical expression.

Solving the inverse problem using the FDRM in a three-shell spherical head model is an original aspect of this study. Investigating the dipole position and orientation error for a large number of test dipoles due to the use of the FDRM is also an original aspect of this work.

Parts of this study were presented at international conferences and appeared as abstracts or papers in proceedings [123, 125, 133] of these conferences. The study is also published in an international journal [138].

Chapter 4

Dipole position errors due to volume conductor model errors

4.1 Introduction

In this chapter, the dipole position errors due to volume conductor model (VCM) errors will be discussed. The impact of omitting the ventricular system on the dipole position error will be investigated. When holes in the skull are present (e.g. fontanelles, trephinations) and these holes are not modeled in the VCM then dipole position errors can occur. We study the impact of omitting a 20 mm hole in the skull on the dipole position error. Finally, the dipole position error is investigated for a wrong estimation of the skull conductivity. When the skull conductivity is modeled lower than the one found in reality, dipole position errors occur. For these three types of volume conductor errors, we also investigated the impact of increasing the number of measuring electrodes on the dipole position error.

The rest of this chapter is organized as follows: the background of the study is presented in section 4.2. Section 4.3 formulates the aims of the study. The methods are discussed in section 4.4. In section 4.5, 4.6 and 4.7, we illustrate the dipole position error due to not incorporating the ventricular system, omitting a hole and wrongfully estimating the skull conductivity, respectively. In section 4.8 a qualitative explanation is given for the dipole position errors found in this study. Finally a conclusion and a summary is presented in sections 4.9 and 4.10.

4.2 Background of the study

Differences in the measured and forward-calculated dipole potentials occur due to two major groups of error contributions. The first group are data related error contributions. The second group are model related error contributions. These errors lead to dipole location and orientation errors in the inverse procedure.

4.2.1 Data related error contributions

The measured EEG is contaminated with noise. Typical noise contributors in the EEG are environmental noise, instrumental noise and biological noise. The major contributor of environmental noise is the 50 or 60 Hz power-line activity. This activity can be suppressed by choosing adequate notch-filters. Digitization noise is considered as instrumental noise. Modern digital EEG acquisition equipment has typically 16 bit analog to digital converters [143], which generate noise smaller than 1.5 μV. A typical EEG signal has a root-mean-square value starting from 50 μV and higher. Subsequently the digitization noise can be neglected. Biological noise in the EEG is electrical activity which is not correlated with the focal brain activity. Some typical contributors are the heart-, muscle-, and eye-movement artifacts. The activity of other brain areas not correlated with the focal activity is often called background EEG. In chapter 5, we will further focus on the background EEG and its impact on dipole position errors.

4.2.2 Model related contributions

A second class of contributors to dipole position and orientation errors are related to the models used in EEG dipole source analysis.

The current dipole is a model for a focal electrical source active in the brain. A larger area of the cortex may be active. Applying a single current dipole to model this area leads to dipole position and orientation errors [41]. It may occur that several brain areas are active simultaneously. A single dipole is again insufficient to model this activity.

A second model related error can be generated by the electrode position. The electrodes are placed on standard positions following the international 10-20 system [49]. However it is possible that certain electrode positions differ from the standard positions due to interpatient variability of head geometry or due to inaccurate placement of the electrodes. Dipole position errors can then occur [115]. One way to overcome this problem is to glue spherical markers, which are visible on magnetic resonance images, on top of the electrodes.

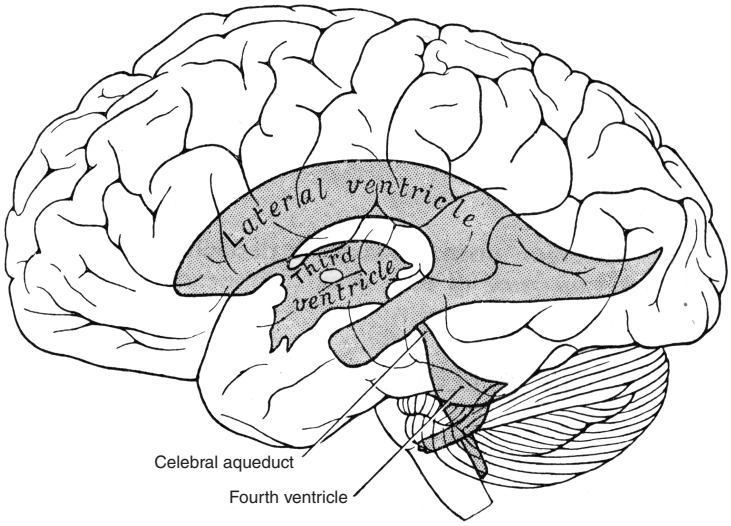

Figure 4.1: Projection of the ventricular system on the left surface of the brain. From [140].

Pattern-recognition software [98, 117] can then be used to allocate the coordinates of each marker.

The last model related error is the VCM error. VCM errors are defined as deviations from the real head geometry or deviations from the real tissue conductivity.

4.3 Aim of the study

In this study, the dipole position error due to three types of VCM errors will be investigated.

In the commonly used realistic VCMs, the ventricular system (VS) is not incorporated. The ventricular system, illustrated in figure 4.1, consists of several cavities in the brain filled with cerebrospinal fluid, which has a higher conductivity than the surrounding brain tissue. A first set of simulations in this study investigates the dipole position error when omitting the ventricular system in the VCM.

In the neonatal skull, fontanelles and sutures occur, as illustrated in figure 4.2. These fontanelles and sutures are regions of soft cartilage tissue with a different conductivity than the skull. These fontanelles close by the eigh-

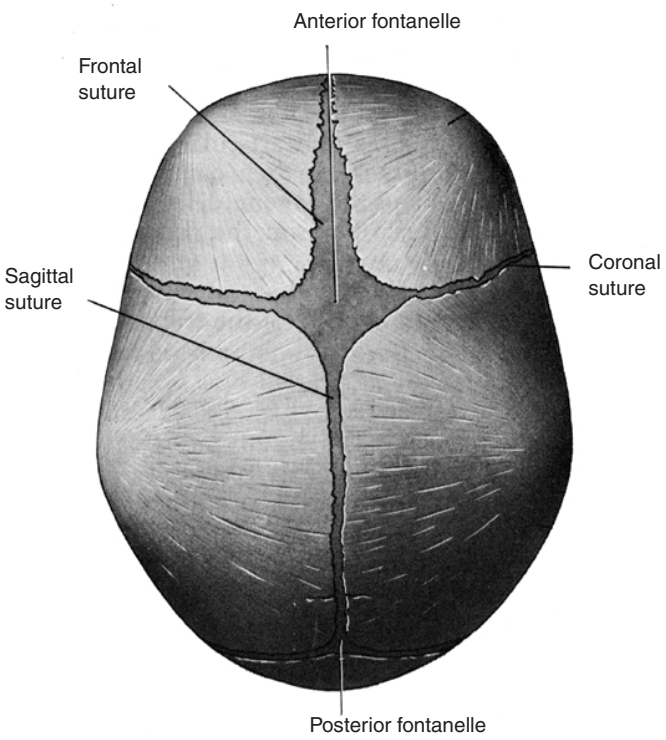

Figure 4.2: A top view of a skull of a newborn infant. From [140].

teenth month to form sutures present in the adult human skull. When these fontanelles are not modeled in the VCM, dipole position errors can occur. Furthermore, for some patients undergoing a presurgical evaluation in epilepsy surgery, intracranial electrodes need to be placed. A trepanation, a removal of a circular piece of skull with a diameter varying between 5 and 20 mm, is made to introduce the electrodes. However, when the holes in the skull are not incorporated in the VCM, dipole position errors occur. In this study, the impact on the dipole position error of omitting a hole of 20 mm diameter in the temporo-parietal area of the skull, is investigated.

Finally, we have investigated the dipole position error due to the usage of an incorrect skull conductivity. The conductivity of the skull is still a controversial issue. Some publications [27, 37, 87] indicate a conductivity of the skull which is 80 times smaller than the scalp and brain conductivity. In more recent publications [53, 80] a value of 16 is proposed. We have tried to answer

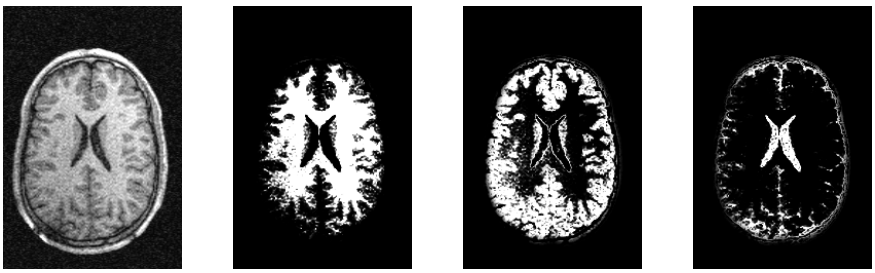

(a) (b) (c) (d)

Figure 4.3: A T1-weighted MR image of an axial slice (a) with the white matter (b), gray matter (c), and CSF region images (d) obtained with SPM.

the following question: what is the dipole position error when utilizing a skull conductivity which is 80 times smaller than the scalp conductivity instead of a skull conductivity which is 16 times smaller? Or, in other words, what is the dipole position error when underestimating the skull conductivity?

In addition, we have tried to answer the question: when increasing the number of electrodes, will there be a reduction of the dipole position error due to the VCM errors?

4.4 Methods

4.4.1 Geometrical construction of the volume conductor model

The SPM99 segmentation tool [3] generates 3 region images from T1-weighted magnetic resonance (MR) images. These region images are the white matter, gray matter and cerebrospinal fluid (CSF) region image, as illustrated in figure 4.3. The voxel volume is 1 mm^3.

The value of each voxel, in a region image, gives the probability of the voxel belonging to that particular region image. A voxel value equal to zero indicates that the voxel does not belong to the region image, while a voxel value equal to 255 indicates that the voxel belongs to the region image.

From the CSF region image, the VS region used in our VCM, is extracted. First, the CSF region image is transformed to a binary image by choosing a threshold value. All the voxel values higher than that threshold value are set to one in the binary image. The other voxel values are set equal to zero. Then, a box is manually introduced which encloses the VS. All the binary voxel values are kept in the box and all the values outside the box are set to zero to delete the CSF not located in the VS. Finally, the high spatial frequencies are removed

by smoothing [89].

The values corresponding with the same voxel in the white matter, gray matter and CSF region images are added. An image is obtained where the voxels in the brain have a high value while voxels elsewhere have a low value. Next, a sufficiently high threshold is chosen to obtain the binary brain region. Finally, the high spatial frequencies are removed by smoothing the brain region.

The binary scalp region is obtained by thresholding the unsegmented T1-weighted MR images. The threshold value is chosen small enough so that all tissues are incorporated in the scalp region. Next the interior volumes, not generating a T1-weighted MR signal, such as the mouth, nose and sinus cavities, are automatically filled [89]. Finally, a smoother is utilized.

It is difficult to extract the skull region from MR images, as the skull does not generate a high T1-weighted signal. Computed tomography images, based on x-rays, give a high intensity value to skull tissue. However, this imaging modality is not incorporated in the presurgical protocol due to the radiation load and the load involving an additional investigation on the patients. The skull region is obtained by eroding [63] the scalp region and by dilating [63] the brain region. An erosion operator removes a shell from the outer surface of the volume in the binary image. A dilation operator adds a layer to the outer surface of the volume in the binary image. These operations are performed until by visual inspection, the boundary of the skull region coincides with the skull boundary depicted on the MR image. We have developed a graphical user interface for this purpose, as illustrated in figure 4.4. The obtained scalp, skull, brain and VS regions are presented in figure 4.5.

4.4.2 Allocating conductivity values

It is known that the brain and skull are electrically anisotropic. However, as in most studies on source localization, we have utilized an isotropic and homogeneous conductivity for each region. It is still an open question how this assumption effects the accuracy of dipole source analysis. The electrical conductivity of the human cerebrospinal fluid at body temperature has been recently investigated [7]. A conductivity of 1.79 S/m was reported. A recent study of the skull conductivity in vitro and in vivo [80] yielded a skull conductivity in the order of 0.014 S/m, which is chosen in our study as reference value. The soft tissue conductivity (i.e. the conductivity of the brain and scalp region) is set to 0.22 S/m, taking in consideration the values reported in [4,42]. The conductivity ratio between the soft tissue and skull then becomes of the order of 16. However, a conductivity ratio of 80 has been used by most of the

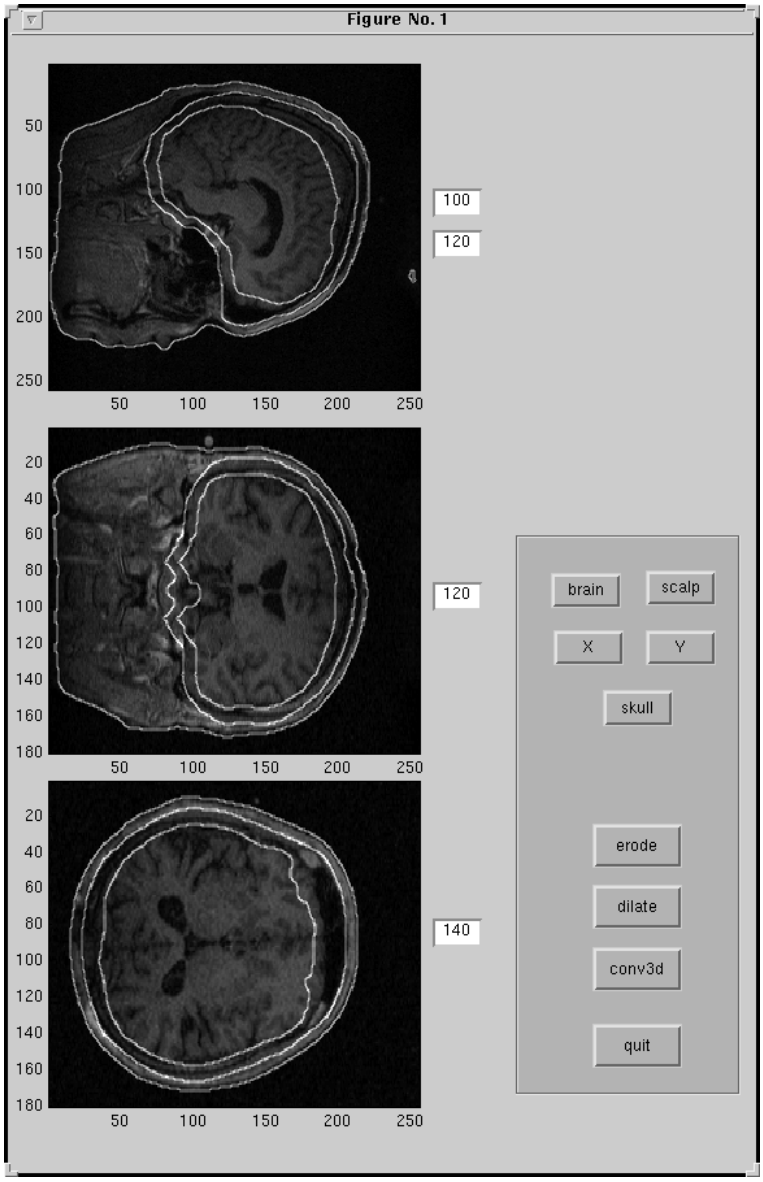

Figure 4.4: The graphical user interface to distinguish the skull region from the scalp and brain region by way of image processing tools. The boundaries of the brain, skull, and scalp region are shown in a sagital, coronal and axial slice.

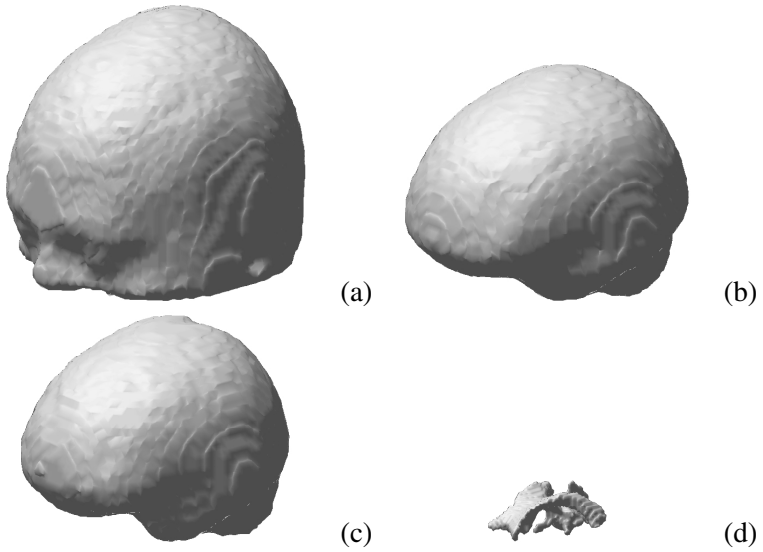

Figure 4.5: A rendered 3D representation of the scalp (a), skull (b), brain (c) and VS region (d) is given.

modelers and is based on contributions of Rush and Driscoll [87] and Cohen and Cuffin [27]. The reference values of the relative and absolute conductivities are summarized in table 4.1.

4.4.3 Electrode placement

The electrodes are placed following the international 10-20 system [49] with 3 additional electrodes on each temporal area as schematically illustrated with the bright-gray dots in figure 4.6. To have a higher spatial sampling, extra

regions	absolute conductivity S/m	relative conductivity
VS	1.79	8
brain	0.22	1
skull	0.014	$\frac{1}{16}$
scalp	0.22	1

Table 4.1: The reference values of the absolute and relative conductivity of the regions incorporated in the VCM.

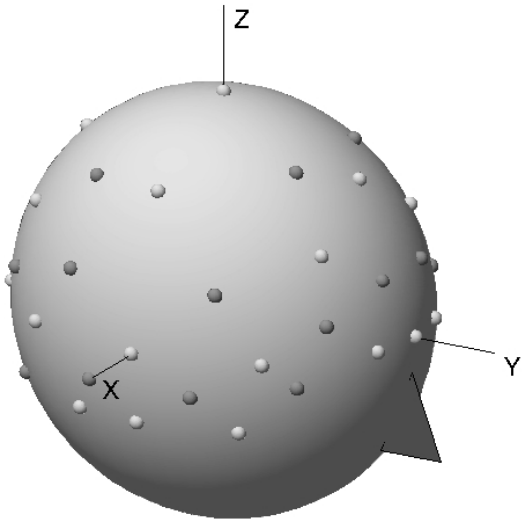

Figure 4.6: A schematic representation of the electrode positions. The light-gray dots represent the 27 electrode positions, while the dark-gray dots indicate the additional electrode positions summing up to 53 electrodes.

electrodes illustrated as dark-gray dots in figure 4.6 are placed adding up to 53 measuring points. In this study fictive electrode positions are utilized. A sphere is fitted through the cube centers or nodes at the scalp surface. Only the nodes of the upper part of the scalp, where most of the electrodes are located, are used. For each standard electrode position on the fitted sphere, the nearest node at the scalp surface of the realistic VCM is looked up. This node is then allocated as electrode node in the VCM.

4.4.4 The different volume conductor models

Four VCMs are constructed utilizing the regions obtained from the segmented MR images. In table 4.2 the VCMs are given with the relative conductivities for each region. VCM-1 consists of a scalp, skull, brain and VS region with conductivity values given in table 4.1. In VCM-2 the conductivity of the region containing the VS equals the conductivity of the brain region. Hence the VS is neglected in this VCM. VCM-3 consists of the same regions as VCM-1 but

regions	VCM-1	VCM-2	VCM-3	VCM-4
scalp	1	1	1	1
skull	$\frac{1}{16}$	$\frac{1}{16}$	$\frac{1}{16}$	$\frac{1}{80}$
brain	1	1	1	1
VS	8	1	8	8
hole	$\frac{1}{16}$	$\frac{1}{16}$	1	$\frac{1}{80}$

Table 4.2: The relative conductivities for the VCMs used.

a 20 mm diameter hole in the temporo-parietal area of the skull is included, as illustrated in figure 4.7. The conductivity of the hole in the skull equals the conductivity of the brain and scalp regions. VCM-4 consists of the same regions as VCM-1 but the conductivity of the skull region is 80 times smaller than the conductivity of the brain or scalp region. This corresponds with an underestimation of the skull conductivity. The 'hole' conductivity in table 4.2 set equal to the conductivity of the skull in VCM-1,2,4 implies that in those cases no hole in the skull is present.

4.4.5 The test dipoles

The dipole position errors are investigated for test dipole positions covering the brain region in a typical coronal and axial slice containing the VS, as illustrated in figure 4.7. The line in the coronal slice corresponds to the position of the axial slice and vice versa. The test dipole positions, illustrated by the dots in figure 4.7, are placed 5 mm apart. The coordinate axes are also illustrated in figure 4.7. Four dipole configurations are evaluated, i.e., dipoles located in the coronal slice oriented along the x-axis (cor-x), dipoles located in the coronal slice oriented along the z-axis (cor-z), dipoles located in the axial slice oriented along the x-axis (ax-x) and dipoles located in the axial slice oriented along the y-axis (ax-y). In total, 2458 test dipoles are used.

4.4.6 The forward and inverse problem

The finite difference method in combination with the reciprocity theorem, is used to solve the forward problem. Subsection 2.7.6 and appendix B give further details on the finite difference method and on the reciprocity theorem, respectively. The segmented regions obtained from the MR images are used to generate a cubic grid with a cube side equal to 2 mm. Each cube is allocated a specific conductivity, depending on the region in which it is located. The obtained VCM of the human head consists of about half a million cubes. The

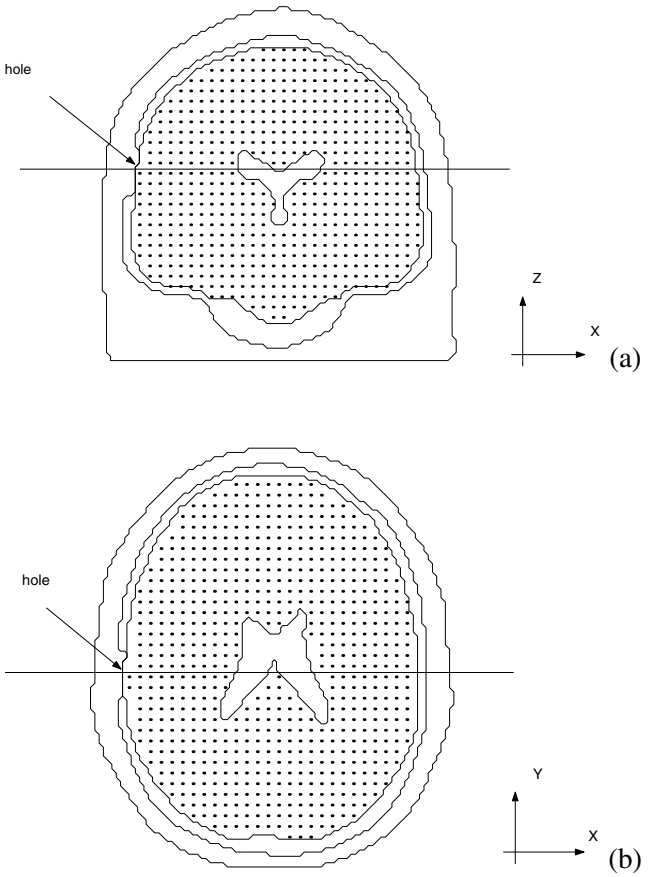

Figure 4.7: The coronal (a) and axial (b) slice that contain the test dipoles. The dots indicate the original dipole positions. The line in the coronal slice indicates the position of the axial slice and vice versa. The position of the hole and the coordinate axes are also illustrated.

potentials in the cube centers or nodes are calculated applying the successive overrelaxation method as given in appendix A.

In the inverse procedure, dipole location and orientation parameters are estimated by iteratively minimizing the residual energy given in equation 2.38. We refer to section 2.8 for more details on solving the inverse problem.

4.5 Dipole position errors due to omitting the VS

VCM-1 (see table 4.2) is used to solve the forward problem while VCM-2 is used in the inverse-problem solver. We have solved the inverse problem utilizing 27 and 53 electrodes. Each fit yields a position error Δr, the distance between the original and the fitted dipole position. Figure 4.8 presents the histograms of the position error due to omitting the VS for 27 and 53 electrodes. Each mark, '+' for 53 and '$\circ$' for 27 electrodes, presents the center of an interval with 0.5 mm width. When the number of electrodes increases, a slight reduction in the position error occurs, which is observed by the shift to the left of the curve representing 53 electrodes. It is also noticed that the majority of the test dipoles has a location error between 0-3 mm. The maximum position error for 27 and 53 electrodes is 7.6 mm and 6.1 mm, respectively.

In figure 4.9, the dipole position error is given for the four test dipole configurations. The tail of the arrow represents the original position, while the head of the arrow represents the fitted position projected on the slice containing the original positions. It should be noticed that the arrows do not represent the dipole position error orthogonal to this slice. The color scale represents the distance between the original and the fitted position. The positions with the largest position errors are in the vicinity of the VS.

Minor differences in the topography of the dipole position error are observed between the configurations utilizing 27 and 53 electrodes. Therefore, the results for 27 electrodes are not given.

Comparing our results with the literature

The major finding of van den Broek et al. [23, 24] was that electrode potentials obtained from VCMs with and without the VS included, differ for dipoles in the vicinity of the VS. In their study only a limited number of test dipole positions is considered. Furthermore only the scalp potentials were investigated and the inverse problem was not solved.

Awada et al. [4] investigated the dipole position error due to omitting the VS in a 2D finite element VCM. In their study dipole position errors up to 5 mm were found. However, their calculations were performed in an axial

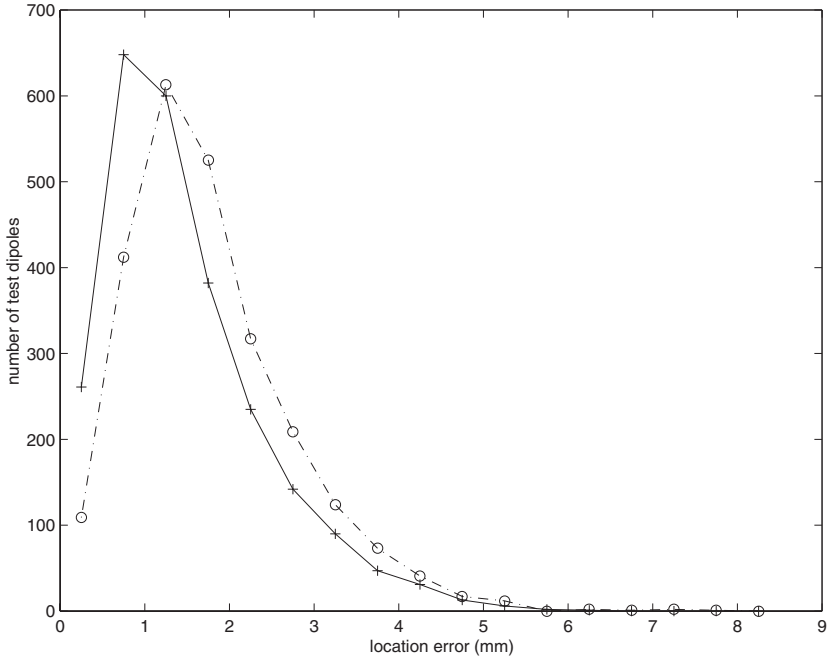

Figure 4.8: Histogram of the dipole position error due to omitting the VS, for 27 (-·○)and 53 (-+) scalp electrodes.

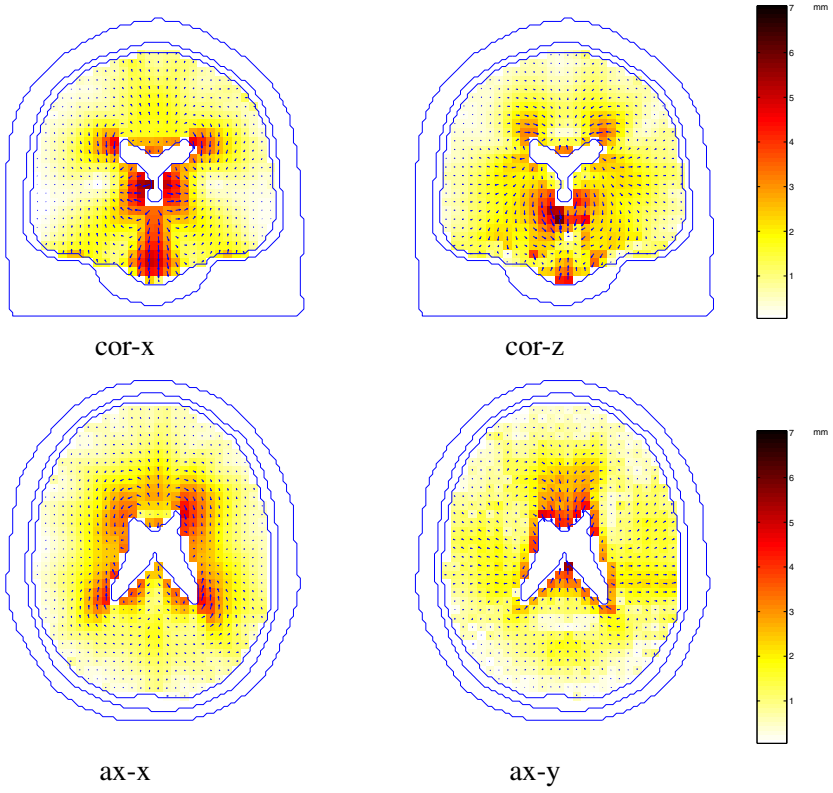

Figure 4.9: Dipole position errors due to omitting the VS are presented. The tail of the arrow represents the original position while the head of the arrow represents the fitted position projected on the corresponding slice. The color scale indicates the distance between the original and the fitted dipole. The dipole configurations cor-x, cor-z, ax-x and ax-y are depicted. 53 electrodes are used.

slice in 2D. Due to the fact that the human head is an intrinsic 3D object the 2D representation may be an oversimplification. In their study all the nodes at the boundary between scalp and air were used as measurement points which is in contrast with the fact that only a discrete set of electrodes on the scalp surface are used in reality.

We have solved the inverse problem when omitting the VS in the VCM. These simulations are performed in a 3D realistic head model and for a large number of test dipoles. Two realistic sets of electrode configurations are used. The maximum location errors obtained for 27 and 53 electrodes are 7.6 mm and 6.1 mm, respectively. The dipole location errors occur around the VS.

4.6 Dipole position errors due to omitting a hole in the skull

The forward problem is solved with VCM-3, while the inverse problem is solved applying VCM-1. The maximum position error for 27 and 53 electrodes is 5.6 mm and 5.2 mm, respectively. In figure 4.10, the histograms of the dipole position errors are presented due to omitting a hole for 27 and 53 electrodes. The interval size is 0.5 mm. Increasing the number of electrodes gives almost no improvement of the position error. Furthermore, the majority of the test dipoles has a dipole location error between 0 mm - 1 mm.

In figure 4.11, the dipole position error is given for the four test dipole configurations and for 53 electrodes. The positions with the largest position errors are in the vicinity of the hole. For these test positions, the dipole is fitted closer to the hole. For dipoles radially oriented with respect to the hole as in cor-x and ax-x the largest position errors are found in front of the hole in the brain region. For dipoles tangentially oriented with respect to the hole the largest position errors are found in positions next to the hole in the brain region. Figure 4.11 also illustrates large areas where no position errors are observed. When a source is located somewhat away from a hole in the skull, the dipole position error due to this hole will be negligible. A similar topography of the dipole position error can be found for 27 scalp electrodes. A hole with a smaller diameter than the one used in our simulation, is expected to have a smaller impact on the dipole position error.

Finally, the dipole position error due to omitting a hole in the VCM also depends on the conductivity of the matter in the hole. In our simulation we have suggested that the hole is filled with matter having the same conductivity as the scalp and brain region. Consider the hole filled with a matter having a conductivity smaller than the one used in our simulation, but still larger than

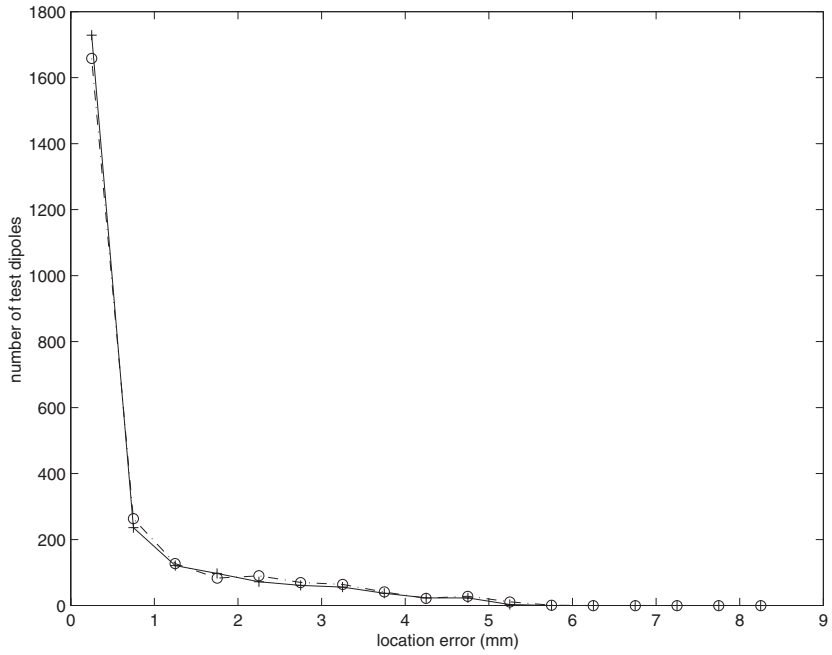

Figure 4.10: Histogram of the dipole position error due to omitting a hole in the skull, for 27 (-·○) and 53 (-+) scalp electrodes.

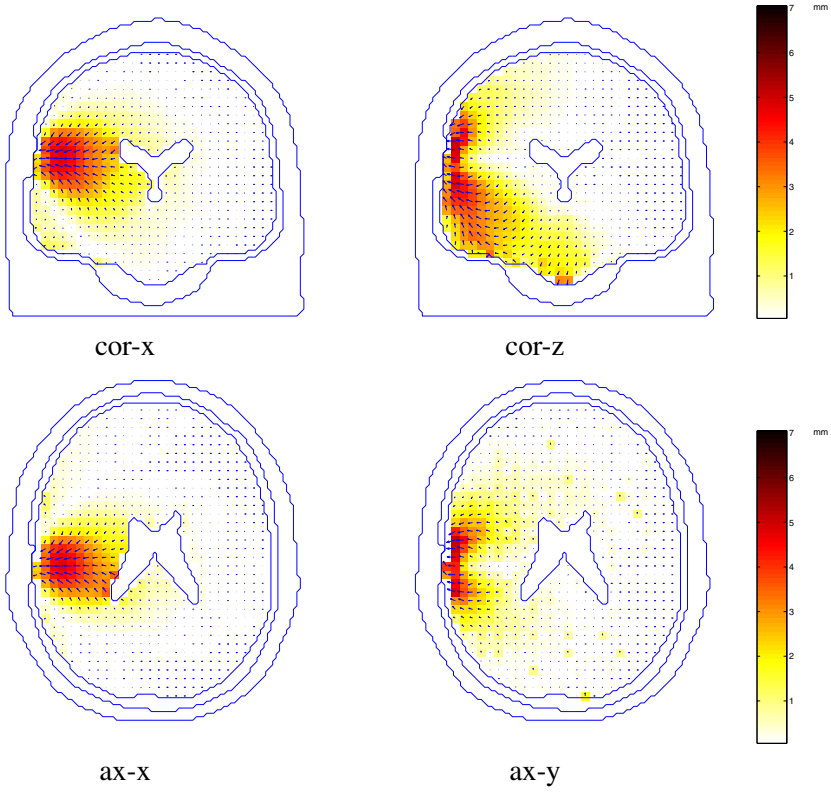

Figure 4.11: Dipole position errors due to omitting a hole in the skull are presented. The tail of the arrow represents the original position while the head of the arrow represents the fitted position projected on the corresponding slice. The color scale indicates the distance between the original and the fitted dipole. The dipole configurations cor-x, cor-z, ax-x and ax-y are depicted. 53 electrodes are used.

the skull conductivity. Then we can expect to have a smaller deviation in potential distribution at the scalp surface, when for a given dipole the forward problem is solved with and without a hole in the skull. In the limit, if the conductivity of the matter filling the hole was almost as small as the conductivity of the skull, almost no deviation in scalp potentials would be observed. Thus smaller dipole position errors can be expected.

If the conductivity of the matter filling the hole was higher than the one used in our simulation, for example in [54], where titanium screws were used to anchor the intracranial electrodes, then we would expect larger position errors. The direction of the displacement of the fitted dipole would be the same as in figure 4.11. If on the other hand, the conductivity of the matter filling the hole is lower than the skull conductivity, as in [28] where plastic screws were used to close the holes, then the direction of the displacements of the fitted dipoles would be opposite to the ones found in our simulation.

Comparing our results with the literature

Van den Broek et al. [23, 24] investigated the dipole position errors due to omitting a hole in a three-shell spherical head model for a small number of dipoles beneath the hole. The hole had a 30 mm diameter. Dipole position errors up to 16 mm were found.

Ollikainen et al. [79] examined the dipole position errors due to omitting a 5 mm diameter hole in the skull for a set of dipoles beneath the hole. It was found that position errors of approximately 10 mm can be encountered which can not be compensated for by increasing the number of electrodes.

In a recent study of van Burik et al. [26], the measured scalp potentials, generated at couples of intracranial electrodes, were compared with the potentials simulated by a dipole positioned halfway between the intracranial electrodes and oriented along the line connecting them. The scalp potentials simulated with the dipole source were calculated in different VCMs. Some of these models contained the holes through which the intracranial electrodes were introduced, others did not contain the holes. By comparing the measured and simulated potentials it was not clear which VCM was superior. However, in their study no inverse problem was solved.

In our simulation we have investigated the dipole position error when omitting a hole in the VCM. The location error is investigated for a large number of test dipoles. The maximum dipole location errors for 27 and 53 electrodes are 5.6 mm and 5.2 mm. These values are lower than the values found by van den Broek and Ollikainen. In their simulations a conductivity ratio of 80 between the soft tissue and skull is used, while we used a ratio of 16. We

believe that this caused the difference in location errors. By not incorporating the hole in the VCM large areas in the brain are not affected. However for test dipoles in the vicinity of the hole, dipole location errors occur.

4.7 Dipole position errors due a wrong skull conductivity

The forward problem is solved utilizing VCM-1. The forward evaluations in the inverse-problem solver are done using VCM-4. The skull conductivity in the inverse-problem solver (1/80) is five times smaller than the one used in the forward calculations (1/16). The maximum position error for 27 and 53 scalp electrodes is 33.4 mm and 28.0 mm, respectively. Figure 4.12 illustrates the histograms of the dipole position errors due to underestimating the skull conductivity, for 27 and 53 electrodes. Notice that the range of the x-axis of figure 4.12 is much larger than in figure 4.8 and in figure 4.10. The size of the intervals is 1 mm here. One can observe that the position errors due to underestimating the skull conductivity are typically larger than the ones due to omitting the VS or a hole in the skull. The majority of the test dipoles have a dipole location error between 5 mm-20 mm. Increasing the number of electrodes slightly reduces the position error for the given test dipoles.

In figure 4.13 the dipole position error is given for the four test dipole configurations with 53 scalp electrodes. Notice again that the range of the color bar is much larger than the range of the color bars used in figures 4.9 and 4.11. Large dipole position errors can be found for most of the test dipoles. The test dipoles are fitted outward radially from their original position. Again for 27 electrodes a similar topography can be found for the dipole position errors.

Comparing the results with literature

Awada et al. [4] found position errors up to 20 mm for a skull conductivity which is 3.3 times smaller than the baseline skull conductivity, in a 2D finite element grid. The dipoles were fitted outward radially. The nodes at the boundary between scalp and air were used as measurement points. In reality the scalp potentials are measured at a discrete set of electrodes on the scalp surface, which are only distributed on the upper half of the scalp. Furthermore the human head is an intrinsic 3D object, a 2D representation may be an oversimplification.

Pohlmeier et al. [83] found that when the conductivity is underestimated in the inverse-problem solver, the dipoles are fitted in an outward radial sense. For a conductivity of the skull which is 5 times smaller than the baseline skull

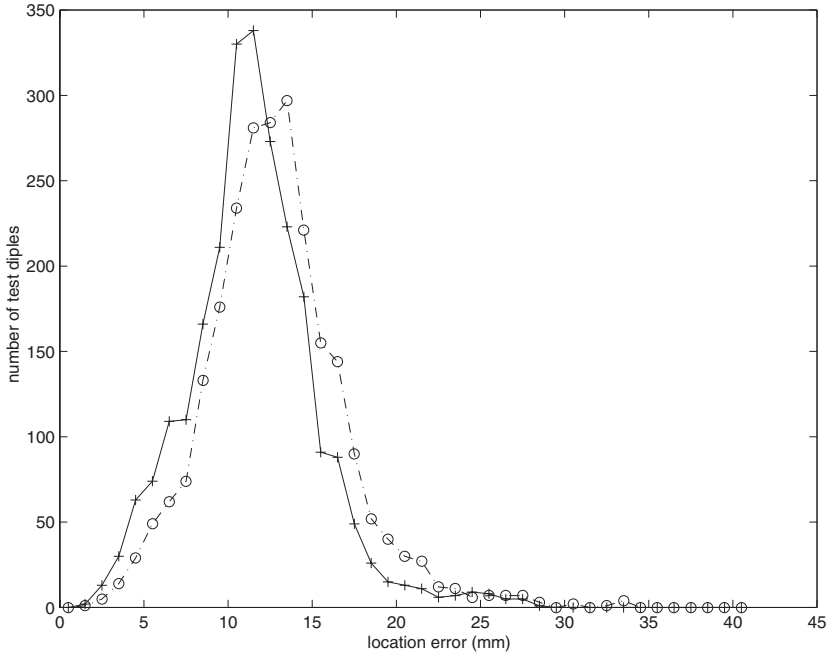

Figure 4.12: Histograms of the dipole position error due to underestimating the skull conductivity, for 27 (- ·○) and 53 (-+) scalp electrodes.

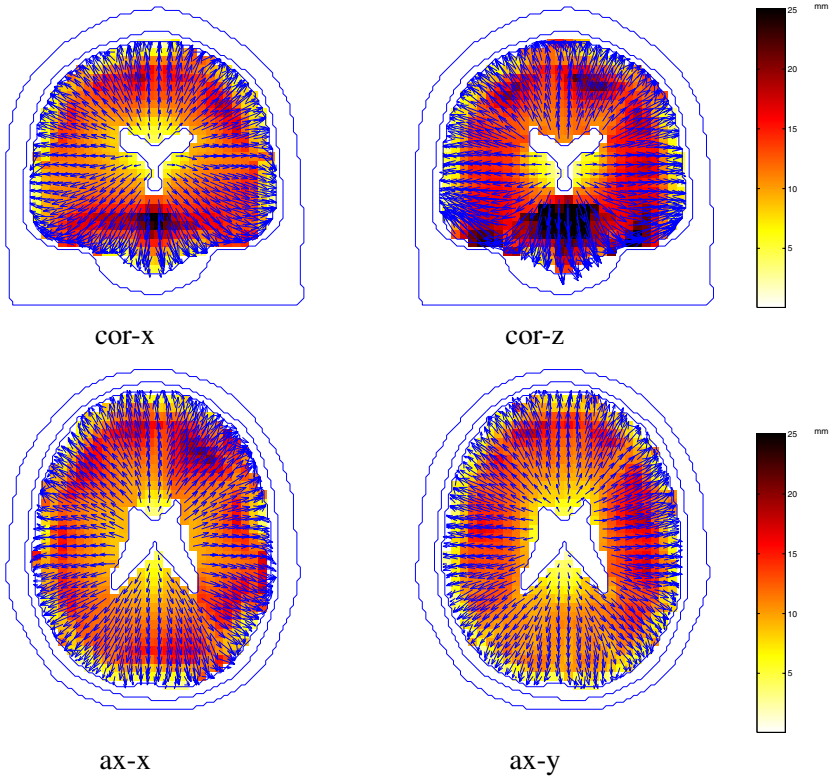

Figure 4.13: The dipole position error due to underestimating the skull conductivity, is presented. The tail of the arrow represents the original position while the head of the arrow represents the fitted position projected on the corresponding slice. The color scale indicates the distance between the original and the fitted dipole. The dipole configurations cor-x, cor-z, ax-x and ax-y are depicted. 53 electrodes are used.

conductivity, a ratio also used in our study, an average dipole position error of about 10 mm was found. Sixty-five electrodes were used. The impact on the dipole position error of increasing or decreasing the number of electrodes was not investigated.

In the paper published by Laarne et al. [57], the average dipole position error due to underestimating the skull conductivity, was studied for 45 test dipoles originating from 15 dipole positions. They have used the same conductivity ratios as in our study. The average dipole position error was about 7.5 mm when using 19 electrodes and 6.5 mm when using 58 electrodes.

We have simulated the dipole position error due to underestimating the skull conductivity. We have used a large number of test dipoles and a 3D VCM. We further applied realistic scalp electrode configurations. The maximum dipole location errors are 33.4 mm and 28.0 mm for 27 and 53 electrodes. Dipole position errors occur for test dipoles in the entire brain volume. The fitted dipoles are found outward radially from the original position which confirms the results found by the other authors.

4.8 Qualitative explanation of the dipole position errors

4.8.1 The scalp potentials for a radial dipole at several depths

The potentials at the scalp surface are investigated for radial dipoles at several depths. The results will then be used to explain the dipole position errors found in our study. VCM-1 is used to calculate the potential distribution at the scalp surface for dipoles located 10 mm, 20 mm and 30 mm from the skull surface in the coronal slice used in our simulations. The dipole is oriented along the x-axis, which is orthogonal (radial) to the skull surface. In this simulation, the reciprocal current sources at the electrodes are replaced by a dipole. Figure 4.14 illustrates the equipotential lines for dipoles located at 10 mm (a), 20 mm (b) and 30 mm (c) from the skull surface.

The potentials along the scalp surface are illustrated in figure 4.15. The successive scalp points are taken starting from the bottom node, marked with a, to the top node marked with a along the scalp surface illustrated in figure 4.14 (a), (b) and (c). The potentials are normalized so that the maximum coincides with one. Notice that the closer the dipole is located to the skull, the more rapid the variation of the potential distribution becomes. Or the further the dipole is located from the skull, the slower the variation of the potential distribution becomes. With this knowledge, we move on to the next paragraph where a qualitative explanation will be sought for the dipole position errors

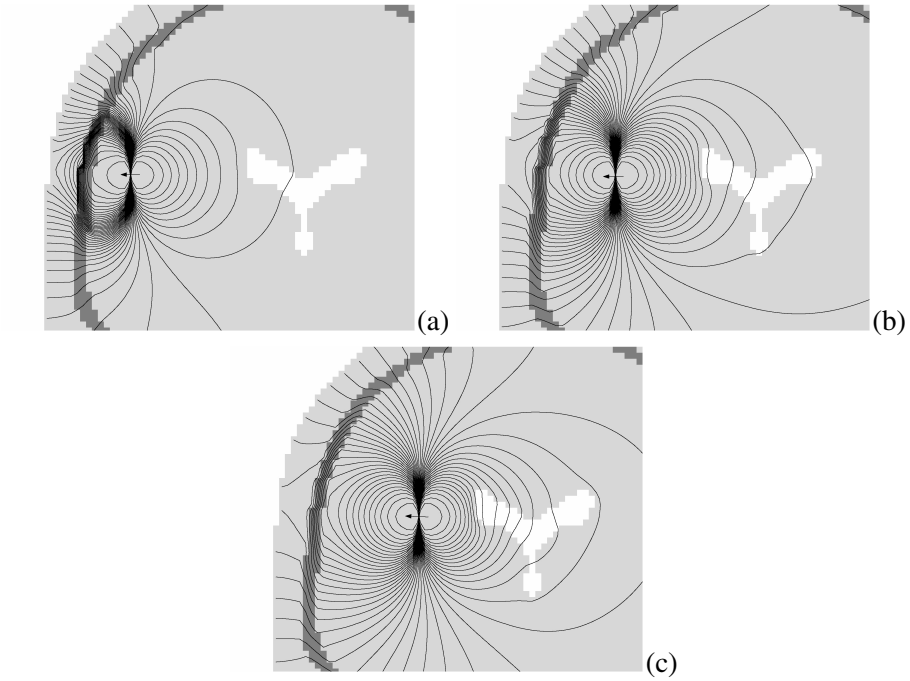

Figure 4.14: The equipotential lines for a potential distribution generated by a dipole oriented radially to the skull surface, and 10 mm (a), 20 mm (b), and 30 mm (c) from the brain-skull boundary. VCM-1 is used.

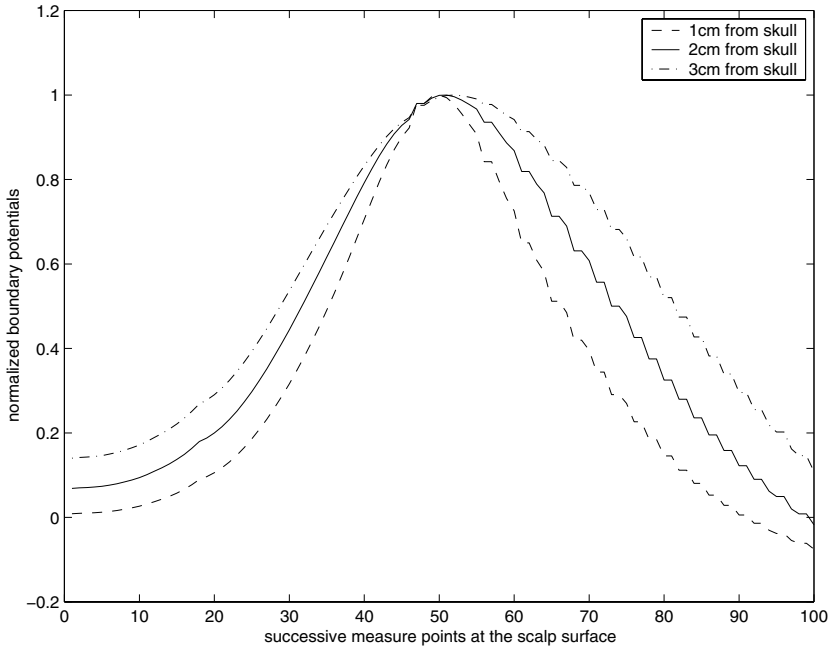

Figure 4.15: The potentials at successive scalp boundary nodes obtained with VCM-1, for a radial dipole positioned at 10 mm (- -), 20 mm (-) and 30 mm (- ·) from the skull.

due to VCM errors.

4.8.2 Comparing potential distributions for a given test dipole

Figure 4.16 presents the equipotential lines for a dipole positioned 20 mm from the skull boundary radially oriented along the x-axis and utilizing VCM-1 through VCM-4. In figure 4.17, the potential distribution at the scalp surface is illustrated for the dipole coordinates given in figure 4.16 and using VCM-1 through VCM-4. The successive scalp-surface potentials are normalized so that the maximum of each distribution coincides with 1.

Notice, by comparing VCM-1 with VCM-2 that the impact of omitting the VS on the scalp potentials is negligible for this dipole position. Hence a small dipole position error occurs, which is illustrated in figure 4.9 for cor-x.

When a hole in the skull is neglected as in VCM-1, a slower variation of the potential distribution is found compared with the one obtained with VCM-3. To have a more rapid variation which is more in concordance with the distribution given with VCM-3, the dipole will be located closer to the hole, as

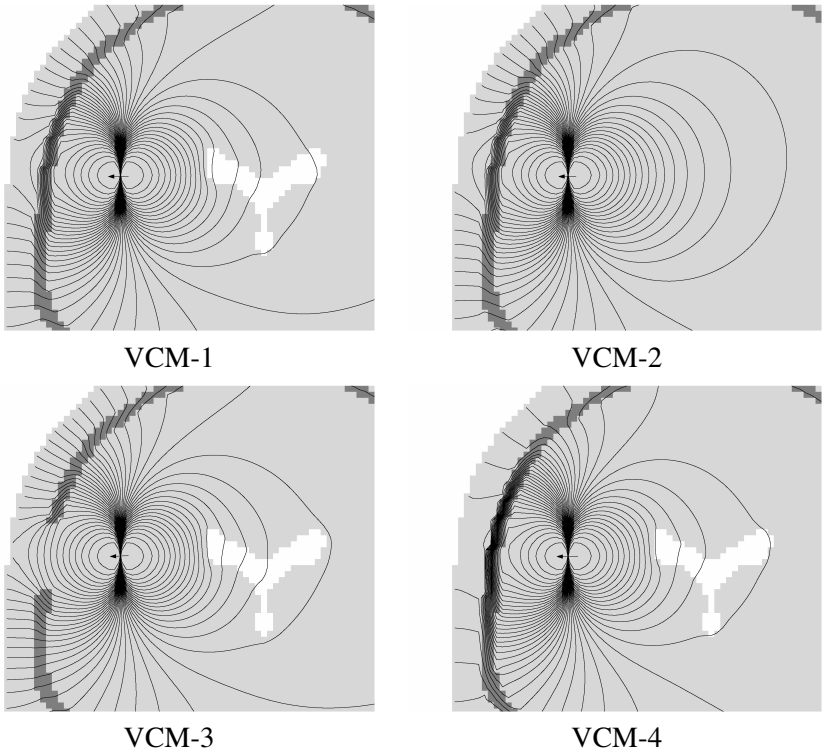

Figure 4.16: The equipotential lines for a potential distribution generated by a dipole oriented along the x-axis and 20 mm from the brain-skull boundary. VCM-1 through VCM-4 are used.

illustrated in figure 4.11 for cor-x.

Underestimating the skull conductivity as simulated with VCM-4, gives a slower variation of the potential distribution than the one obtained with VCM-1. To have a sharper distribution the dipole will be located closer to the brain boundary in a radial sense, which is illustrated in figure 4.13 for cor-x.

4.9 Conclusion

We have investigated the dipole position errors due to omitting the ventricular system, omitting a hole in the skull and underestimating the skull conductivity. The maximum dipole location error encountered, utilizing 27 and 53 electrodes is 7.6 mm and 6.1 mm, respectively for omitting the VS, 5.6 mm and 5.2 mm, respectively for omitting the hole in the skull, and 33.4 mm and

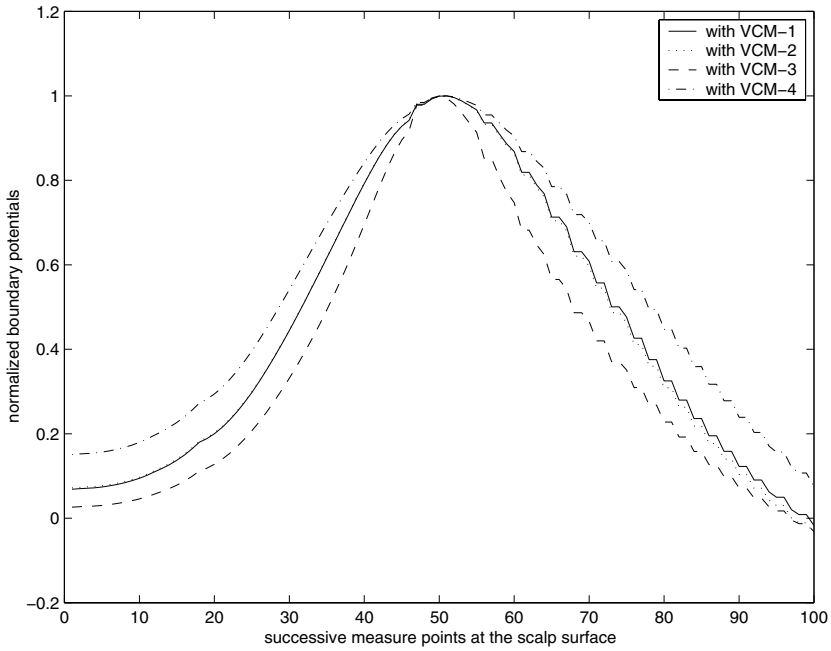

Figure 4.17: The potentials at successive scalp boundary nodes obtained with VCM-1 through VCM-4, for a dipole oriented along the x-axis and 20 mm for the brain-skull boundary.

28.0 mm, respectively for underestimating the skull conductivity. We found that the position errors due to omitting the VS are mainly located in the vicinity of the VS. Furthermore, omitting a hole in the skull yielded position errors mainly in the vicinity of the hole. The dipoles were fitted closer to the hole. The impact of underestimating the skull conductivity yielded position errors in the entire brain volume which are typically higher than the ones found due to omitting the VS or omitting a hole in the skull. We found that the dipoles were fitted outward radially from their original position. Increasing the number of electrodes improved the dipole position errors marginally for the three cases investigated.

4.10 Summary and original contributions

Environmental noise, instrumental noise and biological noise are data related errors. Wrongfully choosing an electrical source, wrongfully estimating the electrode positions and errors in the VCM are grouped in model related errors. Dipole position errors can occur due to noise related and/or model related errors. We examined dipole position errors in EEG source analysis, due to VCM errors, which are model related errors.

The impact on the dipole position error is investigated for not incorporating the ventricular system, omitting a hole in the skull and underestimating the skull conductivity.

An original aspect is that a large number of test dipoles was used which enabled us to make topographies of the dipole position error. Furthermore, the investigation of the impact of the number of electrodes, on the dipole position error, is also original for the cases where the VS and the hole in the skull are neglected. The largest position errors due to omitting the VS can be found in the vicinity of the VS. The largest position errors due to omitting a hole can be found in the vicinity of the hole. At these positions the fitted dipoles are found closer to the hole. When the skull conductivity is underestimated, the dipole is fitted closer to the skull-brain border in a radial direction for all test dipoles. We found that the position errors due to underestimating the skull conductivity are typically higher than the ones found due to omitting the VS or omitting a hole in the skull. Increasing the number of electrodes reduces the dipole position errors marginally for the three cases investigated.

The study presented in this chapter appeared in an international journal [135]. A part of this study is also published in an abstract of an international conference [134].

Chapter 5

Comparing dipole position errors due to noise

5.1 Introduction

In chapter 3 the finite difference reciprocity method (FDRM) is validated in a three-shell spherical head model. The previous chapter reported dipole position errors due to volume conductor model errors. Another contributor to dipole position errors is noise. In this chapter we focus on noise.

The performance when solving the inverse problem with the three-shell spherical head model versus the performance when solving the inverse problem with the realistic head model is investigated in the presence of noise. It will be demonstrated that increasing the noise level reduces the performance of the realistic head model compared to the spherical head model. Furthermore it will be shown that increasing the number of electrodes from 27 to 44 has a limited impact on the performance of the realistic head model compared to the spherical head model. Moreover, we will show that the performance of the realistic head model gains importance compared to the three-shell spherical head model, when increasing the number of time samples. Finally we will replace Gaussian noise with background EEG, which is spatially and temporally correlated. It will be demonstrated that background EEG compared to Gaussian noise reduces the performance of the realistic head model compared to the spherical head model.

The rest of this chapter is organized as follows: the background of the study is presented in section 5.2. We proceed with presenting the applied methods in section 5.3. In section 5.4 we validate the local linearization used for a fast calculation of the inverse problem. The results obtained applying Gaussian noise are given in section 5.5. In section 5.6, the results are presented for back-

ground EEG. Finally, a summary and the original contributions are presented in section 5.7.

5.2 Background of the study

5.2.1 Dipole position errors due to applying the spherical head model

The dipole position error due to utilizing a three-shell concentric spherical head model instead of a realistic head model is addressed in the literature [86, 124, 145]. It was found that the dipole position errors for the basal part of the brain typically amounts to 15 - 25 mm. In these publications, the dipole position error was found by utilizing noise-free potentials.

5.2.2 Dipole position errors due to background EEG

Dipole position errors occur due to noise. In reality, noise is superposed to the focal EEG. Typical noise contributors in the EEG are environmental noise, instrumental noise and biological noise (see section 4.2). We further focus on biological noise. It can be seen as a biological electrical activity that is not correlated with the focal brain activity. Some typical contributors are the heart, muscle and eye-movement artifacts. Apart from these electrically active tissues, other brain areas may be active too. The EEG generated by these areas is often called background EEG. Due to background EEG, dipole location errors occur in EEG dipole source analysis. When EEG source analysis is performed with an ideal head model and an ideal source, then the so-called unbiased estimator is applied. Unbiased estimators give dipole position errors due to noise only. This is in contrast with a biased estimator such as the spherical head model, which gives dipole position errors due to noise but also due to the usage of a simplified volume conductor model.

To calculate the position error due to noise, different techniques can be found in the literature. In [72], the Cramer-Rao lower bound estimator is derived to provide a lower bound on the average position error and on the variance of the dipole position error due to additive Gaussian noise. Position errors due to biased estimators are not included in their study. The error bounds are presented for EEG and MEG measurements and for several sensor configurations among which the 10 - 20 system and 127 sensors covering the upper hemisphere.

Local linearization [39, 92], can also be used to calculate the average position error due to additive noise. This technique is used in this chapter and is

explained next.

The local linearization of the forward problem

The potential U_{ij} at electrode $i = 1, ..., l$ with l being the number of electrodes, and at time instance $j = 1, ..., s$ with s the number of time samples, is obtained by the non-linear forward function:

$$U_{ij} = f_{ij}(x, y, z, d_x, d_y, d_z, m_2, ..., m_s), \text{ with } \begin{matrix} i = 1, ..., l, \\ j = 1, ..., s. \end{matrix}$$

We have assumed that the dipole coordinates x, y and z are fixed for all time samples. Furthermore, d_x, d_y and d_z are the dipole components of the first time sample. The orientation of the dipole stays fixed for all the time samples but the dipole magnitude can change as a function of time. The absolute dipole moment M_j at time instance j becomes, $m_j \|[d_x d_y d_z]\|$, where m_j is the relative dipole moment and $\|\cdot\|$ is the Euclidian norm. For s time samples we have $s + 5$ dipole parameters, which are rewritten as $p_1, ..., p_{s+5}$. For small deviations of the dipole parameters $\Delta p_1, ..., \Delta p_{s+5}$, the deviation in scalp potential ΔU_{ij} becomes, utilizing the first order terms of the Taylor expansion :

$$\Delta U_{ij} = \sum_{k=1}^{s+5} D_{ijk} \Delta p_k, \text{ with } \begin{matrix} i = 1, ..., l, \\ j = 1, ..., s, \end{matrix} \tag{5.1}$$

where

$$D_{ijk} = \frac{\partial U_{ij}}{\partial p_k}|_{p_1,...,p_{s+5}} \text{ with } \begin{matrix} i = 1, ..., l, \\ j = 1, ..., s, \\ k = 1, ..., s + 5. \end{matrix}$$

For each of the $l.s$ electrode potentials a linear equation (5.1) can be written. Hence an over determined linear system of $l.s$ equations and $s + 5$ unknowns is obtained. In matrix and vector notation we can write,

$$\mathbf{\Delta U} = \mathbf{D} \cdot \mathbf{\Delta p}, \tag{5.2}$$

where

$$\mathbf{\Delta U} = \begin{pmatrix} \Delta U_{11} \\ \vdots \\ \Delta U_{l1} \\ \vdots \\ \Delta U_{1s} \\ \vdots \\ \Delta U_{ls} \end{pmatrix} \in \mathbb{R}^{(l.s)\times 1}, \ \mathbf{D} = \begin{pmatrix} D_{1\,1\,1} & \cdots & D_{1\,1\,s+5} \\ \vdots & \vdots & \vdots \\ D_{l\,1\,1} & \cdots & D_{l\,1\,s+5} \\ \vdots & \vdots & \vdots \\ D_{1\,s\,1} & \cdots & D_{1\,s\,s+5} \\ \vdots & \vdots & \vdots \\ D_{l\,s\,1} & \cdots & D_{l\,s\,s+5} \end{pmatrix} \in \mathbb{R}^{(l.s)\times(s+5)},$$

and $\mathbf{\Delta p} \in \mathbb{R}^{(s+5)\times 1}$. The linear system (5.2) can be solved for $\mathbf{\Delta p}$ in a least-squares sense, utilizing the Penrose-Moore pseudo inverse [29]:

$$\mathbf{\Delta p} = (\mathbf{D^T D})^{-1}\mathbf{D^T} \cdot \mathbf{\Delta U}, \tag{5.3}$$

where ^{T} denotes the transpose operator.

For a given noise contribution $\mathbf{\Delta U}$, we obtain with equation (5.3) the deviation in dipole parameters and subsequently the deviation in dipole position parameters. The inverse problem is solved through a matrix multiplication as illustrated in equation (5.3). This is much faster than the classical method (see section 2.8) where the dipole parameters are iteratively adjusted until a cost-function is minimized To calculate the average dipole position error for a larger number of noisy potentials generated from one noiseless potential, equation (5.3) can be reapplied.

However we have to investigate whether the local linearization is still a good approximation for the noise values in our study. It is expected that the larger the noise values, the poorer the local linearization will perform. We come back to this issue in section 5.4.

5.2.3 The noise level

An important measure is the noise level. It gives us an idea of the amount of noise that occurs in the EEG signal applied to perform EEG source analysis. The noise level (nl) reads,

$$nl = \frac{U^b_{RMS}}{U_{RMS}}.$$

To have an idea of the signal contribution the root-mean-square (RMS) value U_{RMS} is calculated for the average referenced epoch of EEG, applied to solve the inverse problem. This epoch consists of s time samples and l electrode potentials. U_{ij} is the potential at electrode i and time sample j. The RMS value then becomes,

$$U_{RMS} = \sqrt{\frac{1}{l.s}\sum_{j=1}^{s}\sum_{i=1}^{l} U_{ij}^2}. \tag{5.4}$$

Figure 5.1 shows a 10 s EEG. At 5.5 s a spike occurs. Typically an epoch around the peak activity is used to perform EEG dipole source analysis.

To have an idea of the noise contribution, we can calculate the RMS value of the average referenced EEG prior to the spike. For the EEG presented in figure 5.1 we can for example apply the 5 first seconds of EEG with s_b time

samples. $U_{ij,b}$ is the background EEG at electrode i and time sample j. The RMS value of the background EEG then becomes,

$$U^b_{RMS} = \sqrt{\frac{1}{l.s_b}\sum_{j=1}^{s_b}\sum_{i=1}^{l} U^2_{ij,b}}. \tag{5.5}$$

For spikes the noise level typically equals 0.2. A patient can have several spikes coming from the same brain area. Aligning the peak activity and summing the corresponding potentials, is done to reduce the noise level. The resulting EEG is often called an averaged spike. The noise level of an averaged spike typically equals 0.1. In chapter 6 the noise level is calculated for real data.

In this chapter we use the first 5 s (or 1000 samples) of the EEG presented in figure 5.1 as background EEG. The signal contribution U_{RMS} is simulated. The potentials are obtain by a forward calculation in a realistic head model.

We also apply Gaussian noise. We assume that Gaussian noise is not correlated between the different scalp electrodes. Furthermore the noise values at successive time samples are also not correlated. Hence we use spatially and temporally white zero mean Gaussian noise with a standard deviation of $\mathcal{N}$. The noise level then becomes:

$$nl = \frac{\mathcal{N}}{U_{RMS}},$$

Notice that for a certain dipole magnitude, a superficial source gives a larger U_{RMS} than a deeper source. Subsequently when noise with a certain RMS-value is added to both signals, the noise level of a deeper source is higher than that of the superficial source. In this chapter we investigate the dipole location errors for a given set of test dipoles as a function of the noise levels. For a given noise level, a superficial test dipole has then a dipole magnitude which is smaller than the one of deeper test dipole. We have to keep this in mind while reading the results presented in this chapter.

5.3 Methods

5.3.1 The electrode positions, the realistic and spherical head model

In our simulations, the scalp electrodes are placed following the 10-20 international system, with three electrodes on each of the inferior temporal regions

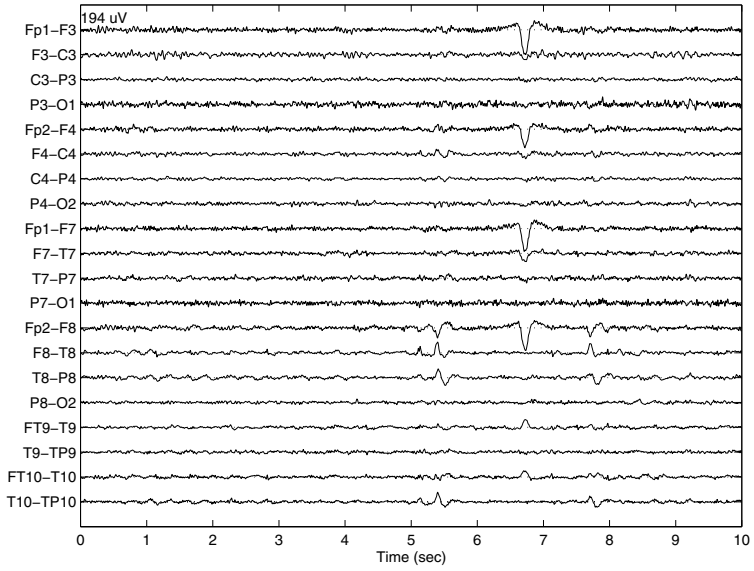

Figure 5.1: A 10 sec epoch of a 27 channel EEG in a bipolar montage. The first 5 s or the first 1000 samples are used as background activity in our simulations.

adding up to 27 electrodes, illustrated as '*' in figure 5.2. To have a higher spatial sampling of the potentials at the scalp, 17 additional electrodes are placed, illustrated as '$\circ$' in figure 5.2.

A 3D, T1-weighted magnetic resonance (MR) image of the human head (voxel size of 1 mm^3) is transformed utilizing the SPM segmentation tool [3] in a ventricular system, a brain, a skull, and a scalp region, having relative conductivities of 8, 1, 1/16 and 1, respectively. More details on the geometrical construction of the realistic head model and the choice of the conductivity values can be found in section 4.4.

The segmented regions obtained from the MR images are used to generate a cubic grid with a cube side equal to 2 mm. Each cube is allocated a specific conductivity, depending on the region in which it is located. The obtained VCM of the human head consists of about a half million cubes. The finite difference method in combination with the reciprocity theorem is utilized to solve the forward problem in the realistic head model. Subsection 2.7.6 and appendix B give further details on the finite difference method and on the reciprocity theorem, respectively.

The spherical head model is constructed as follows. Through the 27 or 44 electrode nodes located at the scalp surface, used in the finite difference

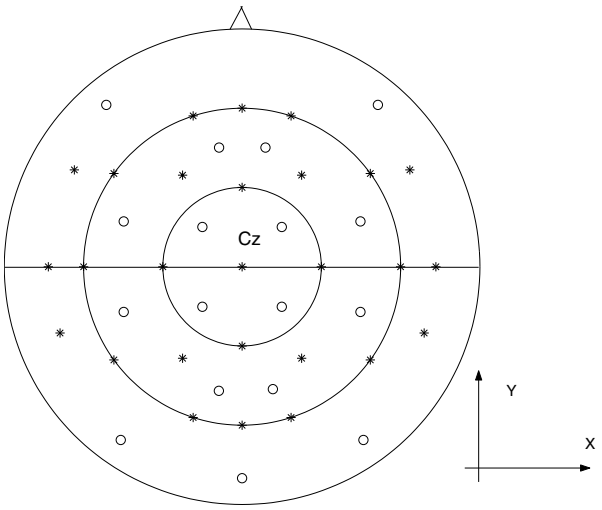

Figure 5.2: Top view of the electrode positions is given. The large circles are positions with a constant azimuthal angle θ. From the inner to the outer circle we have a θ of $45°$, $90°$ and $120°$, respectively. The 27 electrodes '$*$' and the additional 17 electrodes '$\circ$' are also illustrated. The coordinate axes are also shown. The line parallel with the x-axis and going through the center of the circles represents the slice containing the test dipoles.

volume conductor model, a best-fitting sphere is constructed with a radius R. A radial projection of the electrodes on the surface of the sphere is performed to obtain the electrode coordinates in the spherical head model. The radii of the outer shell of the scalp, skull and brain are R, $\frac{85}{92}R$ and $\frac{80}{92}R$, respectively. The conductivity of the brain and scalp regions is then set 16 times larger than the conductivity of the skull region. The conductivity ratio between the soft tissue and the skull is then equal to the one used in the realistic head model. The ventricular system is not incorporated in the three-shell spherical head model.

The construction of the realistic head model is more demanding than the construction of the spherical head model. When applying the spherical head model, the electrode positions need to be obtained to construct the best-fitting sphere. In contrast, when applying a realistic head model, the segmented MR-image needs to be constructed, the electrode positions need to be obtained and the numerical preprocessing needs to be performed. All these steps need user interaction. It is clear that the latter is more demanding.

5.3.2 Setup of the simulations

The construction of $E(\Delta r_i^{sphere})$, $E(\Delta r_i^{real})$ and ΔR

Figure 5.3 illustrates the steps taken to calculate the dipole position errors applying the spherical and realistic head model. For a given test dipole, with dipole position $\mathbf{r}$ and orientation $\mathbf{d}$, the forward problem is solved in a realistic head model, yielding a set of average referenced scalp potentials. With these potentials, the inverse problem is solved in a spherical head model yielding dipole position $\mathbf{r}_{sphere}$ and orientation $\mathbf{d}_{sphere}$. In figure 5.4 the dipole position $\mathbf{r}_{sphere}$ is marked with a '$\circ$'. A local linearization of the forward problem with the spherical head model at these dipole parameters is then performed. This gives us the opportunity to solve for the deviations of the dipole positions $\mathbf{\Delta r}^{\mathbf{sphere}}_{\mathbf{noise,\,i}}$ as a function of the noise values at the electrodes. Furthermore, $\mathbf{\Delta r}^{\mathbf{sphere}}_{\mathbf{noise,\,i}}$ is a subset of $\mathbf{\Delta p}$ in equation (5.3). These results are obtained with a matrix multiplication, which is faster than solving the inverse problem iteratively. Here $i = 1, \ldots, 1000$ is the index corresponding with one of the 1000 noisy potential sets. The noise values added to the noiseless potentials, come from a zero mean Gaussian distribution or from average referenced background EEG. The fitted dipole position $\mathbf{\Delta r}^{\mathbf{sphere}}_{\mathbf{noise,i}} + \mathbf{r}_{\mathbf{sphere}} + \mathbf{r}$ is marked with '#' in figure 5.4. The position error due to noise and due to the spherical head model then becomes: $\Delta r_i^{sphere} = \|\mathbf{\Delta r}^{\mathbf{sphere}}_{\mathbf{noise,\,i}} + \mathbf{r}_{\mathbf{sphere}} - \mathbf{r}\|$, where $\|\cdot\|$ is the Euclidian norm. Δr_i^{sphere} corresponds with the length of line (a) in figure 5.4. For the 1000 noisy potentials sets, we obtain the average position error

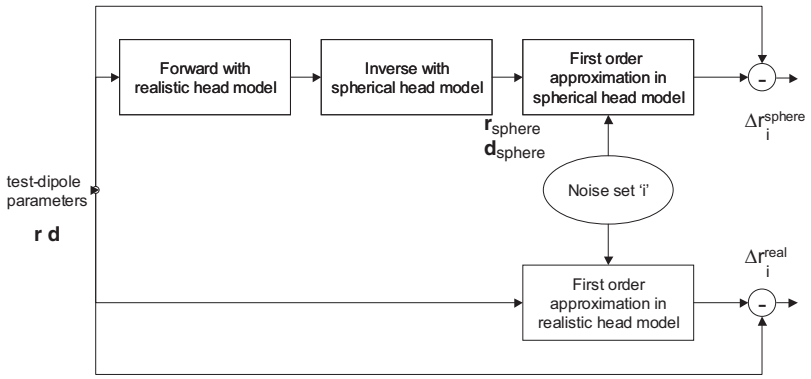

Figure 5.3: A flowchart of the steps taken.

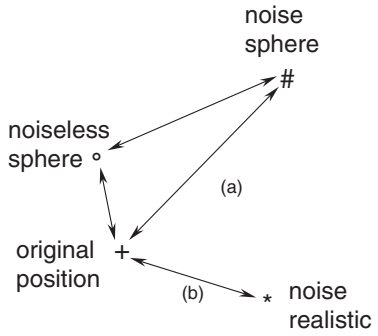

Figure 5.4: A schematic representation of the dipole position errors.

$E(\Delta r_i^{sphere})$.

The deviation of the dipole coordinates, Δr_i^{real}, due to noise when utilizing a realistic head model, is calculated in a similar way. A local linearization of the forward problem with the realistic head model at the test dipole position $\mathbf{r}$ and orientation $\mathbf{d}$, is performed. The position error due to noise then becomes: $\Delta r_i^{real} = \|\mathbf{\Delta r^{real}_{noise,\,i}}\|$, where $\mathbf{\Delta r^{real}_{noise,\,i}}$ is the deviation from the test dipole position for a given set of noise values. The fitted position is then given by $\mathbf{\Delta r^{real}_{noise,\,i}} + \mathbf{r}$ and is marked with '*' in figure 5.4. Δr_i^{real} is represented with the length of line (b). For the same 1000 noisy potential sets as in the spherical head model case we then calculate the average position error, $E(\Delta r_i^{real})$.

The smaller the average dipole position error, the better a model performs. Furthermore we notice that $E(\Delta r_i^{sphere})$ is larger than $E(\Delta r_i^{real})$.

When $E(\Delta r_i^{sphere})$ is much larger than $E(\Delta r_i^{real})$, for a certain noise

level, then it is worthwhile using the realistic head model instead of the spherical head model. On the other hand, when $E(\Delta r_i^{sphere})$ has about the same value as $E(\Delta r_i^{real})$, then it does not matter whether a realistic or a spherical head is used. Therefore, the difference between the two average position errors $\Delta R = E(\Delta r_i^{sphere}) - E(\Delta r_i^{real})$ is introduced.

The validation of the local linearization

A first simulation is carried out to evaluate the local linearization for one test dipole. We have calculated $E(\Delta r_i^{sphere})$ and $E(\Delta r_i^{real})$ for several noise levels and for 1000 noisy potential distributions, utilizing the local linearization. On the other hand we have calculated, for the same noisy scalp potentials, the inverse problem on an iterative bases in a spherical and realistic head model. This approach is often called a Monte-Carlo simulation. The average position errors are derived and compared to the ones found utilizing the local linearization.

The construction of quantitative parameters

In this simulation study, 472 test dipole positions located in a coronal slice containing the vertex electrode 'Cz', are used. For each test position a dipole along the x-, y-, and z-axis is generated yielding 1416 test dipoles. The x-axis is oriented from the left towards the right ear, the y-axis is oriented from the back of the head towards the nose, and the z-axis is oriented from the bottom of the head towards the vertex electrode 'Cz'.

The grand average over the 1416 test dipoles of $E(\Delta r_i^{sphere})$, $E(\Delta r_i^{real})$ and ΔR is investigated for different noise levels.

We further suggest that a ΔR smaller than 5 mm indicates that for a given dipole and for a given noise level both models, the spherical and the realistic head model perform equally well. On the other hand when ΔR is larger than 5 mm for a given dipole and for a given noise level we argue that in this case the realistic head model performs better than the spherical model. The 5 mm threshold is arbitrarily chosen.

To have a more quantitative measure for a given noise level, the number of test dipoles which have a ΔR larger than the chosen 5 mm are counted. This gives us the opportunity to investigate, for a given noise level and for a large number of test dipoles, whether it is still worthwhile utilizing the more demanding realistic head model, instead of the spherical head model.

The configurations applied

There are five configurations under investigation. And for each of these configurations the aforementioned variables are calculated.

- In configuration 27el-1s-Gauss, 27 scalp electrodes, an EEG epoch of one time sample and Gaussian noise is used.
- In configuration 44el-1s-Gauss, 44 scalp electrodes, an EEG epoch of one time sample and Gaussian noise is used. The results utilizing this configuration are compared to results obtained in configuration 27el-1s-Gauss.
- In configuration 27el-6s-Gauss, 27 scalp electrodes, an EEG epoch of six time samples and Gaussian noise is used. The epoch of six time samples consists of six times the same noiseless potential distribution from the same test dipole with spatially and temporally white Gaussian noise superposed. As such, a block-function superposed with noise is used. Notice that we assume that only one focal source is active during this time interval. The results obtained here are again compared to the ones found utilizing configuration 27el-1s-Gauss.
- In configuration 27el-1s-background, 27 scalp electrodes, an EEG epoch of one time sample and background EEG is used. The results for utilizing this configuration are again compared to the ones of configuration 27el-1s-Gauss.
- And finally in configuration 27el-6s-background, 27 scalp electrodes, an EEG epoch of six time samples and background EEG is used. The results obtained here are compared to the ones of configuration 27el-6s-Gauss. To the six equal noiseless potentials, background EEG is added, composed of six successive time samples. As such, a block-function superposed with background EEG is used.

5.4 Validation of the local linearization

The performance of the local linearization is evaluated for one test dipole. The average position errors obtained with Monte-Carlo simulations are derived and compared to the ones found utilizing the local linearization.

The solid line in figure 5.5 presents $E(\Delta r_i^{real})$, as a function of the noise level. These values are obtained by applying the local linearization. The dashed line in figure 5.5 corresponds with $E(\Delta r_i^{sphere})$ obtained with the local

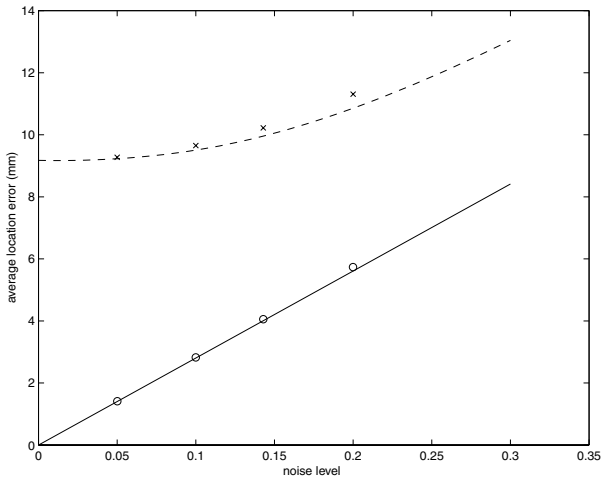

Figure 5.5: The solid line (-) and the dashed line (- -) depict the average dipole position error as a function of the noise level obtained with the local linearization of the forward function when utilizing a realistic and spherical head model, respectively. The ($\circ$) and ($\times$) present the average dipole position errors obtained with a Monte-Carlo simulation, for noise levels 0.05, 0.1, 0.14, and 0.2, utilizing the realistic and spherical head model, respectively.

linearization. When the noise level is zero, the solid line gives no average position error while the dashed line gives an average position error corresponding with the dipole fit of the biased estimator. The '$\circ$' depicts the average position errors obtained from a Monte-Carlo simulation for the noise levels 0.05, 0.1, 0.14 and 0.2, utilizing the realistic head model. The '$\times$' depicts the average position errors obtained from a Monte-Carlo simulation, utilizing a spherical model. One notices that the average position errors obtained with the Monte-Carlo simulation correspond well with the values obtained through local linearization, and this even for large noise levels. It can also be observed that by increasing the noise level the value of $\Delta R = E(\Delta r_i^{sphere}) - E(\Delta r_i^{real}$ decreases.

Each dot in figure 5.6(a) presents the result of the Monte-Carlo simulation for the dipole located at position '$+$' and orientation along the x-axis. The inverse problem is solved in the realistic head model and the noise level is 0.14. Figure 5.6(b) presents the result of the Monte-Carlo simulation, utilizing the spherical head model in the inverse solver, with the same noise level. The fitted position utilizing the spherical head model with the noiseless potentials is given by '$\times$'. It can be observed that the cloud of dots is centered on the

fitted position '$\times$'.

5.5 Simulations with Gaussian noise

5.5.1 Results for configuration 27el-1s-Gauss

First the average position error $E(\Delta r_i^{sphere})$ for different noise levels is illustrated as a function of the dipole position and orientation in figure 5.7. The first, second and third column present the results for dipoles oriented along the x-, y-, and z-axis, respectively. The color scale indicates the average position error. The first, second, third and fourth row in figure 5.7 present the value $E(\Delta r_i^{sphere})$ for the noise level equal to 0, 0.05, 0.1 and 0.2, respectively. One can observe that $E(\Delta r_i^{sphere})$ for a given noise level not only depends on the dipole position but also on the dipole orientation. Notice further that when no noise is added, a dipole position error occurs for most of the test dipoles. This is due to the use of the spherical head model, a biased estimator. However, for other test dipoles, for example the larger part of the test dipoles oriented along the z-axis, a small dipole position error occurs in the noiseless case. This indicates that for these dipole parameters, both models, the spherical and realistic head model, perform equally well. Furthermore, it is observed that $E(\Delta r_i^{sphere})$ for all test dipoles increases when increasing the noise level.

Next the average position error $E(\Delta r_i^{real})$ is presented in a similar way. Notice that for a zero noise level no average position error is found. This is due to the fact that we have assumed that the realistic head model is an unbiased estimator. Subsequently, when no noise is added, no position error is observed. Apart of being dependent of the dipole position, the average position error $E(\Delta r_i^{real})$ also depends on the orientation. One can again notice that $E(\Delta r_i^{real})$ increases with increasing noise level.

Above, we have observed that $E(\Delta r_i^{sphere})$ and $E(\Delta r_i^{real})$ increase with the noise level. Now we investigate how ΔR changes as a function of the noise level. The first, second, third and fourth row in figure 5.9 present the value $\Delta R = E(\Delta r_i^{sphere}) - E(\Delta r_i^{real})$ for a noise level equal to 0, 0.05, 0.1 and 0.2, respectively. A contour with ΔR equal to 5 mm is also given. For a noise level of zero ΔR equals $E(\Delta r_i^{sphere})$. By increasing the noise level the ΔR values decrease for all test dipoles. Hence the areas where ΔR is larger than 5 mm decrease when increasing the noise level. Notice too that large areas can be found where ΔR is smaller than 5 mm for dipoles oriented along the y- and z-axis, and for noise levels from 0.05 and higher.

In table 5.1, the grand average over the 1416 test dipoles of $E(\Delta r_i^{sphere})$, $E(\Delta r_i^{real})$ and ΔR is presented for all configurations considered. The sub-

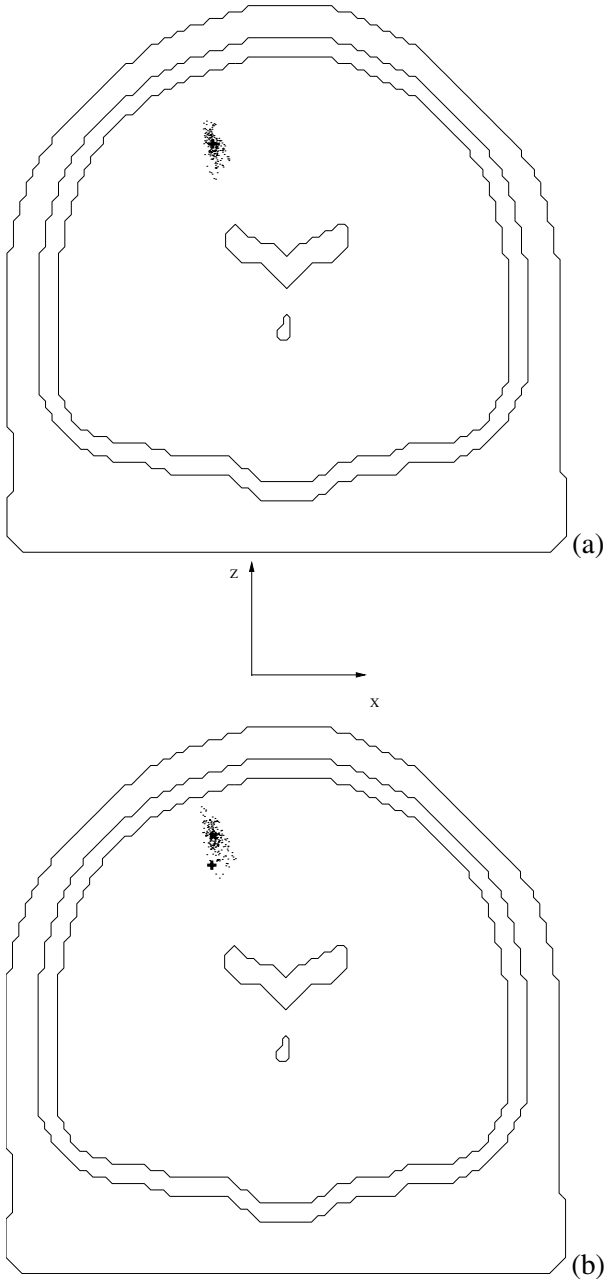

Figure 5.6: Each dot presents the result of a dipole fit performed with the realistic (a) and spherical head model (b). The noise level is 0.14, Gaussian noise and 27 electrodes are used. The '+' indicates the position of the test dipole, which is oriented along the x-axis. The '$\times$' indicates the fitted position in the noiseless case utilizing the spherical head model.

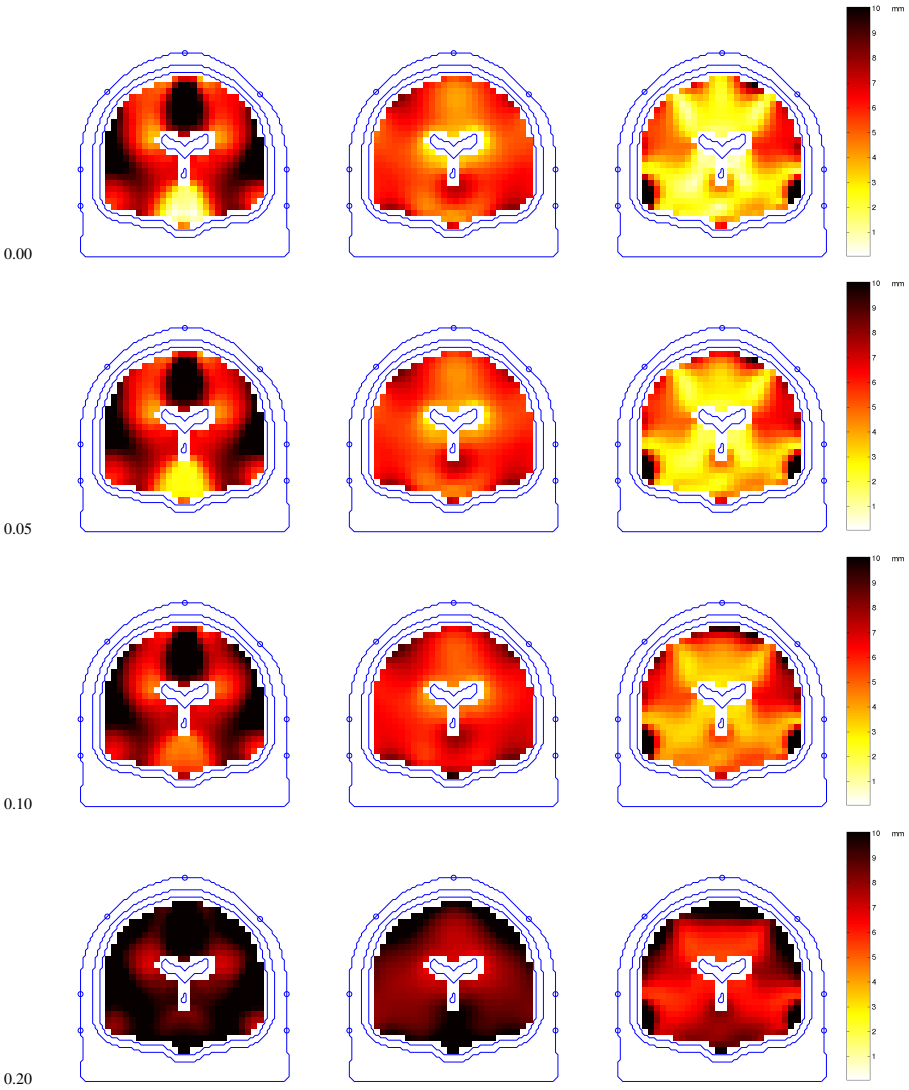

Figure 5.7: The first, second, third and fourth row illustrate $E(\Delta r_i^{sphere})$ for noise levels equal to 0, 0.05, 0.1 and 0.2, respectively. The configuration 27el-1s-Gauss is used. The first, second, and third column present the results for dipoles oriented along the x-, y-, and z-axis, respectively.

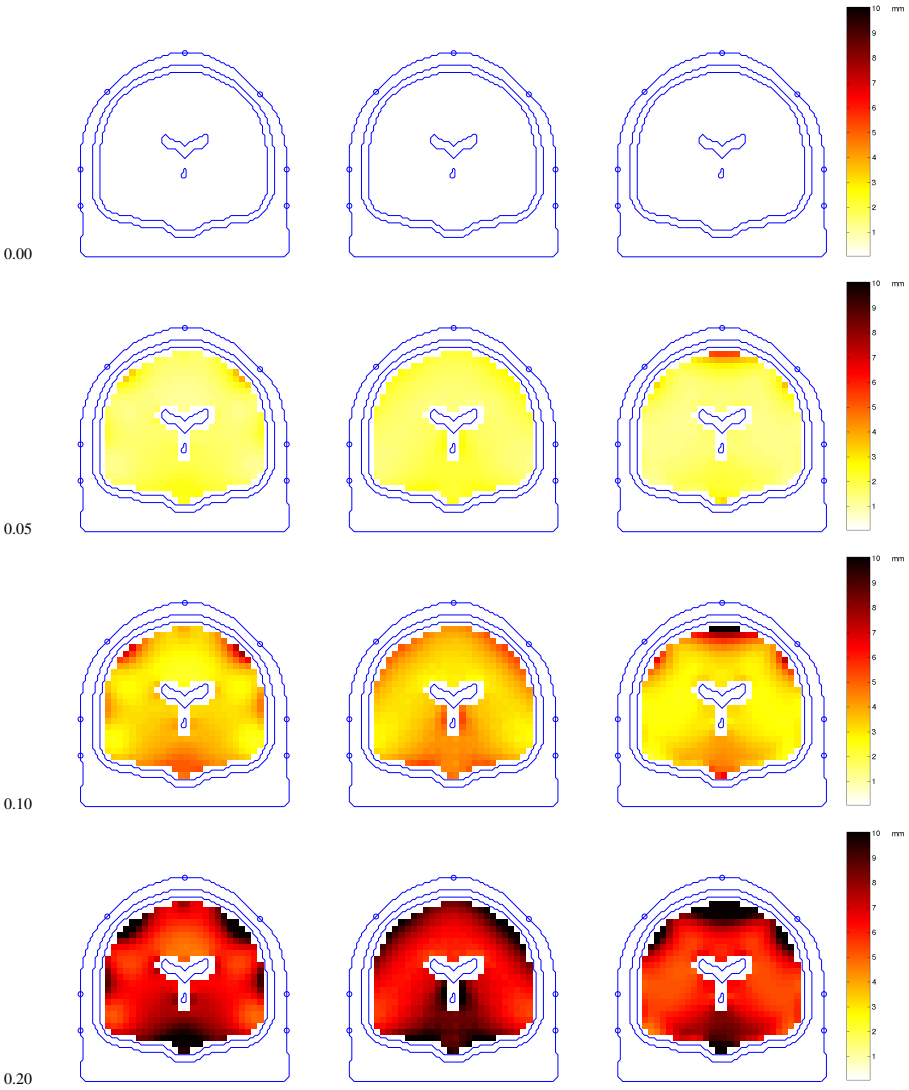

Figure 5.8: The first, second, third and fourth row illustrate $E(\Delta r_i^{real})$ for noise levels equal to 0, 0.05, 0.1 and 0.2, respectively. The configuration 27el-1s-Gauss is used. The first, second, and third column present the results for dipoles oriented along the x-, y-, and z-axis, respectively.

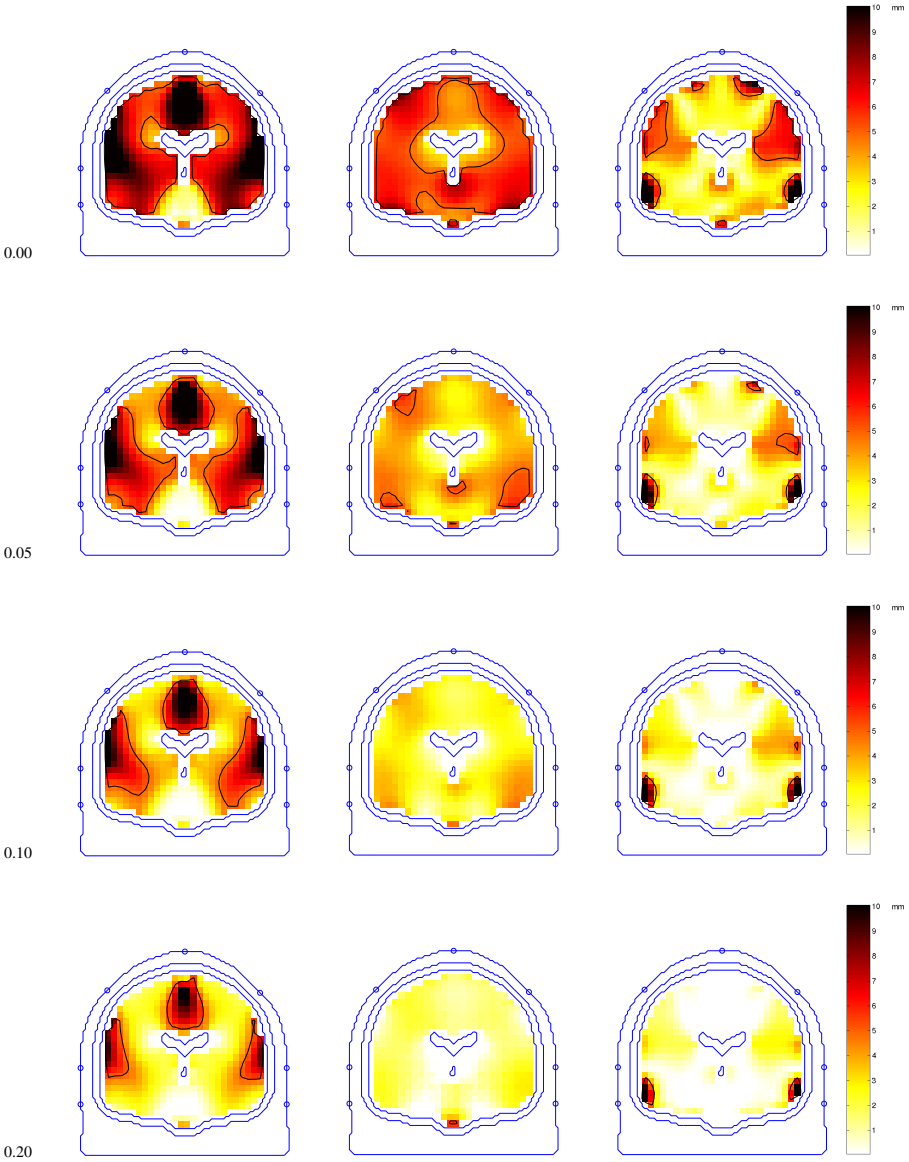

Figure 5.9: The first, second, third and fourth row illustrate $\Delta R = E(\Delta r_i^{sphere}) - E(\Delta r_i^{real})$ for noise levels equal to 0, 0.05, 0.1 and 0.2, respectively. A contour with ΔR equal to 5 mm is also given. The configuration 27el-1s-Gauss is used. The first, second, and third column present the results for dipoles oriented along the x-, y-, and z-axis, respectively.

table marked with 27el-1s-Gauss gives the variables for the configuration at hand. The grand average of $E(\Delta r_i^{sphere})$, marked with A_s, in the noiseless case is 5.5 mm. For a noise level of 0.2, the grand average has increased to 9.0 mm. Notice that the grand average of Δr_i^{real}, marked with A_r, for the noise level of 0.2, 7.2 mm is twice the value given for a noise level 0.1, which is 3.6 mm. This can be explained as follows: Δr_i^{real}, the distance between the fitted and original dipole position, is proportional to the noise values as illustrated in equation (5.3). These noise values on their turn are proportional to the noise level. Subsequently, the position error Δr_i^{real} is proportional with the noise level. Hence, the average position error $E(\Delta r_i^{real})$ is proportional with the noise level. Moreover, the grand average over all the test dipoles of $E(\Delta r_i^{real})$ is proportional with the noise level. The grand average over all test dipole positions of ΔR is presented in the column marked with $A_{\Delta R}$. Notice that $A_{\Delta R}$ equals to $A_s - A_r$. It can be observed that by increasing the noise level the grand average of ΔR, decreases from 5.5 mm to 1.8 mm.

In table 5.1, the relative number of ΔR values larger than 5 mm, marked with '# $>$ 5 mm', are given for the applied noise levels. Notice that for configuration 27el-1s-Gauss, 60% of the test dipoles have a ΔR larger than 5 mm for the noiseless case. For the averaged spikes the noise level is typical of the order of 0.1. For this noise level, 13.4% of the test dipoles in our simulation have a ΔR larger than 5 mm. This number decreases to 7.6% for a noise level of 0.2, which corresponds with an unaveraged epileptic spike.

As a conclusion we can state that, the higher the noise level, the less important becomes the usage of the realistic head model over the spherical head model.

5.5.2 Results for configuration 44el-1s-Gauss

In figure 5.10, ΔR is presented in the first and second row for a noise level equal to 0 and 0.1, respectively, utilizing configuration 44el-1s-Gauss. It can be observed, for a noise level equal to zero, by comparing the first row of figure 5.10 with the first row of figure 5.9, that the $\Delta R = E(\Delta r_i^{sphere})$ decreases for several test dipoles. Hence, by increasing the number of electrodes the spherical head model will yield smaller dipole position errors in the noise-free case for certain test dipoles, but not systematically for all test dipoles. This result was also found in [145]. It can be observed, when comparing the second row of figure 5.10 with the third row of figure 5.9, that for some test dipoles ΔR is larger and for others ΔR is smaller when utilizing 44 electrodes instead of 27 electrodes.

The alteration of ΔR values by increasing the number of electrodes and

noise level	27el-1s-Gauss			
	A_s(mm)	A_r(mm)	$A_{\Delta R}$(mm)	# $>$ 5 mm(%)
0.0	5.5	0.0	5.5	60.0
0.05	5.8	1.8	4.0	25.5
0.1	6.6	3.6	3.1	13.4
0.2	9.0	7.2	1.8	7.6
noise level	44el-1s-Gauss			
	A_s(mm)	A_r(mm)	$A_{\Delta R}$(mm)	# $>$ 5 mm(%)
0.0	4.7	0.0	4.7	43.7
0.05	4.8	1.0	3.8	26.6
0.1	5.1	2.1	3.0	14.8
0.2	6.3	4.3	2.0	6.5
noise level	27el-6s-Gauss			
	A_s(mm)	A_r(mm)	$A_{\Delta R}$(mm)	# $>$ 5 mm(%)
0.0	5.5	0.0	5.5	60.0
0.05	5.6	0.7	4.9	44.5
0.1	5.7	1.4	4.3	31.0
0.2	6.2	2.9	3.3	16.1
noise level	27el-1s-background			
	A_s(mm)	A_r(mm)	$A_{\Delta R}$(mm)	# $>$ 5mm(%)
0.0	5.5	0.0	5.5	60.0
0.05	5.9	2.0	3.9	23.4
0.1	6.8	4.0	2.8	11.2
0.2	9.7	8.0	1.7	4.5
noise level	27el-6s-background			
	A_s(mm)	A_r(mm)	$A_{\Delta R}$(mm)	# $>$ 5mm(%)
0.0	5.5	0.0	5.5	60.0
0.05	5.7	1.6	4.1	28.6
0.1	6.3	3.2	3.1	13.9
0.2	8.3	6.4	1.9	6.3

Table 5.1: Grand average over all test dipoles for $E(\Delta r_i^{sphere})$ (A_s), $E(\Delta r_i^{real})$ (A_r) and ΔR ($A_{\Delta R}$). Furthermore the relative number of test dipoles yielding a ΔR larger than 5 mm (# $>$ 5 mm), is also given. These values are given for all the applied configurations. The noise levels 0, 0.05, 0.1 and 0.2 are considered.

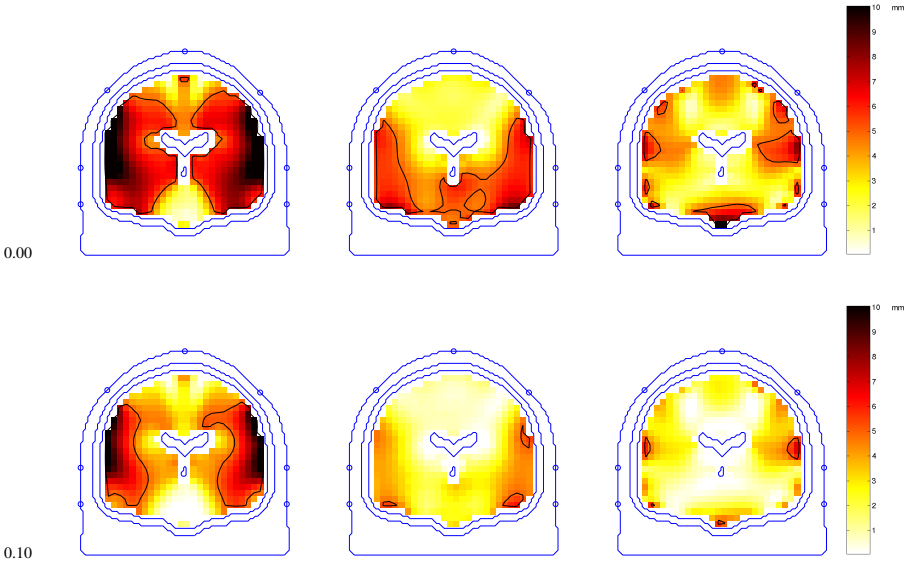

Figure 5.10: The first and second row illustrate $\Delta R = E(\Delta r_i^{sphere}) - E(\Delta r_i^{real})$ for the noise levels 0 and 0.1, respectively. A contour with ΔR equal to 5 mm is also given. The configuration 44el-1s-Gauss is used. The first, second, and third column present the results for dipoles oriented along the x-, y-, and z-axis, respectively.

for the given test dipoles can then be divided in two groups. Figure 5.11(a) illustrates a typical example of a test dipole where a reduction in ΔR can be observed. The solid and dashed curves depict $E(\Delta r_i^{real})$ and $E(\Delta r_i^{sphere})$ as a function of the noise level, for 27 and 44 electrodes, respectively. For a given noise level, the systematic reduction of $E(\Delta r_i^{real})$ is observed by increasing the number of electrodes. But for the same noise level an even larger reduction is observed for $E(\Delta r_i^{sphere})$. Hence for this test dipole the ΔR value decreases by increasing the number of electrodes. In figure 5.11(b) a typical example is given for a test dipole belonging to the other group in which an increase of ΔR can be found. Here again a reduction of $E(\Delta r_i^{real})$ is observed by increasing the number of electrodes, for a given noise level. However, a smaller reduction of $E(\Delta r_i^{sphere})$ is observed. This yields a ΔR which is larger than for 27 electrodes.

In table 5.1 the subtable marked with 44el-1s-Gauss gives the variables for the configuration at hand. We notice that the grand average of $E(\Delta r_i^{sphere})$ over all test dipoles, again marked with A_s, reduces compared to the one found for 27el-1s-Gauss. This is in concordance with the results found by comparing figures 5.9 and 5.10 for the noiseless case.

It was found in [67] that by increasing the number of electrodes, the position error due to Gaussian noise decreases proportionally to one over the square root of the number of sensors. Hence by increasing the number of electrodes, $E(\Delta r_i^{real})$ decreases for a given noise level. This can be observed by comparing the grand average of $E(\Delta r_i^{real})$, marked with A_r in table 5.1, in the subtables 27el-1s-Gauss and 44el-1s-Gauss. It is noticed that the grand average values of ΔR, marked $A_{\Delta R}$ in table 5.1, do not change much for a given noise level with the values found with 27el-1s-Gauss. Finally, for a noise level equal to zero, the number of dipoles having a $\Delta R = E(\Delta r_{sphere})$ larger than 5 mm in table 5.1, are reduced from 60 % for 27 electrodes to 43.7 % for 44 electrodes. However, in the presence of noise this number does not change so much between the configurations.

As a conclusion we can state that increasing the number of electrodes from 27 to 44 does not increase the advantage of the usage of a realistic over the spherical head model when dipole source analysis is performed.

5.5.3 Results for configuration 27el-6s-Gauss

Figure 5.12 gives the ΔR values for a noise level 0.1, 27 electrodes, an epoch of six time samples and Gaussian noise as a function of the dipole position. By comparing figure 5.12 with the third row of figure 5.9, it is found that the ΔR values increase when increasing the number of samples.

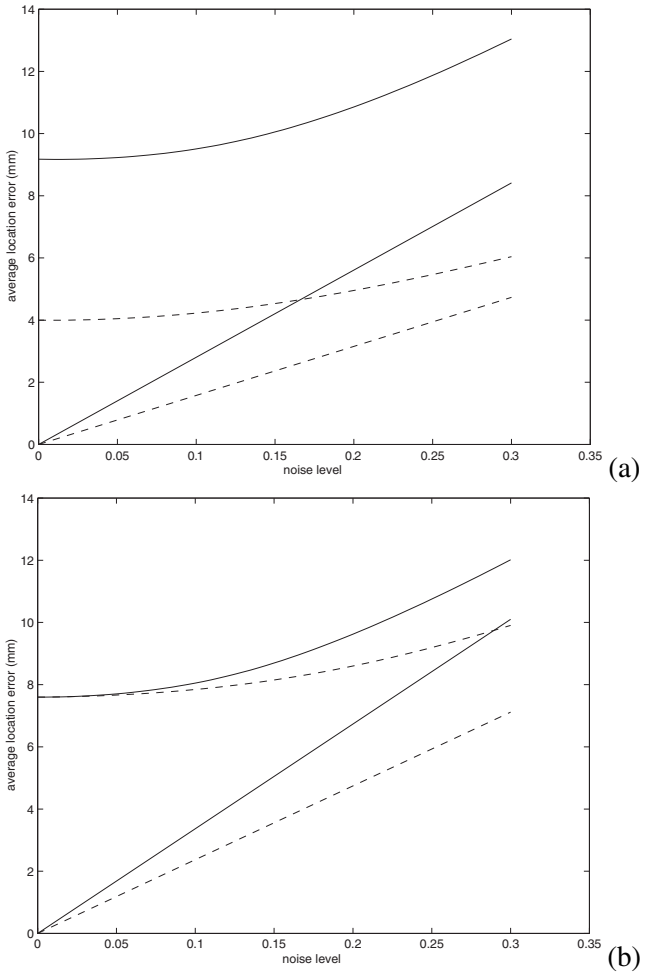

Figure 5.11: The solid curves (-) in (a) and (b) present $E(\Delta r_i^{sphere})$ and $E(\Delta r_i^{real})$ as a function of the noise level, for two different test dipoles, utilizing configuration 27el-1s-Gauss. The dashed curves (- -) in (a) and (b) present again $E(\Delta r_i^{sphere})$ and $E(\Delta r_i^{real})$ for the same test dipoles, utilizing configuration 44el-1s-Gauss. In (a) and (b), ΔR decreases and increases, respectively, when increasing the number of electrodes.

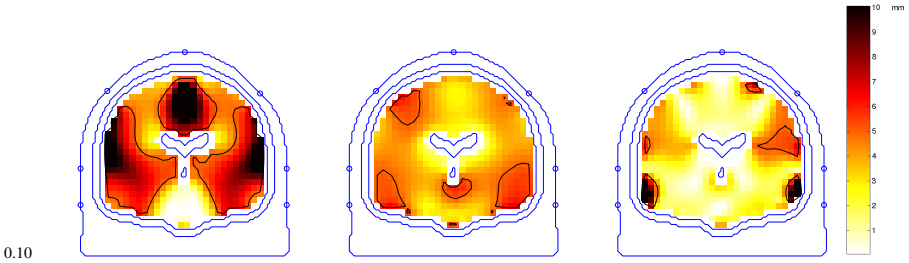

Figure 5.12: The ΔR values are illustrated for a noise level equal to 0.1. A contour with ΔR equal to 5 mm is also given. The configuration 27el-6s-Gauss is used. The first, second, and third column present the results for dipoles oriented along the x-, y-, and z-axis, respectively.

Notice for the noiseless case, that the grand average of $E(\Delta r_i^{sphere})$ and ΔR, found in table 5.1 for the subtable 27el-6s-Gauss are the same as the values found for 27el-1s-Gauss. This means that the performance in the noise-free case of the biased estimator does not improve when increasing the number of time samples in EEG dipole source analysis. For a given noise level the grand average of the $E(\Delta r_i^{sphere})$ values for the configuration 27el-6s-Gauss, is smaller than the ones found for 27el-1s-Gauss. Furthermore, it is known from [36, 115] that the average position error due to temporal white Gaussian noise is proportional to one over the square root of the number of samples for a given noise level. When using 6 time samples, then $E(\Delta r_i^{real})$ is reduced by $1/\sqrt{6} \approx 0.4$, for a given noise level. This can be noticed when comparing the grand average values of $E(\Delta r_i^{real})$ for configuration 27el-6s-Gauss to the ones found for configuration 27el-1s-Gauss. Furthermore it is noticed from table 5.1 that the grand average of ΔR increases when increasing the number of time samples. In table 5.1, it can also be observed that for a non-zero noise level, the number of test dipoles with a ΔR larger than 5 mm increases by increasing the number of time samples. Hence increasing the number of time samples leads to larger areas in the brain where the performance of the realistic head model is superior to the spherical head model.

In figure 5.13 we compare the $E(\Delta r_i^{sphere})$ and $E(\Delta r_i^{real})$ found for one time sample (solid curves) with the ones found for six time samples (dashed curves). $E(\Delta r_i^{sphere})$ and $E(\Delta r_i^{real})$ are given as a function of the noise level. The solid line through the origin corresponds with $E(\Delta r_i^{real})$ as a function of the noise level, for one time sample . The dashed line through the origin corresponds with $E(\Delta r_i^{real})$ as a function of the noise level for six time samples. It

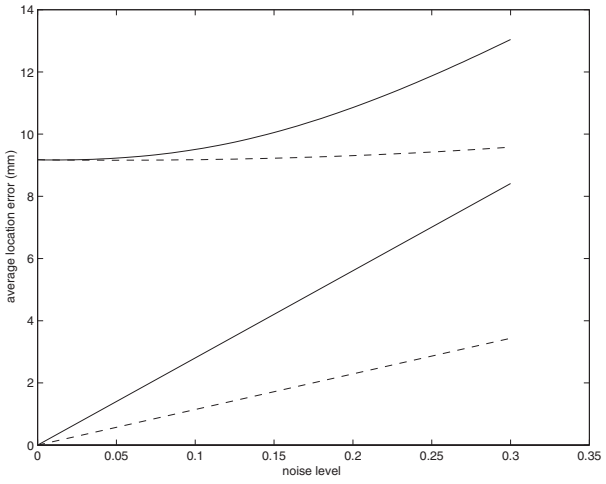

Figure 5.13: The solid curves (-) present $E(\Delta r_i^{sphere})$ and $E(\Delta r_i^{real})$ as a function of the noise level, utilizing configuration 27el-1s-Gauss. The dashed curves (- -) present again $E(\Delta r_i^{sphere})$ and $E(\Delta r_i^{real})$ for the same test dipole, utilizing configuration 27el-6s-Gauss.

can be observed that the dashed line yields a smaller value for $E(\Delta r_i^{real})$ than the solid line and this proportional with $1/\sqrt{6}$. We can also observe by comparing the solid and dashed line not going through the origin, that $E(\Delta r_{sphere})$ also decreases when increasing the number of samples. However, this reduction is much smaller than the reduction found with $E(\Delta r_{real})$, for a given noise level. This leads to an increase of ΔR when increasing the number of time samples, for a given noise level. This is observed for all test dipoles.

From figure 5.13 one can observe that increasing the number of time samples can be seen as having the same effect as decreasing the noise level when utilizing epoch of one time sample. Furthermore from the results found with 27 electrodes and one time sample it was clear that ΔR increases when decreasing the noise level. Subsequently, ΔR increases when increasing the number of time samples.

So, in conclusion, we state that by increasing the number of time samples, the advantage of the realistic over the spherical head model becomes larger.

5.6 Simulation with background EEG

5.6.1 Results for configuration 27el-1s-background

In reality, background EEG, instead of Gaussian noise, is superposed to the noise-free potentials generated from a focal source. Background EEG is spatially correlated. The background EEG is average referenced and normalized. In the subtable marked 27el-1s-background of table 5.1, the results of the configuration considered are presented. It can be observed that the grand averages for $E(\Delta r_i^{sphere})$ and $E(\Delta r_i^{real})$ are somewhat larger than the ones found under 27el-1s-Gauss which utilizes Gaussian noise. This is due to the spatial correlation of the background EEG. A slight reduction of the grand average of ΔR values can be noticed when compared to the same values found under 27el-1s-Gauss, in the presence of noise. The number of dipoles which have a ΔR larger than 5 mm is also reduced when compared to the one found under configuration 27el-1s-Gauss.

In figure 5.14 the $E(\Delta r_i^{sphere})$ and $E(\Delta r_i^{real})$ values are presented as a function of the noise level. The solid curves depict the $E(\Delta r_i^{sphere})$ and $E(\Delta r_i^{real})$ values when Gaussian noise is superposed while the dashed curves show the values when background EEG is superposed. An increase of the average position errors in the spherical and realistic head model can be observed when background EEG is utilized. Correlation in space acts as if the noise level is increased when applying Gaussian noise. And as seen in section 5.5.1, this indicates that ΔR decreases.

So in conclusion we state that background EEG, which is correlated in space, reduces the performance of the realistic head model over the spherical head model compared to Gaussian noise.

5.6.2 Results for configuration 27el-6s-background

Background EEG is also temporally correlated. In other words, there is a strong correlation between the noise values of successive time samples. The subtable marked with 27el-6s-background in table 5.1 shows the values under consideration. The values found for the grand average of $E(\Delta r_i^{sphere})$, $E(\Delta r_i^{real})$ are larger than the ones found for 27el-6s-Gauss. This indicates that the temporal and spatial correlation increase the position error compared to spatial and temporal white Gaussian noise. The grand average of the ΔR values is smaller when utilizing background EEG (subtable 27el-6s-background), then when utilizing Gaussian noise (subtable 27el-6s-Gauss). On the other hand it is noticed that the grand average of $E(\Delta r_i^{sphere})$, $E(\Delta r_i^{real})$ are smaller than the ones found for 27el-1s-background which indicates in its turn

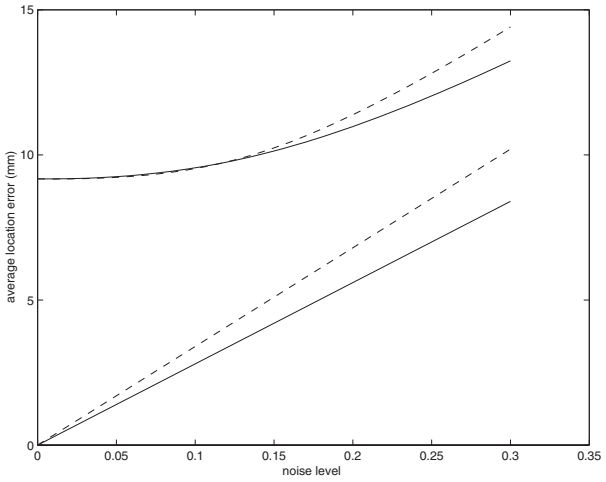

Figure 5.14: The solid curves (-) present $E(\Delta r_i^{sphere})$ and $E(\Delta r_i^{real})$ as a function of the noise level, utilizing configuration 27el-1s-Gauss. The dashed curves (- -) present $E(\Delta r_i^{sphere})$ and $E(\Delta r_i^{real})$ for the same test dipole, utilizing configuration 27el-1s-background.

that the inclusion of additional samples gives rise to a reduction of position errors. Furthermore, the number of dipoles with ΔR larger than 5 mm is reduced compared to the one in subtable 27el-6s-Gauss. However these values are increased when compared to the ones found in subtable 27el-1s-background.

Figure 5.15 depicts $E(\Delta r_i^{sphere})$ and $E(\Delta r_i^{real})$ values as a function of the noise level for a given dipole and for spatially and temporally white Gaussian noise (solid curves), and for background EEG (dashed curves). A six sample EEG epoch is considered in both configurations and 27 electrodes are used. The $E(\Delta r_i^{sphere})$ and $E(\Delta r_i^{real})$ values are larger for a given noise level when utilizing background EEG instead of Gaussian noise. Again we can notice that temporal and spatial correlation acts as if the noise level is increased for temporal and spatial white Gaussain noise. This by its turn yields a reduction of ΔR, as illustrated in section 5.5.3.

In conclusion it is found that when applying six successive time samples of background EEG, instead of Gaussian noise, the realistic model loses performance compared to the spherical head model. However, compared to background EEG and one time sample, it is found that the realistic model gains importance over the spherical head model as was also found for Gaussian noise.

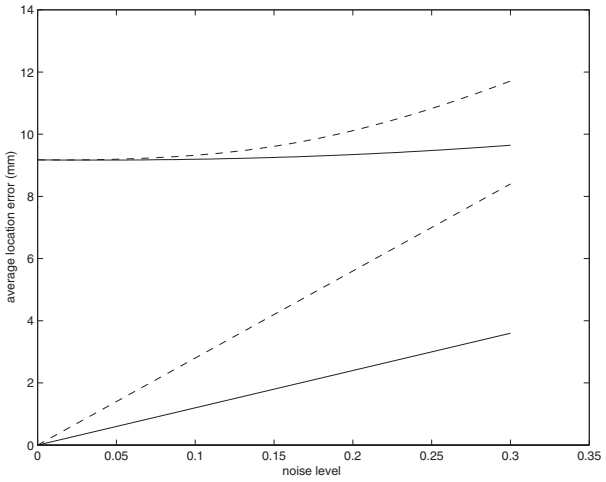

Figure 5.15: The solid curves (-) present $E(\Delta r_i^{sphere})$ and $E(\Delta r_i^{real})$ as a function of the noise level, utilizing configuration 27el-6s-Gauss. The dashed curves (- -) present $E(\Delta r_i^{sphere})$ and $E(\Delta r_i^{real})$ for the same test dipole, utilizing configuration 27el-6s-background.

5.7 Summary and original contributions

The aim of this study was to evaluate the performance of the three-shell spherical head model versus the performance of the realistic head model, in solving the inverse problem, in the presence of noise. The performance was evaluated by calculating the average dipole position error, for 1000 noisy scalp potentials, having the same noise level, utilizing a spherical- and a realistic head model. Utilizing the realistic head model, the average dipole position error $E(\Delta r_i^{real})$ is assumed to be due to noise only, while in the spherical head model, the average position error $E(\Delta r_i^{sphere})$ is due to both the noise and the usage of the simplified spherical head model. The difference between $E(\Delta r_i^{sphere})$ and $E(\Delta r_i^{real})$ is defined as ΔR. When ΔR is large, for a large number of test dipoles and a certain noise level, it is worthwhile utilizing the more demanding realistic head model. However, when ΔR is small, for a large number of test dipoles, it does not matter whether the realistic or spherical head model is used. In our simulations, the average position errors $E(\Delta r_i^{sphere})$ and $E(\Delta r_i^{real})$ are obtained through a local linearization. As a verification we found for one dipole that the values of $E(\Delta r_i^{sphere})$ and $E(\Delta r_i^{real})$ obtained through local linearization are in good agreement with the ones obtained when utilizing a Monte Carlo approach.

When utilizing 27 electrodes, an epoch of one time sample and Gaussian noise, it was found that by increasing the noise level from 0 to 0.2, ΔR decreases for all test dipoles. Moreover, the grand average over all the test dipoles of ΔR decrease from 5.5 mm to 1.8 mm, respectively. For a noise level of 0.1, corresponding with an averaged epileptic spike, 13.4% of the test dipoles have a ΔR larger than 5 mm. For a noise level of 0.2, corresponding with an unaveraged epileptic spike, less than 10 % of the test dipoles have a ΔR larger than 5 mm. The importance of the realistic head model over the spherical head model reduces by increasing the noise level. We further found by increasing the amount of scalp electrodes from 27 to 44 that the grand average of ΔR changes marginally. Hence, increasing the number of electrodes has limited impact on the importance of the realistic head model over the spherical head model in EEG dipole source analysis. By increasing the number of time samples to six, it was found that the ΔR value increases for all the test dipoles compared with the case where only one time sample is used. Hence the performance of the realistic head model in the inverse calculation gains importance compared to the three-shell spherical head model, when increasing the number of time samples used. When utilizing background EEG which is spatially and temporally correlated, with one or with six time samples, it was observed that ΔR decreases for all test dipoles compared with the cases utilizing Gaussian noise. Subsequently, utilizing background EEG deteriorates the performance of the realistic head model over the spherical head model compared with Gaussian noise. However as with Gaussian noise, increasing the number of time samples increases the ΔR when applying background EEG.

An original aspect of this work is that average dipole position errors obtained with the spherical and realistic head model are compared for the different configurations.

The study presented in this chapter has been submitted as an article to an international journal [137]. Parts of this study are also published as articles in proceedings of international conferences [136, 139].

Chapter 6

Case studies

6.1 Introduction

EEG dipole source analysis has been performed in the epilepsy-monitoring unit of the Ghent University Hospital since the beginning of the 90's. The clinical findings of EEG dipole source analysis, applying a spherical head model, are presented in several publications [9, 12, 15]. In this chapter we will perform EEG dipole source analysis, using a realistic head model, with the data obtained from two epilepsy patients. Epileptic spikes are used to perform the source analysis. A realistic head model is constructed from MR images. We use electrode detection software to localize the electrodes. Then, the inverse problem is solved with a realistic and spherical head model. The dipole position and orientation are compared between both models. The dipole position is compared to the surgically removed brain tissue. Furthermore, we determine the noise level. We fit a large number of dipoles with a similar noise level, to be aware of the location error due to the background activity. From these errors an average location error is calculated.

The chapter is organized as follows: first, the electrode detection method is presented in section 6.2. Then, we continue by presenting the two case studies in section 6.3 and section 6.4. Next, a discussion on the limitations on EEG dipole source analysis is given in section 6.5. Finally, a summary and conclusions are given in section 6.6.

6.2 Detection of electrode positions

Patients who are admitted to the long-term video/EEG-monitoring unit, are also subjected to a T1-weighted MR scan with the electrodes fixed on the scalp.

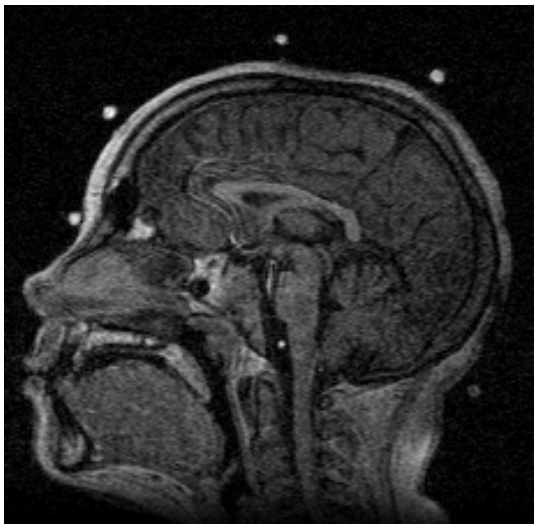

Figure 6.1: MR image, where several electrode markers can be noticed.

The metal electrodes generate no signal in the MR scan. Therefore, a spherical marker is attached on top of each electrode. The markers have a 5 mm diameter. In figure 6.1, a sagittal slice is given with several markers. A software tool is developed and validated [117, 121], which uses pattern recognition algorithms to detect the spherical markers. Figure 6.2 presents the graphical user interface for this tool. Apart from the localization of the markers, the software tool also presents the results on the MR images and gives the user the ability to allocate a label to each of the detected markers.

6.3 First patient

6.3.1 Patient information and EEG

The first patient (nr 439) is a 24 year-old male who has been experiencing epileptic seizures since the age of 16. He is admitted to the presurgical protocol which incorporates long-term video EEG monitoring, MR imaging, neuropsychological tests, and nuclear imaging. The presurgical protocol was suggestive for a right-medial temporal focus. Resection of the right hippocampus and the anterior part of the right temporal lobe was performed on 15/11/97 and the patient has been seizure free since.

The EEG is recorded at a 200 Hz sample rate using a Beehive© (Telefactor, USA) monitoring system. The EEG data are recorded with a common

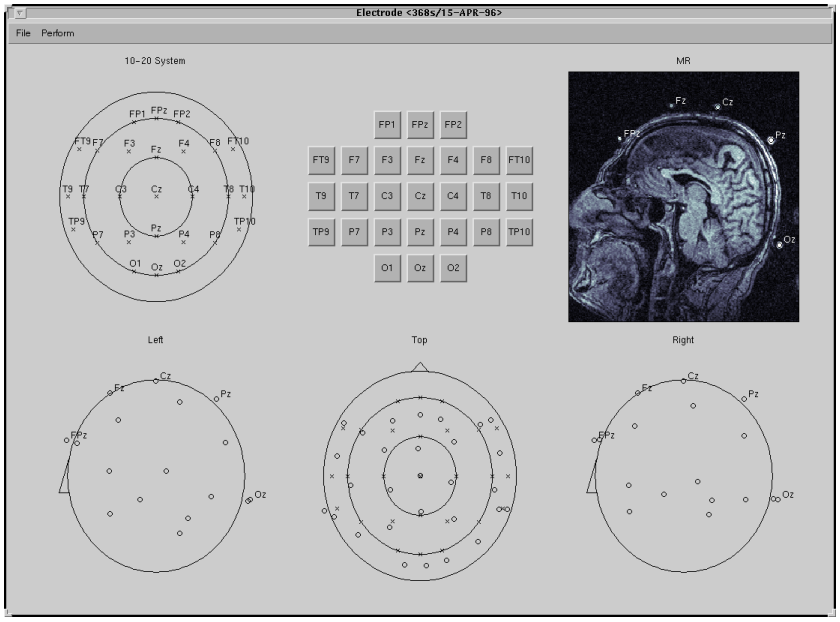

Figure 6.2: Graphical user interface to detect, visualize and label electrode markers.

reference. The 895 ms epoch containing the spike is manually selected and presented in figure 6.3. A zero phase shift band-pass filter is applied between 2-20 Hz. The potentials at each electrode are average referenced. All 27 electrode potentials are represented on the same axis. The epileptic spike starts at 300 ms. Furthermore, a 40 ms (or 8 samples) interval is marked by two vertical lines. This interval is used to perform EEG dipole source analysis with a single dipole.

The RMS value of the background EEG, U^b_{RMS}, is calculated by applying equation (5.5) for the first 250 ms (or 50 time samples) of EEG. This gives us an idea of the noise contribution to the EEG. The RMS value of the spike U_{RMS} is calculated using equation (5.4) for the marked interval of 40 ms . The noise level then becomes 0.16 and the signal-to-noise ratio (SNR) is then 6.1.

Figure 6.4 presents the potential distribution on a schematic scalp surface for a left, top, and right view. The potential distribution is given for the peak activity of the spike at 360 ms. The full equipotential lines have a positive value, the dashed equipotential lines have a negative value. Around the minimum, located in the right fronto-temporal area, a strong gradient in the potential distribution is observed. The 27 electrodes are also represented on this schematic representation.

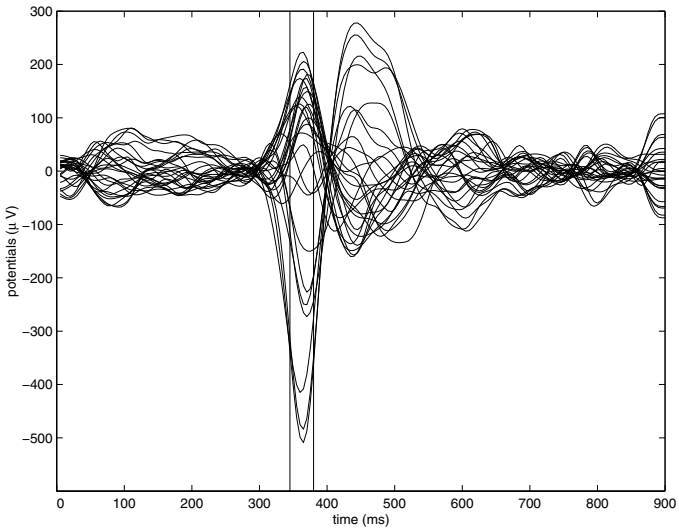

Figure 6.3: Plot of an average referenced EEG epoch. The two vertical lines mark the interval used to perform dipole source analysis.

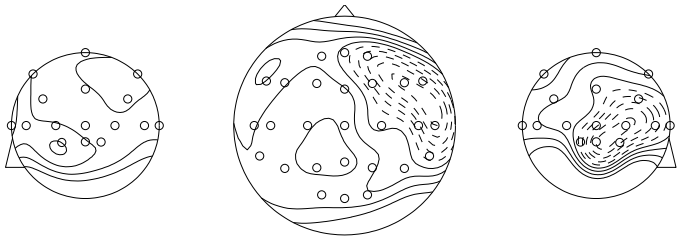

Figure 6.4: The potential distribution on a schematic scalp surface is presented for the peak activity of the spike.

6.3.2 Preparations

A best fitting sphere through the 27 electrode marker positions, is calculated with radius R. The markers are located about 8 mm above the scalp surface. Therefore, we chose the outer shell of the spherical head model at a radius of $(R - 8)$ mm. A typical choice of the radii of the outer shell of the scalp, skull and brain region are then $(R - 8)$ mm, $(R - 8).85/92$ mm and $(R - 8).80/92$ mm. A radial projection of the electrodes on the outer shell gives the electrode positions in the three-shell spherical head model.

From the T1-weighted MR images, a volume conductor model (VCM) is constructed consisting of a scalp, skull and brain region utilizing the SPM segmentation tool. More details on how the segmentation is performed can be found in subsection 4.4.1. The scalp, skull, and brain regions are allocated a homogenous isotropic conductivity with relative values of 1, 1/16 and 1, respectively. The same values are applied in the spherical head model. The VCM of the patient's head has about 500000 computational points or nodes. The electrode node is the node located closest to the position of the electrode marker. For the 27 electrode positions, 27 electrode nodes are determined in the VCM. Applying the FDRM, 26 numerical forward calculations need to be performed.

6.3.3 Dipole source analysis

The inverse problem applying both models, the spherical and realistic head model, is performed as given in section 2.8. The dipole parameters are changed until a minimum is reached in the relative residual energy.

The inverse problem is solved in the three-shell spherical head model. The fitted dipole coordinates are then transformed to MR coordinates [126–128, 132]. This is done by adding the center of the concentric spheres to the dipole position in the spherical head model. The dipole components remain unchanged. The first row of figure 6.5 represents the dipole position obtained with the spherical head model, in the corresponding axial, coronal and sagittal slice of the MR image.

The inverse problem is also solved using the realistic head model. The obtained dipole coordinates are again mapped on the MR image. The results are presented in the second row of figure 6.5.

Furthermore the yellow area around the fitted position represents the area where the residual energy is smaller than twice the residual energy at the fitted position which is 3.5 %.

The red area around the fitted position give the location error due to background EEG. This area is obtained as follows: the forward problem is solved in

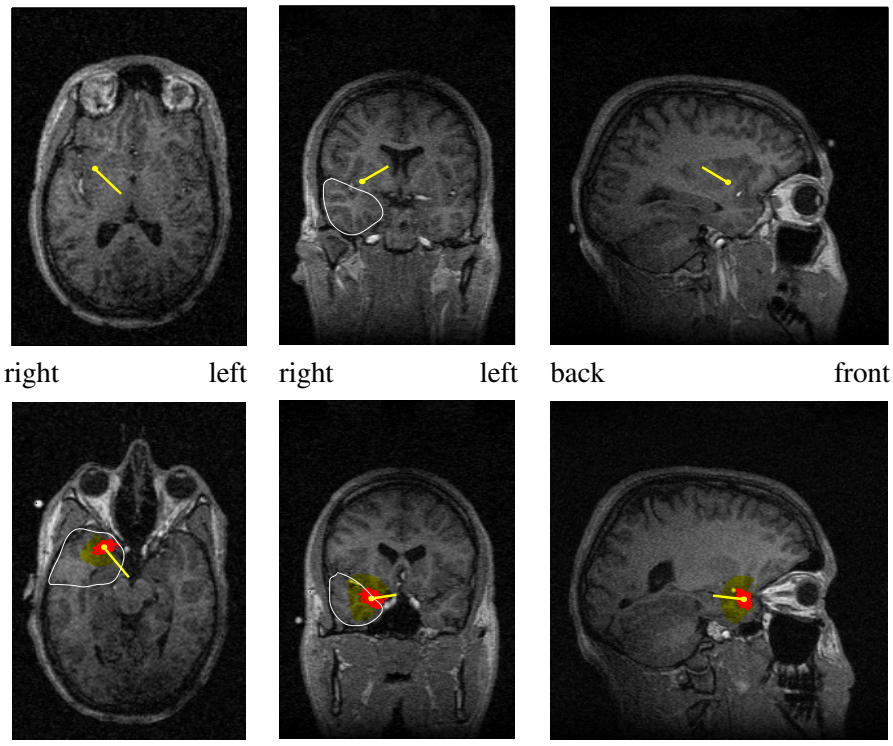

Figure 6.5: The dipole coordinates are mapped on the corresponding axial, coronal and sagittal MR slice. The first row gives the results when applying a spherical head model while the second row gives the results for the realistic head model. For the realistic head model a yellow area is presented where the relative residual energy is smaller than twice the relative residual energy of the fitted position. The red area simulates the deviation of the dipole position when superposing background EEG. The area that is surgically removed is also given.

the realistic head model for the fitted dipole parameters. Background EEG is added to the simulated potentials. The obtained signal has then the same noise level and the same number of samples as the real EEG. The inverse problem is solved by applying the local linearization as presented in section 5.2.2. The average location error for a large number of noisy potential sets is 4.2 mm. The red area in figure 6.5 is composed of dots representing dipole fits with noisy potentials. This area gives us an idea of the impact of noise on the dipole position error.

The distance between the fitted position applying a spherical head model and the fitted position applying a realistic head model is 21.4 mm. The angle between the dipole orientation obtained with the spherical and realistic head model is 18.1°. We notice from figure 6.5 that the spherical head model fits the dipole mainly higher, and more to the back of the head, than the realistic head model. In figure 6.5 the surgically removed area is marked. The realistic head model yields a fit position better in concordance with this area than the spherical head model.

6.4 Second patient

6.4.1 Patient information and EEG

The second patient is a 39 year-old female (nr 683) who has epileptic seizures since the age of 34. The presurgical evaluation was suggestive for a left medial-temporal focus and a resection was proposed of the left hippocampus and the anterior part of the left temporal lobe. However the patient decided not to go to surgery.

A plot of the 27 average referenced EEG potentials is presented in figure 6.6. The vertical lines represent the 40 ms epoch of EEG which is applied to perform EEG dipole source analysis. We also use this interval to calculate U_{RMS} from equation (5.4). The first 250 ms are applied to calculate U^b_{RMS} from equation (5.5). The noise level is 0.2 and the SNR equals 4.6.

The potential distribution on the scalp surface is given in figure 6.7 for the peak activity at 360 ms. A strong gradient can be observed around the minimum potential in the left fronto-temporal area.

6.4.2 Dipole source analysis

For the construction of the spherical and realistic head model we refer to the previous section.

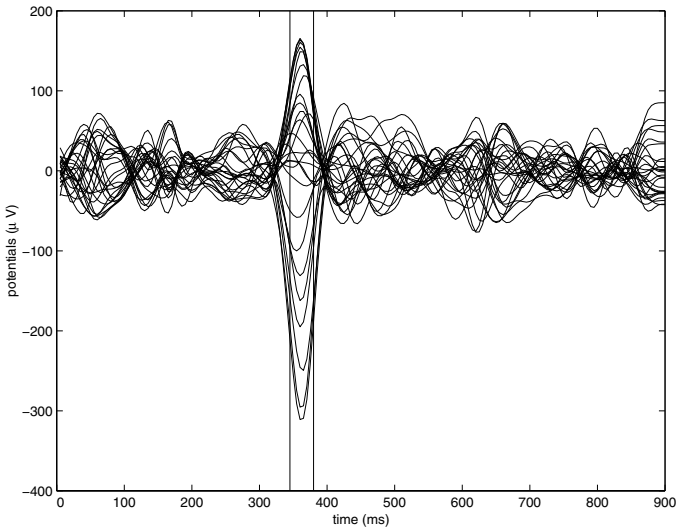

Figure 6.6: Plot of the average referenced spike. The two vertical lines mark the interval used to perform dipole source analysis.

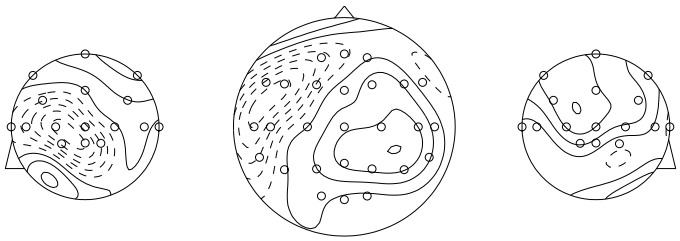

Figure 6.7: Potential distribution on a schematic scalp surface for the peak activity of the spike.

Figure 6.8 represent the dipole fits mapped on the corresponding MR image. The first and second row represents the results for the dipole fit when applying a spherical and realistic head model, respectively.

The yellow area has a relative residual energy smaller than twice the minimum value of 5.17 % found for the fitted position.

The red area represents the dipole location error due to the superposition of background EEG. The average location error due to the presence of background EEG is 4.8 mm.

The distance between both dipoles is 20.1 mm, the angle between the orientation of both dipoles is 5.3°. Here again we notice that the spherical head model fits the dipole mainly higher and more to the back of the head, compared to the fit of the realistic head model.

In figure 6.8 the area which would have been surgically removed, is represented. It can be noticed that the dipole fitted with the realistic head model, is localized closest to this area.

6.5 Discussion

We noticed that the dipole obtained with the realistic head model is found closer to the surgically resected area for the first patient. For the second patient the dipole obtained with the realistic head model is found closer to the area which was suggested to be removed. However, the fitted dipole position needs to be interpreted with a certain caution.

First, the electrical activity of other brain areas leads to dipole location errors. To reduce the contribution of background EEG one can average similar spikes. This is done by shifting the time axes so that the maxima of the spikes coincide. Thereby we hope to increase the contribution of the signal and reduce the contribution of noise. Another way to reduce the contribution of noise is to take the largest possible time epoch to perform EEG source analysis. In section 5.6.2 we noticed that by increasing the number of time samples the average location error reduces. The spike has only a certain extend in time, which limits the size of this EEG epoch.

A second contributor of dipole location errors is the error due to the application of the numerical method. This error is smaller than the one found when applying the spherical head model. In chapter 3 we found location errors which were on average equal to the internode distance and in general not larger than twice the internode distance. These results give us an idea of the contribution of the numerical errors to the dipole location error.

Another contributor to the dipole location error is the uncertainty of the skull conductivity. In literature there is controversy on the value of the skull

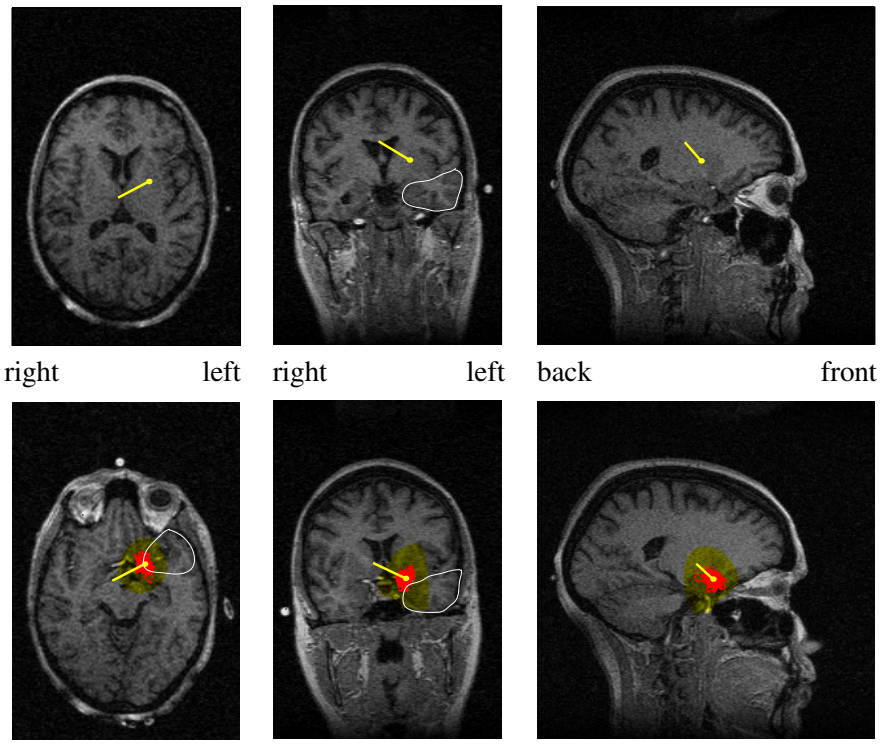

Figure 6.8: The dipole coordinates are mapped on the corresponding axial, coronal and sagittal MR slice. The first row gives the results when applying a spherical head model while the second row gives the results for the realistic head model. For the realistic head model a yellow area is presented where the relative residual energy is smaller than twice the relative residual energy of the fitted position. The red area gives the deviation of the dipole position when superposing background EEG. The area which would have been removed when surgery would have been performed is also given.

conductivity. We have applied the value $1/16$ for the conductivity ratio between the soft tissue (brain and scalp) and skull. This is the value presented by the most recent publication in this field [80]. In chapter 4 we have investigated the impact of underestimating the skull conductivity. This led to dipole location errors typically in the range of 5-15 mm.

The impact of increasing the number of electrodes on the dipole location error is also investigated in this thesis. It was found in section 5.5.2 that increasing the number of electrodes, reduces the dipole location error due to noise. The numerical accuracy will not improve when further increasing the number of electrodes as illustrated in section 3.5. Increasing the number of electrodes also gives a marginal improvement of the dipole location error when the skull conductivity is underestimated.

It is also known that tissues such as the skull and the white matter have an anisotropic conductivity. When applying isotropic conducting regions instead of anisotropic conducting regions, dipole location errors occur [24, 64].

Another problem is the construction of the skull region from MR images. The skull is a tissue which gives a low signal on MR images. It is therefore difficult to distinguish on these images. We have performed a dilation operation [63] on the brain region to obtain the skull region. This gives an outer skull surface with a shape similar to the brain region surface. However, the outer surface of the skull has not the same shape as the inner part of the skull. This can also lead to location errors [48]. A more realistic skull region can be obtained by using CT images, which have a high signal intensity for bone tissue.

A last contributor to the dipole location error is the electrical source model. The current dipole unites a patch of pyramidal neurons in the cortex which are all synchronously active. When this surface is curved it is possible that the resulting dipole is somewhat away from this active area. Furthermore, when several brain areas are synchronously active, a single dipole is an insufficient model.

We can state that the localization of a single dipole applying EEG can be performed with a spatial accuracy 10 mm, taking dipole location error contributors into account, and taking furthermore the result of phantom studies [59] into consideration,

6.6 Summary, conclusion and contributions

We have performed EEG dipole source analysis of interictal spikes in two patients with epilepsy. A 40 ms interval containing the first peak of the spike was used for this purpose. From the measured EEG we also derived the noise level.

The electrode markers which were placed on top of the electrodes were detected. Through the marker positions a best-fitting sphere was constructed which in its turn was applied to construct a three-shell spherical head model. The fitted dipole position obtained using the spherical head model was then mapped on the MR images.

By segmenting the MR images with the SPM99 segmentation tool, three realistically shaped volume conductor regions, i.e. scalp, skull and brain, were constructed. Then, the FDRM was applied to solve numerically 26 forward problems.

A distance of 20 mm was found between the dipole position obtained with the spherical head model and the one with the realistic head model. The position obtained when applying the realistic head model was located closer to the area which was (would be) surgically removed.

Simulated scalp potentials are obtained by a forward calculation in the realistic head model for the fitted dipole parameters. Background EEG was superimposed to this signal. The obtained EEG is set to the same noise level as found for the spike. We calculate the dipole location error due to the superimposed background EEG. The average location error due to this noise contributor is 4.1 mm for the first case and 4.8 mm for the second case.

The fitted dipole position should be treated with a certain caution. Several causes are given which contribute to the dipole location error. Even in the most ideal case the accuracy of the localization of a single dipole is in the order of 10 mm. An original aspect is the application of the FDRM for EEG dipole source analysis in epilepsy.

The mapping on MR images of the dipole position applying a three-shell spherical head model has been reported on conferences in the form of abstracts and articles in the proceedings [126–128, 132]. A group of about 30 patients has been evaluated with a realistic head model over the last three years. The patient data have been presented in the presurgical evaluation of patients with focal epilepsy. The results have also led to contributions on international conferences in the form of an abstract [13, 19, 20, 130]. Furthermore, the clinical relevance of EEG dipole source analysis with a realistic head model has been published in international journals [11, 14].

Chapter 7

Conclusions and original contributions

In this chapter the major results and conclusions are summerized. Furthermore the original contributions are presented.

In chapter 3 the finite difference reciprocity method (FDRM) is validated. This method is applied throughout the thesis. The FDRM is a combination of the finite difference method (FDM) and reciprocity. With the FDM it is possible to incorporate a large number of tissues with different conductivity values. The reciprocity theorem eases the computational burden encountered when applying the FDM. Subsequently reciprocity makes the FDM usable to solve the inverse problem. The exact potentials at 27 and 44 electrodes are obtained in an analytically solvable three-shell spherical head model. The dipole location and orientation error is investigated for a large number of test dipoles, when applying the FDRM in the inverse procedure. We found that in general the dipole location error is not larger than twice the grid size, and on average about equal to the grid size for a 2 mm and 3 mm grid. We further noticed that these results are independent of the number of electrodes used, i.e., 27 or 44. The orientation error is smaller than 4°, for the 2 mm an 3 mm grid, and when applying 27 and 44 electrodes. The sensitivity to noise of the inverse procedure applying the FDRM, is compared with the sensitivity to noise of the inverse procedure applying the analytical equation. It was found that the inverse procedure applying the FDRM is not more sensitive to noise than the inverse procedure applying the analytical equation. The validation of the FDRM by inspecting the dipole location and orientation error in an analytically solvable three-shell spherical head model is an original aspect of this work.

In chapter 4 the FDRM is applied to study the dipole location errors, for a large number of test dipoles, due to not incorporating the ventricular system

(VS), omitting a hole in the skull and underestimating the skull conductivity. We also investigated the impact of increasing the number of electrodes, from 27 to 53, on the dipole location error. The dipole location errors due to omitting the (VS) are mainly located in the vicinity of the VS. The maximum location errors found are 7.6 mm and 6.1 mm for 27 and 53 electrodes, respectively. Holes in the skull occur when a trepanation (i.e., a circular removal of skull) is made to introduce depth electrodes. The largest dipole location errors due to omitting a hole in the skull can be found in the vicinity of the skull. For a 20 mm diameter hole we found the maximum location errors of 5.6 mm and 5.2 mm for 27 and 53 electrodes, respectively. Underestimating the skull conductivity generates dipole location errors in the entire brain region. The location errors are typically a magnitude larger than the ones found when not incorporating the VS or omitting a hole in the skull, and. The maximum errors are 33.4 mm and 28.0 mm for 27 and 53 electrodes respectively. We further found that increasing the number of electrodes only marginally improves the dipole location error. These simulations are done in a 3D realistic head model, with a realistic number of scalp electrodes and for a large number of test dipoles. This is an original setup for the case where the VS is not incorporated and the case where a hole in the skull is omitted.

In chapter 5 we have compared the performance of EEG dipole source analysis, applying a realistic and a spherical head model in the presence of noise. In the realistic head model we assume that the location error is only due to the presence of noise. Subsequently the realistic head model is assumed to be an ideal volume conductor model. For the spherical head model, the dipole location error is due to noise and due to the simplified representation of the head. For a given test dipole the scalp potentials are calculated with the realistic head model. To these potentials, noise values with a certain noise level are superposed. For each of the volume conductor models the average dipole location error is calculated utilizing these potentials. When the average location error applying the spherical head model is much larger than the one applying the realistic head model, then it is worthwhile to use the more demanding realistic head model instead of the spherical head model. On the other hand, when the average location errors for both cases are of the same size, then it does not matter which model is used. The difference between the average location errors when applying a spherical and a realistic head model, for a given test dipole and a given noise level, is represented by ΔR. Utilizing 27 electrodes, an epoch of one time sample and Gaussian noise, gave the following results. By increasing the noise level from 0 to 0.2, ΔR decreases for all 1416 test dipoles applied. The grand average of all the test dipoles of ΔR decreases from 5.5 mm to 1.8 mm when increasing the noise level from 0 to

0.2. For a noise level of 0.1, corresponding with an averaged epileptic spike, 13.4% of the test dipoles have a ΔR larger than 5mm. For a noise level of 0.2, corresponding with an unaveraged epileptic spike, less than 10 % of the test dipoles have a ΔR larger than 5mm. The importance of the realistic head model over the spherical head model is reduced by increasing the noise level. We further found that by increasing the amount of scalp electrodes from 27 to 44, the grand average of all the test dipoles of ΔR only marginally changes. Hence, the performance of the realistic head model compared to the spherical head model, marginally changes by increasing the number of electrodes. The ΔR value is larger when applying 6 time samples instead of one time sample. Hence, the performance of the realistic head model in the inverse calculation gains importance compared to the three-shell spherical head model, when increasing the number of time samples. When utilizing background EEG which is spatially and temporally correlated, with one or with six time samples, ΔR decreases for all test dipoles, compared to the cases utilizing Gaussian noise. Subsequently, using background EEG, deteriorates the performance of the realistic head model over the spherical head model, compared to Gaussian noise. Increasing the number of time samples from one to six, increases ΔR when applying background EEG as was also found with Gausssian noise. An original aspect of this study is that a comparison is made between the performance in solving the inverse problem applying a realistic head model and applying a spherical head model.

In chapter 6 EEG dipole source analysis is performed on the EEG of two patients with epilepsy. The EEG of the 40 ms peak activity of the epileptic spike is applied in the inverse procedure. A best-fitting sphere is computed, through the 27 electrode markers in the MR-images. This sphere is applied to construct the three-shell spherical head model. The dipole is computed with this model, and afterwards mapped on the corresponding MR images. From the MR images a realistic head model is constructed, applying the SPM99 segmentation tool. The FDRM is then used to compute the dipole, which is also mapped on the corresponding MR images. The distance between the dipole position obtained in the spherical head model and the realistic head model is in both cases about 20 mm. The position obtained in the realistic head model is more in concordance with the surgically removed area for the first patient. For the second patient this position is closer to the hypothetically removed area. The superposed background EEG introduces location errors. We simulated for the given noise level the average location error due to the superposed background EEG. The average location error due to background EEG is 4.1 mm for the first case and 4.8 mm for the second case. Finally, we may conclude that an accuracy of 10 mm can be obtained in EEG dipole source analysis under

ideal conditions.

Appendix A

Successive overrelaxation

A.1 Basic idea

For very large and sparse linear systems, direct solvers such as Gaussian elimination [29], become impractical. Assume a system,

$$\mathbf{A}\mathbf{x} = \mathbf{b}, \tag{A.1}$$

with $\mathbf{A} \in \mathbb{R}^{n\times n}$, $\mathbf{x} \in \mathbb{R}^{n\times 1}$ the unknowns, and $\mathbf{b} \in \mathbb{R}^{n\times 1}$ the right hand side terms. Iterative methods give a solution of eqn. (A.1) for a given $\mathbf{b}$. When another $\mathbf{b}$ is presented, the method needs to be reapplied. The idea of iterative solvers is to rewrite the previous equation in

$$\mathbf{x} = \mathbf{B}\mathbf{x} + \mathbf{g}. \tag{A.2}$$

Here $\mathbf{B} \in \mathbb{R}^{n\times n}$ is called the iteration matrix and $\mathbf{g} \in \mathbb{R}^{n\times 1}$ the iteration vector. We start with an initial guess $\mathbf{x}^0$ of the solution $\mathbf{x}$ and generate a sequence of approximations $\{\mathbf{x}^k\}$ iteratively obtained by

$$\mathbf{x}^{(k+1)} = \mathbf{B}\mathbf{x}^{(k)} + \mathbf{g}, \quad k = 1, 2, \ldots. \tag{A.3}$$

Then we hope that the sequence $\{\mathbf{x}^{(k)}\}$ converges to the solution when k goes to ∞. For each iteration, we apply $\mathbf{B}$ to an approximation $\mathbf{x}^{(k)}$ and add $\mathbf{g}$ to the result. What does each iteration do? The error vector is defined as $\mathbf{er}^{(k)} = \mathbf{x}^{(k)} - \mathbf{x}$. Then eqn. (A.3) becomes,

$$\begin{aligned} \mathbf{x}^{(k+1)} &= \mathbf{B}\mathbf{x}^{(k)} + \mathbf{g} \\ &= \mathbf{B}(\mathbf{x} + \mathbf{er}^{(k)}) + \mathbf{g} \\ &= \mathbf{x} + \mathbf{B}\,\mathbf{er}^{(k)}. \end{aligned}$$

Hence each iteration does not affect the correct part of $\mathbf{x}^k$ but each iteration does affect the error vector $\mathbf{er}^{(k)}$. Rewriting the last eqn. gives $\mathbf{er}^{(k+1)} = \mathbf{B}\ \mathbf{er}^{(k)}$. The spectral radius of $\mathbf{B}$ is defined as $\rho(\mathbf{B}) = \max|\lambda_i|$ with λ_i an eigenvalue of $\mathbf{B}$. It is apparent that when $\rho(\mathbf{B}) < 1$ then $\mathbf{er}^{(k)} \rightarrow 0$ as $k \rightarrow \infty$. And, the smaller $\rho(\mathbf{B})$, the faster the speed of convergence.

A.2 The Jacobi method

Each linear equation of system A.1,

$$a_{i1}x_1 + \cdots + a_{ii}x_i + \cdots + a_{in}x_n = b_i, \;\; i = 1, \ldots, n,$$

can be rewritten as,

$$x_i = \frac{1}{a_{ii}}(b_i - a_{11}x_1 - \cdots - a_{in}x_n), \;\; i = 1, \ldots, n. \tag{A.4}$$

We rewrite $\mathbf{A}$ in the form:

$$\mathbf{A} = \mathbf{Lo} + \mathbf{D} + \mathbf{Up},$$

with $\mathbf{Lo}$ a matrix which diagonal elements and upper diagonal elements are zero and which lower diagonal elements are identical to those in $\mathbf{A}$, with $\mathbf{D}$ a matrix which diagonal elements are equal to those of $\mathbf{A}$ and upper and lower diagonal elements are zero, and with $\mathbf{Up}$ a matrix which diagonal elements and lower-diagonal elements are zero and which upper-diagonal elements are identical to those in $\mathbf{A}$. From eqn. (A.4) we then write:

$$\mathbf{x} = -\mathbf{D}^{-1}(\mathbf{Lo} + \mathbf{Up})\mathbf{x} + \mathbf{D}^{-1}\mathbf{b}.$$

The Jacobi iteration matrix and the Jacobi vector are

$$\mathbf{B}_{JAC} = -\mathbf{D}^{-1}(\mathbf{Lo} + \mathbf{Up}), \tag{A.5}$$

$$\mathbf{g}_{JAC} = \mathbf{D}^{-1}\mathbf{b}. \tag{A.6}$$

The Jacobi iteration scheme then becomes

$$x_i^{(k+1)} = \frac{1}{a_{ii}}(b_i - \sum_{j=1, j\neq i}^{n} a_{ij}x_j^{(k)}), \;\; i = 1, \ldots, n.$$

A.3 The successive overrelaxation method

A.3.1 The SOR iteration matrix and vector

To compute the components of the vector $\mathbf{x}^{(k+1)}$, in the Jacobi method, only the components of the vector $\mathbf{x}^{(k)}$ are used. Note however that to compute $x_i^{(k+1)}$, we could have used $x_1^{(k+1)}$ through $x_{i-1}^{(k+1)}$. Furthermore, we can introduce a parameter ω which places more weight on the last approximation in the hope that the convergence will be faster. The successive overrelaxation iteration (SOR) is defined as

$$x_i^{(k+1)} = \frac{\omega}{a_{ii}}[b_i - \sum_{j=1}^{i-1} a_{ij}x_j^{(k+1)} - \sum_{j=i+1}^{n} a_{ij}x_j^{(k)}] + (1-\omega)x_i^{(k)}, \;\; i = 1, \ldots, n. \tag{A.7}$$

In matrix notation the SOR iteration becomes

$$\begin{aligned} & \mathbf{D}\mathbf{x}^{(k+1)} = \omega[\mathbf{b} - \mathbf{Lo}\,\mathbf{x}^{(k+1)} - \mathbf{Up}\,\mathbf{x}^{(k)}] + (1-\omega)\mathbf{D}\mathbf{x}^{(k)} \\ \Leftrightarrow \quad & (\mathbf{D} + \omega\mathbf{Lo})\,\mathbf{x}^{(k+1)} = \omega\mathbf{b} + [(1-\omega)\mathbf{D} - \omega\mathbf{Up}]\mathbf{x}^{(k)}. \end{aligned} \tag{A.8}$$

The SOR Matrix and the SOR vector then becomes

$$\mathbf{B}_{SOR} = (\mathbf{D} + \omega\mathbf{Lo})^{-1}[(1-\omega)\mathbf{D} - \omega\mathbf{Up}], \tag{A.9}$$

$$\mathbf{g}_{SOR} = \omega(\mathbf{D} + \omega\mathbf{Lo})^{-1}\mathbf{b}. \tag{A.10}$$

A.3.2 The optimal choice of ω

When A is a symmetric positive definite matrix, which is the case in our application when a reference node is chosen, then the SOR iteration converges when ω lies inside the interval $[0, 2]$ [29].

The optimal ω is obtained by trial and error. The initial guess $\mathbf{x}^{(0)}$ is set to a vector containing only zeros. The residual is defined as $re^{(k)} = |\mathbf{A}\mathbf{x}^{(k)} - \mathbf{b}|$. The ω value for which the residual becomes $re^{(k)} < 10^{-3}$ in the smallest number of iterations is chosen to be the optimal value for a given volume conductor model. Figure A.1 gives the number of iterations as a function of ω for a digitized spherical head model with node spacing 2 mm (full line), 3 mm (dashed line) and 4 mm (dotted line). The optimal ω for a 2 mm grid with 372189 nodes, for a 3 mm grid with 110483 nodes and for a 4 mm grid with 50877 nodes is 1.95, 1.93 and 1.91, respectively. The number of updates in each iteration is equal to n, the number of nodes, which is by its turn proportional to $1/h^3$, with h the node spacing. Hence when we halve the internode spacing, about 8 times more updates need to be performed per iteration.

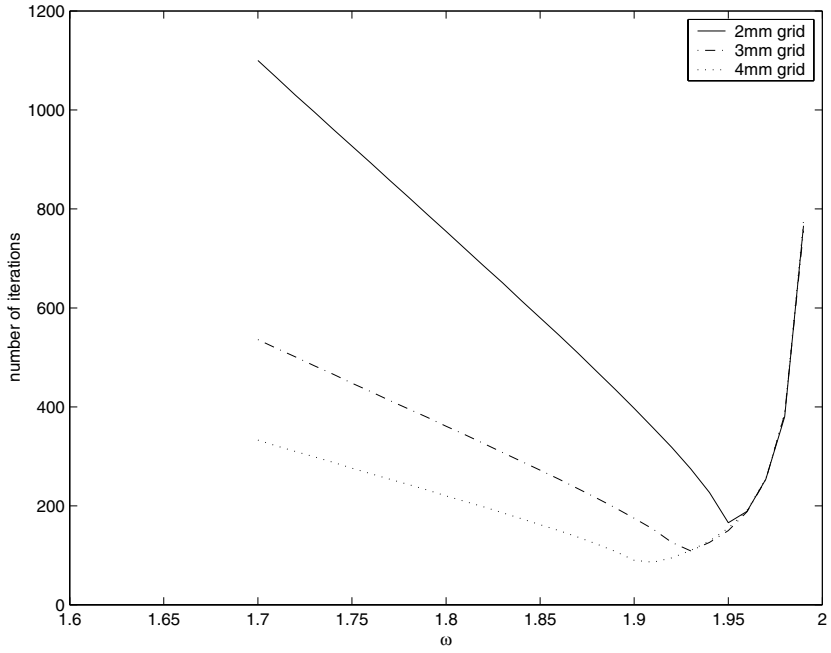

Figure A.1: The number of iterations needed to obtain a residual of $re^{(k)} < 10^{-3}$ is presented as a function of ω. This value is given for a digitized spherical head model with node spacing 2 mm (full line), 3 mm (dashed line) and 4 mm (dotted line).

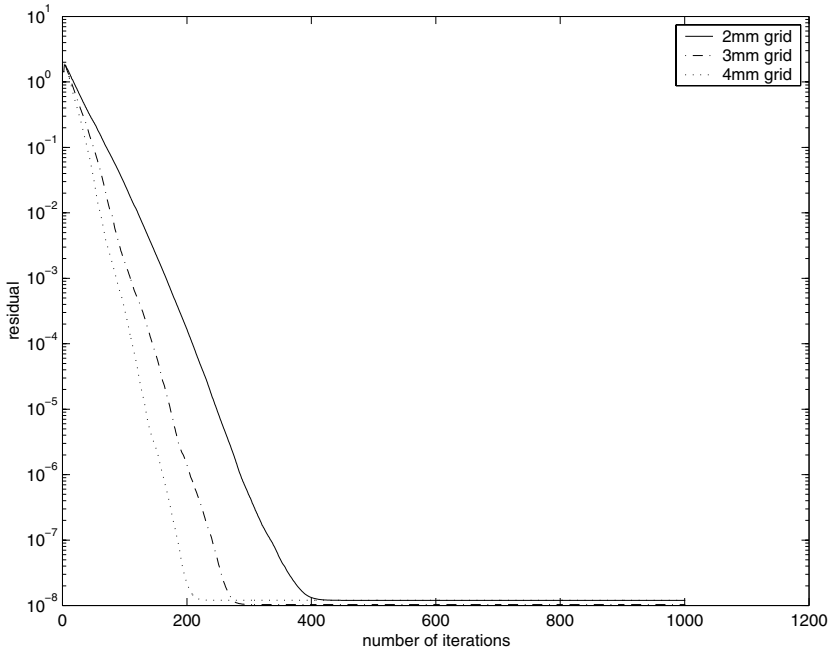

Figure A.2: The residual as a function of the number of iterations. This value is given for a digitized spherical head model with node spacing 2 mm (full line), 3 mm (dashed line) and 4 mm (dotted line).

The iterations are stopped when the residual does not decreases anymore. For the 2 mm, 3 mm and 4 mm grid this happens after 440, 310 and 240 iterations as illustrated in figure A.2.

The CPU time needed on a SUN Ultra 60 360 MHz to perform a forward calculation with the optimal chosen ω and for a 2 mm, 3 mm and 4 mm grid equals to 2 min 7 sec, 25 sec, 8 sec, respectively. When we half the node spacing from 4 mm to 2 mm, the computation time becomes about 16 times longer.

Appendix B

Reciprocity

B.1 The general idea of reciprocity

Consider a resistor circuit, with two clamps AB and r_x as illustrated in figure B.1. The clamp AB represents a pair of scalp electrodes. The clamp r_x is located in the brain region.

First we introduce a current I_{r_x} at clamp r_x. This source will generate a potential $U_{AB}(I_{r_x})$ at AB as illustrated in figure B.1(a). Next, we introduce a current I_{AB} at AB. This will give rise to a potential difference $V_{r_x}(I_{AB})$ at r_x illustrated in figure B.1(b). The reciprocity theorem states:

$$U_{AB}\, I_{AB} = V_{r_x}\, I_{r_x}. \tag{B.1}$$

B.2 Mathematical treatment

We give a mathematical treatment for a digitized volume conductor model. Consider a digitized volume conductor model with n computational points or nodes. At each of the nodes the potential V_i with $i = 1 \ldots n$ is calculated for given sources which are the current monopoles I_i with $i = 1 \ldots n$. Poisson's equation can then be transformed to a linear equation at each node, as illustrated for the FEM and FDM in subsections 2.7.5 and 2.7.6. This set of linear equations can be written in matrix notation. The system matrix then becomes $\mathbf{A} \in \mathbb{R}^{n \times n}$ and has the following properties: it is sparse, symmetric and regular. We can write:

$$\mathbf{A}\, \mathbf{V} = \mathbf{I},$$

with $\mathbf{V} = [V_1 \ldots V_n]^T \in \mathbb{R}^{n \times 1}$ and $\mathbf{I} = [I_1 \ldots I_n]^T \in \mathbb{R}^{n \times 1}$ and with ^{T} the transpose operator. We want to obtain the potential difference $V_k - V_l$ between

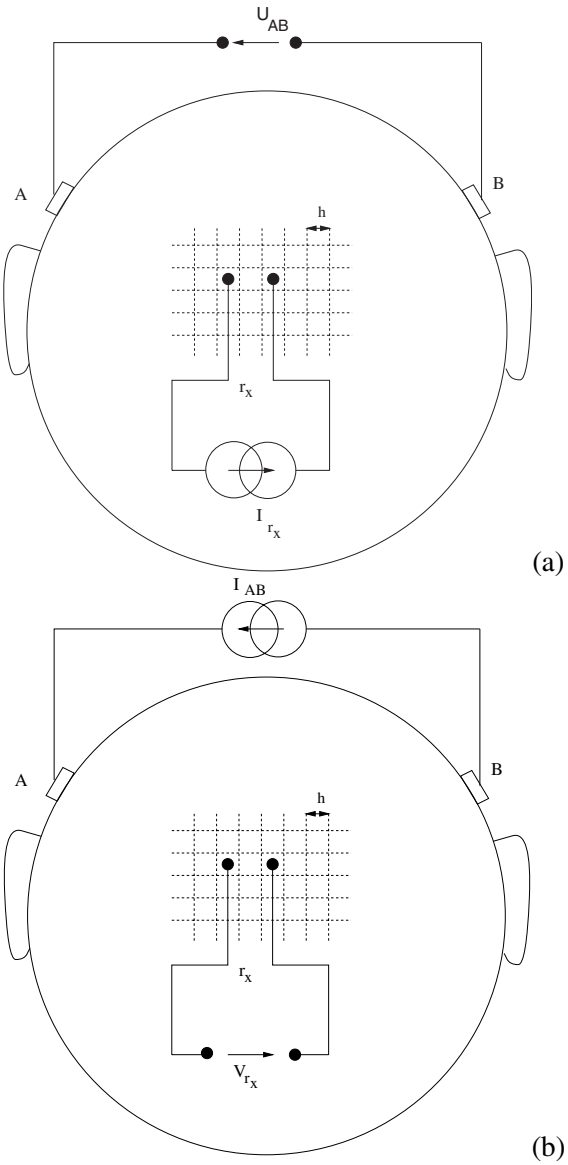

Figure B.1: A resistor network where (a) a current source I_{r_x} is introduced and the potential U_{AB} is measured, and (b) a current source I_{AB} is introduced and a potential V_{r_x} is measured.

node k and l for a current source I_f at node f and a current sink I_g at node g with $I_f = -I_g$. All other sources are zero. Cramer's solution for a linear system then becomes:

$$V_k = \frac{I_f[(-1)^{k+f+1}A_{fk} - (-1)^{k+g+1}A_{gk}]}{\det \mathbf{A}}, \tag{B.2}$$

$$V_l = \frac{I_f[(-1)^{l+f+1}A_{fl} - (-1)^{l+g+1}A_{gl}]}{\det \mathbf{A}}, \tag{B.3}$$

with $A_{*\circ}$ the minor for row $*$ and column $\circ$.

On the other hand the potential V_f and V_g for a current source I_k and current sink I_l with $I_k = -I_l$, are:

$$V_f = \frac{I_k[(-1)^{f+k+1}A_{kf} - (-1)^{f+l+1}A_{lf}]}{\det \mathbf{A}}, \tag{B.4}$$

$$V_g = \frac{I_k[(-1)^{g+k+1}A_{kg} - (-1)^{g+l+1}A_{lg}]}{\det \mathbf{A}}. \tag{B.5}$$

Furthermore, we know that $A_{*\circ}$ is equal to $A_{\circ *}$ due to the fact that $\mathbf{A}$ is symmetric. Hence, (eqn.(B.2) – eqn.(B.3))/I_f equals (eqn.(B.4) – eqn.(B.5))/I_k. Subsequently the reciprocity theorem is deduced:

$$I_k(V_k - V_l) = I_f(V_f - V_g).$$

B.3 Reciprocity for a dipole source with random orientation

We inspect equation (B.1) again. A dipole can be represented as two current monopoles, a current source and sink, providing I_{r_x} and $-I_{r_x}$, separated by a distance $2h$. The dipole is oriented from the negative to the positive current monopole and is assumed to be along the x-axis of the resistor network with node spacing h. The magnitude of the dipole moment is then $2hI_{r_x}$. The center $\mathbf{r}$ of the two monopoles can then be seen as the dipole position. The scalp electrodes are located sufficiently far from the sources compared with the distance $2h$ between the sources so that we can assume a dipole field. We rewrite equation (B.1) as:

$$U_{AB} = \frac{V_{r_x}\, I_{r_x}}{I_{AB}}. \tag{B.6}$$

The forward problem in EEG source analysis gives the potential U_{AB} for a current dipole located at $\mathbf{r}$ and oriented along the x-axis. Rewriting equation(B.6) with $d_x = 2hI_{r_x}$ and

$$\frac{\partial V}{\partial x} \approx \frac{[V_{I_{AB}}(\mathbf{r} + h\mathbf{e}_x) - V_{I_{AB}}(\mathbf{r} - h\mathbf{e}_x)]}{2h},$$

gives:

$$U_{AB} = \frac{d_x \frac{\partial V}{\partial x}}{I_{AB}}. \tag{B.7}$$

In a similar way, U_{AB} can be calculated for a dipole located at $\mathbf{r}$ oriented along the y-axis and the z-axis.

Consider a dipole at position $\mathbf{r}$ and with dipole components $\mathbf{d} = (d_x, d_y, d_z)^T \in \mathbb{R}^{3\times 1}$. The potential U_{AB} reads:

$$U_{AB}(\mathbf{r}, \mathbf{d}) = \frac{\mathbf{d}^T \cdot \nabla V(\mathbf{r})}{I_{AB}}, \tag{B.8}$$

with $\nabla V(\mathbf{r}) = (\partial V(\mathbf{r})/\partial x, \partial V(\mathbf{r})/\partial y, \partial V(\mathbf{r})/\partial z)^T \in \mathbb{R}^{3\times 1}$. Notice that this equation corresponds with equation (3.1).

Bibliography

[1] ANT software bv. *ASA users manual*, 2000.

[2] J. P. Ary, S. A. Klein, and D. H. Fender. Location of sources of evoked scalp potentials: Corrections for skull and scalp thicknesses. *IEEE Transactions on Biomedical Engineering*, BME-28(6), pp. 447–452, 1981.

[3] J. Ashburner and K. Friston. Multimodal image coregistration and partitioning - a unified framework. *Neuroimage*, 6, pp. 209–217, 1997.

[4] K. A. Awada, D. R. Jackson, J. T. Baumann, Stephen B.and Williams, D. R. Wilton, P. Fink, and B. Prasky. Effects of conductivity uncertainties and modeling errors on EEG source localization using a 2-D model. *IEEE Transactions on Biomedical Engineering*, 45(9), pp. 1135–1145, 1998.

[5] K. A. Awada, D. R. Jackson, J. T. Williams, D. R. Wilton, S. B. Baumann, and A. C. Papanicolaou. Computational aspects of finite element modeling in EEG source localization. *IEEE Transactions on Biomedical Engineering*, 44(8), pp. 736–752, August 1997.

[6] A. C. L. Barnard, I. M. Duck, and M. S. Lynn. The application of electromagnetic theory to electrocardiography: I. derivation of the integral equations. *Biophysics Journal*, 7, pp. 443–462, 1967.

[7] S. Baumann, D. Wozny, S. Kelly, and F. Meno. The electrical conductivity of human cerebrospinal fluid at body temperature. *IEEE Transactions on Biomedical Engineering*, 44(3), pp. 220–223, 1997.

[8] P. Boon. *Refractory lesional epilepsy: clinical and neurophysiological localisaton*. Ph.D. thesis, Department of Neurology, Ghent University Hospital, 1994.

[9] P. Boon and M. D'Havé. Interictal and ictal dipole modelling in patients with refractory partial epilepsy. *Acta Neurologica Scandinavica*, 92, pp. 7–18, 1995.

[10] P. Boon, M. D'Havé, G. Van Hoey, B. Vanrumste, T. Vandekerckhove, E. Achten, C. Adam, M. Baulac, L. Goossens, and J. De Reuck. Dipole modelling and intracranial EEG in epilepsy surgery candidates. *Epilepsia*, 38, suppl. 3, p. 23, 1997. Abstracts from the 22nd International Epilepsy Congress, Dublin, Ireland, 1997.

[11] P. Boon, M. D'Havé, G. Van Hoey, B. Vanrumste, K. Vonck, C. Adam, T. Vandekerckhove, G. Michielsen, M. Baulac, and J. De Reuck. Source localization in refractory partial epilepsy. *Revue Neurologique*, 155(6-7), pp. 499–508, 1999.

[12] P. Boon, M. D'Havé, T. Vandekerckhove, E. Achten, C. Adam, S. Clemenceau, M. Baulac, L. Goossens, L. Calliauw, and J. De Reuck. Dipole modelling and intracranial EEG recordings: Correlation between dipole and ictal onset zone. *Acta Neurochirurgica*, 139, pp. 643–652, 1997.

[13] P. Boon, M. D'Havé, B. Vanrumste, G. Van Hoey, K. Vonck, E. Achten, and T. Vandekerckhove. Anatomical accuracy of source localization in focal epilepsy. *Epilepsia*, 40, suppl. 7, p. 195, 1999. Abstracts from the Annual Meeting of the American Epilepsy Society, Orlando, Florida, December 3–8, 1999.

[14] P. Boon, M. D'Havé, B. Vanrumste, G. Van Hoey, K. Vonck, P. Van Walleghem, T. Vandekerckhove, and J. De Reuck. Ictal source localization in presurgical patients with refractory epilepsy. *Neurology*, 2000. Submitted.

[15] P. Boon, M. D'Havé, K. Vonck, M. Baulac, T. Vandekerckhove, and J. De Reuck. Dipole modeling in epilepsy surgery candidates. *Epilepsia*, 38(2), pp. 208–218, 1996.

[16] P. Boon, G. Van Hoey, B. Vanrumste, and M. D'Havé. True versus standard international 10-20 EEG electrode positions and the spherical head model. *Electroencephalography and Clinical Neurophysiology*, 103(1), pp. 196–197, 1997. Abstracts of the 14th International Congress of EEG and Clinical Neurophysiology, Florence, Italy, August 24-29, 1997.

[17] P. Boon, G. Van Hoey, B. Vanrumste, K. Vonck, M. D'Havé, R. Achten, T. Vandekerckhove, M. Baulac, and J. De Reuck. Ictal source localization in epilepsy surgery candidates: Enhanced dipole modeling in a spherical model. *Epilepsia*, 38, suppl. 8, p. 64, 1997. Abstacts from the Annual Meeting of the American Epilepsy Society, Boston, Massachussetts, December 7–10, 1997.

[18] P. Boon, T. Vandekerckhove, E. Achten, E. Thiery, L. Goossens, K. Vonck, M. D'Havé, G. Van Hoey, B. Vanrumste, B. Legros, L. Defreyne, and J. De Reuck. Epilepsy surgery in Belgium, the experience in Gent. *Acta Neurologica Belgica*, 99, pp. 256–265, 1999.

[19] P. Boon, K. Vonck, M. D'Havé, B. Vanrumste, G. Van Hoey, and T. Vandekerckhove. Clinical applicability of source localization of epileptic foci in presurgical candidates, a prospective study of 100 patients. *Epilepsia*, 40, suppl. 7, p. 153, 1999. Abstracts from the Annual Meeting of the American Epilepsy Society, Orlando, Florida, December 3–8, 1999.

[20] P. Boon, K. Vonck, M. D'Havé, B. Vanrumste, G. Van Hoey, T. Vandekerckhove, and J. De Reuck. Ictal source localisation based on scalp EEG and MRI compared with intracranial EEG recording in patients with refractory epilepsy. *Epilepsia*, 39 suppl. 6, p. 64, 1998. Abstracts from the Annual Meeting of the American Epilepsy Society, San Diego, California, December 6–9, 1998.

[21] G. Boterbergh. *EEG dipole source analysis applying BEM*. Master's thesis, Faculty of Applied Sciences, Ghent University, 1999.

[22] W. L. Briggs. *A multigrid tutorial*. SIAM, 1987.

[23] S. van den Broek. *Volume conduction effects in EEG and MEG*. Ph.D. thesis, University of Twente, 1997.

[24] S. van den Broek, F. Reinders, M. Donderwinkel, and P. M. Volume conduction effects in EEG and MEG. *Electroencephalography and Clinical Neurophysiology*, 106, pp. 522–534, 1998.

[25] H. Buchner, G. Knoll, M. Fuchs, A. Rienäcker, R. Beckmann, M. Wagner, J. Silny, and J. Pesch. Inverse localization of electric dipole current sources in finite element models of the human head. *Electroencephalography and Clinical Neurophysiology*, 102(4), pp. 267–278, April 1997.

[26] M. J. van Burik and M. J. Peters. EEG and implanted sources in the brain. *Archives of physiology and biochemistry*, 107(5), pp. 367–375, 2000.

[27] D. Cohen and B. N. Cuffin. Demonstration of useful difference between magnetoencephalogram and electroencephalogram. *Electroencephalography and Clinical Neurophysiology*, 56, pp. 38–51, 1983.

[28] B. N. Cuffin, D. Cohen, K. Yunokuchi, R. Maniewski, C. Purcell, R. Cosgrove, J. Ives, J. Kennedy, and D. Schomer. Test of EEG localization accuracy using implanted sources in the human brain. *Annals of Neurology*, 29, pp. 132–138, 1991.

[29] B. N. Datta. *Numerical Linear Algebra and Applications*. Brooks/Cole Publishing Company, 1995.

[30] J. S. Ebersole and P. B. Wade. Spike voltage topography and equivalent dipole localization in complex partial epilepsy. *Brain Topography*, 3(1), pp. 21–34, 1990.

[31] J. Engel. The use of PET scanning in epilepsy. *Annals of Neurology*, 15, pp. 180–91, 1984.

[32] A. S. Ferguson and G. Stroink. Factors affecting the accuracy of the boundary element method in the forward problem-i:calculating the surface potentials. *IEEE Transactions on Biomedical Engineering*, 44(11), pp. 1139–1155, 1997.

[33] E. Frank. Electric potential produced by two point current sources in a homogeneous conduction sphere. *Journal of Applied Physics*, 23(11), pp. 1225–1228, November 1952.

[34] J. A. Freeman and C. Nicholson. Experimental optimization of current source-density technique for anuran cerebellum. *Journal of Neurphysiology*, 38, pp. 369–382, 1975.

[35] M. Fuchs, R. Drenckhahn, H.-A. Wischmann, and M. Wagner. An improved boundary element method for realistic volume-conductor modeling. *IEEE Transactions on Biomedical Engineering*, 45(8), pp. 980–997, 1998.

[36] M. Fuchs, W. Michael, H.-A. Wischmann, T. Köhler, A. Theißen, R. Drenckhahn, and H. Buchner. Imporving source reconstruction by combining bioelectric and biomagnetic data. *Electroencephalography and Clinical Neurophysiology*, 107, pp. 93–111, 1998.

[37] L. A. Geddes and L. E. Baker. The specific resistance of biological materials—a compendium of data for the biomedical engineer and physiologist. *Med. Biol. Engr.*, 5, pp. 271–293, 1967.

[38] D. B. Geselowitz. On bioelectric potentials in an inhomogeneous volume conductor. *Biophysics Jounal*, 7, pp. 1–11, 1967.

[39] M. S. Hämäläinen, R. Hari, R. J. Ilmoniemi, J. Knuutila, and O. V. Lounasmaa. Magnetoencephalography—theory, intrumentation, and applications to noninvasive studies of the working human brain. *Reviews of Modern Physics*, 65(2), pp. 413–497, 1993.

[40] M. S. Hämäläinen and J. Sarvas. Realistic conductivity geometry model of the human head for interpretation of neuromagnetic data. *IEEE Transactions on Biomedical Engineering*, 36(2), pp. 165–171, February 1989.

[41] J. Hara, T. Musha, and W. R. Shankle. Approximating dipoles from human EEG activity: The effect of dipole source configuration on dipolarity using single dipole models. *IEEE Transactions on Biomedical Engineering*, 46(2), pp. 125–129, February 1999.

[42] J. Haueisen, C. Ramon, M. Eiselt, H. Brauer, and H. Nowak. Influence of tissue resistivities on neuromagnetic fields and electric potentials studied with a finite element model of the head. *IEEE Transactions on Biomedical Engineering*, 44(8), pp. 727–735, August 1997.

[43] T. Heinonen, H. Eskola, P. Dastidar, P. Laarne, and J. Malmivuo. Segmentation of T1 MR scans for reconstruction of resistive head models. *Computer Methods and Programs in Biomedicine*, 54, pp. 173–181, 1997.

[44] H. L. F. von Helmholtz. Ueber einige Gesetze der Verteilung elektrischer Ströme in körperlichen Leitern mit Anwendung auf die tierisch elektrischen Versuche. *Ann. Physik und Chemie*, 89, pp. 211–233,354–377, 1853.

[45] R. Hoekema, K. Venner, J. Struijk, Johannes, and J. Holsheimer. Multigrid solution of the potential field in modeling electrical nerve stimulation. *Computers and Biomedical Research*, 31, pp. 348–362, 1998.

[46] M. A. Huerta and G. Gonzalez. The surface potentials produced by electric sources in stratified spherical and prolate spheroidal volume

conductors. *International Journal of Electronics*, 54(5), pp. 657–671, 1983.

[47] J. R. Hughes. The significance of the interictal spike discharge: A review. *Journal of Clinical Neurophysiology*, 6(3), pp. 207–226, 1989.

[48] G. Huiskamp, M. Vroeijenstijn, R. van Dijk, G. Wieneke, and A. van Huffelen. The need for correct realistic geometry in the inverse EEG problem. *IEEE Transactions on Biomedical Engineering*, 46(11), pp. 1281–1287, 1999.

[49] H. Jasper. Report of committee on methods of clinical exam in EEG. *Electroencephalography and Clinical Neurophysiology*, 10, pp. 370–375, 1958.

[50] C. R. Johnson. Numerical methods for bio-electric field problems. In J. D. Bronzino, editor, *The biomedical engineering handbook*, chapter 12. CRC press, IEEE press, 1995.

[51] L. G. Kiloh, A. J. Mc Comas, J. W. Osselton, and U. A. R. M. *Clinical Electroencephalography*. Butterworths, 1981.

[52] Z. J. Koles. Trends in EEG source localization. *Electroencephalography and Clinical Neurophysiology*, 106, pp. 127–137, 1998.

[53] J. D. Kosterich, K. R. Foster, and S. R. Pollack. Dielectric properties of fluid-saturated bone-the effect of variations in conductivity of immersion fluid. *IEEE Transactions on Biomedical Engineering*, 31, pp. 369–373, 1984.

[54] T. Krings, K. H. Chiappa, B. N. Cuffin, J. I. Cochius, S. Connolly, and G. R. Cosgrove. Accuracy of EEG dipole source localization using implanted sources in the human brain. *Clinical Neurophysiology*, 110, pp. 106–114, 1999.

[55] P. Laarne, E. H., J. Hyttinen, V. Suihko, and J. Malmivuo. Validation of a detailed computer model for the electric fields in the brain. *Journal of Medical Engineering and Technology*, 19(2-3), pp. 84–87, 1995.

[56] P. Laarne, J. Hyttinen, S. Dodel, J. Malmivuo, and H. Eskola. Accuracy of two dipolar inverse algorithms applying reciprocity for forward calculation. *Computers and Biomedical Research*, 33(3), pp. 172–185, 2000.

[57] P. Laarne, M. Tenhunen-Eskelinen, H. J., and H. Eskola. Effect of EEG electrodes density on dipole localization accuracy using two realistically shaped skull resistivity models. *Brain Topography*, 12(4), pp. 249–254, 2000.

[58] M. Le Van Quyen, J. Martinerie, V. Navarro, P. Boon, M. D'Havé, C. Adam, B. Renault, F. Varela, and B. M. Anticipation of epileptic seizures from standard eeg recordings. *Lancet*, 357, pp. 183–188, 2001.

[59] R. M. Leahy, J. C. Mosher, M. C. Spencer, M. X. Huang, and J. D. Lewine. A study of dipole localization accuracy for MEG and EEG using a human skull phantom. *Electroencephalography and Clinical Neurophysiology*, 107(2), pp. 159–173, 1998.

[60] L. Lemieux, A. McBride, and J. W. Hand. Calculation of electrical potentials on the surface of a realistic head model by finite differences. *Phys. Med. Biol.*, 41, pp. 1079–1091, 1996.

[61] B. Lütkenhöner, R. Greenblatt, M. Hämäläinen, J. Mosher, M. Scherg, C. Tesche, and P. Valdes Sosa. Comparison between different approaches to the biomagnetic inverse problem — workshop report. In C. Aine, Y. Okada, G. Stroink, S. Swithenby, and C. Wood, editors, *Advances in Biomagnetism Research: Biomag96*. Springer-Verlag, New York, 1996. In press.

[62] J. Malmivuo and R. Plonsey. *Bioelectromagnetism: Principles and Applications of Bioelectric and Biomagnetic Fields*. Oxford University Press, New York, 1995.

[63] P. Maragos and R. W. Schafer. Morphological systems for multidimensional signal processing. *Proceedings of the IEEE*, 78(4), pp. 690–709, April 1990.

[64] G. Marin, C. Guerin, S. Baillet, L. Garnero, and G. Meunier. Influence of skull anisotropy for the forward and inverse problem in EEG: Simulation studies using FEM on realistic head models. *Human brain mapping*, 6, pp. 250–269, 1998.

[65] F. Marino, E. Halgren, J.-M. Badier, M. Gee, and V. Nenev. A finite difference model of electric field propagation in the human head: Implementation and validation. In *Proceedings of the 19th Annual Northeast Bioengineering Conference*, pp. 82–85. 1993.

[66] J. H. Martin. Cortical neurons, the EEG, and the mechanisms of epilepsy. In E. R. Kandel and J. H. Schwartz, editors, *Principles of Neural Science*, chapter 48, pp. 636–647. Elsevier, 1985.

[67] H. Matsuba, J. Vrba, and T. Cheung. Current dipole localization errors as a function of system noise and the number of sensors. In *Biomag96:Advances in Biomagnetism Research*. Springer-Verlag, 1996. Available on url:www.ctf.com.

[68] J. W. H. Meijs, O. W. Weier, M. J. Peters, and A. van Oosterom. On the numerical accuracy of the boundary element method. *IEEE Transactions on Biomedical Engineering*, 36(10), pp. 1038–1049, October 1989.

[69] A. Mitchell and D. Griffiths. *The Finite Difference Method in Partial Differential Equations*. John Willey and Sons, 1980.

[70] M. Mohr and B. Vanrumste. Fast solvers for an elliptic problem from dipole localization. In *Proceedings in Applied Mathematics and Mechanics*. Willey-InterScience, 2001. Submitted.

[71] J. C. Mosher, P. S. Lewis, and R. M. Leahy. Multiple dipole modeling and localization from spatio-temporal MEG data. *IEEE Transactions on Biomedical Engineering*, 39(6), pp. 541–557, June 1992.

[72] J. C. Mosher, M. E. Spencer, R. M. Leahy, and P. S. Lewis. Error bounds for EEG and MEG dipole source localization. *Electroencephalography and Clinical Neurophysiology*, 86, pp. 303–321, 1993.

[73] J. C. de Munck. The potential distribution in a layered anisotropic speroidal volume conductor. *Journal of Applied Physics*, 64(2), pp. 464–470, July 1988.

[74] J. C. de Munck, B. W. Van Dijk, and H. Spekreijse. Mathematical dipoles are adequate to discribe realistic generators of human brain activity. *IEEE Transactions on Biomedical Engineering*, 35(11), pp. 960–966, 1988.

[75] J. A. Nelder and R. Mead. A simplex method for function minimization. *Computer Journal*, 7, pp. 308–313, 1965.

[76] P. W. Nicholson. Specific impedance of cerebral white matter. *Experimental Neurology*, 13, pp. 386–401, 1965.

[77] E. Niedermeyer. Epileptic seizures disorders. In E. Niedermeyer and F. Lopes da Silva, editors, *Electroencephalography, Basic Principles, Clinical Applications and Related Fields*, chapter 27, pp. 405–510. Urban and Schwarzenberg, 2nd edition, 1987.

[78] E. Niedermeyer. Sleep and EEG. In E. Niedermeyer and F. Lopes da Silva, editors, *Electroencephalography, Basic Principles, Clinical Applications and Related Fields*, chapter 10, pp. 119–132. Urban and Schwarzenberg, 2nd edition, 1987.

[79] J. Ollikainen, M. Vauhkonen, P. Karjalainen, and J. Kaipio. Effects of local skull inhomogenities on EEG source estimation. *Medical engineering and physics*, 21, pp. 143–154, 1999.

[80] T. F. Oostendorp, J. Delbeke, and S. D. F. The conductivity of the human skull : Results of in vivo and in vitro measurements. *IEEE Transactions on Biomedical Engineering*, 47(11), pp. 1487–1492, 2000.

[81] R. D. Pascual-Marqui. Review of methods for solving the eeg inverse problem. *International journal of bioelectromagnetism*, 1(1), pp. 75–86, 1999.

[82] R. Plonsey and D. B. Heppner. Considerations of quasistationarity in electrophysiological systems. *Bulletin of Mathematical Biophysics*, 29(4), pp. 657–664, 1967.

[83] R. Pohlmeier, H. Buchner, G. Knoll, A. Reinäcker, R. Beckmann, and J. Pesh. The influence of skull-conductivity misspecification on inverse source localization in realistically shaped finite element head models. *Brain topography*, 9(3), pp. 157–162, 1997.

[84] W. H. Press, S. A. Teukolsky, W. T. Vetterling, and B. P. Flannery. *Numerical Recipes in C*. Cambridge University Press, 1995.

[85] Rojansky. *Electromagnetic fields and waves*. Dover, 1971.

[86] B. Roth, A. Gorbach, and S. Sato. How well does a three-shell model predict positions of dipoles in a realistically shaped head? *Electroencephalography and Clinical Neurophysiology*, 87, pp. 175–184, 1993.

[87] S. Rush and D. A. Driscoll. Current distribution in the brain from surface electrodes. *Anesth. Analgesia*, 47, pp. 717–723, 1968.

[88] S. Rush and D. A. Driscoll. EEG electrode sensitivity — an application of reciprocity. *IEEE Transactions on Biomedical Engineering*, BME-16(1), pp. 15–22, 1969.

[89] J. C. Russ. *The image processing handbook*. CRC Press, 1999.

[90] H. I. Saleheen and K. T. Ng. New finite difference formulations for general inhomogeneous anisotropic bioelectric problems. *IEEE Transactions on Biomedical Engineering*, 44(9), pp. 800–809, September 1997.

[91] Y. Salu, L. G. Cohen, D. Rose, S. Sato, C. Kufta, and M. Hallett. An improved method for localizing electric brain dipoles. *IEEE Transactions on Biomedical Engineering*, 37(7), pp. 699–705, July 1990.

[92] J. Sarvas. Basic mathematical and electromagnetic concepts of the biomagnetic inverse problem. *Phys. Med. Biol.*, 32(1), pp. 11–22, 1987.

[93] N. Schaul. The fundamental neural mechanisms of electroencephalography. *Electroencephalography and Clinical Neurophysiology*, 106, pp. 101–107, 1998.

[94] K. Scheirlinck. *Dipole source analysis applying FEM*. Master's thesis, Faculty of Applied sciences, Ghent University, 2000.

[95] M. Scherg. Functional imaging and localization of electromagnetic brain activity. *Brain Topography*, 5(2), pp. 103–111, 1992.

[96] H. A. Schlitt, L. Heller, R. Aaron, E. Best, and D. M. Ranken. Evaluation of boundary element methods for the EEG forward problem: Effect of linear interpolation. *IEEE Transactions on Biomedical Engineering*, 42(1), pp. 52–58, January 1995.

[97] J. Sijbers, B. Vanrumste, G. Van Hoey, P. Boon, M. Verhoye, A. Van der Linden, and D. Van Dyck. Automatic detection of EEG electrode markers on 3D MR data. In K. M. Hanson, editor, *Proc. of SPIE*, volume 3979, pp. 1476–1481. 2000.

[98] J. Sijbers, B. Vanrumste, G. Van Hoey, P. Boon, M. Verhoye, A. Van der Linden, and D. Van Dyck. Automatic localization of EEG electrode markers within 3D MR data. *Magnetic Resonance Imaging*, 18, pp. 485–488, 2000.

[99] F. Lopes da Silva. Computer-assisted EEG diagnosis: Pattern recognition techniques. In E. Niedermeyer and F. Lopes da Silva, editors,

Electroencephalography, Basic Principles, Clinical Applications and Related Fields, chapter 54, pp. 899–919. Urban and Schwarzenberg, 2nd edition, 1987.

[100] F. Lopes da Silva. Event-related potentials: Methodology and quantification. In E. Niedermeyer and F. Lopes da Silva, editors, *Electroencephalography, Basic Principles, Clinical Applications and Related Fields*, chapter 46, pp. 763–772. Urban and Schwarzenberg, 2nd edition, 1987.

[101] F. Lopes da Silva and A. Van Rotterdam. Biophysical aspects of EEG and magnetoencephalogram generation. In E. Niedermeyer and F. Lopes da Silva, editors, *Electroencephalography, Basic Principles, Clinical Applications and Related Fields*, chapter 3, pp. 29–41. Urban and Schwarzenberg, 2nd edition, 1987.

[102] E. J. Speckmann and C. E. Elger. Introduction to the neurophysiology, basis of the EEG and DC potentials. In E. Niedermeyer and F. Lopes da Silva, editors, *Electroencephalography, Basic Principles, Clinical Applications and Related Fields*, chapter 1, pp. 1–13. Urban and Schwarzenberg, 2nd edition, 1987.

[103] W. Theodore, R. Dorwart, M. Holmes, R. Porter, and G. Dichiro. Neuroimaging in epilepsy: comparison of PET, MRI and CT. In P. Wolf, M. Dara, and E. Janz, editors, *Advances in epileptology*, pp. 283–286. Raven Press, 1987.

[104] J. F. Thompson, B. K. Soni, and N. P. Weatherrill. *Handbook of grid generation*. CRC Press, 1998.

[105] G. Van Hoey. *Detectie en bronlokalisatie van epileptische hersenactiviteit met behulp van EEG-signalen*. Ph.D. thesis, Ghent University, 2000.

[106] G. Van Hoey, J. De Clercq, B. Vanrumste, R. Van de Walle, M. D'Havé, I. Lemahieu, and P. Boon. An artificial neural network for EEG dipole source localization. In *Abstract Book of the 10th World Congress of the International Society for Brain Electromagnetic Topography, October 9–13, Adelaide, Australia*, p. 39. 1999.

[107] G. Van Hoey, J. De Clercq, B. Vanrumste, R. Van de Walle, M. D'Havé, I. Lemahieu, and P. Boon. EEG dipole source localization using artificial neural networks. *Physics in Medicine and Biology*, 45, pp. 997–1011, 2000.

[108] G. Van Hoey, B. Vanrumste, P. Boon, M. D'Havé, and I. Lemahieu. Dipole model based detection of focal interictal EEG events. *Brain Topography*, 11(1), p. 86, 1998. Proceedings of the 9th World Congress of the International Society for Brain Electromagnetic Topography, New Orleans, Louisiana, October 6–9, 1998.

[109] G. Van Hoey, B. Vanrumste, P. Boon, M. D'Havé, R. Van de Walle, and I. Lemahieu. Accuracy and noise sensitivity of EEG dipole source localisation. In J. P. Veen, editor, *Proceedings of the ProRISC Workshop on Circuits, Systems and Signal Processing*, pp. 561–566. Mierlo, The Netherlands, November 1998.

[110] G. Van Hoey, B. Vanrumste, P. Boon, M. D'Havé, R. Van de Walle, and I. Lemahieu. Combined detection and source analysis of epileptic EEG spikes. In *Proceedings of 20th Annual International Conference of the IEEE Engineering in Medicine and Biology Society*, volume 20, part 4/6, pp. 2159–2162. Hong Kong, 1998.

[111] G. Van Hoey, B. Vanrumste, P. Boon, and I. Lemahieu. Reconstructing focal EEG sources with dipole and distributed source models. In *Proceedings of the URSI Forum*, p. 60. Union Radio-Scientifique Internationale, Ghent, Belgium, December 1997.

[112] G. Van Hoey, B. Vanrumste, P. Boon, R. Van de Walle, and I. Lemahieu. Automatic localization on MR images of spherical markers attached to scalp electrodes. *Electroencephalography and Clinical Neurophysiology*, 103(1), p. 197, 1997. Abstracts of the 14th International Congress of EEG and Clinical Neurophysiology, Florence, Italy, August 24-29, 1997.

[113] G. Van Hoey, B. Vanrumste, P. A. J. M. Boon, M. D'Havé, and I. Lemahieu. Detection and source analysis of epileptic EEG spikes based on dipole source localisation. *Epilepsia*, 39 suppl. 6, p. 74, 1998. Abstracts from the Annual Meeting of the American Epilepsy Society, San Diego, California, December 6–9, 1998.

[114] G. Van Hoey, B. Vanrumste, P. A. J. M. Boon, M. D'Havé, R. Van de Walle, and I. Lemahieu. Detection of focal epileptic EEG sources using dipole analysis in a realistically shaped head model. *Epilepsia*, 40 suppl. 2, p. 13, 1999. Abstracts from the 23rd International Epilepsy Congress, Prague, Czech Republic, September 12–17, 1999.

[115] G. Van Hoey, B. Vanrumste, M. D'Havé, R. Van de Walle, I. Lemahieu, and P. Boon. The influence of measurement noise and electrode mislocalisation on EEG dipole-source localisation. *Med. Biol. Eng. Comput.*, 38(3), pp. 287–296, 2000.

[116] G. Van Hoey, B. Vanrumste, C. Phillips, P. Boon, M. D'Havé, R. Van de Walle, and I. Lemahieu. Interpolation technique for scalp potentials based on spherical and realistically shaped head models. In *Fifth International Conference on Functional Mapping of the Human Brain*, volume 9, nr 6 part 2, p. S180. Academic Press, Düsseldorf, 1999.

[117] G. Van Hoey, B. Vanrumste, R. Van de Walle, P. Boon, and I. Lemahieu. Automatic marker recognition on MR images for EEG electrode localization. In J. P. Veen, editor, *Proceedings of the ProRISC Workshop on Circuits, Systems and Signal Processing*, pp. 625–630. Mierlo, The Netherlands, November 1997.

[118] G. Van Hoey, B. Vanrumste, R. Van de Walle, P. Boon, I. Lemahieu, M. D'Havé, and K. Vonck. Detection and localization of epileptic brain activity using an artificial neural network for dipole source analysis. In *Proceedings of the EUSIPCO2000 Conference, September 5–8, 2000, Tampere, Finland*. 2000.

[119] G. Van Hoey, B. Vanrumste, R. Van de Walle, G. Boterbergh, I. Lemahieu, M. D'Havé, and P. Boon. Interpolation of spatially sampled potential distributions in electroencephalography. In *Abstract Book of the Fifth Conference of the European Society for Engineering and Medicine*, pp. 165–166. Barcelona, May 1999.

[120] G. Van Hoey, B. Vanrumste, R. Van de Walle, I. Lemahieu, and P. Boon. Automatic localization of scalp electrodes using markers visible on MR images. *Medical and Biological Engineering and Computing*, 35, suppl. part I, p. 677, 1997. Proceedings of the World Congress on Medical Physics and Biomedical Engineering, Nice, France, September 14–19, 1997.

[121] G. Van Hoey, B. Vanrumste, R. Van de Walle, I. Lemahieu, and P. Boon. Automatic localization on MR images of spherical markers attached to scalp electrodes. In *Book of abstracts European Society for Engineering and Medicine (ESEM), 4th Conference*, pp. 287–288. Warsaw, 1997.

[122] B. Vanrumste, G. Van Hoey, P. Boon, M. D'Havé, and I. Lemahieu. The accuracy of the finite difference method applied in the forward prob-

lem of EEG source analysis. In *Proceedings of the 8th International IMEKO conference on Measurement in Clinical Medicine*, pp. 35–38. Dubrovnik, September 1998.

[123] B. Vanrumste, G. Van Hoey, P. Boon, M. D'Havé, and I. Lemahieu. Inverse calculations in EEG source analysis applying the finite difference method, reciprocity and lead fields. In *Proceedings of the 20th Annual International Conference of the IEEE Engineering in Medicine and Biology Society*, pp. 2112–2115. 1998.

[124] B. Vanrumste, G. Van Hoey, P. Boon, M. D'Havé, and I. Lemahieu. The need for realistically shaped head models in EEG source analysis. In *ACOMEN'98 Advanced Computational Methods in Engineering*, pp. 527–535. Maastricht, The Netherlands, 1998.

[125] B. Vanrumste, G. Van Hoey, P. Boon, M. D'Havé, and I. Lemahieu. Reciprocity and leadfields used in the numerical inverse procedure of EEG source analysis. In *Brain Topography*, volume 11, p. 86. 1998. Proceedings of the 9th World Congress of the International Society for Brain Electromagnetic Topography, New Orleans, Louisiana, October 6-9, 1998.

[126] B. Vanrumste, G. Van Hoey, P. Boon, M. D'Havé, R. Van de Walle, and I. Lemahieu. Dipole mapping on magnetic resonance images of patients with epilepsy. In J. P. Veen, editor, *Proceedings ot the ProRISC Workshop on Circuits, Systems and Signal Processing*, pp. 643–645. Mierlo, The Netherlands, November 1997.

[127] B. Vanrumste, G. Van Hoey, P. Boon, M. D'Havé, R. Van de Walle, and I. Lemahieu. Mapping on MR images of current dipoles in epilepsy. *Medical and Biological Engineering and Computing*, 35, suppl. part I, p. 678, 1997. Proceedings of the World Congress on Medical Physics and Biomedical Engineering, Nice, France, September 14–19, 1997.

[128] B. Vanrumste, G. Van Hoey, P. Boon, M. D'Havé, R. Van de Walle, and I. Lemahieu. Mapping on MR images of current dipoles obtained from patients with refractory partial epilepsy. *Electroencephalography and Clinical Neurophysiology*, 103(1), p. 78, 1997. Abstracts of the 14th International Congress of EEG and Clinical Neurophysiology, Florence, Italy, August 24-29, 1997.

[129] B. Vanrumste, G. Van Hoey, P. A. J. M. Boon, M. D'Havé, and I. Lemahieu. Dipole analysis using the finite difference method. *Epilep-*

sia, 39 suppl. 6, p. 74, 1998. Abstracts from the Annual Meeting of the American Epilepsy Society, San Diego, California, December 6–9, 1998.

[130] B. Vanrumste, G. Van Hoey, P. A. J. M. Boon, M. D'Havé, R. Van de Walle, and I. Lemahieu. Realistically shaped head models versus three-shell spherical head models in EEG source analysis of interictal events. *Epilepsia*, 40 suppl. 2, p. 13, 1999. Abstracts from the 23rd International Epilepsy Congress, Prague, Czech Republic, September 12–17, 1999.

[131] B. Vanrumste, G. Van Hoey, M. D'Havé, P. Boon, and I. Lemahieu. The finite difference method applied in EEG source analysis. In *Proceedings of the URSI Forum*, p. 61. Union Radio-Scientifique Internationale, Ghent, Belgium, December 1997.

[132] B. Vanrumste, G. Van Hoey, M. D'Havé, P. Boon, R. Van de Walle, and I. Lemahieu. EEG dipole mapping on magnetic resonance images. In *Book of abstracts European Society for Engineering and Medicine (ESEM), 4th Conference*, pp. 285–286. Warsaw, 1997.

[133] B. Vanrumste, G. Van Hoey, M. D'Havé, P. Boon, R. Van de Walle, and I. Lemahieu. The finite difference method and reciprocity applied in EEG source analysis. In *Abstract Book of the 5th Conference of the European Society for Engineering and Medicine, ESEM(Barcelona)*, pp. 215–216. 1999.

[134] B. Vanrumste, G. Van Hoey, R. Van de Walle, M. D'Havé, I. Lemahieu, and P. Boon. The influence of the ventricular system in EEG dipole analysis. In *10th world congress of the internatonal society for brain electromagnetic topography, program and abstracts*, p. 26. 1999.

[135] B. Vanrumste, G. Van Hoey, R. Van de Walle, M. D'Havé, I. Lemahieu, and P. Boon. Dipole location errors in electroencephalogram source analysis due to volume conductor model errors. *Med. Biol. Eng. Comput.*, 38(5), pp. 528–534, 2000.

[136] B. Vanrumste, G. Van Hoey, R. Van de Walle, M. D'Havé, I. Lemahieu, and P. Boon. Localization errors due to noise versus localization errors due to the 3-shell spherical head model. In *Proceedings of the 3rd international conference on bioelectromagnetism*, pp. 67–68. 2000.

[137] B. Vanrumste, G. Van Hoey, R. Van de Walle, M. D'Havé, I. Lemahieu, and P. Boon. Comparing the performance of EEG dipole source analysis

utilizing a spherical and realistic head model in the presence of noise. *Medical Engineering & Physics*, 2001. Submitted.

[138] B. Vanrumste, G. Van Hoey, R. Van de Walle, M. D'Havé, I. Lemahieu, and P. Boon. The validation of the finite difference method and reciprocity for solving the inverse problem in EEG dipole source analysis. *Brain Topography*, 2001. In press.

[139] B. Vanrumste, G. Van Hoey, R. Van de Walle, P. Van Hese, M. D'Havé, I. Lemahieu, and P. Boon. The realistic versus the spherical head model in EEG dipole source analysis in the presence of noise. In *Proceedings of the 23th Annual International Conference of the IEEE Engineering in Medicine and Biology Society*. 2001. In press.

[140] R. Warwick and P. L. Williams. *Gray's anatomy*. Longman, 1973.

[141] D. Weinstein, L. Zhukov, and C. Johnson. Lead-field bases for electroencephalography source imaging. *Annals of biomedical engineering*, 28, pp. 1059–1065, 2000.

[142] J. G. Witwer, G. J. Trezek, and D. L. Jewett. The effect of media inhomogeneities upon intracranial electrical fields. *IEEE Transactions on Biomedical Engineering*, BME-19(5), pp. 352–362, September 1972.

[143] G. Wuytens and K. Van Damme. *Description of Brainlab for windows*. OSG bvba, Bussestraat 17, B-2840 Rumst, Belgium, 1996.

[144] Yan.Y., P. Nunez, and R. Hart. Finite element model of the human head: Scalp potentials due to dipole sources. *Med. Biol. Eng. Comput.*, 29, pp. 475–481, September 1991.

[145] B. Yvert, O. Bertrand, M. Thévenet, J. F. Echallier, and J. Pernier. A systematic evaluation of the spherical model accuracy in EEG dipole localization. *Electroencephalography and Clinical Neurophysiology*, 102, pp. 452–459, May 1997.